ISTANBUL TECHNICAL UNIVERSITY ★ GRADUATE SCHOOL

TAILORING MICROSTRUCTURE AND MORPHOLOGY IN PRINTED CARBON NANOMATERIALS FOR STRAIN SENSING

Ph.D. THESIS

Adel ALRAI

Department of Aeronautical & Astronautical Engineering

Aeronautical & Astronautical Engineering Programme

JUNE 2025

ISTANBUL TECHNICAL UNIVERSITY ★ GRADUATE SCHOOL

TAILORING MICROSTRUCTURE AND MORPHOLOGY IN PRINTED CARBON NANOMATERIALS FOR STRAIN SENSING

Ph.D. THESIS

Adel ALRAI
(511192101)

Department of Aeronautical & Astronautical Engineering

Aeronautical & Astronautical Engineering Programme

Thesis Advisor: Prof. Dr. Hülya CEBECİ
Thesis Co-Advisor: Assoc. Prof. Dr. Elif ÖZDEN YENİGÜN

JUNE 2025

İSTANBUL TEKNİK ÜNİVERSİTESİ ★ LİSANSÜSTÜ EĞİTİM ENSTİTÜSÜ

GERİNİM ALGILAMA İÇİN BASKILI KARBON NANOMALZEMELERDE MİKROSTRUKTUR VE MORFOLOJİNİN ÖZELLEŞTİRİLMESİ

DOKTORA TEZİ

Adel ALRAİ
(511192101)

Uçak ve Uzay Mühendisliği Anabilim Dalı

Uçak ve Uzay Mühendisliği Programı

Tez Danışmanı: Prof. Dr. Hülya CEBECİ
Eş Danışman: Doç. Dr. Elif ÖZDEN YENİGÜN

HAZİRAN 2025

Adel ALRAI, a Ph.D. student of ITU Graduate School student ID 511192101, successfully defended the thesis/dissertation entitled “TAILORING MICROSTRUCTURE AND MORPHOLOGY IN PRINTED CARBON NANOMATERIALS FOR STRAIN SENSING”, which he prepared after fulfilling the requirements specified in the associated legislations, before the jury whose signatures are below.

Thesis Advisor : **Prof. Dr. Hülya CEBECİ** ....
Istanbul Technical University

Co-advisor : **Assoc. Prof. Dr. Elif ÖZDEN YENİGÜN** ....
Royal College of Art

Jury Members : **Prof. Dr. Fevzi Çakmak CEBECİ** ....
Sabancı University

Asst. Prof. Dr. Ramazan YENİÇERİ ....
Istanbul Technical University

Prof. Dr. Akram ALOMAINY ....
Queen Mary University of London

Asst. Prof. Dr. Semih DOĞU ....
Istanbul Technical University

Asst. Prof. Dr. Kaan YILDIZ ....
Istanbul Technical University

Date of Submission : 30 May 2025
Date of Defense : 17 June 2025

To my family and all my beloved ones, near and far, especially those from whom I have been parted,

FOREWORD

It took me approximately 2,145 days to complete this PhD thesis, during which I was only able to see my family once, for 18 days. That's less than 1% of the total time. Although technology made it possible to video chat and communicate daily, it was never quite enough. Still, each evening, a simple "good night" message on WhatsApp gave me the peace of mind I needed to sleep—and the strength to start my work the next day—knowing they were safe. Despite the distance, my family supported me in every way they could. For that, and for every day we could not be together, I dedicate this thesis to them.

While I wasn't lucky enough to have direct support from my family during these years, I was incredibly fortunate to find a home away from home with the ACUNER family. I would like to express my deepest appreciation to Numan Bey and Firdevs Hanım Acuner for their kindness, care, and unwavering support. My gratitude also extends to my friend Mansur ACUNER, whose presence and friendship made a meaningful difference throughout this journey.

The core idea behind the research presented in this thesis was inspired by my supervisor, Prof. Hülya CEBECİ. I am deeply grateful to her for giving me the opportunity to develop this work and for welcoming me as part of ITUarc/ Istanbul Technical University Aerospace Research Center (ITU ARC). Her mentorship and guidance were instrumental throughout this journey. I sincerely appreciate every moment she dedicated, whether to help make progress or to overcome a challenge. Her unwavering support was critical at every stage.

I would also like to extend my sincere thanks to my co-supervisor, Assoc. Prof. Dr. Elif ÖZDEN YENİGÜN, for her interest and insightful comments. Her kindness was a constant source of motivation, and her constructive input significantly enriched the quality of this thesis.

I am thankful to my jury members for their valuable feedback and contributions:

- Prof. Dr. Fevzi C. CEBECİ, for his comments and support during testing and measurements in the laboratories at Sabancı University.
- Asst. Prof. Dr. Ramazan YENIÇERİ, for his insights into wireless sensing applications.
- Prof. Dr. Akram ALOMAINY, for his valuable comments regarding wireless sensing.

I also extend my gratitude to Asst. Prof. Dr. Kaan YILDIZ, whose technical support and generous use of his time helped me overcome many challenges.

I would also like to thank Asst. Prof. Dr. Alptekin YILDIZ for his feedback, and Dr. İpek ÖSKEN for her kindness and support since my first day at ITU ARC.

Special thanks go to Asst. Prof. Dr. Semih DOĞU and his student Ahmet Caner GÜL, whose expertise and support were essential in developing and testing wireless antenna systems.

I am grateful to Prof. İbrahim ÖZKOL, Director of ITU ARC, whose warm greetings and kind presence at the center brought moments of encouragement that meant more than words.

I am thankful for Dr. Deniz KÖKEN, the co-PI of the industrial project, for his guidance and contributions throughout the research.

To all ITU ARC members, past and present, thank you for the moments we shared, the knowledge exchanged, and the time we sheared together. I am particularly thankful to Yunus Emre BOZKURT, Dilan ARSLAN-ÇATAK, Melisa DINÇER, Uğur EMANETOĞLU, Suat EBIL, Ramazan YÜKSEL, Asya YILDIZ, Furkan TEPE, and Ersin BEYHAN for their direct and indirect contributions to this work.

To my dear friend Arda ÇIKAROĞLU—thank you for your friendship, which made the hardest parts of this journey feel lighter. I am deeply grateful for your constant presence, support, and, of course, your unforgettable cheesecake. My gratitude also extends to your wonderful family for their kindness and warmth.

A special mention to Ragıp ÖZDIKEN of ITU ARC —your cheerful spirit and kind gestures brought joy and warmth to the environment we worked in every day.

I would like to thank Yelda YORULMAZ and Onur ZIRHLI from Sabancı University for their assistance with morphological assessments and other measurements.

Finally, I would like to thank TUSAŞ for their valuable support and funding of my thesis project (Project No: TM1041) and Scientific and Technological Research Council of Türkiye (TÜBİTAK) for travel funding support to attend conferees abroad.

May 2025

Adel ALRAI
(Mechanical Engineer)

TABLE OF CONTENTS

Page

ABBREVIATIONS

BVID	: Barely Visible Impact Damage
CB	: Carbon Black
CFRP	: Carbon Fiber-Reinforced Polymer
CNC	: Cellulose Nanocrystal
CNF	: Cellulose Nanofiber
CNT	: Carbon Nanotube
CNTCT	: Carbon Nanotube (supplied by Cheap Tubes)
CNTNC	: Carbon Nanotube (supplied by Nanocyl)
CNTNI	: Carbon Nanotube (supplied by NanoIntegris)
CNTSA	: Carbon Nanotube (supplied by Sigma-Aldrich)
CPDMS	: Carbon Black- Polydimethylsiloxane
DI-water	: Distilled Water
FBG	: Fiber Bragg Grating
FRP	: Fiber Reinforced Polymer
GF	: Gauge Factor
GFRP	: Glass Fiber-Reinforced Polymer
GNP	: Graphene Nanoplatelets
IF	: Intermediate Frequency
IoT	: Internet of Things
IPA	: Isopropyl Alcohol
LIG	: Laser-Induced Graphene
LVR	: Linear Viscoelastic Region
MFC	: Macro Fiber Composites
MWCNT	: Multi-Walled Carbon Nanotubes
NDT	: Nondestructive Testing
PDMS	: Polydimethylsiloxane
PEG	: Polyethylene Glycol
PEO	: Polyethylene Oxide
PET	: Polyethylene terephthalate
PVA	: Polyvinyl Alcohol

PVDF-HFP : Poly(Vinylidene Fluoride-Hexafluoropropylene)

PWAS : Piezoelectric wafer active sensors

PZT : Lead zirconate titanate

RFID : Radio-Frequency Identification

rGO : Reduced Graphene Oxide

S_{11} : Reflection Coefficient

SDS : Sodium Dodecyl Sulfate

SEM : Scanning Electron Microscopy

SHM : Structural Health Monitoring

SWCNT : Single-Walled Carbon Nanotubes

TCR : Temperature Coefficient of Resistance

TEM : Transmission Electron Microscopy

TPU : Thermoplastic Polyurethane

TX-100 : Triton X-100 (a nonionic surfactant)

UAV : Unmanned Aerial Vehicle

UTM : Universal Testing Machine

VNA : Vector Network Analyzer

SYMBOLS

A	: Area
Hz	: Hertz
J	: Joule
L	: Length
MHz	: Megahertz
mN/m	: Millinewtons Per Meter
N	: Newton
Pa	: Pascal
Pa·s	: Pascal-seconds
R	: Resistance
R_0	: Initial Resistance
R^2	: Coefficient of Determination
Sec	: Second
ε	: Strain
ρ	: Resistivity
Ω	: Ohm
GHz	: Gigahertz
GPa	: Gigapascal
G'	: Storage Modulus
G''	: Loss Modulus
G^*	: Complex Modulus
ν	: Poisson's ratio

LIST OF TABLES

Page

LIST OF FIGURES

Page

TAILORING MICROSTRUCTURE AND MORPHOLOGY IN PRINTED CARBON NANOMATERIALS FOR STRAIN SENSING

SUMMARY

Composites offer significant advantages in the aerospace industry, including reduced structural weight, lower fuel consumption, and enhanced resistance to corrosion. However, unlike metals, which exhibit well-characterized mechanical behavior and predictable service life, composites display greater variability in mechanical performance. Their inherent heterogeneity makes them susceptible to various failure mechanisms, such as delamination, fiber fracture, and matrix microcracking. To address these challenges, Non-Destructive Testing (NDT) techniques have been developed to detect and monitor damage without compromising material integrity. Nevertheless, NDT methods share common limitations, including slow testing speeds, complex result interpretation, and limited detection of deep or small defects. While effective for periodic inspections, many NDT methods lack the capability for continuous real-time monitoring.

As an alternative, Structural Health Monitoring (SHM) offers advanced early damage detection. Unlike NDT, which requires manual inspection and on-site evaluation and often leads to increased aircraft downtime, SHM enables continuous in-flight monitoring of structural components, reducing inspection time by up to 44%. This capability translates to an overall maintenance cost reduction of approximately 30%. Three main sensor technologies used in SHM systems are piezoelectric transducers, optical fiber sensors, and strain gauges. However, these technologies face challenges related to wiring and integration complexity, pre-surface treatment requirements, and noise cancellation.

In the past decade, piezoresistive sensors have emerged as a promising solution for strain measurement in composite structures, offering benefits such as compatibility with composite materials, lightweight and tailored designs, and excellent sensing performance. Their integration into composites has proven both practical and effective. The sensing mechanism of these materials relies on dimensional changes that occur when the sensor is subjected to external stimuli, altering the distance between nanomaterials and leading to a change in resistance. In other words, the piezoresistive behavior depends on the physical dimensions of the nanomaterials. Low-aspect-ratio nanomaterials, such as zero-dimensional ones, result in higher resistance changes than one-dimensional particles.

Chapter 2 provides a summary of sensor technologies commonly used in SHM, including piezoelectric sensors, optical fiber sensors, and metal strain gauges. A comprehensive literature review is presented on the state-of-the-art in carbon-based piezoresistive sensors. Various carbon nanomaterials reported in the literature, such as carbon nanotubes (CNTs), carbon nanofibers (CNFs), graphene, and carbon black (CB), are examined in detail. The review also discusses the effectiveness of different

dispersants, including cellulose nanocrystals (CNCs), sodium dodecyl sulfate (SDS), and Triton X-100 (TX-100), in dispersing these nanomaterials in aqueous media.

The chapter further explores the influence of sensor design parameters such as length, width, thickness, and geometry on electromechanical behavior. Various methods for integrating carbon-based materials with composite structures are reviewed, such as embedding the materials into the polymer matrix (self-sensing), coating fibers prior to composite fabrication, coating the surface of cured composites, and direct printing onto composite substrates.

In addition, the multifunctional potential of carbon nanomaterial-based sensors is surveyed, with attention given to their ability to perform simultaneous sensing and other functionalities. Finally, antennas integrated with composite structures for use as strain or damage sensors are discussed, although this area is still at an early stage of development.

Despite significant efforts, a comprehensive understanding of the electromechanical performance of carbon-based piezoresistive strain sensors compatible with composite structures remains lacking. Current carbon-based strain sensors are typically printed or engraved on an intermediate polymer substrate, such as Kapton film, which is then adhered to the composite surface. Although these solutions have demonstrated good compatibility with fiber-reinforced plastic (FRP) composites, their fabrication process is often multistep and requires careful attention to ensure proper adhesion.

Chapter 3 introduces various types of CNTs, CNFs, graphene, and CB. Using these materials, both standalone and hybrid formulations were developed, and their dispersibility was assessed. The chapter also describes the fabrication of glass fiber-reinforced polymers (GFRPs) as composite substrates. Four unique strain sensor designs were developed: line, grid, o-line, and omnidirectional. The formulated inks were integrated using three methods: direct coating, screen printing, and spray printing.

Chapter 4 discusses the printability and applicability of the developed inks based on the integration method. While direct ink application onto GFRPs was straightforward, it was limited by the deposited amount of ink and the lack of pattern precision. Screen printing and spray printing offered more precise ink deposition and better control over design. The sensor designs introduced in Chapter 3 were successfully demonstrated using these two printing methods. The screen printing method required careful adjustment and tailoring of the inks to improve wettability and enhance printing quality. This was achieved by controlling total solid content, solvent mixtures, and using different surfactant ratios. Notably, screen-printing of aqueous-based carbon inks was demonstrated using both high-viscosity inks and low-viscosity inks, the latter achieved by using a water/isopropyl alcohol (IPA) solvent mixture. Rheological tests were conducted to correlate printing quality with changes in rheological properties. Similarly, inks were prepared for spray printing, albeit with much lower viscosities compared to those used for screen printing. The spray printing method was shown to be easily adaptable for the aerospace industry. By using various carbon inks and adjusting their content, their printability was successfully demonstrated.

In Chapter 5, the electromechanical performance of various sensors printed using different methods was investigated. CNT/CNC aqueous-based inks with various ratios were directly applied onto GFRP coupons. Following the ASTM D3039 testing standard, the host composites were subjected to tensile testing up to 1.3% strain. The sensitivity and linearity of the sensors depended on the CNT/CNC ratio. A modified fitting model was employed to differentiate between sensor performances.

Further in Chapter 5, using the sensor patterns designed earlier and optimized ink formulations, including CNTs (from both research- and industrial-grade sources), CNF, CB, and various hybrids—sensors were printed onto GFRP coupons and subjected to 50-cycle cyclic loading at 0.6% strain. Sensor performance was quantified in terms of reliability, sensitivity, and linearity. Results showed that performance depended on pattern geometry. Sensitivity correlated with sensor length, with single-leg designs (line, o-line) showing higher sensitivity and more damage than multi-leg designs (grid, omnidirectional).

Additionally in Chapter 5, electromechanical behavior of nanomaterials was further compared using the grid pattern. Resistance changes in 1D sensors (CNT, CNF) varied: research-grade CNT and CNF showed downward drift; industrial-grade CNT showed upward drift. All had sensitivity near 2, similar to metal strain gauges. CB (0D) showed slight upward drift and sensitivity up to 15× higher. Graphene (2D) also showed high sensitivity and downward drift. Hybrid sensors (CB with CNT or CNF) demonstrated significant improvements in sensitivity and reliability. All sensors showed good linearity.

Continuing in Chapter 5, spray-printed sensors showed similar trends. However, finer lines resulted in less reliable but more sensitive behavior, especially in CB sensors, due to line width effects.

Moreover in Chapter 5, complementary tests included higher strain loading (1.2%) on screen-printed CNT sensors, SEM imaging before and after cycling, and directional tests. Grid sensors' transverse sensitivity varied with filler type, indicating a need for design optimization. Omnidirectional CNT sensors confirmed multidirectional sensing. Thermal tests showed TCR depended on filler dimensionality, with 1D most sensitive. Impact tests revealed sensitivity decreased from 0D to hybrid to 1D.

In Chapter 6, the investigation focused on patch antenna sensors printed onto GFRP substrates. The host composites were subjected to both tensile and bending forces to evaluate the sensors' mechanical and electromagnetic performance. Frequency response tests revealed that the electromagnetic properties of the antennas were sensitive to mechanical deformation, with measurable shifts in resonant frequency corresponding to the applied strain. These findings demonstrate the potential of printed patch antennas for use as strain sensors in composite structures.

GERİNİM ALGILAMA İÇİN BASKILI KARBON NANOMALZEMELERDE MİKROSTRUKTUR VE MORFOLOJİNİN ÖZELLEŞTİRİLMESİ

ÖZET

Kompozit malzemeler, havacılık endüstrisinde yapısal ağırlığın azaltılması, yakıt tüketiminin düşürülmesi ve korozyona karşı direnç gibi önemli avantajlar sunmaktadır. Ancak, mekanik davranışları iyi tanımlanmış ve hizmet ömürleri öngörülebilir olan metallerin aksine, kompozitler daha değişken mekanik performans sergilemektedir. Doğaları gereği heterojen yapıya sahip olan kompozit malzemeler, delaminasyon, lif kırılması ve matris mikroskopik çatlaklar gibi çeşitli hasar mekanizmalarına karşı daha hassastır. Bu tür zorlukların üstesinden gelmek amacıyla, malzeme bütünlüğünü bozmadan hasarın tespiti ve izlenmesine olanak tanıyan Tahribatsız Muayene Teknikleri (NDT) geliştirilmiştir. Ancak, NDT yöntemleri; düşük test hızları, sonuçların yorumlanmasındaki karmaşıklık ve derin ya da küçük boyutlu kusurların tespitindeki sınırlamalar gibi ortak dezavantajlara sahiptir. Dönemsel denetimler için etkili olsalar da, pek çok NDT yöntemi sürekli ve gerçek zamanlı izleme kabiliyetinden yoksundur.

Alternatif bir yöntem olarak, Yapısal Sağlık İzleme (SHM) sistemleri erken hasar tespiti konusunda ileri düzey olanaklar sunmaktadır. NDT yöntemlerinin aksine, genellikle manuel inceleme ve sahada değerlendirme gerektiren ve bu nedenle uçakların hizmet dışı kalma süresini artıran süreçler yerine, SHM sistemleri yapısal bileşenlerin uçuş esnasında kesintisiz olarak izlenmesine imkan tanır. Bu sayede denetim süresi %44'e varan oranlarda azaltılabilir ve bu yetkinlikle, toplam bakım maliyetlerinde yaklaşık %30'luk bir azalma sağlanabilir. SHM sistemlerinde yaygın olarak kullanılan üç temel sensör teknolojisi; piezoelektrik dönüştürücüler, optik fiber sensörler ve gerinim ölçerlerdir. Ancak bu teknolojiler; kablolama ve entegrasyon zorlukları, yüzey ön işlem gereksinimleri ve gürültü giderme konularında çeşitli teknik engellerle karşı karşıyadır.

Son on yılda, piezorezistif sensörler, kompozit yapılarda gerinim ölçümü için umut verici bir çözüm olarak öne çıkmıştır. Bu sensörler; kompozit malzemelerle uyumluluk, hafiflik, özelleştirilebilir tasarım imkanı ve üstün algılama performansı gibi avantajlar sunmaktadır. Kompozit yapılar içerisine entegrasyonları hem pratik hem de etkili bulunmuştur. Bu malzemelerin algılama mekanizması, dış etkilere maruz kaldığında sensörün boyutsal değişime uğramasıyla, nanomalzemeler arasındaki mesafenin değişmesi ve buna bağlı olarak elektriksel dirençte meydana gelen değişim esasına dayanır. Başka bir ifadeyle, piezorezistif davranış, nanomalzemelerin fiziksel boyutlarına bağlıdır. Düşük en-boy oranına sahip nanomalzemeler, örneğin sıfır boyutlu (0B) yapılar, bir boyutlu (1B) partiküllere kıyasla daha yüksek direnç değişimlerine yol açmaktadır.

2. bölüm, literatürde bildirilen çeşitli karbon nanomalzemeleri özetlemektedir; bunlar arasında karbon nanotüpler (CNT'ler), karbon nanolifler (CNF'ler), grafen ve karbon siyahı (CB) yer almaktadır. Literatür taramasında ayrıca, bu nanomalzemelerin sulu

ortamlarda başarılı bir şekilde dağılmasını sağlamak amacıyla selüloz nanokristaller (CNC), sodyum dodesil sülfat (SDS) ve Triton X-100 (TX-100) gibi farklı dispersiyon ajanlarının kullanımına da yer verilmiştir. Bununla birlikte, karbon esaslı malzemelerin kompozitlerle entegrasyonuna yönelik çeşitli yöntemler de incelenmiştir. Bu yöntemler arasında; karbonun polimer matris içerisine dağıtıldığı kendinden algılayıcı malzeme yaklaşımları, kompozit üretiminden önce liflerin doğrudan kaplanması, kompozit yüzeyine doğrudan kaplama yapılması ve kompozit yüzeyine baskı teknikleri ile entegrasyon yer almaktadır.

Tüm çabalara rağmen, kompozit yapılarla uyumlu karbon esaslı piezorezistif gerinim sensörlerinin elektromekanik performansına dair kapsamlı bir anlayış henüz tam olarak sağlanamamıştır. Günümüzde kullanılan karbon bazlı gerinim sensörleri genellikle ara bir polimer tabaka, örneğin Kapton filmi, üzerine baskı veya kazıma yoluyla üretilmekte ve bu tabaka daha sonra kompozit yüzeyine yapıştırılmaktadır. Bu tür çözümler, lif takviyeli plastic/polimer (FRP) kompozitlerle iyi bir uyumluluk göstermiş olsa da, üretim süreçleri çok aşamalıdır ve uygun yapışmanın sağlanabilmesi için dikkatli işlem kontrolü gerektirmektedir.

3. bölüm, CNT'ler, CNF'ler, grafen ve CB gibi çeşitli karbon nanomalzeme türlerini tanıtmaktadır. Bu malzemeler kullanılarak hem tek bileşenli hem de hibrit formülasyonlar geliştirilmiş ve dağılım özellikleri değerlendirilmiştir. Ayrıca, kompozit alt tabaka olarak cam elyaf takviyeli polimerlerin (GFRP) üretim süreci de ayrıntılı olarak açıklanmıştır. Dört farklı özgün gerinim sensörü deseni geliştirilmiştir: line, grid, o-line ve omnidirectional. Hazırlanan iletken mürekkepler üç farklı yöntemle kompozit yüzeylerine entegre edilmiştir: doğrudan kaplama (direct coating), serigrafi baskı (screen printing) ve püskürtme baskı (spray printing).

4. bölüm, geliştirilen iletken mürekkeplerin baskı kabiliyeti ve uygulanabilirliğini, entegrasyon yöntemine bağlı olarak ele almaktadır. Mürekkebin doğrudan GFRP yüzeyine uygulanması yöntemi oldukça basit olmakla birlikte, bırakılan mürekkep miktarının sınırlı olması ve desen hassasiyetinin yetersizliği gibi dezavantajlar barındırmaktadır. Buna karşılık, serigrafi baskı ve püskürtme baskı yöntemleri, mürekkebin daha hassas bir şekilde uygulanmasına ve tasarım üzerinde daha iyi kontrol sağlanmasına olanak tanımıştır. 3. bölümde tanıtılan sensör desenleri, bu iki baskı yöntemi ile başarılı bir şekilde hayata geçirilmiştir. Serigrafi baskı yöntemi ile mürekkebin yüzeye düzgün yayılabilmesi ve baskı kalitesinin artırılabilmesi için dikkatli bir şekilde uygulama yapılması gerekmiştir. Bu uygulama, toplam katı madde içeriği, çözücü karışımları ve yüzey aktif madde oranlarının ayarlanması yoluyla gerçekleştirilmiştir. Özellikle, su bazlı karbon mürekkeplerin hem yüksek viskoziteli hem de düşük viskoziteli halleriyle serigrafi baskısı yapılabileceği gösterilmiştir. Bu sonuca düşük viskoziteye sahip su/izopropil alkol (IPA) çözücü karışımı kullanılarak ulaşılmıştır. Baskı kalitesi ile reolojik özelliklerdeki değişimler arasındaki ilişkiyi ortaya koymak amacıyla reolojik testler uygulanmıştır. Benzer şekilde, püskürtme baskı için de düşük viskoziteli mürekkepler hazırlanmıştır. Serigrafi baskıya kıyasla daha düşük viskoziteye sahip bu mürekkeplerle yapılan püskürtme baskı yöntemi, havacılık endüstrisine kolayca adapte edilebilecek bir yöntem olarak öne çıkmıştır. Farklı karbon esaslı mürekkeplerin içeriği ayarlanarak bu yönteme uygunlukları başarıyla gösterilmiştir.

5. bölümde, farklı baskı yöntemleri kullanılarak üretilen çeşitli sensörlerin elektromekanik performansları incelenmiştir. Farklı oranlarda hazırlanmış CNT/CNC su bazlı mürekkepler, doğrudan GFRP numuneler üzerine uygulanmıştır. ASTM

D3039 test standardına uygun olarak, ana kompozit yapılar %1,3'e kadar çekme gerinimi altında test edilmiştir. Sensörlerin duyarlılığı (sensitivite) ve doğrusal yanıtları (lineerlik), kullanılan CNT/CNC oranına bağlı olarak değişiklik göstermiştir. Ayrıca, sensörlerin performanslarını ayırt edebilmek amacıyla değiştirilmiş bir uyum (fitting) modeli kullanılmıştır.

5. bölümün devamında, daha önce tasarlanan çeşitli sensör desenleri ve optimize edilmiş mürekkep formülasyonları kullanılarak, araştırma ve endüstriyel kaynaklı 1B CNT'ler, 1B CNF, 0B karbon CB ve CB'nin CNT ve CNF ile oluşturduğu çeşitli hibrit kompozisyonlar dahil olmak üzere sensörler GFRP numuneleri üzerine basılmıştır. Ayrıca, ticari olarak temin edilen 2B grafen mürekkebi de GFRP yüzeylerine uygulanmıştır. Ana kompozit numuneler, %0,6 gerinim seviyesinde 50 döngü boyunca çevrimsel yüke maruz bırakılmıştır. Sensör performansları; güvenilirlik, duyarlılık ve doğrusal yanıt parametreleri üzerinden değerlendirilmiştir. Elde edilen sonuçlar, CNT ve CB gibi nanomalzemelerle üretilen sensörlerin performansının uygulanan desenle doğrudan ilişkili olduğunu ortaya koymuştur. Başka bir deyişle, duyarlılığın sensör uzunluğu (desendeki iletken yol) ile ilişkili olduğu görülmüştür. Tek bacaklı tasarımlar (örneğin, line ve o-line) çok bacaklı tasarımlara (grid ve omnidirectional) kıyasla daha yüksek duyarlılık göstermiş, ancak ilk çevrim sonrası daha fazla hasar belirtisi sergilemiştir. Bu bulgu, uygulamaya özel sensör tasarımları geliştirmek için önemli tasarım ilkeleri sunmaktadır.

Bu çalışmalara ek olarak, farklı karbon nanomalzemelerin elektromekanik davranışları, ortak bir desen olan "grid" geometrisi üzerinden karşılaştırılmıştır. Araştırma düzeyindeki CNT ve CNF gibi 1B karbon nanomalzemelere dayalı sensörlerde maksimum direnç değişimi aşağı yönlü sapma (downward drift) göstermişken, endüstriyel kaynaklı CNT sensörlerinde bu değişim yukarı yönlü sapma (upward drift) şeklinde gözlemlenmiştir. Tüm 1B karbon bazlı sensörlerin duyarlılığı yaklaşık 2 civarında seyretmiş ve bu değer, geleneksel metal gerinim ölçerlerin hassasiyetine yakın bulunmuştur. 0B CB esaslı sensörlerde hafif bir yukarı yönlü sapma gözlemlenmiş, ancak bu sapma endüstriyel CNT'lere göre oldukça düşük düzeyde kalmıştır. Buna karşılık, CB sensörlerin duyarlılığı, 1B malzemelere kıyasla 15 kat daha yüksek çıkmıştır. Grafen esaslı grid sensörlerde ise aşağı yönlü sapma görülmekle birlikte, duyarlılık değeri 1B sensörlere kıyasla 8 kat daha fazla olarak ölçülmüştür. CB'nin hem araştırma düzeyindeki hem de endüstriyel CNT'ler ile ve ayrıca CNF ile hibritleştirilmesi sonucunda elde edilen sensörlerde, hem güvenilirlik hem de duyarlılık açısından belirgin iyileşmeler elde edilmiştir. Tüm bu sensörlerde ortak olarak gözlenen bir özellik, kullanılan nanomalzeme türünden bağımsız olarak oldukça iyi doğrusal (lineer) tepki vermeleridir. Bu bulgular, karbon nanomalzemelerin fiziksel boyutlarının, GFRP yüzeyine basılan piezorezistif gerinim sensörlerinin güvenilir.

Ayrıca, farklı desen ve nanodoldurucu içeren püskürtme baskı ile üretilmiş sensörler ve bunlara ait kompozit numuneler de %0,6 gerinimde 50 döngülük çevrimsel yüke tabi tutulmuştur. Elde edilen sonuçlar, serigrafi baskı yöntemiyle elde edilen sensörlerle benzer eğilimler göstermiştir. Ancak temel fark, sensörlerin çizgi genişliğinde ortaya çıkmıştır: püskürtme baskı ile üretilen sensörlerde, serigrafi baskıya kıyasla daha ince çizgiler elde edilmiştir.

Bu durum, özellikle CB esaslı sensörlerde belirginleşmiştir. CB içeren püskürtme baskılı sensörler, serigrafi baskılı muadillerine göre daha düşük güvenilirlik sergilemiş, ancak çok daha yüksek duyarlılık göstermiştir. Bu farkın temel nedeni, çizgi genişliğindeki farklılık olup, bu da başlangıçtaki elektriksel direnç değerini doğrudan etkilemiştir.

5. Bölüm aynı zamanda tamamlayıcı testleri de içermektedir. Örneğin, serigrafi baskı ile üretilmiş araştırma düzeyindeki CNT sensörler, %1,2 gerinim seviyesinde 50 döngü boyunca test edilerek elektromekanik performansları nicel olarak değerlendirilmiştir. Test öncesi ve sonrası olmak üzere farklı yükleme aşamalarındaki sensörlerin morfolojik karşılaştırması, taramalı elektron mikroskobu (SEM) kullanılarak gerçekleştirilmiştir. Ayrıca, grid desenli sensörlerin enine yöndeki duyarlılığı da karşılaştırılmıştır. Bu testte, sensörler hem uygulanan yük yönünde hem de bu yöne dik olacak şekilde serigrafiyle basılmıştır. Literatürde daha düşük enine/hassasiyet oranları tercih edilmekle birlikte, elde edilen sonuçlar karbon nanodoldurucunun türüne bağlı olarak gerinim duyarlılığının değiştiğini ve grid deseninin genel olarak yüksek orana sahip olduğunu ortaya koymuştur. Bu durum, sensör tasarımında daha fazla optimizasyon gerektiğine işaret etmektedir. Çok yönlü CNT sensörü de farklı açılarda test edilmiş ve %0,6 gerinimle 50 çevrim uygulanmıştır. Elde edilen sonuçlar, sensörün davranışında anlamlı bir farklılık gözlemlenmediğini ve bu nedenle çok yönlü algılama yeteneğine sahip olduğunu doğrulamıştır. Sensörlerin çok işlevliliği de ayrıca değerlendirilmiştir. Sıcaklık değişimlerine maruz bırakılan sensörlerde, Direnç Sıcaklık Katsayısı (TCR) değerinin karbon nanodoldurucuların fiziksel boyutlarına bağlı olduğu görülmüştür; özellikle 1B nanomalzemeler sıcaklık değişimlerine karşı daha yüksek duyarlılık sergilemiştir. Darbe testi sonuçları ise, duyarlılığın kullanılan nanodoldurucunun türüne bağlı olduğunu göstermiştir. Elde edilen verilere göre, duyarlılık sıralaması 0B, hibrit ve 1B karbon nanomalzemelerden oluşan sensörler için azalan şekilde ilerlemiştir ve nanodoldurucu türünün duyarlılık üzerindeki etkisini açıkça ortaya koymaktadır.

6. bölümde, GFRP alt tabakalar üzerine baskı ile üretilmiş yama anten sensörleri üzerinde araştırma yapılmıştır. Ana kompozit malzemeler, sensörlerin mekanik ve elektromanyetik performanslarını değerlendirmek amacıyla hem çekme hem de bükülme kuvvetlerine maruz bırakılmıştır. Frekans yanıtı testleri, antenlerin elektromanyetik özelliklerinin mekanik deformasyona karşı hassas olduğunu ve uygulanan gerilmeye bağlı olarak rezonans frekansında ölçülebilir kaymalar olduğunu ortaya koymuştur. Bu bulgular, baskı ile üretilmiş yama antenlerin kompozit yapılarda gerilme sensörü olarak kullanılma potansiyelini göstermektedir.

1. INTRODUCTION

Aerospace market contributes almost one percent of the total global market share representing approximately 800 billion USD Ensuring the safe operation of aircraft and maintaining mission readiness requires the early detection of structural damage and the implementation of routine maintenance procedures. Aircraft maintenance, encompassing both labor and repair costs, is highly expensive and varies significantly depending on the type of aircraft [1]. For instance, the annual maintenance cost of combat aircraft ranges from several hundred thousand dollars (*e.g.*, F-16) to tens of millions of dollars (*e.g.*, F-22) [2]. Summarizes the operating and maintaining costs of U.S. fighter aircrafts in 2018. The total cost of inspection of an entire Air Force fleet (e.g. Royal Air Force) could reach billions of dollars each year, as shown in Figure 1.1. In the civil aviation sector, maintenance costs also vary by aircraft generation and model. For example, the B737 commercial airframe is among the least costly to maintain, with airframe maintenance expenses reaching up to 300 USD per flight hour [3]. The average annual maintenance cost for civil aircraft is estimated to exceed 10 billion USD. Furthermore, the aerospace industry is expected to experience a growth in maintenance personnel of more than 5% annually [4].

As the aerospace industry seeks to reduce maintenance costs and improve aircraft performance, materials like composites have gained prominence due to their lightweight construction and resistance to corrosion [5]. Advanced composites, such as fiber-reinforced polymers (FRPs), offer significant advantages due to their excellent physical and chemical properties, including reduced weight and lower associated costs. For example, the airframe of the Boeing 787 aircraft is made up of up to 50% advanced composites in weight fraction, enabling fuel savings of up to 20% [6]. However, unlike metals, which exhibit predictable mechanical behavior and service life, composites are inherently less predictable and may suffer from delamination, fiber breakage, or matrix cracking under stress.

Figure 1.1 : Operating and maintaining cost of U.S. fighter aircrafts in 2018 [2].

In aerospace applications, loss of mechanical properties is unacceptable due to safety concerns. These issues are particularly problematic because damage may not always be visible in composites. Non-Destructive Testing (NDT) techniques have been developed to address these challenges, enabling better detection and monitoring of damage without compromising the material integrity. Ultrasonic testing, acoustic emission, eddy current testing, infrared thermography, laser shearography, and x-ray radiography are all common NDT methods used for material inspection and damage detection [7]. Figure 1.2a-b shows the principle of infrared thermography technology and actual application of the method.

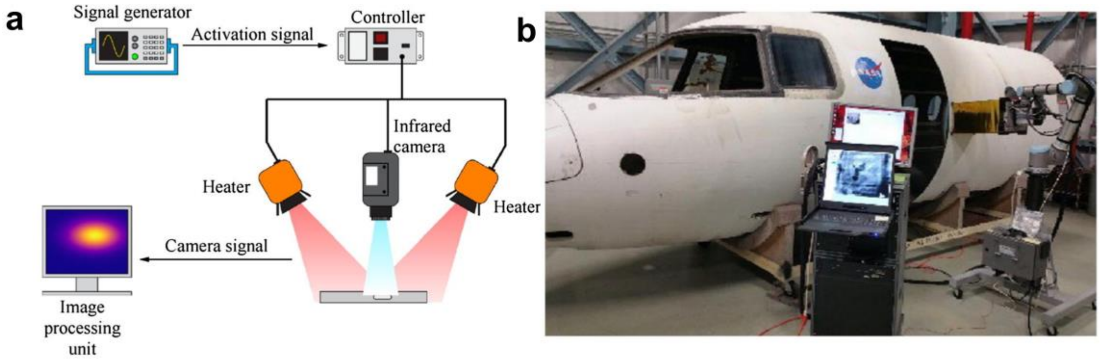

Figure 1.2 : a) Principle of infrared thermography and b) actual application [7].

NDT methods encounter various shared challenges, regardless of the specific technique [7]. These include slower testing speeds and difficulties in interpreting results. Many methods are limited to detecting only near-surface defects, while their effectiveness decreases for deep or small-scale damages. Additionally, material properties such as impedance mismatch or complex shapes can affect the resolution of expected results. Some techniques also require external factors to induce deformation, and advanced methods may face limitations related to sample size, shape, or material characteristics. Moreover, while these methods are effective for periodic inspections, they may not always provide the continuous monitoring required for real-time assessment. These challenges highlight the need for advanced monitoring systems capable of overcoming limitations in testing speed, defect detection, material properties, and continuous monitoring for real-time assessment [5].

Structural Health Monitoring (SHM) is an advanced early damage detection method and an alternative to traditional NDT techniques used for composites [8]. Unlike NDT, which requires manual inspection and onsite evaluation and often increases aircraft downtime, SHM enables continuous in-flight monitoring of structural components, reducing inspection time by up to 44% [9,10]. This capability translates to an overall maintenance cost reduction of approximately 30% [11].

The potential of SHM has already been demonstrated in fighter jets such as of F-16 (3% composite [12]) and Eurofighter Typhoon (more than 80% composite [13]) aircrafts, both of which employ ultrasonic guided-wave solutions [14–16]. This technology has proven effective in detecting and localizing damage in composites with high accuracy. A key sensor technology used in ultrasonic guided-wave SHM systems is piezoelectric transducers [17]. Another widely adopted technology in SHM is optical fiber sensors, usually utilized for monitoring strain, temperature, vibration, and acoustic signals and fiber-optic sensors [18].

Piezoelectric transducers, which are widely used in metal structures, have recently been integrated into composites for damage detection [19]. Although these sensors support large-area monitoring capabilities [20], their application in aerospace structures presents several challenges. These include mechanical property degradation caused by surface treatments, extensive wiring requirements, and high power consumption, all of which increase system complexity and raise safety concerns [21]. Similarly, fiber optic sensors, despite their potential, suffer from performance degradation due to micro-bending, stress concentrations that weaken composite properties, and complex repairs often requiring full structural replacement [22,23]. Metal strain gauges also face limitations, including adhesion difficulties, thermal expansion mismatches with composite substrates, and wiring constraints [24,25]. These challenges underscore the need for advanced sensor technologies specifically designed for aerospace composite applications.

Although SHM systems have demonstrated significant potential, their effectiveness is often limited by challenges such as sensor compatibility with composite materials, difficulties in seamless integration, and the overall complexity of implementation. Additionally, the vast amount of data generated by these systems necessitates robust data management and processing capabilities. The integration of Internet of Things (IoT) technologies offers a promising solution to these challenges by enabling efficient communication between SHM systems and external units. This enhanced connectivity can improve system performance, streamline maintenance operations, and support more effective monitoring of composite structures under a wide range of operating conditions [27].

To address the challenges of monitoring composite structures, piezoresistive carbon-based sensors have emerged as a highly promising alternative, offering solutions to many limitations of conventional technologies. These sensors provide several key advantages, including excellent compatibility with composite materials [28], lightweight design [29], and outstanding sensing performance [30]. Various printing methods, such as screen printing, spray coating, and direct printing, have been utilized to integrate these sensors seamlessly onto composite substrates, enhancing their adaptability. Their seamless integration into composite structures eliminates the need for additional bonding layers, simplifying fabrication and enhancing the overall mechanical integrity of the composite. This integration has opened new research avenues for optimizing sensor performance and tailoring designs to meet specific requirements [26–40]. These advancements mark a significant step forward in developing more efficient, reliable, and multifunctional structural health monitoring systems.

This thesis focuses on the development and integration of carbon-based strain sensors for SHM in advanced applications. It addresses the growing need for compatible, lightweight, and multifunctional sensors capable of monitoring the health of composite structures under various operational conditions. The research involves the formulation of carbon-based inks, including carbon nanotubes (CNTs), carbon black (CB), and carbon nanofibers (CNFs), optimized for printing techniques such as screen printing, spray coating, and extrusion printing, with an emphasis on understanding their rheology and printability on glass fiber-reinforced polymer (GFRP) substrates to ensure controlled quality. It examines the impact of geometrical patterns and carbon nanomaterial compositions on the electromechanical performance of sensors under cyclic tensile and bending tests. The developed sensors were thoroughly evaluated for their reliability, sensitivity, and linearity to ensure consistent performance under diverse operational conditions. The multifunctional capabilities of these sensors, including thermal and antenna performance, are further explored to ensure compatibility with aerospace environments. Finally, the thesis examines the feasibility of wireless antenna-based sensors as an integrated sensing and communication solution for composite structures.

2. BACKGROUND AND PRIOR WORK

Composites provide significant advantages in the aerospace industry, including reduced structural weight, lower fuel consumption, and enhanced resistance to corrosion [5]. However, unlike metals, which exhibit well-characterized mechanical behavior and predictable service life, composites display more significant variability in their mechanical performance. Their inherent heterogeneity renders them susceptible to various failure mechanisms, such as delamination, fiber fracture, and matrix microcracking [5]. Moreover, certain types of damage, such as barely visible impact damage (BVID), can remain undetected by visual inspection while potentially compromising structural integrity. Such damage may result from seemingly minor impacts, including dropped tools, hail, or bird strikes, yet can pose significant safety risks in aircraft operation [41,42]. To meet the stringent regulations of the aerospace industry, composites need to be monitored for damage [5]. Figure 2.1shows the complex system of sensors in an airplane.

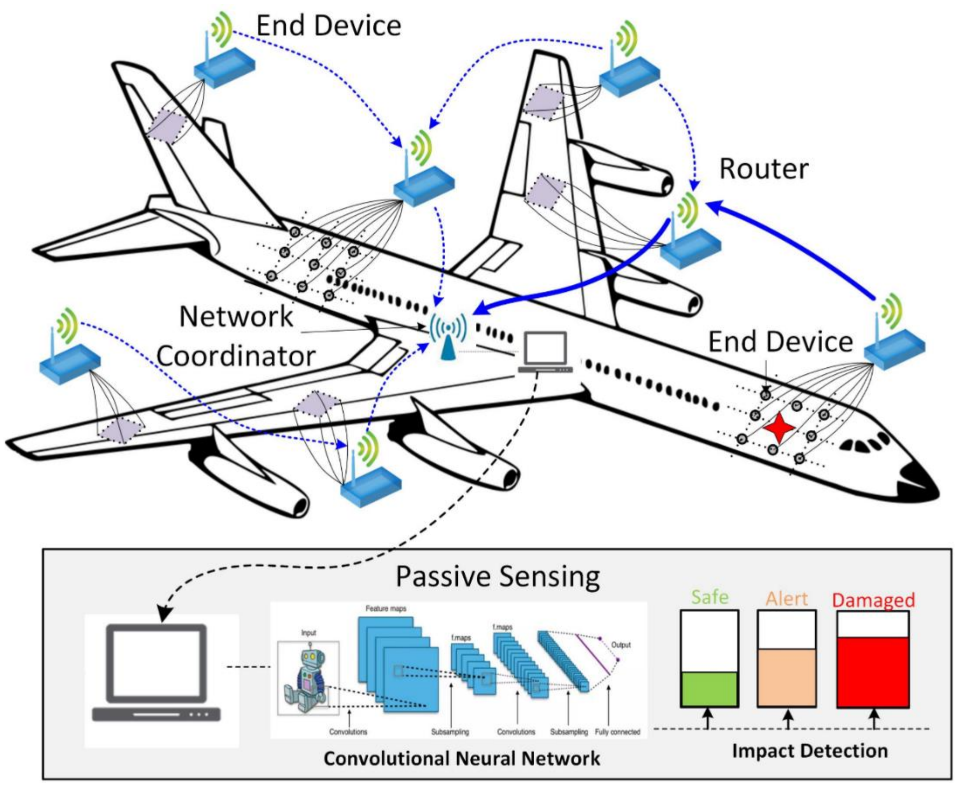

Figure 2.1 : The complex system of sensors in aircraft [43].

The growing adoption of composite structures in aerospace applications has elevated the standards for aircraft maintenance, necessitating more advanced and reliable monitoring techniques. Ensuring the structural integrity of these materials is critical for safety and optimizing maintenance costs and operational efficiency. An SHM system may typically integrate multiple sensors designed to monitor specific parameters such as strain, impact, temperature, or vibration. These sensors facilitate the early detection of anomalies while generating valuable data for real-time and historical analysis. This chapter provides a comprehensive overview of current SHM technologies and explores emerging state-of-the-art solutions aimed at enhancing the reliability and efficiency of composite structural monitoring.

2.1 Structural Health Monitoring Technologies

Given the high costs associated with aircraft maintenance and the necessity for reliable damage detection systems, the aerospace industry remains actively engaged in developing innovative solutions to reduce expenses while ensuring the structural integrity of aircraft. Among these, SHM has emerged as the most promising approach, and it serves as an advanced early damage detection system and offers a viable alternative to conventional NDT methods for composites [8]. Unlike NDT, which needs human intervention and onsite inspections – increasing aircraft downtime – SHM enables continuous, in-flight structural monitoring, thus reducing aircraft downtime (inspection time) by 44%. SHM technologies, therefore, could lead to a total reduction in overall maintenance costs by 30% [11].

Currently, the design of composite aircraft components is primarily based on impact energy levels and the smallest detectable damage size using NDT, as illustrated in Figure 2.2. SHM enhances this process in two fundamental ways [44]:

1. Reducing the detectable damage size beyond visual inspection allows for thinner laminates.
2. Real-time impact energy monitoring enables more accurate designs, minimizing overestimation and reducing structural weight.

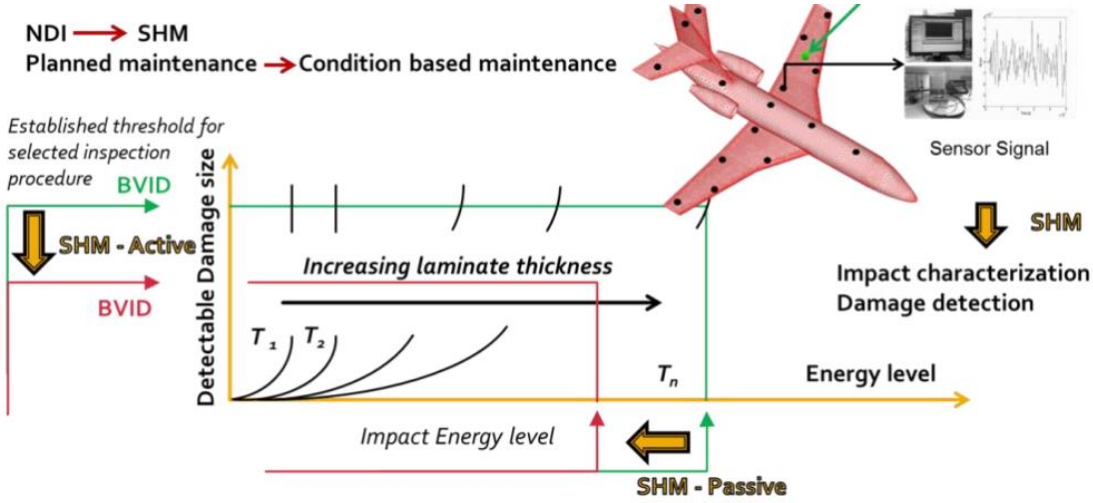

Figure 2.2 : Role of SHM in composite design optimization [44].

Traditionally, impact energy assessments for metallic structures have relied on dent measurements, and this method has been extended to composite designs. However, applying this approach to composites often leads to overly conservative design choices, resulting in unnecessary weight penalties. SHM offers a more precise, data-driven approach, enabling optimized weight savings and transitioning from planned to condition-based maintenance, ultimately improving efficiency and cost-effectiveness.

Significant progress has been made in SHM for impact and damage detection over the past two decades. Integrating installed sensors enables real-time monitoring of an aircraft's structural integrity throughout its operational lifespan. This capability facilitates early damage detection and proactive maintenance, enhancing safety and operational efficiency. The primary sensor technologies employed in SHM are summarized as follows.

2.1.1 Piezoelectric transducers

Piezoelectric transducers operate based on the piezoelectric effect, wherein mechanical stress induces the realignment of electric charges within the material, resulting in a relative displacement of positive and negative charges [45]. This displacement generates surface charges of opposite polarity, which can be measured as an output voltage when electrodes are embedded on the material's surface (Figure 2.3). Leveraging this principle, piezoelectric transducers function as sensors and actuators, generating and detecting Lamb waves in composite structures through in-plane strain coupling [45]. Lamb waves can propagate over long distances, enabling a relatively small number of transducers to monitor extensive areas effectively. This approach detects structural defects such as cracks, corrosion, delamination, and damage around holes, notches, and lap joints in thin-walled structures [46,47].

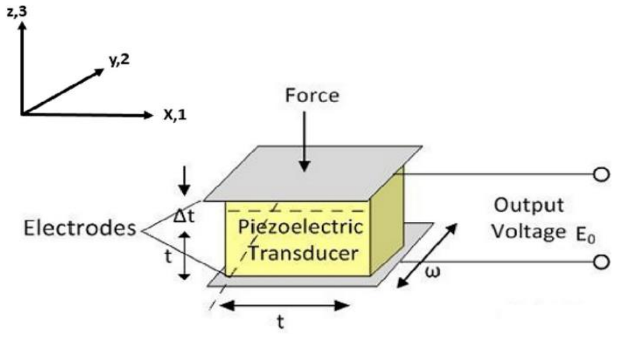

Figure 2.3 : Illustration of a piezoelectric transducer [48].

Recently, research has shifted from using piezoelectric transducers on metallic structures to integrating them directly into composite components [19]. These piezoelectric array sensors, designed to provide broad monitoring coverage for damage detection, are typically mounted on the surface of composite structures. For example, Figure 2.4 shows their application on a wing box skin [20]. To address the complexity of managing large sensor networks, researchers have explored strategies such as connecting sensors in series or parallel. Such approaches have been successfully demonstrated, including in a lightweight impact monitoring system developed for an unmanned aerial vehicle (UAV) wing box composite [20].

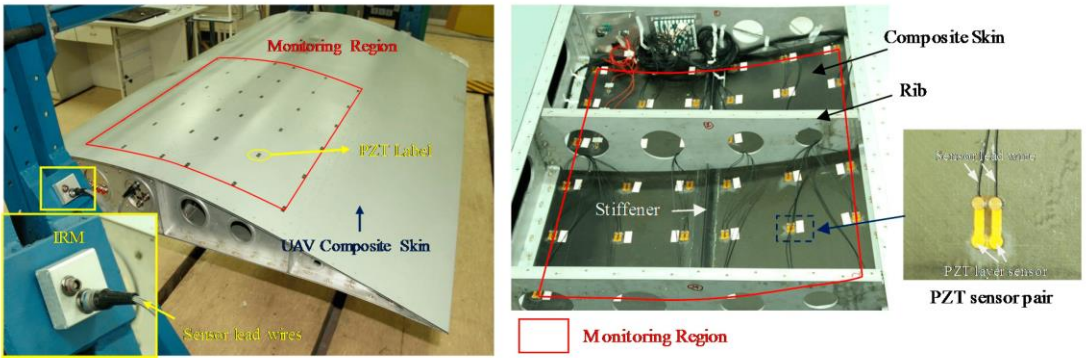

Figure 2.4 : The unmanned aerial vehicle (UAV) composite wing box, including sensor placement, is depicted with detailed views of the components and their arrangement [20].

Masmoudi et al. demonstrated embedding of sensors into GFRP laminated composites to detect acoustic events [49]. The authors subjected the composite to fatigue testing during three-point bending fatigue test, as presented in Figure 2.5.

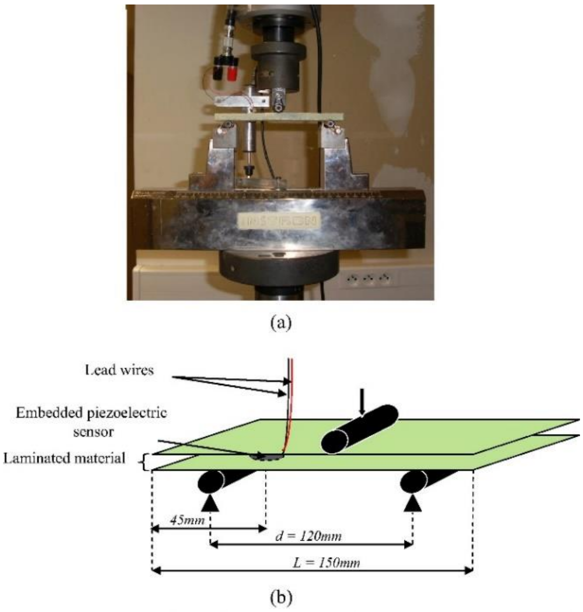

Figure 2.5 : a) Experimental setup for the three-point bending test and b) schematic representation of the laminated specimen used in the three-point bending test [49].

Results showed that embedded sensors exhibit higher sensitivity to fiber breakage and delamination damage than surface-mounted sensors. Furthermore, as shown in Figure 2.6a, composites containing embedded sensors showed mechanical performance comparable to that of sensor-free composites, suggesting that the inclusion of the sensor has minimal impact on the structural integrity of the material. In a follow-up study, the same research group explored the effects of varying sensor dimensions and found that increasing the sensor diameter from 5 mm to 10 mm, along with a corresponding increase in thickness from 0.5 mm to 1 mm, resulted in a noticeable decline in mechanical performance [50]. As shown in Figure 2.6b, these larger embedded sensors introduced stress concentrations and potential weak points within the laminate structure, ultimately compromising its load-bearing capacity.

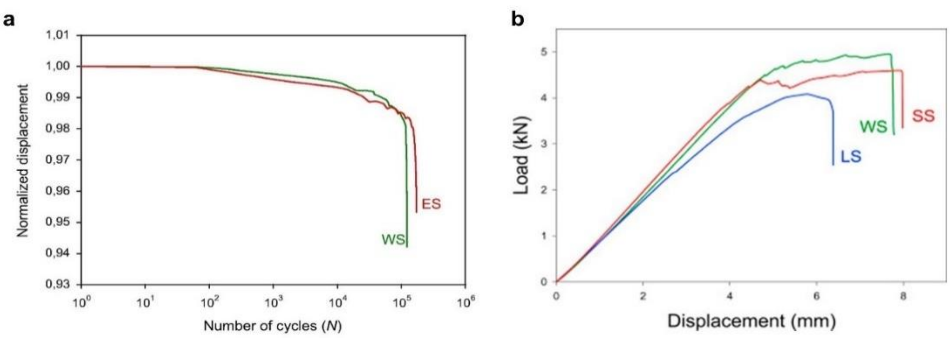

Figure 2.6 : a) Normalized displacement as a function of fatigue cycles for unidirectional laminate composite specimens without a sensor (WS) and with an embedded sensor (ES) [49]. b) Measured load–displacement responses for specimens with no sensor (WS), small sensor (SS), and large sensor (LS) [50].

Piezoelectric wafer active sensors (PWAS) are extensively employed in SHM of aerospace composites due to their cost-effectiveness, compact size, and ease of integration. These sensors are typically made from lead zirconate titanate (PZT) disks or squares, offering versatility as they can be surface-mounted or embedded within the composite structure. PWAS are particularly effective for detecting damage such as cracks, delamination, and corrosion, making them valuable for ensuring the integrity of aerospace materials. However, their limitations include a relatively weak driving force and brittleness, which can impact their durability. Moreover, PWAS can exhibit non-linear responses when subjected to extreme conditions, such as high temperatures, large strains, or elevated voltages, potentially influencing their performance in specific operational environments [51].

The placement of piezoelectric transducers plays a critical role in their performance. Hence, Thomas et al. demonstrated that embedding PWAS within composite structures enhances their effectiveness compared to surface-mounted ones under repeated impact. Electromechanical impedance and capacitance measurements further confirmed the superior durability of the embedded sensors [52]. Furthermore, Ren et al. observed that surface-mounted piezoelectric transducers are significantly more affected by temperature variations than embedded ones [53]. The authors developed a compensation method for temperature-induced effects to address this issue, which can also be applied to structures with varying thicknesses.

To overcome the brittleness associated with traditional lead PZT sensors, alternative piezoelectric transducers such as macro fiber composites (MFCs) have been developed. MFCs offer enhanced flexibility, making them particularly suitable for curved structural applications. These transducers are composed of unidirectional piezoceramic fibers embedded within an epoxy matrix and equipped with integrated electrodes for signal transmission. Unlike conventional PZT sensors, which operate through thickness activation, MFCs function along the fiber direction, generating a driving force up to three times greater than traditional PZT sensors [11].

Nearly two decades ago, advancements in piezoelectric transducers began addressing the impact of thickness on their performance and versatility in various applications. A thin, flexible layer was developed to be embedded during manufacturing and co-cured with composite materials, tolerating temperatures up to 200 °C [54]. In a separate study, the same group successfully employed the thin piezoelectric layer for impact damage detection on composite structures like filament-wound composite bottles, where PZT sensors detect stress waves to monitor structural health and locate damage [55].

In aerospace applications, degradation in mechanical properties is unacceptable due to safety requirements. The extensive wiring needed for piezoelectric sensor nodes and their high power demands increase complexity and raise safety concerns [21]. Attaching sensors to composite surfaces often requires pre-surface treatments, such as sanding, which adds complexity, introduces potential human error, and may reduce sensor performance [11].

2.1.2 Optical fiber sensors

Optical fiber sensors are another widely studied strain sensor technology, a field extensively researched for over five decades due to its high sensitivity [56]. Optical fiber sensors transmit light between a source and a detector through air or fiber-optic cables. This method offers key advantages over electrical sensors, including immunity to electromagnetic interference and enhanced safety in hazardous environments [45].

In SHM, fiber optic sensors are integrated into composites, where dimensional changes in the fiber alter the transmitted light's wavelength, enabling strain detection. A recent study demonstrated that embedding lightweight fiber optic sensors into composites is an effective and cost-efficient method for localizing and detecting BVID [18]. However, the integration of fiber optics into composites can introduce manufacturing challenges. These include performance degradation due to micro-bending [22] and potential reductions in the mechanical properties of the host composite due to stress concentrations. While fiber optic sensors are cost-effective, they are also sensitive to temperature variations, and their maintenance can be costly, as repairing embedded sensors often requires complete structural replacement [23].

A key type of fiber optic sensor is the Fiber Bragg Grating (FBG) sensor, which operates based on Bragg's law. The Bragg wavelength, the specific wavelength of light reflected by the grating, depends on the effective refractive index and the grating period, as detailed in Figure 2.7.

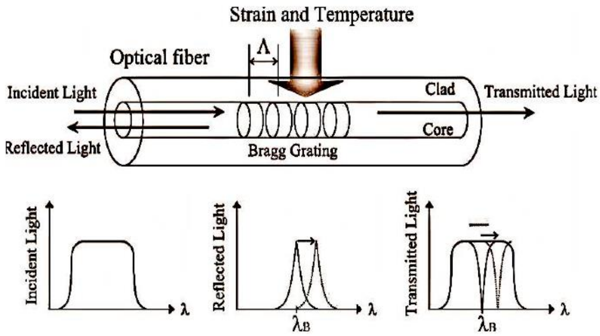

Figure 2.7 : A detailed schematic and fundamentals of a FBG sensor [57].

Embedding FBG sensors in composite structures faces challenges, such as weakened signals and fragile optical fibers. Ramly et al. found that the signal power dropped post-embedment while wavelength shifts before and after embedment were minimal (less than 1 nm) [58]. Optical connectors suited for both manufacturing and operational conditions are essential to improve integration. Giraldo et al. developed a trimmable optical connector for a lower wing root joint simulation, ensuring proper fiber positioning and protection from resin during curing [59]. Once cured, the protective element was removed to allow fiber interrogation. Alternatively, surface mounting FOS with encapsulating protective materials presents a more straightforward solution. Goossens et al. proposed embedding commercial fiber Bragg grating (FBG) sensors within a GFRP cylindrical profile for enhanced protection, enclosing them in a high-density polyethylene sheath to prevent moisture and oil ingress [60]. The sensors were pre-strained, bonded with aerospace-grade carbon fiber polymer reinforced polymer (CFRP) coupons, as shown in Figure 2.8, and subjected to several in-flight simulation tests. It was found that both the bond line and the sensor signal quality were minimally affected by the environmental and mechanical loads simulating in-flight conditions.

Figure 2.8 : FBG sensors embedded into CFRPs [60].

Although FBG is a widely used technology [61] incorporated into composites and sensitive to localized damage, it requires noise-cancelling analysis to improve its performance [62]. The fiber within the composite matrix can create stress raisers, leading to potential complications. Additionally, careful attention must be given to sensor placement, especially when using techniques like vacuum-assisted resin infusion to avoid bending in the fiber as illustrated in Figure 2.9. To ensure accurate strain measurements, addressing the strain-temperature cross-sensitivity issue is essential.

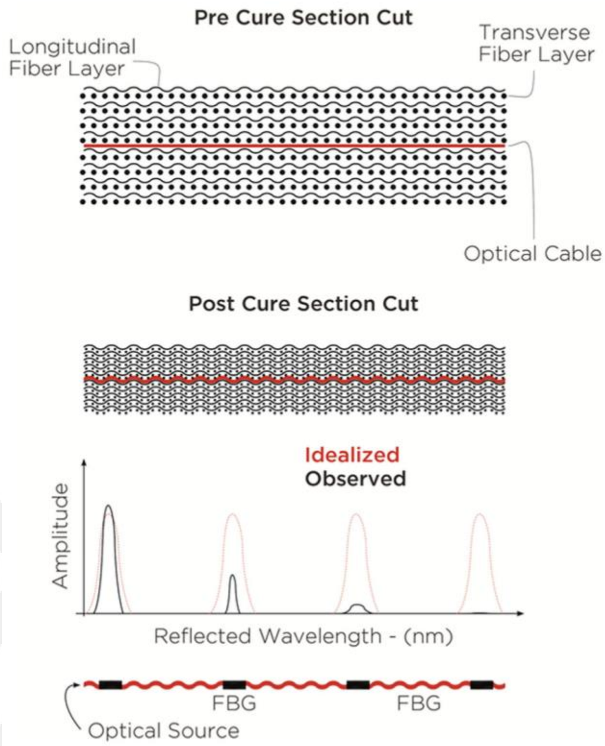

Figure 2.9 : Radius bends in FBG after composite curing [22].

2.1.3 Conventional strain gauges

Conventional metal strain gauges are widely employed in SHM systems to measure strain on metal and composites of aircraft components [24,63]. Originally invented in 1938 [64], these sensors remain a fundamental tool for strain measurement [64]. The most commonly used strain gauges are made of thin copper-nickel foils, which are etched on polymeric substrates (*e.g.* polyimide) [65], as demonstrated in Figure 2.10. Uniaxial strains are measured by positioning the sensor in the direction of the applied force. Uniaxial strain is measured by aligning the sensor with the direction of the applied force. In this configuration, transverse strain arising perpendicular to primary axis, has negligible impact on sensor sensitivity, provided that the foil has a large length-to-width ratio [40], a design principle adhered to in nearly all commercial metal strain gauges.

Additionally, to mitigate the influence of ambient temperature variations on sensor accuracy, a Wheatstone bridge circuit is typically employed for temperature compensation.

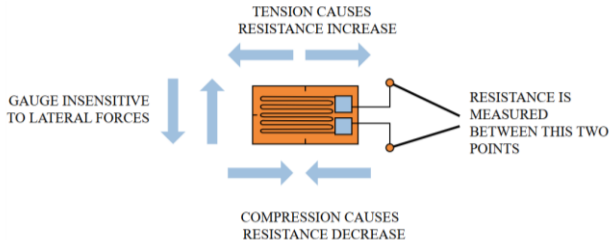

Figure 2.10 : Schematic illustration of a strain gauge with its fundamental mechanisms [66].

The working principle of a metal strain gauge is summarized as follows. When a constant voltage is applied, a change in the geometric dimension (*e.g.* applied strain) in the metal wires induces a change in electrical resistance. The resistance, R, of the wire is [64].

$$R = \rho \frac{L}{A} \tag{2.1}$$

Where ρ, L, and, A are resistivity, length, and cross-sectional area of metal foil, respectively.

By differentiating both sides of equation 2.1 and dividing by 2.1 we get

$$\frac{dR}{R} = \frac{dL}{L} - \frac{dA}{A} + \frac{d\rho}{\rho} \tag{2.2}$$

where $\frac{dA}{A}$ can be written as

$$\frac{dA}{A} = \frac{2\pi r dr}{\pi r^2} = \frac{2dr}{r} \tag{2.3}$$

where r is diameter of the wire. Poisson's ratio of a metal wire can be written as

$\nu = -\frac{\varepsilon_{lateral}}{\varepsilon_{longitudinal}} = -\frac{\frac{dr}{r}}{\frac{dL}{L}} = -\frac{\frac{dA}{A}}{2\frac{dL}{L}}$ thus equation 2.3 can be rewritten as

$$\frac{dA}{A} = -2\nu \frac{dL}{L} \tag{2.4}$$

substituting equation 2.4 into equation 2.3 and after rearranging we have

$$\frac{dR}{R} = (1 + 2\nu)\frac{dL}{L} + \frac{d\rho}{\rho} \tag{2.5}$$

Typical strain gauges are made of metal wires and have sensitivity of around 2 for gauge factor [65,67]. The initial resistance of stain gauges is in range of 60-1000 ohms [68], and operate under voltage range between 1 – 2 V [69]. Figure 2.11 shows a schematic of a typical metal strain gauge used to measure strain induced in a cantilever.

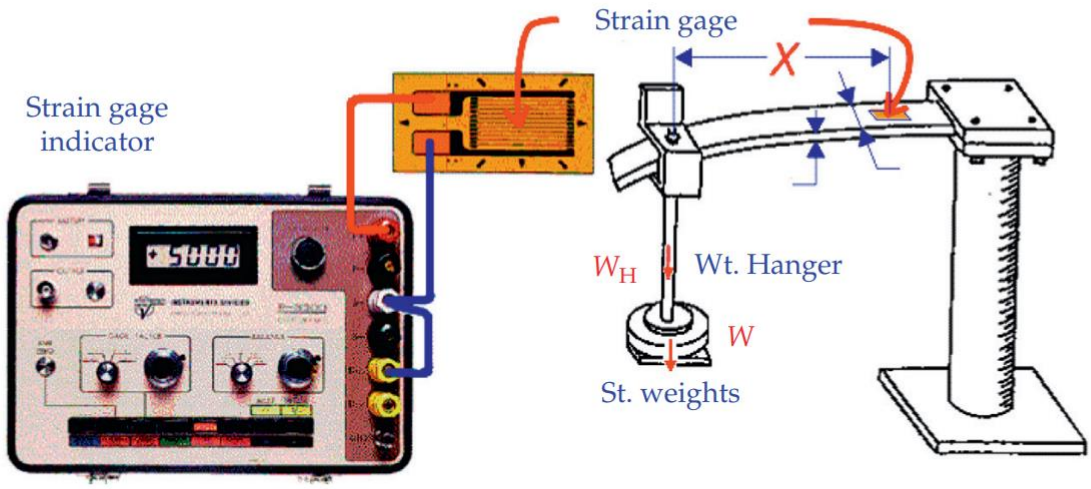

Figure 2.11 : A schematic of cantilever beam strain measurement by a strain gauge [24].

Strain gauges have been utilized for monitoring composite structures in aircraft, as demonstrated in Figure 2.12a [70]. However, their effective application requires addressing several fundamental considerations. One critical factor is the surface treatment of the tested structure to ensure strong adhesion between the composite substrate and the metal sensor [24]. The presence of an adhesion layer between the sensor and the structure can hinder efficient strain transfer to the metal wire or foil, leading to inaccurate readings [64]. However, these adjustments add complexity to the system and require additional time and effort for proper implementation [71]. Furthermore, bonding challenges are aggravated on curved surfaces, where ensuring uniform adhesion becomes increasingly difficult [28].

Furthermore, the dissipated heat of the strain sensor also needs to be factored in to calculate sensitivity. Because the heat generated by the sensor creates a thermal gradient, and due to the thermal expansion coefficient between the substrate and the wire, different resistance values are read [25]. The dissipated heat could damage materials such as composites, which, in turn, could affect the accuracy of the reading [69]. Signal amplification is often necessary to address weak output signals from strain gauges, increasing system complexity with additional costs [45]. Finally, while electrical cables used to connect the sensor to a measurement device are generally not problematic in laboratory environments, they add significant complexity in real advanced applications, as demonstrated in Figure 2.12b [24].

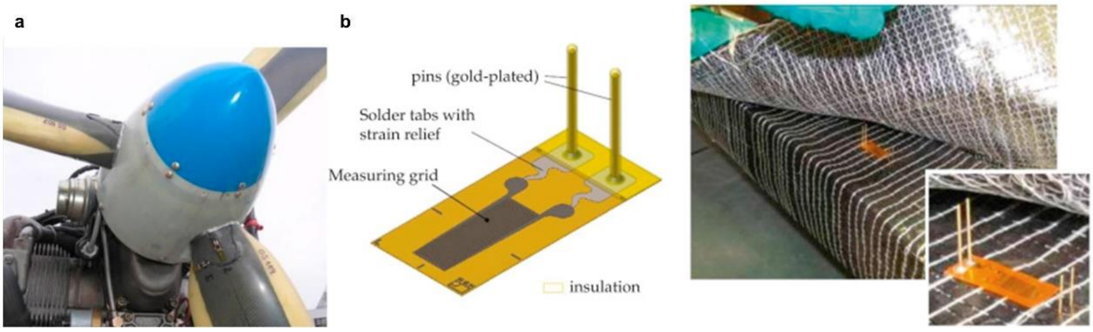

Figure 2.12 : a) Strain gauges mounted on a composite propeller and b) embedding strain gauges within composite structures [70].

To address issues in the readily available SHM solutions, advanced carbon-based sensors have also been proposed for various applications [72]. In the last decade, piezoresistive carbon-based nanomaterial strain sensors emerged as a potential alternative for such critical issues to be resolved [73].

2.2 Carbon-Based Piezoresistive Sensors: State-Of-The-Art

In the last decade, piezoresistive sensors have emerged as a prominent solution for strain measurement in composite structures, offering advantages such as compatibility with composite materials [28], lightweight and tailored designs [74], and excellent sensing capabilities [32]. The research field has gained significant attention, especially with the advancement in the synthesis of conductive nanomaterials, such as carbon-based materials and metal nanoparticles. Their integration into composites proves to be both practical and effective.

The dimensionality of carbon nanomaterials significantly influences the electromechanical response of piezoresistive sensors [75]. As illustrated in Figure 2.13, these materials are categorized into three types: zero-dimensional (0D) such as carbon black (CB), one-dimensional (1D) including carbon nanotubes (CNTs) and carbon nanofibers (CNF), and two-dimensional (2D) like graphene and its derivatives. Given the significant impact of these materials on piezoresistive sensing, a closer examination of carbon nanomaterials and their role in this technology is crucial to understand their contributions and potential for further innovation.

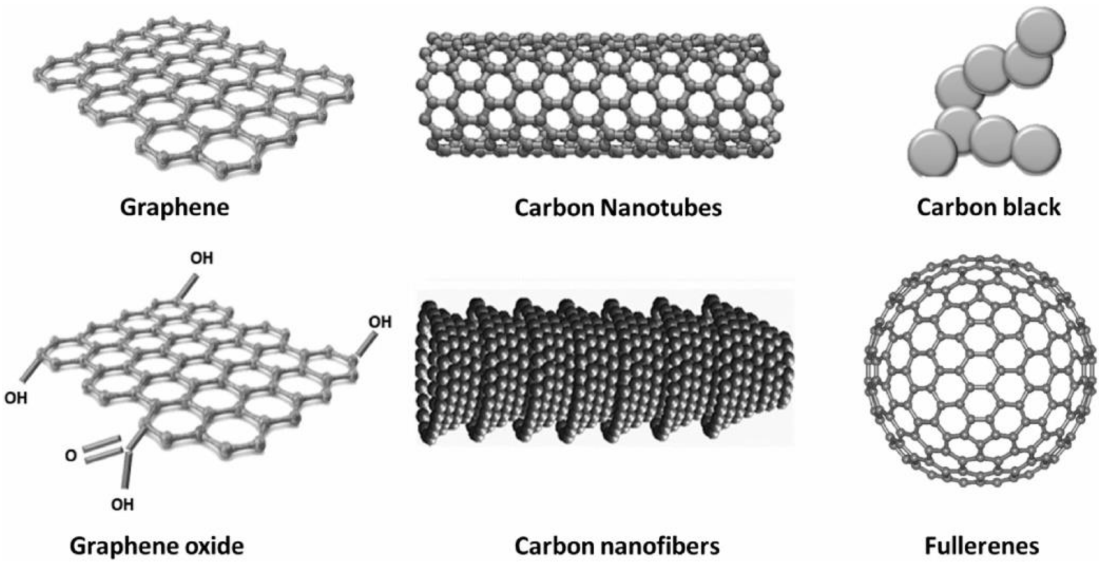

Figure 2.13 : Visualization of diverse carbon nanomaterials and their structural configurations [76].

2.2.1 Carbon nanotubes

CNTs are defined as graphene layers wrapped concentrically to form either single-walled carbon nanotubes (SWCNTs) or multi-walled carbon nanotubes (MWCNTs). The carbon atoms in the graphene sheet that constitute CNTs are arranged in zigzag, armchair, or chiral configurations. Depending on the arrangement of these carbon atoms and the nanotube's diameter, CNTs can present either metallic or semiconducting properties. The unique 1D configuration of CNTs, characterized by a large length-to-diameter ratio, results in remarkable electrical properties. This 1D structure also leads to a lower percolation threshold, enabling CNTs, even at low loading, to form conductive networks within nonconductive matrices, thereby enhancing electrical performance. The sheet resistivity of SWCNTs can reach up to 100 ohms per square [77]. These exceptional electrical properties make CNTs promising candidates for various strain sensor applications.

The intrinsic resistance of a nanostructure depends on its internal crystalline structure and geometric configuration. For example, the inherent resistance of a long 1D nanostructure, such as a SWCNT, is influenced by its length. A 95 nm long SWCNT has a resistance of 1.5 kΩ, while a 150 nm long SWCNT exhibits a higher resistance of 2.7 kΩ [78]. Moreover, Zhou et al. demonstrated that the intrinsic resistance of an SWCNT is also dependent on the Fermi level, which, in turn, is influenced by the type of CNT [79]. Specifically, a semiconducting SWCNT with an armchair configuration has an intrinsic resistance of 36 kΩ, while a metallic SWCNT has a lower inherent resistance of 12 kΩ.

The concept of direct contact electrical resistance between CNTs is complex and requires careful consideration. To simplify the discussion, this section focuses on the direct contact resistance between CNTs, one of the most extensively studied electrically conductive nanofillers. Studies have shown that the direct contact resistance between two CNTs varies depending on their type [80,81] and the contact length [82]. For example, when two zigzag-configuration CNTs are perpendicularly in contact, the resistance is significantly higher (3.21 MΩ) compared to a zigzag-configuration CNT in perpendicular contact with an armchair-configuration CNT (682 kΩ) [82]. Regardless of their crystalline configuration, the direct contact resistance between two parallel CNTs is nonlinear, with the degree of nonlinearity influenced by the periodicity of their crystalline structure. Even small changes in the relative positioning of parallel CNTs can result in dramatic variations in their direct contact resistance [82].

The remarkable properties of CNTs have driven intense research into their use as piezoresistive materials for strain sensing. Their unique shape imparts excellent electrical properties; for instance, the electron mean free path in a CNT is approximately 1 μm, significantly larger than that of copper, which is around 40 nm [83]. CNTs have been explored in various forms, including filler additives, buckypaper, and coated layers for damage sensing and health monitoring applications. Despite their geometry, well-dispersed CNTs are essential for creating a conductive network that provides functional and electrical properties. These properties stem from the direct contact between conductive CNTs and the tunneling effect between adjacent particles, which are not in direct contact but are close enough to influence conductivity [84].

The sensing mechanism of CNTs dispersed in a polymer matrix relies on the dimensional changes that occur when the sensor is subjected to external stimuli. As a result, the distance between nanomaterials changes, leading to a change in resistance, as illustrated in Figure 2.14. This resistance change is primarily attributed to the tunneling effect [54], where electrons overcome small barriers, carbon-to-carbon contact resistance [82], and the formation and destruction of conductive paths [85].

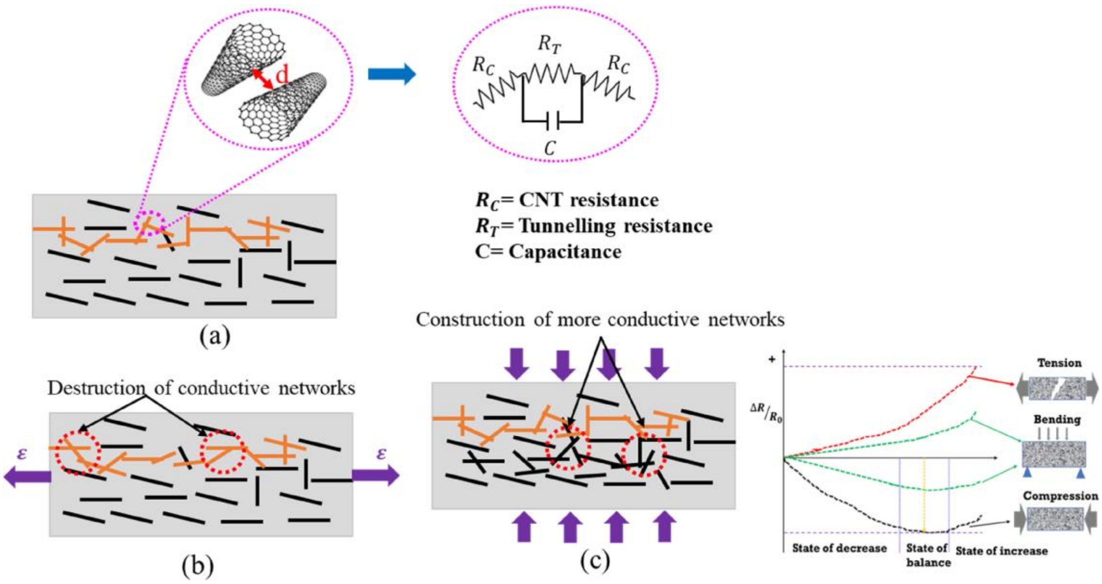

Figure 2.14 : Piezoresistive working principle of CNT-based nanocomposites: a) without external load, b) under tension, and c) under compression [86].

When CNT-based nanocomposites are subjected to applied loads, the CNTs tend to align in the direction of the load. This alignment reduces the overall resistance of the sensor, leading to a downward drift in the electrical signal and compromising the sensor's electrical reliability [87,88], as illustrated in Figure 2.15. While the robustness of the interconnected CNT network results in relatively low sensitivity [89], it enables the sensor to maintain high linearity [90].

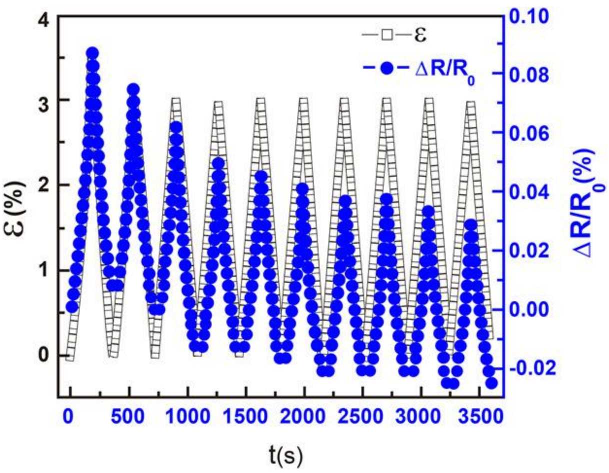

Figure 2.15 : Resistance change of CNT-based PP nanocomposite subjected to cyclic tensile loading [91].

Several studies have embedded carbon nanotube films into composites to address the challenges of dispersing particulates into polymer matrices, as demonstrated in Figure 2.16a-b. Different types of CNTs, such as SWCNTs and MWCNTs, have been employed to investigate the performance of CNT buckypaper sensors [92,93]. As a result, the studies showed that the sensing performance of CNT sensors is strain-dependent, as demonstrated in Figure 2.16c-d [62]. At low strains in the elastic region, the deconstruction and reconstruction of the conductive paths and electron tunneling are the dominant mechanisms. However, at high strains, deconstruction becomes the predominant intrinsic change. For instance, under a three-point bending test and at minor strains, CNT buckypaper embedded in GFRPs exhibited a sensitivity as high as 46 [62]. Additionally, CNT bucky papers used as interlayers in composites have been shown to quantify damage and improve the fatigue resistance of GFRP laminates [92].

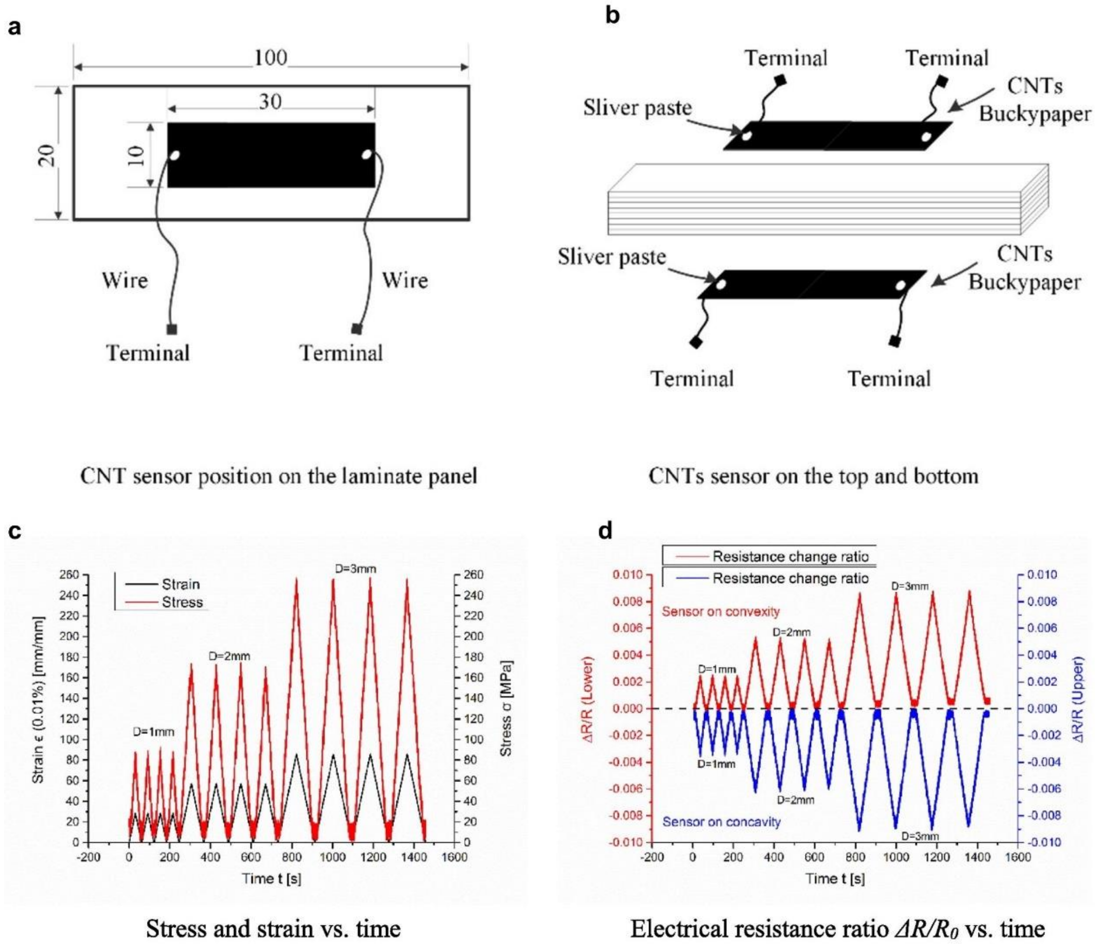

Figure 2.16 : a) Dimension and b) placement of CNT sensors on GFRPs [62]. c) stress and strain as a function of time and d) corresponding electrical resistance of both bottom and top sensors [62].

2.2.2 Carbon nanofibers

Depending on the fabrication method and processing conditions, CNFs possess a disordered graphitic structure. Like CNTs, CNFs have a fibrillated structure that provides a high aspect ratio. Due to their physical and chemical properties and large surface area, CNFs make excellent candidates as reinforcement and electrically conductive fillers.

Some studies presented the concerns on the research for the performance of CNFs as strain sensors [94–100]. The physical configuration of CNFs makes them particularly interesting for sensing mechanical damage with high sensitivity in both compression and tension modes [94]. One study recently demonstrated the durability and maintenance of stable sensitivity levels under large loading cycles for CNF-polyvinyl alcohol (PVA) nanocomposites [96]. Additionally, another recent study showed that aligned CNF-based thin films could be used for sensing multidirectional strains in the same specimen [97].

Wang et al. subjected CNF epoxy nanocomposite with different content ratios to incremental cyclic compressive loading [94]. Results showed that higher load resulted in higher electrical response, as shown in Figure 2.17. Also, the results that the maximum resistance change of the CNF nanocomposite showed dependency on filler content.

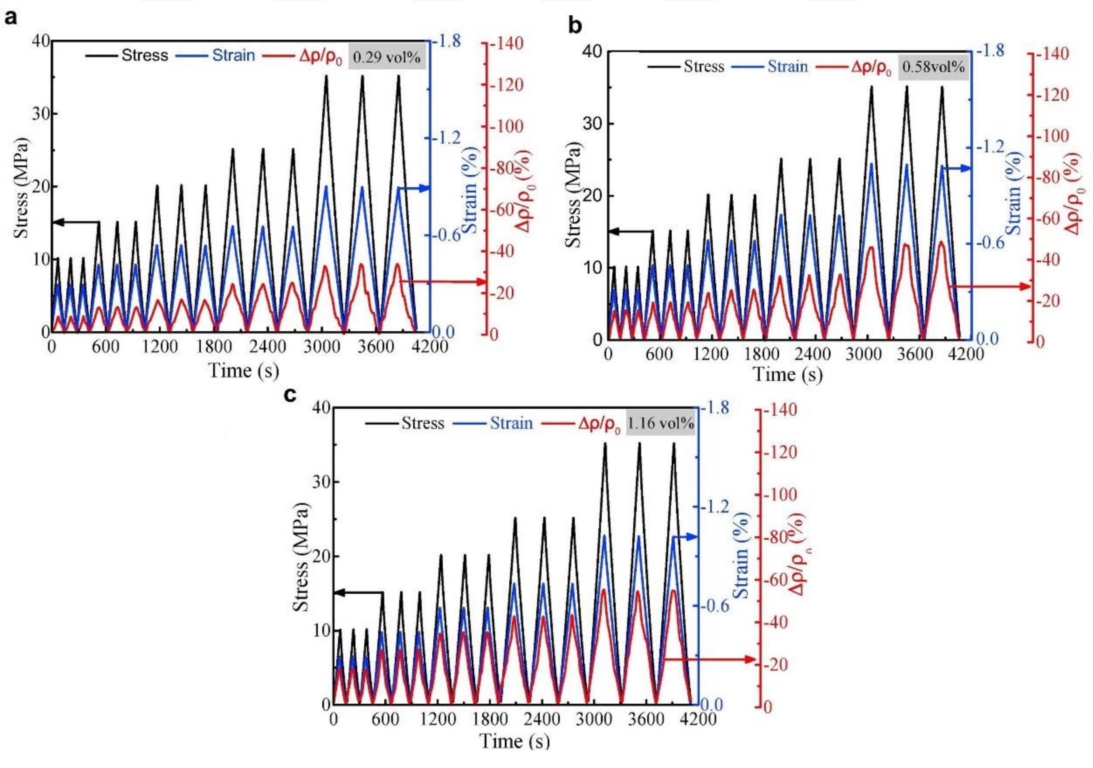

Figure 2.17 : Incremental cyclic compressive loading of CNF/epoxy nanocomposites with filler contents of a) 0.29 vol%, b) 0.58 vol%, and c) 1.16 vol% CNFs [94].

While CNFs have a larger diameter than CNTs, resulting in a lower aspect ratio, their electromechanical performance remains comparable due to the formation of an interconnected network. As with CNT-based sensors, CNF-based sensors are susceptible to signal drift under cyclic loading [101], exhibit moderate sensitivities [102], and maintain high linearity [101].

2.2.3 Graphene and its derivatives

Graphene is a one-atom-thick carbon layer, physically considered a 2D material. The first graphene layer was experimentally isolated at the beginning of this century [103], and since then, it has been the subject of intensive research due to its unique properties [104]. The distinct carbon bonding and electron configuration of graphene give rise to π electrons, which contribute to its superior electrical conductivity [105]. These exceptional physical and electrical properties make graphene an excellent material for developing sensors to detect mechanical damage and sense changes in the surrounding environment.

Graphene-based nanocomposites offer exceptional sensitivity with their unique 2D configuration, making them ideal for piezoresistive strain sensor applications. Recent studies have explored various methods of integrating these sensors into composite structures [106–109]. For example, one study demonstrated that a thin layer of the graphene-epoxy nanocomposite, when attached to the surface of a glass fiber composite, exhibited high sensitivity at relatively low strain levels [106]. Similarly, graphene nanoplatelet (GNP) nanocomposite thin layers have been shown to function as highly sensitive strain sensors. Additionally, reduced graphene oxide (rGO) has proven to be an effective material for strain-sensing applications [109].

Reghat et al. coated glass fibers with graphene prior to the vacuum infusion process and subjected the resulting composites to cyclic tensile loading [110]. As shown in Figure 2.18, when exposed to increasing tensile forces of 2000 N, 3000 N, 4000 N, and 5000 N, the sensitivity of the composite decreased progressively, with values of 14.56 ± 1.08, 13.32 ± 1.62, 11.23 ± 0.56, and 8.69 ± 2.47, respectively. Also, as the cycle number increased the peak resistance change decreased which was attributed to viscoelastic peripeties. A notable drawback was a 26% reduction in tensile strength after the graphene coating, which was attributed to a decrease in fiber volume content resulting from the coating process.

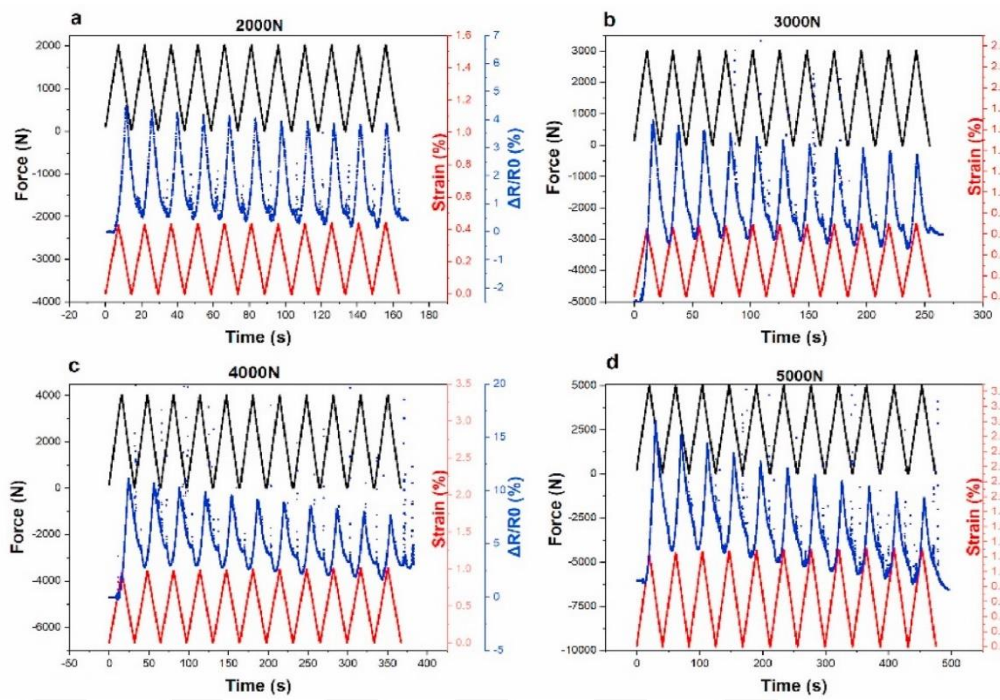

Figure 2.18 : Piezoresistive response of the graphene-coated GFRE composite under cyclic tensile loads of a) 2000 N, b) 3000 N, c) 4000 N, and d) 5000 N, applied at a rate of 0.1 mm/s [110].

2.2.4 Carbon black

CB is a 3D graphitic material with particle sizes ranging between 14-250 nm [111]. Unlike CNTs, CB has an aspect ratio of 1 due to its spherical shape. However, due to its cost-effective fabrication method and adequate electrical properties, CB is considered one of the most well-studied and commonly used fillers in polymeric composites, enhancing both the physical and electrical properties of the resulting composite [112,113]. While CB does not have the high aspect ratio of graphene or CNTs, its porous surface provides a large surface area, contributing to its effectiveness as a filler. CB has been widely explored as an active filler for piezoresistive-based sensor applications [114]. However, its use in wireless applications appears limited, likely due to its higher sheet resistance than its metallic counterparts.

Although CB exhibits a higher percolation threshold than graphene and CNTs due to its 0D configuration, CB-based nanocomposites demonstrate excellent and repeatable piezoresistive behavior under mechanical stimuli [85,115,116]. For example, a study showed that CB thermoplastic polyurethane (TPU) nanocomposites maintained a durable and repeatable self-sensing mechanism over 2000 cycles at relatively high strain rates [115]. However, CB-based nanocomposites are susceptible to an upward drift in electrical signals under cyclic loading. This drift occurs because the initial resistance does not revert to its original value after each cycle, indicating cumulative damage within the conductive network formed by the spherical particles [117]. Such sustained damage exacerbates reliability issues over time.

In addition, CB-based networks offer high sensitivity but often exhibit a nonlinear electrical response primarily driven by the electron tunneling effect. For instance, Zhao et al. demonstrated that CB-based polypropylene (PP) nanocomposites displayed upward drift and high sensitivity but with a nonlinear response under cyclic loading, as demonstrated in [117]. Similarly, Huang et al. reported that highly sensitive CB-based polyvinylidene fluoride-hexafluoropropylene (PVDF-HFP) composites became nonlinear due to tunneling effects [118], limiting their applications.

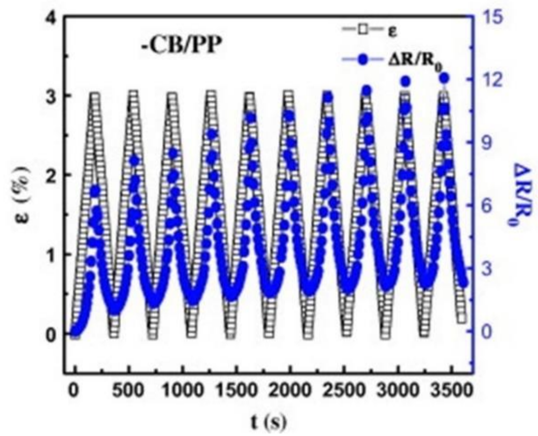

Figure 2.19 : Piezoresistive response of CB-based PP nanocomposite under cyclic tensile loading [117].

These challenges, rapid network degradation and nonlinear responses, pose significant barriers to the widespread adoption of CB-based nanocomposites in practical applications.

2.2.5 Hybrid carbon nanomaterials

Each previously discussed material has its own physical and chemical properties, resulting in different sensing behavior. Hybridization offers a way to combine different piezoresistive properties, allowing complementary effects that enhance overall performance. For instance, the hybridization of graphene (2D) and CB (0D), as shown in Figure 2.20 for graphene/CB hybrid nanocomposite, results in a strain sensor that remains stable over a range of temperatures, unlike sensors made solely from graphene or CB [119]. This stability has been attributed to the counteracting effects of each material at elevated temperatures, leading to a balanced state.

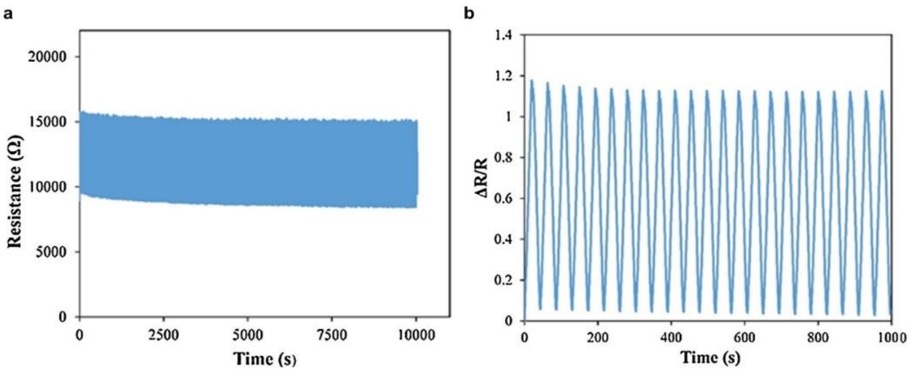

Figure 2.20 : a) Evaluation of the strain sensor's long-term stability over 500 loading cycles, and b) normalized resistance versus time plot for the graphene/CB nanocomposite sensor [119].

Under cyclic loading, Zhang et al. demonstrated that combining CNFs with GNPs enhances signal reliability and reduces drift in gauge factor values [120]. As shown in Figure 2.21a-b, the normalized gauge factor decreases with increasing cycle number for standalone GNP- and CNF-based polydimethylsiloxane (PDMS) nanocomposite sensors, demonstrating downward drifting response. However, upon hybridizing CNFs and GNPs at a 1:3 ratio, signal stability improves significantly, as illustrated in Figure 2.21c. However, the impact of hybridization on linearity remains inconsistent, as it depends on factors such as matrix type, applied load, and the specific carbon nanomaterials used [118,121].

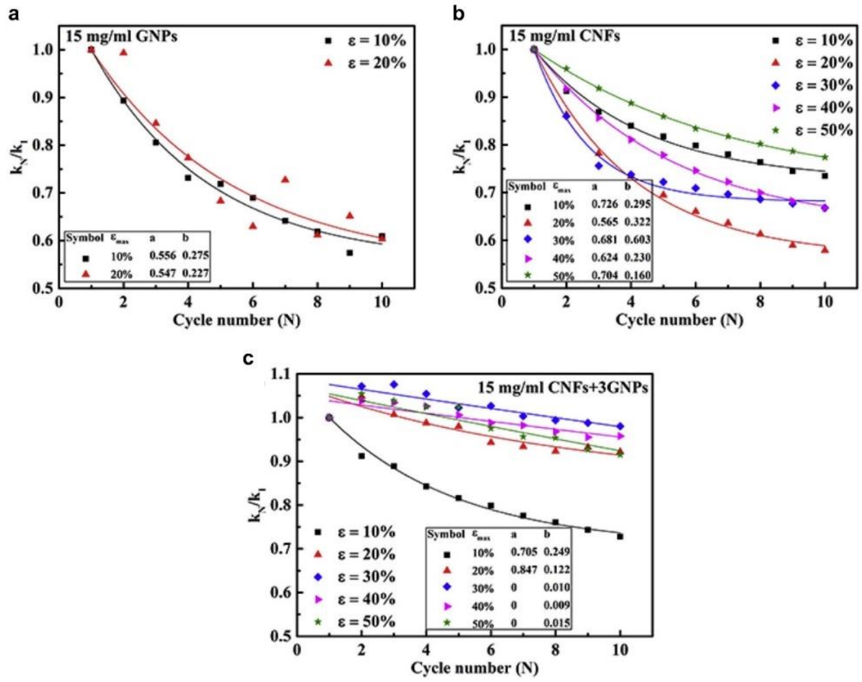

Figure 2.21 : Normalized gauge factor of sensors based on a) 15 mg/mL CNFs, b) 15 mg/mL GNP, and c) a 15 mg/mL CNF+3GNP (1:3 ratio of CNF:GNP) hybrid [120].

Another example of hybridization involves mixing CBs and CNTs, which has been shown to enhance nanocomposites' electrical conductive network while improving their piezoresistive sensitivity [122,123]. The electrical conductivity enhancement was attributed to the mechanical bridges CBs provided, while the piezoresistive improvement was thought to result from the CBs’ sensitivity toward mechanical stimulus.

The electromechanical performance of CB-based sensors, which often hinges on reducing electrical resistance, can be significantly enhanced by incorporating CNTs due to their low percolation threshold [124]. This improvement has motivated researchers to develop highly sensitive strain sensors exhibiting excellent linearity, making them ideal for advanced strain sensing applications [125].

Other hybridized materials reported in the literature are CNT and CNF [126], CNT and graphene [127], CB and silver [128], CNT and silver [129], CB and ionic liquid [130], CNF and ionic liquid, CNF and graphene [131], and silver and copper nanoparticles [132]. It is worth mentioning that a combination of three or more fillers has also been reported for strain-sensing applications [133].

Tailoring the electromechanical properties of a strain sensor to combine properties of 0D, 1D, and 2D carbon nanomaterials can be achieved by hybridizing two or more carbon nanomaterials. Nonetheless, the integration of carbon-based sensors with composite structures is critical.

2.2.6 Dispersion strategies for carbon nanomaterials: Role of surfactants and solvents in ink formulation

In most cases, binders and surfactants are necessary constituents to formulate inks [134–136]. Binders are typically used as thickening agents to control and tailor the rheological properties of the inks. In particular, thickening agents provide thixotropic behavior, creating a printable medium for screen printing applications [137]. In other cases, binders also serve as the matrix in which the electrically conductive nanofillers are dispersed to form conductive pathways. Furthermore, the matrix usually protects the sensor from the external environment. However, polymer matrices require post-processing, subjecting the sensors to high curing temperatures that can lead to unwanted structural changes. In light of these challenges, binder-free inks are also being explored as an alternative to avoid high curing temperatures and potential structural changes in sensors. By eliminating the polymer matrix, these formulations avoid high-temperature curing and reduce the risk of structural degradation. Moreover, investigating binder-free inks enables a clearer understanding of the piezoresistive behavior of conductive carbon fillers, without interference from the viscoelastic properties of a polymer matrix, which can otherwise affect the electromechanical response [110].

Surfactants are used to disperse nanoparticles, ensure homogeneous dispersions, and reduce agglomeration of conductive particles. Six primary surfactants have been identified: carboxymethyl cellulose, cellulose nanocrystals (CNC), sodium dodecyl sulfate (SDS), Tween 20, Tween 80, and Triton X-100 (TX-100) [136,138–141]. TX-100 is highly effective in dispersing carbon nanomaterials [141], while cellulose-based surfactants such as CNC not only facilitate dispersion [142] but also modify rheological properties, making them particularly useful for ink formulations[143].

In the past few years, the emerging hybrid composite of CNC with CNTs has gained the attention of researchers due to its great potential in various applications, such as flexible sensors, patch antennas, and structural applications [144–147]. CNT/CNC dispersions were highly stable in water for over six months [146]. This stability is attributed to the ability of CNCs to disperse and stabilize hydrophobic CNTs in aqueous solutions due to the high charges on the surface of the CNCs [148,149] and covalent bond formation between CNTs and CNCs [142]. Depending on the type of CNTs, either SWCNT or MWCNT, CNCs are expected to partially or perfectly align along the CNTs [149]. Wang et al. showed that CNT/CNC hybrid reinforcement decreased the electrical percolation threshold by fourfold compared to pristine CNT polymer nanocomposites [144]. The strain sensitivity of the CNT/CNC sensor was 43.5 at a strain of 100%. These results were attributed to CNCs' ability to homogenously disperse CNTs in the matrix and prevent excessive slippage of CNTs during mechanical testing. Moreover, for human motion monitoring applications, Yan et al. showed that the CNT/CNC nanocomposite sponge had a sensitivity of 17.1 in compressive mode, exhibited reliable performance for tens of cycles, and improved compressive strength [150]. These findings were attributed to the ability of CNT/CNC to be evenly decorated around the 3D network of the sponge and the enhanced interfacial interaction between the polymer and CNT/CNC.

Furthermore, the addition of CNT/CNC into carbon fiber composites for structural composites resulted in enhanced interfacial interaction in the matrix due to the excess oxygen content found in the hybrid CNT/CNC, which increased flexural and shear strengths [146]. The hybrid CNT/CNC significantly improved the thermal stability of the carbon fiber-reinforced composites. Figure 2.22 shows unit cell of the CNC and interaction of a CNT along the hydrophobic (200) and ($\bar{2}$00) faces of CNC.

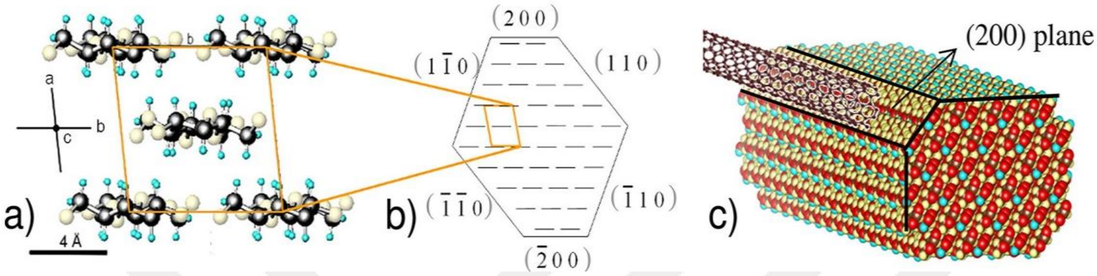

Figure 2.22 : Schematic showing CNC: a) unit cell, b) cross-section, and c) depiction of a CNT near the (200) plane of CNC [151].

The physical properties of solvents, such as surface tension and boiling point, significantly impact printing quality. IPA is commonly used as a solvent due to its relatively low surface tension and wetting capability, which enhance printability. However, using IPA as the sole solvent in carbon-based inks can promote the coffee-ring effect, which diminishes printing quality and resolution [152,153]. When IPA is combined with water as a co-solvent, it helps tune the ink's physical properties and improve printability. A water/IPA mixture with a 70/30 weight ratio significantly lowers the surface tension compared to water alone, making it a potential solvent system [154–156].

Additionally, surfactants like TX-100 are incorporated to reduce surface tension and enhance the ink's wettability. TX-100 also improves dispersion and stability [45,46] while reducing surface tension by up to 50%, making it a critical component for ensuring the ink performs well during printing. Table 2.1 provides a summary of the key physical properties of materials investigated in this study.

Table 2.1 : Physical properties of the selected solvents and surfactants.

Materials	Surface energy (mN/m)	Surface tension (mN/m)	Boiling point	Reference
Water	n/a*	73	100	[152]
IPA	n/a	22	83	[157]
Water/IPA (70/30)	n/a	27	-	[158]
TX-100	n/a	30-35	270	[159]
CNC	73	n/a	n/a	[160]
GFRP	37	n/a	n/a	[161]

* not applicable.

2.3 Design-Driven Factors Affecting Electromechanical Sensor Performance

The performance of the carbon-based piezoresistive sensors is typically affected by several parameters, such as length [28,36], width [137], thickness [38,162], and the number of sensing parts [32,38]. As a result, sensor geometry plays a crucial role in determining strain sensitivity. Several studies have shown that increasing the sensor length results in higher resistance, which in turn enhances sensitivity [28,36,137], as shown in Figure 2.23a. In contrast, a narrower width is generally associated with increased sensitivity [137]. Furthermore, a greater thickness tends to result in diminished sensitivity (Figure 2.23b) [38], while increasing the total length of a strain gauge grid sensor typically enhances sensitivity (Figure 2.23c) [36].

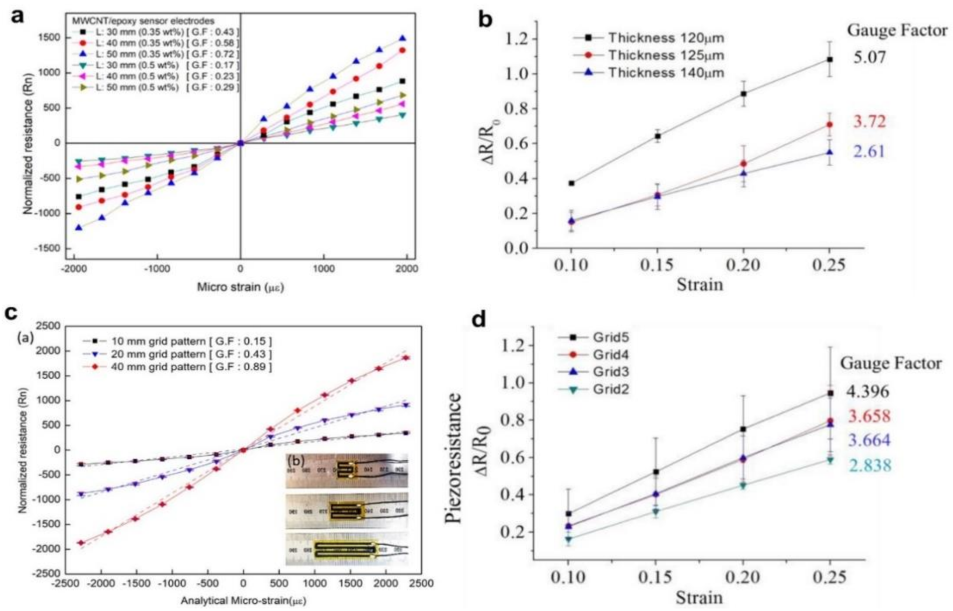

Figure 2.23 : a) Influence of the total length of the CNT strip on sensitivity [36]. b) Effect of thickness variation in carbon-based PDMS strain gauges mounted onto dog-shaped PDMS substrates tested in tensile mode using UTM [38]. c) Influence of the overall length of CNT-based strain gauges on sensitivity [36]. d) Effect of thickness variation in carbon-based PDMS strain gauges with different numbers of sensing grids on gauge factor [38].

Additionally, the number of sensing elements, such as grids or legs, has been found to significantly affect performance. Sensors with a greater number of sensing parts tend to exhibit higher sensitivity [32,38]. For example, Han et al. reported that increasing the number of sensing legs (grid size) in a carbon-based PDMS strain gauge mounted onto dog-shaped PDMS led to a corresponding increase in the gauge factor, as illustrated in Figure 2.23d [38]. This improvement in sensitivity has been attributed to the formation of a longer conductive path.

The importance of the strain gauge grid lies in its directional sensitivity, it is most responsive to strain applied along the direction of the grid lines [40]. Hence, strain gauges are typically designed with their grids aligned parallel to the principal strain direction to maximize sensitivity. Building on this principle, the development of high-performance carbon-based strain gauge grids for composite structures has attracted considerable attention, particularly those offering sensitivities that surpass conventional metal strain gauges, which typically have a gauge factor of around 2.1 [26]. Groo et al. transferred (the transfer method is discussed in detail in the following section) graphene-based strain gauges onto GFRPs with varying numbers of legs [28]. They controlled the initial resistance of the printed sensors by adjusting the total grid count, as shown in Figure 2.24a. Results indicated that increasing the number of grids enhanced the sensor's strain sensitivity, as illustrated in Figure 2.24b. In another study, researchers printed engraved graphene-based strain gauge grids onto a polyimide substrate, which was then mounted onto GFRPs using adhesive [26]. They demonstrated that the sensors exhibited excellent reliability.

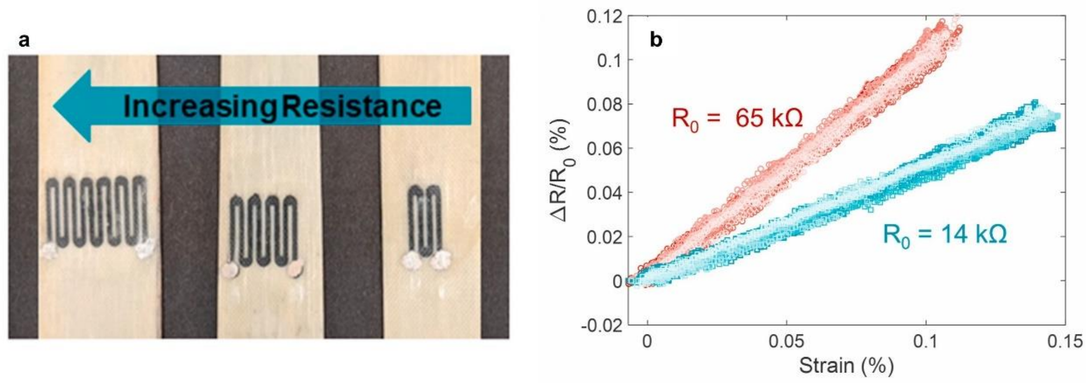

Figure 2.24 : Transfer-printed strain gauges onto GFRPs with varying resistances by varying the total grid number of the grid sensors, and b) resistance change as a function of strain over 20 cycles for two samples with varying initial resistances controlled by the total number of grids [28].

While conventional strain gauge grids are suitable replacements for metal strain gauges in applications with unidirectional loading, such as tensile strain measurement following ASTM D3039, in real-world scenarios, loads can be applied from multiple directions. This has driven interest in the design of sensors capable of multidirectional strain sensing. As a result, the influence of sensor geometry has become a focal point for broadening application potential.

Zymelka et al. designed an unconventional omnidirectional strain sensor and compared its performance with that of a conventional grid pattern by tilting the sensors at various angles after mounting them onto a metal structure (the transfer method is discussed in detail in the following section), as shown in Figure 2.25a [29]. Their results demonstrated that the omnidirectional sensor exhibited high sensitivity and a consistent response when tilted in different directions, unlike the conventional grid design, which showed directional dependency, as illustrated in Figure 2.25b. Similarly, Yang et al. designed various sensors to detect changes in multiple directions [163]. Each design responded distinctly to different loading directions. Nonetheless, these comparative analyses of these designs lacked depth, omitting critical design factors such as the total sensor length, width, and length of the sensing part for each design. Furthermore, a comprehensive analysis of various patterns should also consider electromechanical characteristics such as sensitivity, reliability, and linearity.

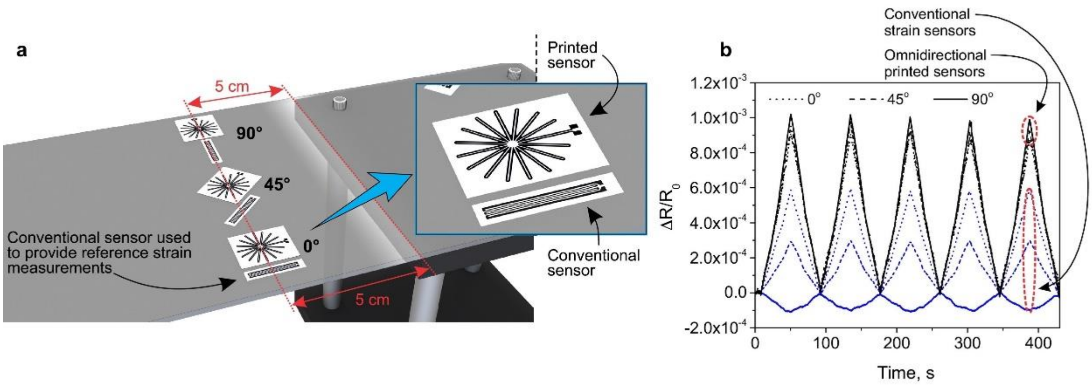

Figure 2.25 : a) Conventional and omnidirectional strain sensors mounted on a metal structure at three different tilt orientations, b) corresponding resistance change under cyclic tensile bending loads [163].

The reliability of a strain sensor is another key electromechanical characteristic influenced by both material and design parameters [91]. In particular, signal drifting in CNT-based sensors, such as self-sensing nanocomposite polymers [91,164,165] and printed sensors [27,166], is frequently reported during cyclic testing, as previously discussed. This drifting is usually attributed to relaxation time [120], reconfiguration of CNTs, applied load, and residual deformation in the electrical network. Since drifting can negatively impact the reliability of a sensor [167], researchers have been keen to address this issue, proposing many solutions: hybridization of nanomaterials, *e.g.* CNT/GNPs [120], pre-straining [168], engineering the type of polymer matrix [164,169], and utilizing Wheatstone bridge [166].

Despite these efforts, the role of sensor geometric patterns in drift behavior remains relatively unexplored. For example, as shown in Figure 2.26, Liang et al. demonstrated that increasing the width of a strain gauge can improve reliability; however, this comes at the cost of reduced sensitivity [137]. It is also worth noting that their study focused on wearable applications rather than structural composites. This highlights the need for further investigation into how sensor geometry affects long-term stability and performance, particularly under cyclic loading in composite structures.

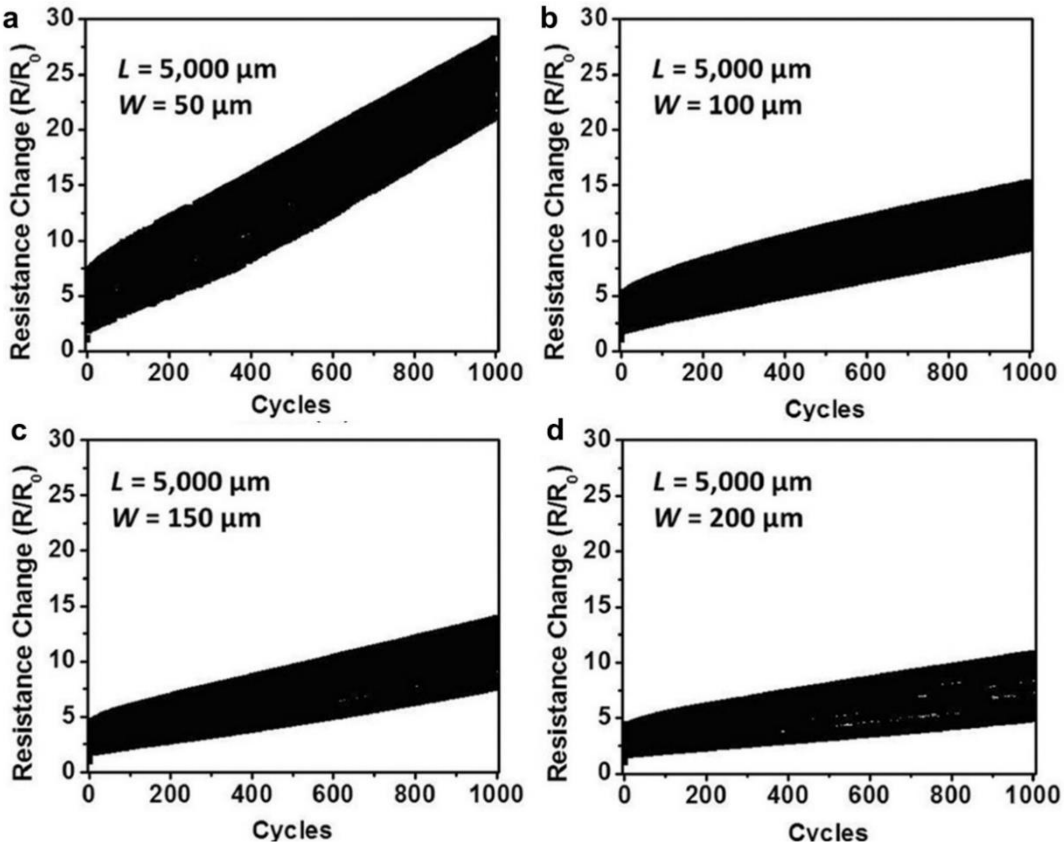

Figure 2.26 : Normalized resistance over 1000 cycles (0–30% strain) for line widths of a) 50, b) 100, c) 150, and d) 200 µm. All lines are 5 mm long, stretched at 1 mm/s along their length [137].

Besides reliability, linearity describes the relationship between the electrical signal and the applied load, and a high linear response simplifies the calibration process of a strain sensor [90,170]. Duan et al. concluded that the high linearity of piezoresistive sensors relies on a sufficiently dense and robust electrically conductive network [90]. Despite its significance, the linearity of a strain sensor has received relatively little attention [90].

2.4 Integration of Strain Sensors with Composites and their Performance

Integrating piezoresistive strain sensors into composites has given researchers more significant opportunities for optimizing sensor performance and design [26–40].

2.4.1 Incorporation of carbon nanomaterials into composites

In a polymer matrix, nanostructures form a conductive network at a critical level of volume fraction, also known as percolation threshold [171]. Assuming a perfect dispersion of the nanostructures in the polymer matrix (although this is not the case), an interphase layer covers the nanostructure. Half of the thickness of the interphase layer is referred to as the tunneling distance. Although the interphase layer isolates the nanostructure, the nanocomposite is electrically conductive so long as the tunneling distance ranges between the minimum distance of about 0.34 nm [172] up to the cutoff distance of 1.8 nm [173,174] (more conservative measurements have accepted 1.4 nm as the cutoff distance [175,176]). The tunneling resistance has been estimated to be 10^{13} Ω [177] which is usually many orders of magnitudes higher than the contact resistance between the nanostructures (*e.g.* in the absence of polymer matrix) or the intrinsic resistance of the nanostructure as was discussed above.

Incorporating CNTs into polymeric matrices as mechanical robustness fillers allows for a self-sensing mechanism, thus eliminating the need for additional external sensing devices. Most of the literature's efforts and reports have focused on this approach for its beneficial synergistic mechanical and electrical effects. To demonstrate, at different CNT concentrations, MWCNT epoxy nanocomposite was manufactured in dog-bone-shaped and subjected to tensile loading. It was shown that the higher the CNT loading, the lower the sensing sensitivity. The authors also emphasized that dispersion contributed to the initial measured resistance of the composite. Another group found that the cyclic piezoresistive behavior of MWCNT-based nanocomposite depended on the applied strain load [179]. They showed that cycling behavior changed at different strain levels. For example, resistance change was stable for over 10 cycles at low strain levels, while at higher strain levels, the resistance change was shown to decrease as the number of cycles increased. Furthermore, in a separate study, MWCNTs epoxy nanocomposite fabricated as Hopkinson pressure bar was demonstrated to effectively detect different forms of mechanical damage impact. It was shown that the nanocomposite registered elastic wave propagation when the bar went under impact pressure testing.

Despite the larger tunneling resistance of a CNT nanocomposite compared with other direct contact and intrinsic resistances, some researchers have proposed analytical models that consider the intrinsic resistance of a CNT [175,176,180] or the direct contact resistance between CNTs [173]. Other researchers have proposed analytical models solely considering tunneling resistance. Despite the different approaches of the aforementioned models, their models are built on Simmons' modified model [181,182] which describes the tunneling resistance of a conductive nanocomposite as the following

$$R_t = \frac{M}{N}\frac{h^2 t}{d^2 e^2 \sqrt{2m\chi}} \exp\left[4\frac{\pi t}{h}\sqrt{2m\chi}\right] \tag{2.6}$$

where M is the number of conductive fillers in a conductive path, N is the number of conductive paths, h is Planck's constant, t is the average tunneling distance, d is the diameter of the conductive filler, e is the electron charge, m is the mass of the electron, and χ is the work function of the conductive filler.

Regardless of the model used, equation 2.6 shows that an electrical nanocomposite's initial resistance exponentially depends on the tunneling distance. When tunneling distance, for example, increases, the total resistance of the nanocomposite increases, and the opposite is true [183].

The sensitivity of a strain sensor is a critical performance measurement. In practice, a strain sensor's sensitivity, also called gauge factor (GF), has been approximated experimentally by measuring the slope of resistance change and strain graph. In theory, the sensitivity of a strain sensor can be quantified in terms of the resistance change to change in dimension in direction, $\frac{dL}{L}$ (strain), of the applied force as follows.

$$GF = \frac{dR}{\varepsilon R} \tag{2.7}$$

Using equation 2.7 and rearranging equation 2.5, GF can be written as [64].

$$GF = \frac{dR}{\varepsilon R} = (1 + 2\nu) + \frac{d\rho}{\varepsilon\rho} \quad (2.8)$$

where ε is strain and equals to $\frac{dL}{L}$.

Equation 2.8 shows that GF depends on the geometric changes in a material and the change in resistivity of that material. The geometric factor depends on Poisson's ratio of materials. For instance, most metals with a Poisson's ratio of 0.30 have a GF of at least 1.6 [64]. Furthermore, equation 2.8 has been used in surface mode measurement to describe the GF for nanocomposites [184–186]. Hence, epoxy nanocomposites with a Poisson's ratio of about 0.35 may have GFs of at least 1.7 [186].

The change in resistivity effect depends on the type of materials. The change in resistivity of metals is dominant in the elastic region due to a volume change. In contrast, no change in resistivity is induced in the plastic region because the volume of a metal remains unchanged [64]. In nanocomposites, however, change in resistivity depends on the relative positions of the nanostructures; therefore, change in resistivity occurs in both the elastic and plastic regions. In other words, tunneling distance is a function of the applied strain and can be quantified as follows.

$$t = t_0(1 + (cos^2 a - \nu\, sin^2 a)\varepsilon) \quad (2.9)$$

where a represents the average angle between the tunneling distance and the direction of the applied force or strain [88,187]. It should be emphasized that other researchers have used different mathematical representations of the change in relative positions of nanostructures in composites under loading [183,188,189].

Several studies have embedded carbon nanotube films (CNT buckypapers) into composites, which is considered an alternative approach to functionalizing composites for strain sensor applications. It was concluded that sensing performance relied upon strain levels in CNT sensors. Wang et al. embedded CNT buckypaper sensors into GFRP composites, as illustrated in Figure 2.27 [62]. Datta et al. embedded CNT BPs as interlayers to induce multifunctional capabilities, such as strain sensing, damage quantification, and improved fatigue resistance, in GFRP laminates [92]. Crack lengths were correlated with the resistance change recorded for the embedded buckypaper sensor into the composites.

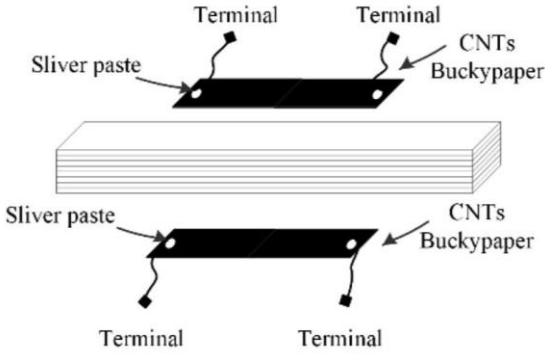

Figure 2.27 : Embedding of CNT buckypaper on prepreg GFRP composite [62].

CNT-based buckypapers have also been successfully employed as damage sensors to detect strain changes [190,191], delamination [192], and the drilling process [193]. A recent study provided a mechanism for the electrical behavior of the CNT-based buckypapers that underwent tension and compression strains [62]. Two buckypapers were attached on both sides of GFRP, and the resultant specimen underwent a three-point bending test. Experimental results showed that changes in electrical resistance due to strains in tension and compression modes not only match each other but also show repeatable measurements for around 100 bending cycles.

2.4.2 Direct coating onto composites

Direct coating methods have been adopted to address the challenges of dispersing carbon nanofillers in composites. These approaches involve coating fibers with CNTs through controlled growth, such as directly applying CNT solutions deposition, as shown in Figure 2.28 [194]. Similarly, the direct coating of graphene and its derivatives onto fibers in GFRP provides an alternative to traditional nanocomposites, eliminating issues like agglomeration. For instance, graphene-coated glass fiber composites have demonstrated high sensitivity in detecting strains during mechanical testing [110].

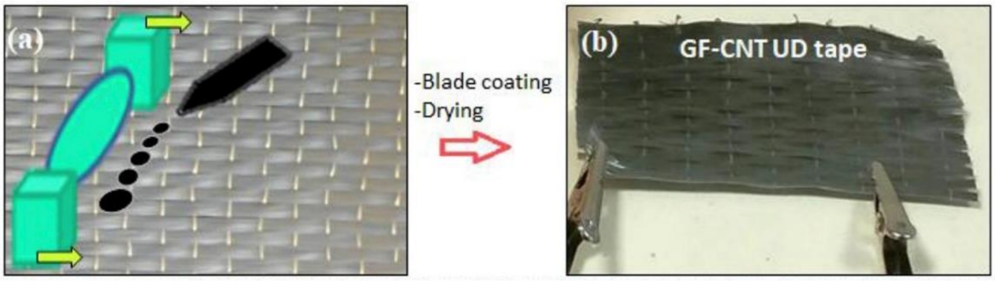

Figure 2.28 : a) Schematic representation of the blade coating process used to fabricate the GF-CNT and b) digital image of the resulting CNT-coated glass fiber before composite fabrication using vacuum infusion method [194].

Trigwell et al. coated the surface of CFRP using CNTs, as shown in Figure 2.29a [195]. Before testing in three-point bending test. At a deflection of around 2.6 mm, the authors measured the resistance which increased with increase in the applied stress as shown in Figure 2.29b. However, the researchers had to scrap off the ends of the coated layer to prevent direct contact with loading supports. This indicates that the direct coating offers minimal control over the design of printed sensors onto composites.

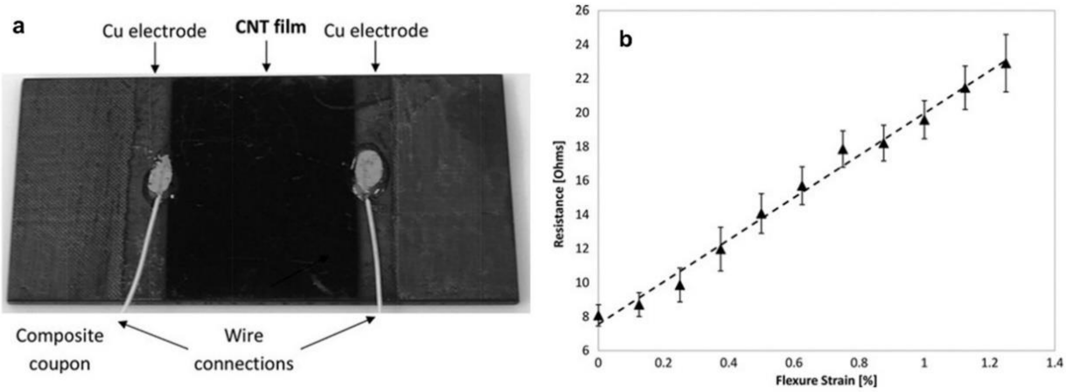

Figure 2.29 : a) Digital image of CNTs coated onto CFRP composite and b) resistance value as a function of flexure stress under three-point bending test.

2.4.3 Printing of strain sensors

Integrating piezoresistive strain sensors onto composites has provided researchers with more significant opportunities for optimizing sensor performance and design due to its ability to avoid bonding and alter the composite's inartistic properties [26–40].

2.4.3.1 Laser printing

Groo et al. transferred a laser-printed strain gauge grid on a Kapton substrate onto the surface of glass fiber prepreg using a rolling press, as shown in Figure 2.30. The laser-induced graphene (LIG) patterns were produced on Kapton® tape using a CO_2 laser cutter and then transferred onto the tacky surface of a heated glass fiber prepreg using a rolling press. The transfer was enabled by the adhesive nature of the prepreg at 80 °C, which allowed the graphene texture to bond without additional adhesives. After transfer, the layup was completed with additional prepreg layers and cured. The embedded sensor structure preserved the printed geometry and required no external bonding, resulting in a fully integrated sensing layer. The laser engraving speed was used to control the sensor's dimensions. While this method successfully produced adhesive-free strain sensors with acceptable quality, it involved multiple steps, and the resulting sensors had a relatively low sensitivity of around 1.

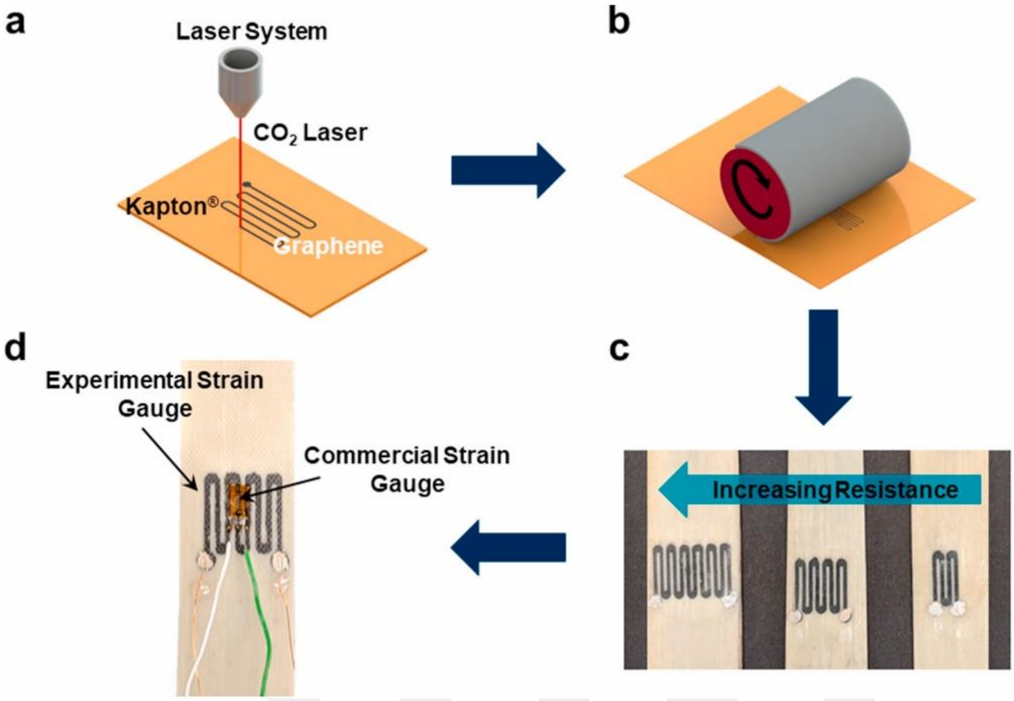

Figure 2.30 : Illustration of the laser-printed strain grid sensor: a) printing process and b) transfer process. c) Image of transfer-printed strain gauges with varying resistance. d) Image of the completed sample featuring both LIG and commercial strain gauges [28].

Luo et al. used direct laser writing to engrave strain sensors on a polyimide film bonded on a GFRP composite's surface [26], as shown in Figure 2.31. They demonstrated that altering fabrication parameters such as scanning paths could control the sensor's sensitivity.

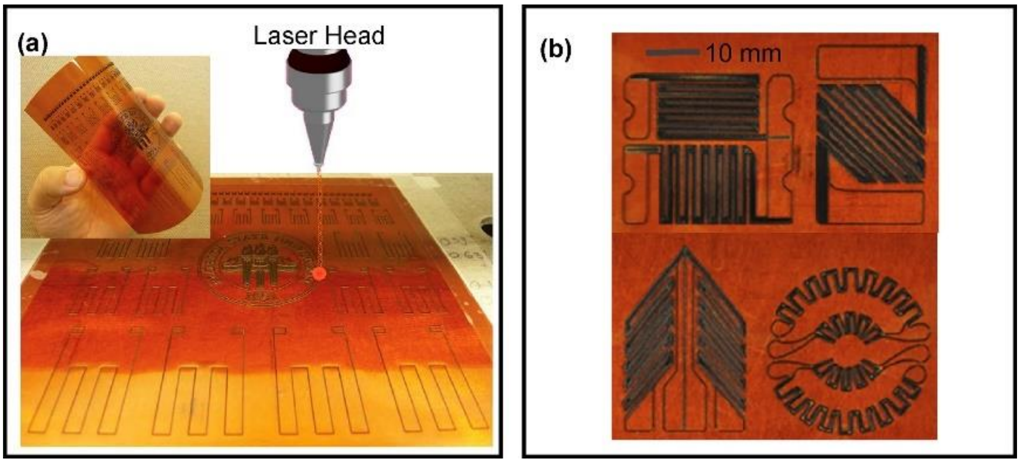

Figure 2.31 : a) Direct laser writing fabricated graphitic sensor patterns on polyimide film. b) Images of printed piezoresistive sensors with various configurations [26].

A curved GFRP was outfitted with seven laser-engraved graphitic strain gird sensors (S1-S7), as depicted in Figure 2.32a. During step-wise compression from 0.6 N to 3.4 N, the graphitic sensor S4 exhibited a significant resistance increase of approximately 0.9% at 0.6 N and 5.6% at 3.4 N, while a commercial strain gauge showed only 0.25% and 0.5% resistance change, respectively (Figure 2.32b). Furthermore, the study revealed that the resistance change and mechanical deformation of mounted laser-engraved graphitic sensors are highly dependent on their location when underwent compression testing (Figure 2.32c). Impressively, sensor S4 maintained negligible performance change even after 10,000 cycles at a frequency of 0.16 Hz (Figure 2.32d), indicating excellent durability comparable to commercial strain gauges.

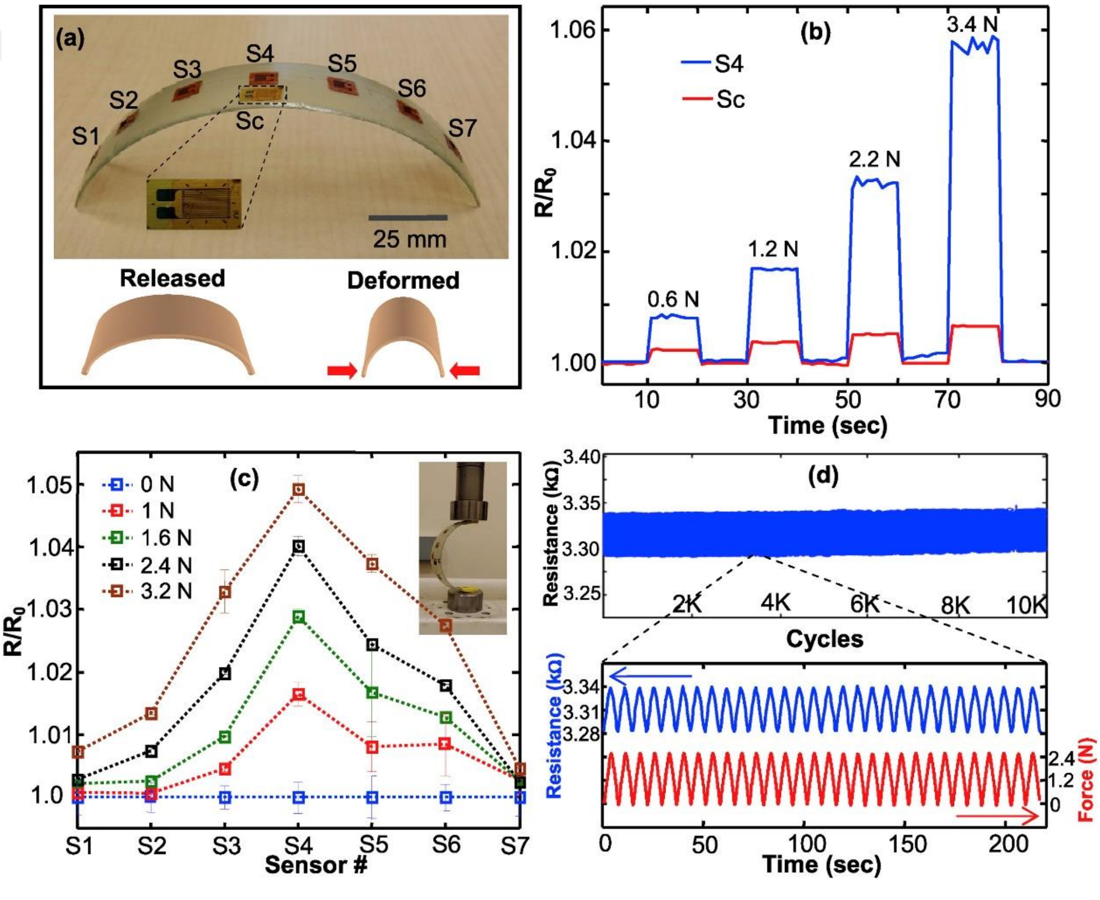

Figure 2.32 : a) Digital image showing strain sensors adhered to a curved GFRP specimen. b) Corresponding resistance changes for sensors S4 and S5 under varying compression loads. c) Resistance responses of Sensors S1–S7 across different compression levels, illustrating the inhomogeneous strain distribution within the composite structure. d) Durability test results highlighting the resistance stability of sensor S4 under repeated loading [26].

2.4.3.2 Screen printing

Recent efforts have focused on fabricating strain gauges made of carbons that can be bonded onto rigid parts. Zymelka et al. used screen printing method to fabricate an omnidirectional strain sensor using a thermosetting graphite paste on poly(ethylene naphthalate) which was subsequently heat-treated at 150 °C for 30 minutes, as illustrated in Figure 2.33 [29]. The cured sensor was bonded on a metal surface using cyanoacrylate adhesive and then was laminated for protection. The highest sensitivity was around 3 when the sensor went under bending stresses.

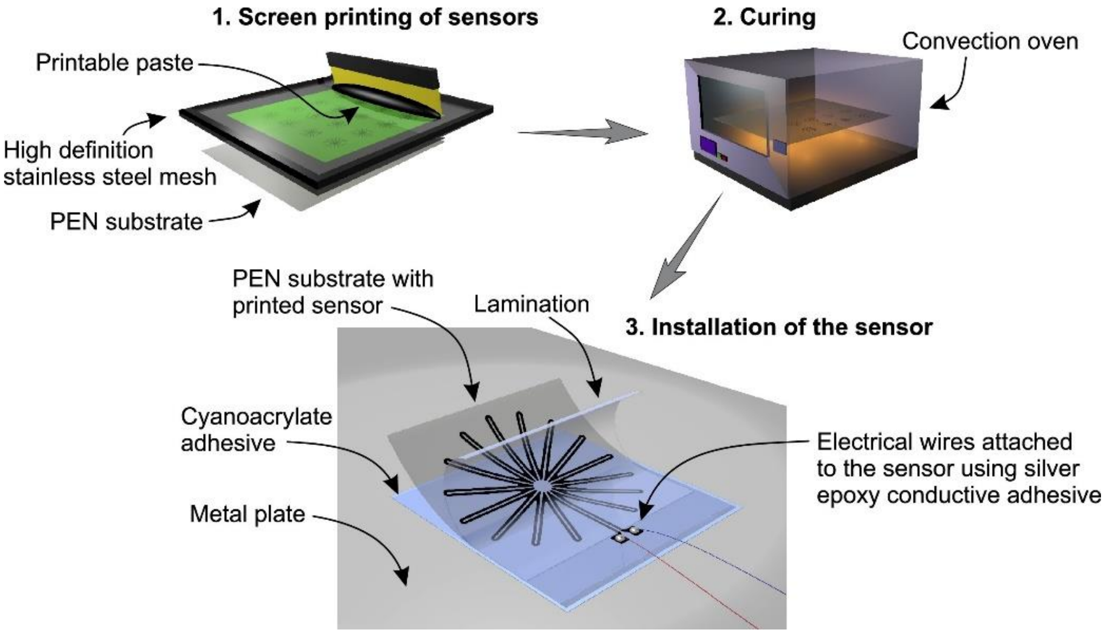

Figure 2.33 : Representation of screen printed carbon-based sensor [29].

Furthermore, the same group applied the same symmetrical design to screen-print a strain sensor on polyethylene terephthalate (PET) [34]. This sensor features a complete Wheatstone bridge structure, which compensates for temperature variations and ensures stable performance under varying conditions. Notably, it consumes significantly less power (0.089 mW compared to 144 mW for a conventional rosette), making it highly suitable for integration into IoT applications. Another study used a commercially available carbon paste to screen-print a grid strain sensor onto PET film, as shown in Figure 2.34 [40]. The sensor exhibited a resistance of 875 kΩ ± 514 kΩ and a gauge factor of 8.8 ± 0.3 under unidirectional tensile loading.

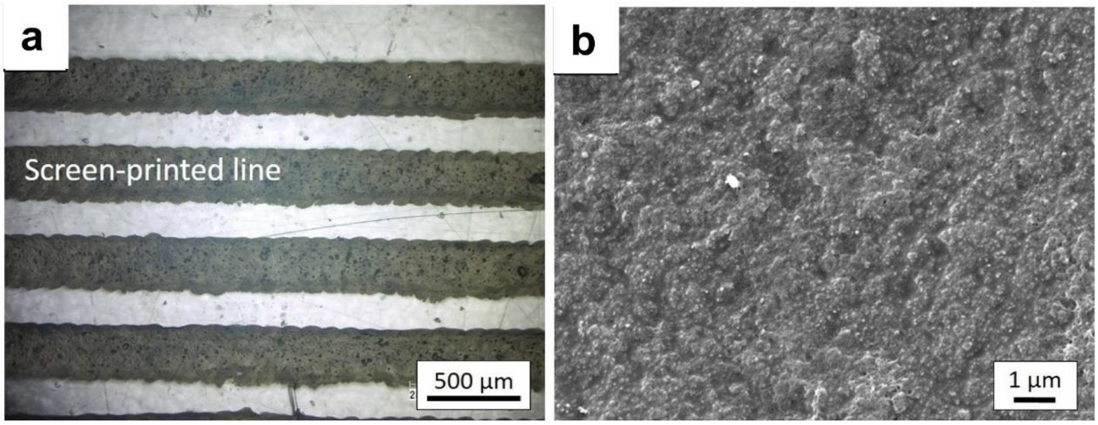

Figure 2.34 : a) Light microscopy image of the screen-printed sensor and b) surface topography of the carbon ink layer [40].

When a carbon paste ink sensor was subjected to a 1% tensile strain along its longer axis, its response to strain was linear, as shown Figure 2.35. This carbon-based sensor achieved a notable gauge factor of 8.8 ± 0.3, indicating its effectiveness in sensing strain.

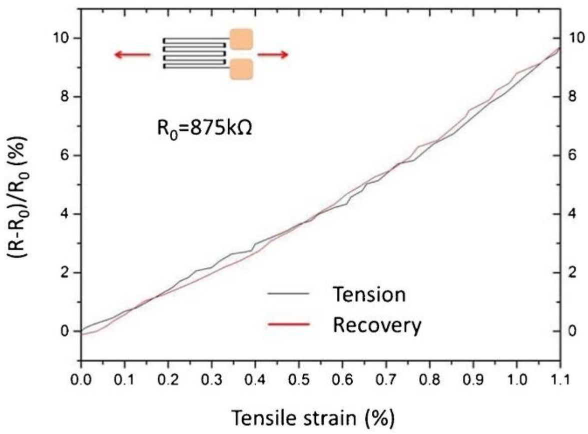

Figure 2.35 : Strain response of a carbon-paste screen-printed sensor on a PET dog-bone specimen under unidirectional tensile loading [40].

2.4.3.3 Direct writing

Other promising approaches have focused on directly transferring strain gauge patterns onto or into rigid substrates, such as metals and composites, using direct writing or printing methods. In one study, the direct writing method was implemented to print a conventional carbon-based (commercially available printable carbon ink) strain gauge pattern on the surface of the titanium metal part using micro-dispensing direct write technology, as demonstrated in Figure 2.36 [196]. The printed line widths were consistent at 175 ± 12 µm, and the measured resistance was 203.2 ± 12 kΩ. The sensor exhibited a sensitivity of 10 under bending conditions. Although the fabrication process does not require an adhesive layer between the sensor and the metal substrate, a post-treatment heat process is necessary to improve bonding quality and ensure mechanical stability of the as-printed sensor.

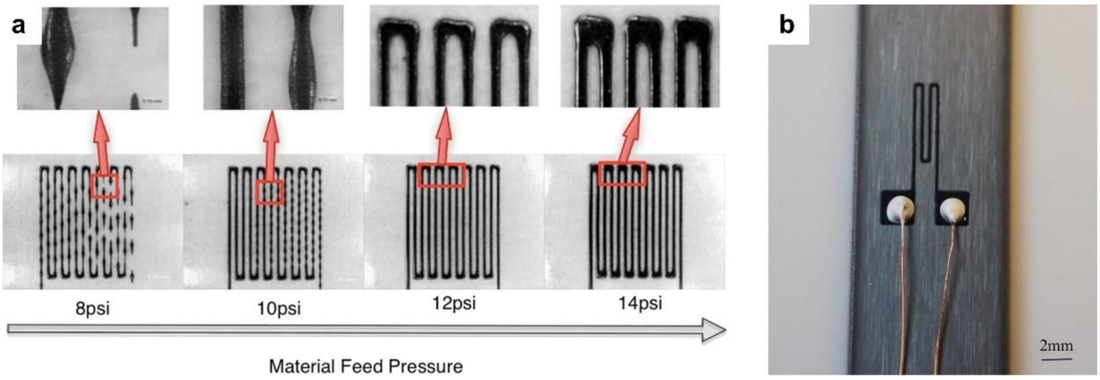

Figure 2.36 : a) Illustration of how material feed pressure influences print resolution in micro-dispensing direct-write process and b) digital image of a carbon-based micro-dispensing direct-write pattern on a titanium plate [196].

When evaluating the performance of the strain gauges, experimental measurements revealed a linear relationship between resistance change and applied strain, as shown in Figure 2.37. The measured gauge factors for the sensors ranged from 9.3 to 10.6, indicating good reproducibility across different samples. In contrast, the commercial strain gauge used for comparison exhibited a significantly lower gauge factor of 2.1. This highlights the superior sensitivity of the developed sensors compared to standard commercial alternatives.

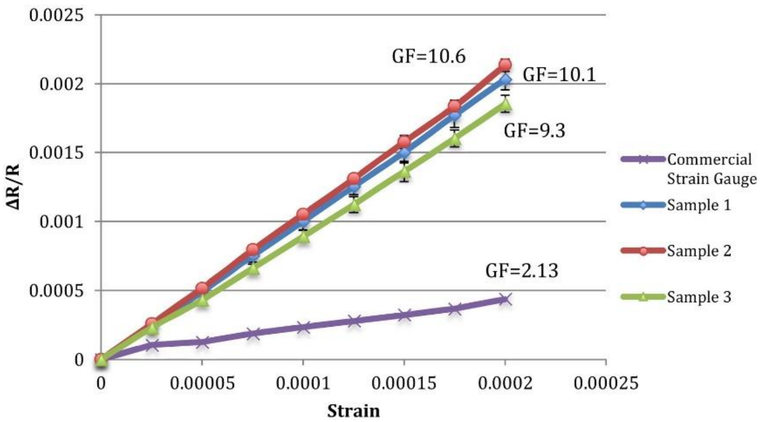

Figure 2.37 : Resistance change of a carbon-based micro-dispensing direct-write pattern on a titanium plate under bending force and alongside a commercial strain gauge mounted on the same titanium plate [196].

In another study, a silver nanoparticle-based strain sensor was fabricated using inkjet printing, achieving a resistance of 65.2 Ω ± 0.3 Ω and a gauge factor of 3.7 ± 0.3. This further highlights the potential of alternative printing techniques for developing high-performance strain sensors [40]. Similarly, Owen et al. presented a direct printing approach to print electronics using polymer-free, aqueous CNT ink, as demonstrated in Figure 2.38 [197]. The study investigated how printing resolution, ink rheology, and ink-substrate interactions influence performance, resulting in printed lines with high conductivity. Applications include conformal printing on curved surfaces, interactive structures, and capacitive sensing.

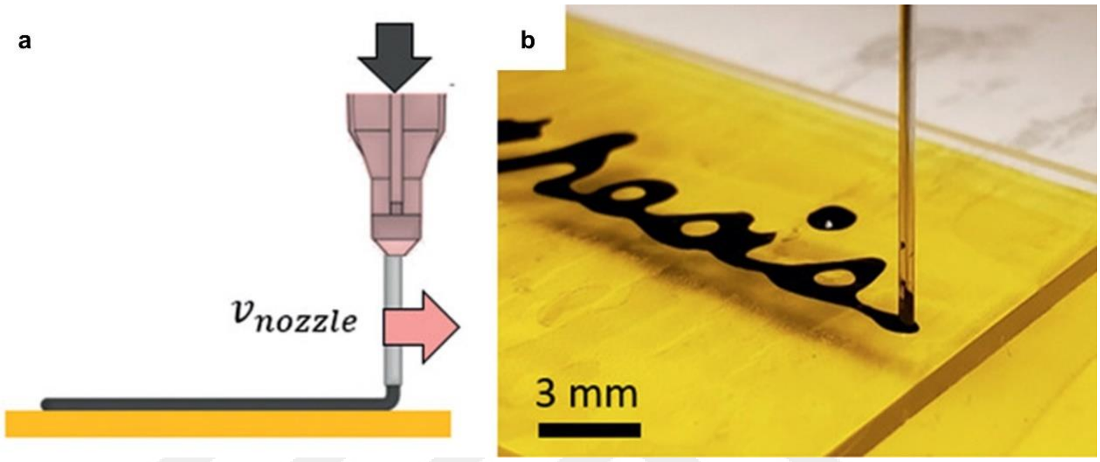

Figure 2.38 : a) Moving direct printing nozzle and b) actual printing using CNT-based aqueous inks [197].

2.4.3.4 Spray printing

Spray printing has emerged as a promising technique for creating highly sensitive and adaptable strain sensors. For instance, the spray coating of CNTs on glass fibers, as illustrated in Figure 2.39, resulted in a well-dispersed and relatively homogeneous nanofiller distribution on the fiber surfaces [198]. This process forms electrically percolated conductive networks within the composite laminates, yielding a gauge factor of 6.5 ± 0.2. These characteristics enhance piezoresistive performance, cyclic stability, and reproducibility, making spray-coated CNT glass fiber composites effective for reliable in-situ damage detection and strain monitoring in structural health applications. Similarly, piezoresistive materials such as CNT/PVDF composites prepared by spray printing have achieved a gauge factor of up to 4.4, showcasing the method’s potential for cost-effective, large-scale sensor applications [199].

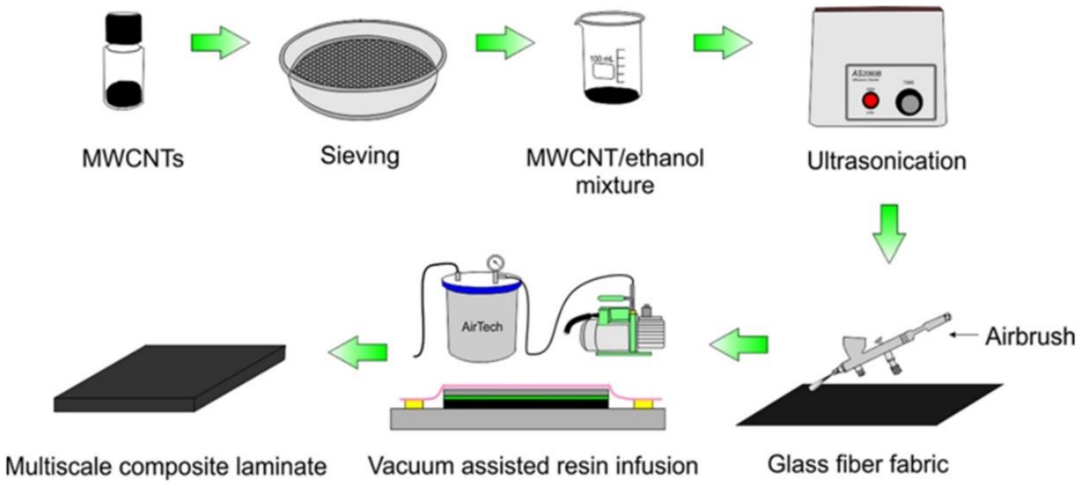

Figure 2.39 : Schematic representation of ink preparation and printing onto glass fiber fabric prior to the vacuum infusion method for composite laminate fabrication [198].

Spray printing is a highly effective technique for fabricating strain sensors, exemplified by the work of Sethy et al [108,200]. They developed GNP/PMMA sensors spray-printed onto GFRPs, which, under unidirectional loading at a strain of 0.45%, exhibited impressive gauge factors of 55 ± 0.5, 70 ± 2, and 77 ± for baseline resistances of 1, 7, and 21 kΩ, respectively [108]. This same group also highlighted the adaptability of their spray-coated GNP/PMMA strain sensors by directly applying them onto stainless steel substrates, as shown in Figure 2.40 [200]. In this particular study, eight sensors with varying initial resistances, ranging from 200 Ω to 3.5 kΩ, were fabricated using a Scotch tape exfoliation method, which enabled resistance tuning by mechanically cleaving the coated surface. The sensitivity of each sensor was assessed in terms of gauge factor, revealing that the sensor with a 400 Ω baseline resistance achieved the highest gauge factor of 263 at a strain of 0.15%. This performance significantly exceeds that of a standard industrial strain gauge (350 Ω, GF ≈ 1.5), underscoring the strong impact of initial resistance on strain sensitivity and the promise of this fabrication approach for customizable, high-performance sensor applications.

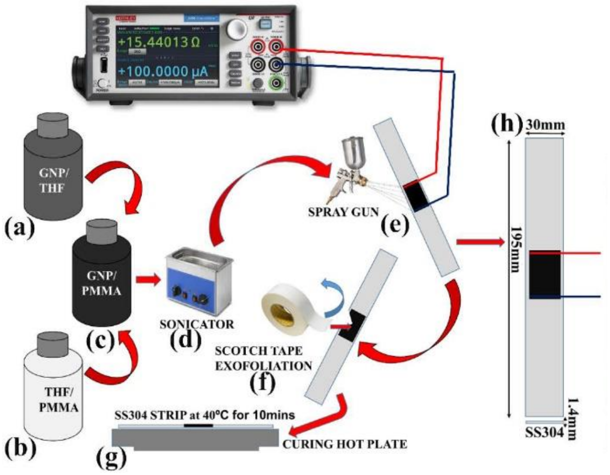

Figure 2.40 : Spray printing of carbon-based sensors onto stainless steel [200].

2.4.3.5 Others

One group used spray-depositing CNT-based solution onto PI films to achieve a uniform coating, then shaping the films into a serpentine pattern using an engraver machine [27,30,31]. The performance of the strain sensors can be significantly enhanced by optimizing various parameters such as grid geometry, polymer coatings, and surface treatments. Adjusting the geometry of the CNT grid can increase the gauge factor, with a 13% improvement observed through such optimizations [27]. Polymer coatings like polysulfone improve repeatability and linearity, albeit with reduced sensitivity compared to polyurethane. Surface treatments, such as those involving HNO3/H2SO4, enhance the adhesion of CNTs to polyimide substrates by increasing surface roughness and introducing functional groups, leading to improved strain transfer and higher gauge factors [30]. Furthermore, computational models, including finite element and multiscale approaches, provide valuable insights into the piezoresistive behavior of CNT networks, with the latter accounting for nanoscale effects like electron tunneling [31]. These advancements collectively contribute to more reliable, sensitive, and tunable strain sensors suitable for various applications.

Implementing photolithography and micromoulding, the carbon black-polydimethylsiloxane (CPDMS) composite strain gauge sensor was sandwiched between two layers of PDMS [38]. Briefly, CPDMS was poured into silicon molds and cured in an oven environment, and lithography patterning was used to pattern strain gauges. The prepared sensors were embedded into two layers of PDMS, cured at elevated temperatures, and mechanically pressed. A five-grid gauge sensor had a sensitivity of 4.4 at strains of 250%.

Using a drilling machine, an engraved conventional strain gauge on the surface of an acyclic beam was fabricated [201]. Carbon nanotube-epoxy composite filled the engraved pattern and was cured in a vacuum, as shown in Figure 2.41. The surface of the sensor was polished before testing. The authors reported a sensitivity of around 2.5 under cantilever bending stress.

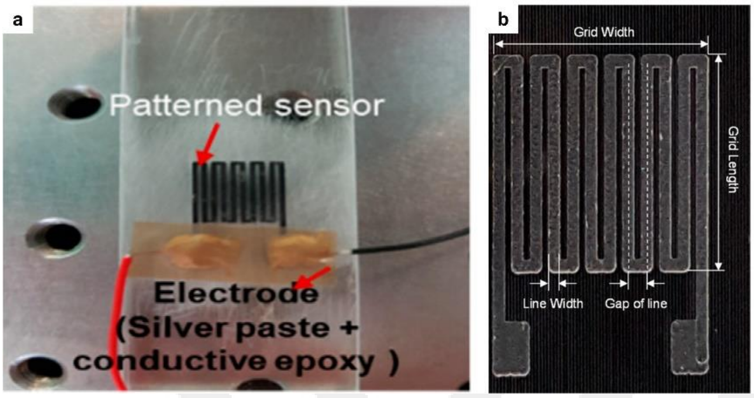

No.	Specification	MWCNT/epoxy sensor
1	Grid width (mm)	9.5
2	Grid length (mm)	10
3	Line width (mm)	0.25
4	Gap of line (mm)	1
5	Depth (mm)	0.5
6	Total length (mm)	87

Figure 2.41 : a) Final CNT-based strain gauge grid pattern filling the drilled area and b) geometry of the patterned CNT-based grid pattern [201].

A cost-effective shadow mask printing method was employed to create flexible sensors by brushing liquid sensing material onto a substrate, with a custom taping scheme to prevent ink leakage [35]. The sensor's functional area was then packaged using thermal compression bonding. When the sensor was subjected to a three-bending test, a sensitivity as high as 17 was reported.

In another method, CNT-epoxy was mold-casted to prepare a conventional strain gauge sensor [36]. After bonding the sensor to the surface of a steel part and allowing the part to undergo bending stresses, the sensor had a sensitivity of 0.9.

Lee et al. successfully printed silver nanoparticle-based strain sensors onto GFRP using an aerodynamically focused nanoparticle technique, with the printed sensor shown on a GFRP specimen in Figure 2.42 [202]. They subjected this composite to a four-point bending cyclic test in a UTM, spanning a strain range from 0.2% to 1% (Figure 2.42b). Notably, the resistance change for their printed sensor was significantly higher compared to a commercial strain gauge mounted on the same GFRP, as depicted in Figure 2.42c. The printed sensor achieved an impressive gauge factor of 14, substantially outperforming the commercial gauge's GF of 2. Moreover, this nanoparticle sensor proved reliable over 200 cycles of 1% peak strain, showing only a minor drift of about 1.5% in peak resistance change (Figure 2.42).

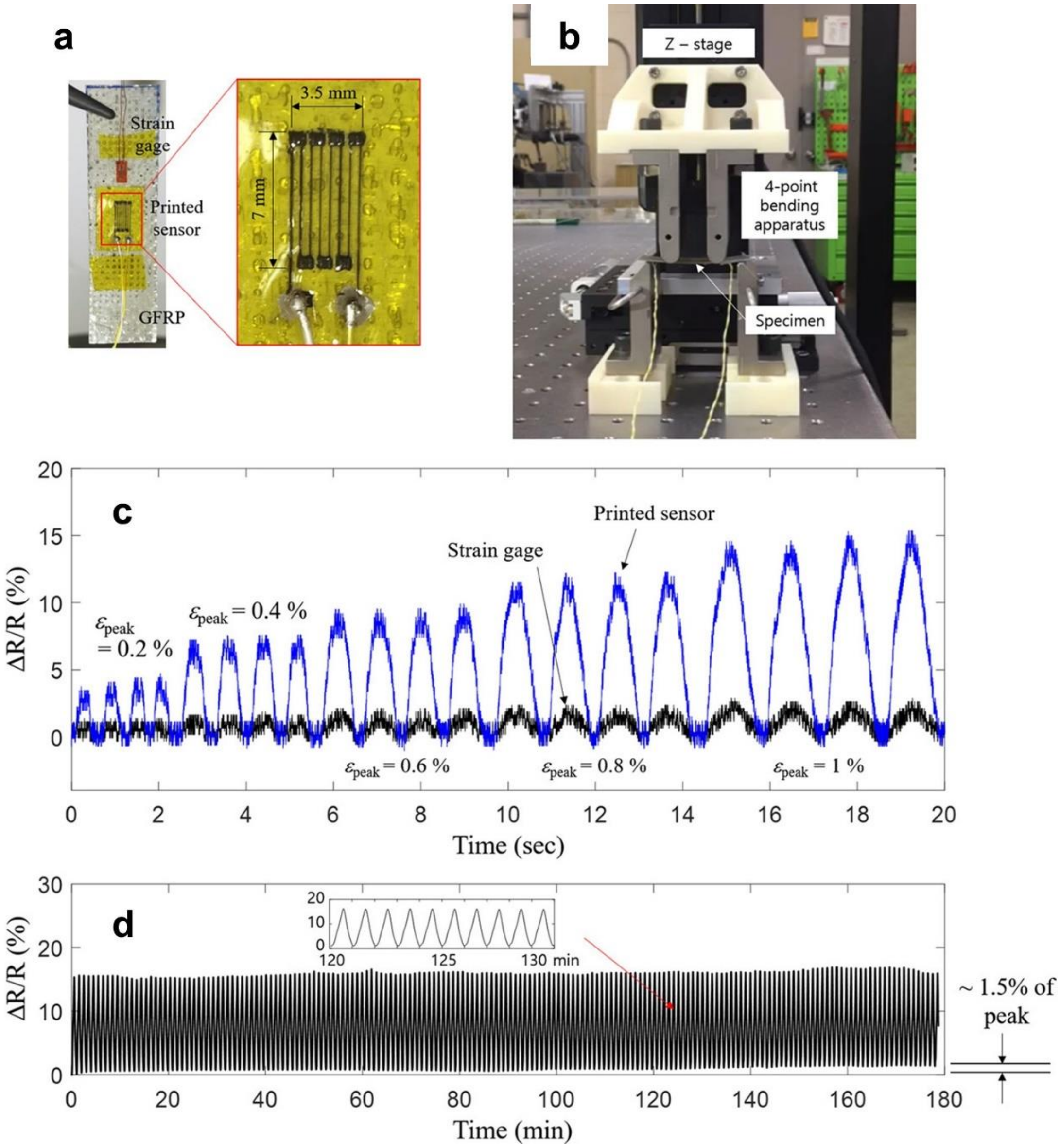

Figure 2.42 : Performance of aerodynamically focused silver nanoparticle-based strain sensors on GFRP. a) Printed silver-based sensor on GFRP specimen. b) Host composite under four-point bending cyclic test. c) Comparison of resistance change between printed and commercial sensors [202].

Despite all the efforts mentioned above, a comprehensive understanding of the electromechanical performance of carbon-based piezoresistive strain sensors compatible with composite structures is lacking. Current carbon-based strain sensors are printed or engraved on an intermediate polymer substrate, such as Kapton film, which is then adhered to the composite surface. However, while these solutions have demonstrated good compatibility with FRP composites, the fabrication process is often multistep [26,28] and attention is required to ensure proper adhesion [29].

2.5 Multifunctional Sensing Capabilities

The operational temperature range of aircraft typically spans from -60°C to 80°C, depending on the season and flight conditions [60,203]. Such fluctuations can significantly affect sensor measurements in SHM applications, highlighting the need for accurate temperature compensation [204]. To address this, hybridization of carbon nanomaterials has been explored. For example, Kurian et al. demonstrated that a graphene–CB hybrid sensor exhibits minimal resistance variation under temperature changes, as shown in Figure 2.43 [119].

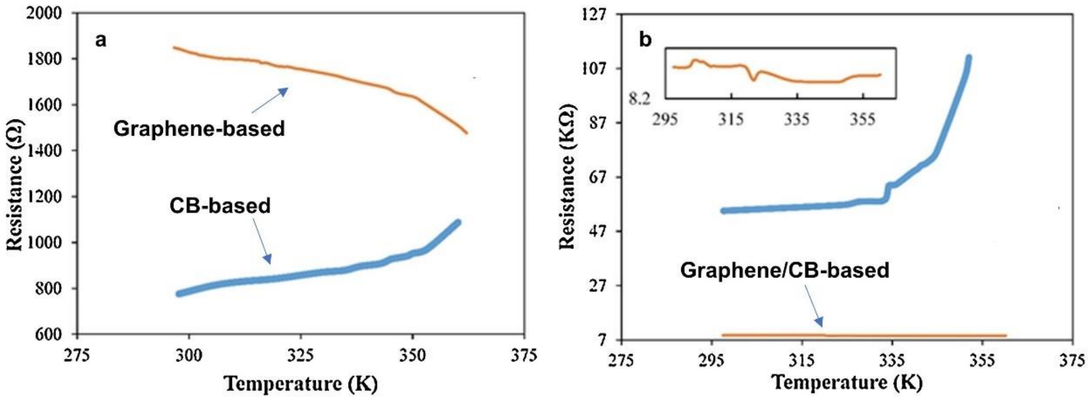

Figure 2.43 : Measured resistance as a function of temperature for a) graphene- and CB-based sensors and b) graphene- (at lower content compared with that shown in Figure 2.43a) and graphene/CB-based hybrid sensors [119].

In a similar approach, Luo et al. developed SWCNT/GNP-based film sensors to achieve temperature compensation [205]. While GNP and SWCNT films exhibited upward and downward resistance drift with temperature, respectively, their hybrids at specific ratios demonstrated self-compensating behavior, as shown in Figure 2.44. This behavior is due to the opposite thermal responses of the two materials: in GNPs, increased temperature enhances phonon scattering, which reduces charge carrier mobility and raises resistance; in contrast, SWCNTs follow a hopping conduction mechanism, where higher temperatures improve charge transport and lower the resistance.

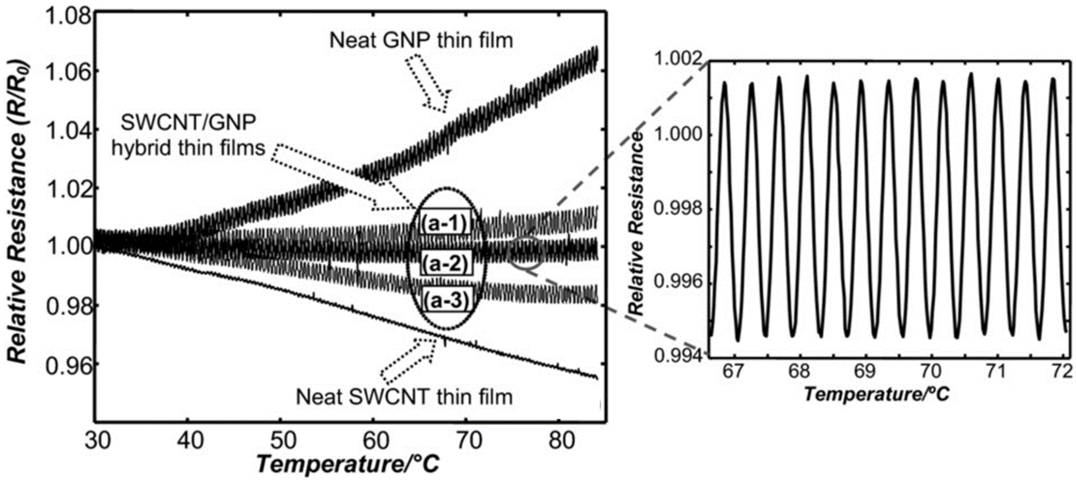

Figure 2.44 : Piezoresistive response of neat GNP, SWCNT, and hybrid SWCNT/GNP films under 30–85 °C ramp [205].

In addition to strain sensing, piezoresistive sensors can also respond to environmental stimuli such as gases [206–208], humidity [209,210], and temperature [211,212], demonstrating multifunctional sensing capability. However, temperature sensing in composites remains less developed than strain sensing. Building on efforts to address temperature effects in SHM, one common strategy involves tracking resistance changes in conductive materials [213,214]. For instance, CNT–graphene hybrid sensors, like those discussed above, have also been engineered for temperature detection, demonstrating responsiveness to temperature changes exceeding 100 °C [215].

Similarly, screen-printed graphene-based inks printed onto textile exhibit both thermoresistive and piezoresistive properties, making them suitable for detecting temperature and deformation [135]. In addition, screen-printed triboelectric nanogenerators have shown the capability to sense both environmental humidity and human motion, further demonstrating the multifunctional potential of printed sensors [216]. These innovations emphasize the promise of modern sensor technologies, though integrating multifunctional sensors seamlessly into composite structures remains lacking.

2.6 Antenna Applications of Carbon-Based Materials

In the late 2000s, attempts to integrate antenna systems with other composite structures were reported. The composite structures must be thick enough to incorporate patch antennas to provide the needed electrical properties, i.e., dielectric constant. To use composite structures besides sandwich structures, one group utilized 3D-waved composites that allowed the antenna to be waved in, and its 3D shape was thick enough to deliver the required electrical performance [217,218]. Under static conditions, the performance of the antenna system was shown to be promising. Another interesting attempt concerned the multi-functionalities of CFRP laminates as composite structures and the conductive carbon fibers as a simple dipole antenna [219], as shown in Figure 2.45. Despite the simplicity of the approach, it could only be applicable for parts that are long enough and can be separated into two parts, e.g. rotor blades in helicopters, to constitute the entire dipole antenna. Furthermore, one paper demonstrated the detection of delamination cracks in laminated CFRPs through a resistance change coupled with an oscillating circuit to make up a wireless system capable of detecting delamination cracks [220]. Despite the novelty of the idea, the oscillating circuit contains rigid parts that render it applicable to any feasible application.

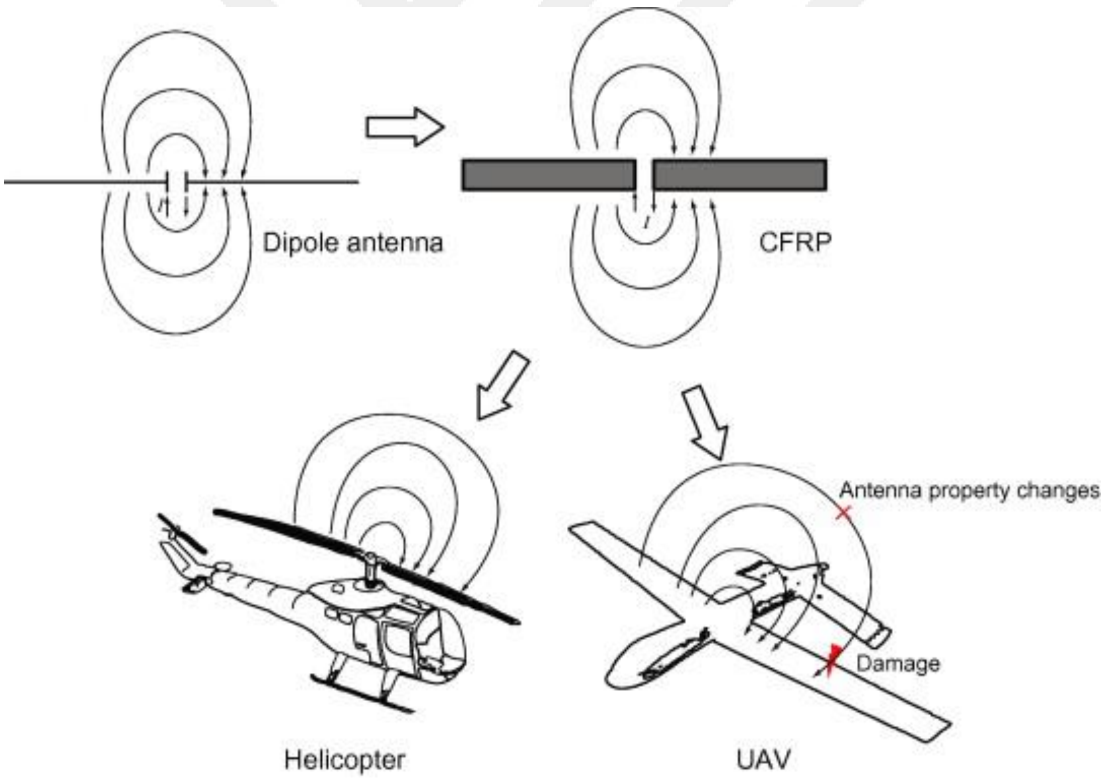

Figure 2.45 : Evolution of antenna designs from dipoles to multifunctional antenna/sensor wing structures [219].

The last decade has increased interest in integrating wireless systems with composites. For example, the same group that developed 3D-woven antenna composites in the late 2000s has been advancing such an approach to encompass complex antenna designs and composite geometries [221,222] (Figure 2.46), detection of damages wirelessly

[223], and flexibility [224]. Although these studies have successfully demonstrated the integration of antenna systems with 3D-woven composites, the approach they are following limits the possibility of expanding material selection for the antennas, as discussed in the material section of this literature review. The full potential of a communication system is yet to be fully exploited.

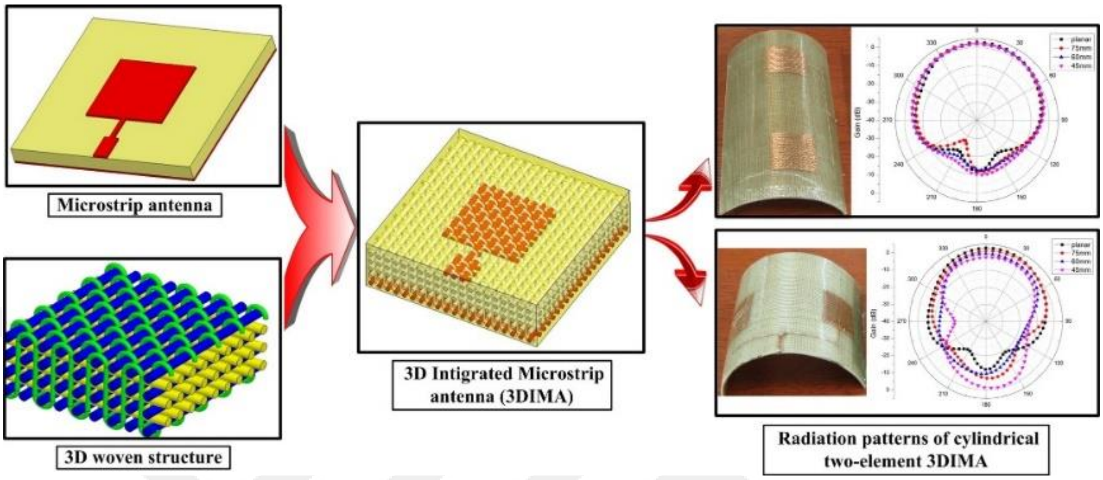

Figure 2.46 : Integrated microstrip antennas into 3D woven GFRP structures [222].

Other notable attempts that followed different approaches include using an embedded Radio Frequency Identification (RFID) tag, which contains solid circuit parts, into the laminated composite to signal out chemical attacks by monitoring changes in signal strength [225]. Another report described a harvesting circuit element that derives its energy from the vibrations of the composite itself, using a piezoelectric element to harvest these mechanical changes. These changes power the circuit, enabling sensing capabilities [226]. However, using such wireless sensors, which contain solid circuits, presents several disadvantages, such as issues with structural compatibility and the potential for mechanical failure due to the solid components acting as points of stress concentration.

Patch antennas, also known as microstrip antennas, have been utilized for strain and temperature sensing applications due to their ease of integration and compact size. Patch antennas operate at frequencies, typically between 300 MHz and 300 GHz. For strain sensing applications, depending on the materials used, the frequency range reported in the literature spans from around 900 MHz to 12 GHz [227–229]. The strain-sensing mechanism relies on physical changes to the antenna, particularly internal resistance or electrical conductivity changes, when the sensor undergoes tensile or compressive strains [228]. Most patch antenna strain sensors developed to date have been applied to metal parts [229,230]. This is mainly because these sensors use copper foils as the conductive material, as discussed in the Materials section, and the fabrication process typically involves conditions such as chemical etching and high temperatures, which are more suited to metal structures than composites. The few attempts to integrate patch antennas with composites as mechanical damage sensors have involved using copper wires woven into 3D-woven composites or inserting pre-fabricated patch antennas between sandwich composite layers [223,231].

RFID antennas are generally larger than patch antennas because they operate in the radio frequency range and require power sources, such as batteries, to function. Developing wireless systems for applications like wearable textiles and the IoT has gained significant attention [232–234]. However, RFID systems require a power source, which is not an ideal feature for composites. Including such solid components can act as a defect point, potentially compromising the mechanical properties of the composite structure. On the other hand, passive RFID antennas do not require an external power source, making them attractive for applications in strain sensing for SHM, IoT, and textiles [230,235–237]. In composite applications, one study reported embedding readily available RFID tags containing a solid chip into laminated composite structures to serve as chemical attack sensors [225]. However, embedding incompatible foreign objects, such as antennas, into composites often results in delamination over time [238]. Therefore, it can be concluded that both passive and active RFID sensors are not well-suited for integration with composites.

Copper-based wireless systems are the most developed and studied for strain sensor applications among all the materials reported in the literature [227,229,236,239–243]. This is primarily due to copper's high electrical conductivity, which results in excellent antenna performance, its relative abundance compared to silver and its outstanding electrical properties [244]. For instance, recent work has shown that a carefully designed copper-based antenna can detect cracks and their orientation [242]. Another study demonstrated that a simple rectangular copper-based patch antenna could simultaneously sense changes in both strain and temperature [239]. Overall, copper-based wireless systems are a strong candidate for wirelessly detecting mechanical stimuli-related changes.

Although significant progress has been made with copper-based sensors, direct integration of copper-based wireless systems with structural composites has been limited. Such integration was demonstrated in preliminary works over a decade ago [245], as shown in Figure 2.47, or textile structural composites [221–224]. In the latter, copper yarns were sewn into 3D structural fiber-reinforced composites as radiation patches and ground planes. While integrating a patch antenna with 3D structural composites is feasible, this approach may not be adaptable for non-3D structural composites. The copper-epoxy chemical stability and antenna performance over long periods have not been thoroughly studied. These limited works also fail to demonstrate the sensing performance of these systems. This suggests that copper-based wireless sensors for structural composites remain underdeveloped and highlights the potential difficulty in integrating copper FRPs, as will be further discussed next.

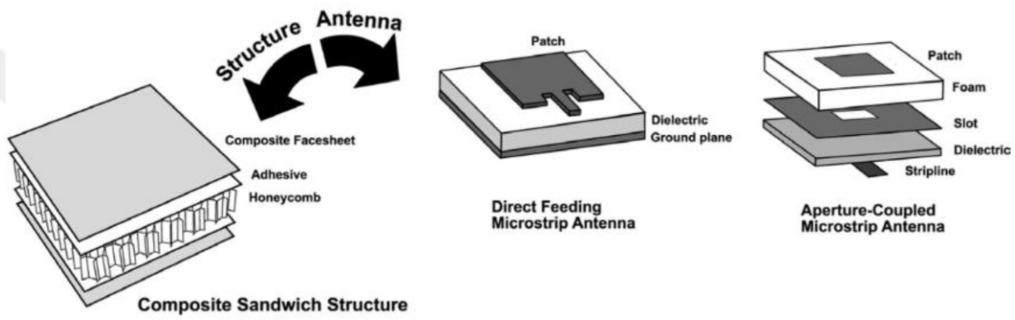

Figure 2.47 : Integrated antenna into composite sandwich structure [245].

Oxidation is a significant issue for all copper-based materials, including during manufacturing processes such as chemical etching for copper-based bulk materials and even in the final product, especially for copper-based nanomaterials when exposed to air [244]. The harsh etching process is not only a complex fabrication procedure, which may not be suitable for various plyometric-based substrates, but it is also environmentally hazardous due to byproducts like halogenated compounds [246]. Additionally, copper-based inks affect performance reliability over a long time [244].

These challenges have been addressed in recent literature to continue utilizing copper for antenna-based applications, although the primary focus has been on textile applications. For instance, the oxidation problem has been mitigated by alloying copper with oxidation-resistant substances such as silver, graphene, and glucose [244,247,248]. Additionally, the complication of the etching fabrication process has been overcome by adopting direct printing and spraying techniques, which involve developing nanoscale copper-based printable inks [249–251], screen printable inks [40,252], and sprayable inks [253].

While CNTs have been tested for their applications in wireless systems [232,254,255], their development is not as advanced as the piezoresistive sensors discussed earlier. For example, a SWCNT-based RFID tag was fabricated using inkjet technology for gas sensing applications [256]. Another study demonstrated that by slightly modifying a silver-paint antenna, a small area coated with SWCNTs could sense temperature variations [257]. However, CNT-based antennas do not perform as effectively as copper-based ones due to challenges in controlling CNTs and their liquid-form electrical properties [255]. Consequently, there is a lack of substantial literature on the performance of CNT-based wireless systems.

The development of graphene-based antennas, mainly for textile applications, has been the focus of some recent research [258–262] and, to some lesser extent, its strain sensor application. To my knowledge, most of the recent work mainly concerns textile applications [228,234,263]. For instance, a highly sensitive, flexible graphene-based patch antenna strain sensor has been demonstrated [263]. This sensor was shown to distinguish between tension and compression strains. However, the fabrication approach used in this study cannot be transformed or incorporated into structural composites. That said, other graphene-based wireless systems have been reported in the literature, such as gas sensors [206], pressure sensors [264], and humidity sensors [209].

Hybridization for wireless systems is a relatively underdeveloped area compared to piezoresistive-based sensors. This may be due to the dominance of copper, an excellent candidate for such applications because of its high conductivity and the fact that carbon-based antennas are still emerging. Nevertheless, one study demonstrated the direct printing of rGO and silver ink in the shape of a patch antenna used as a gas sensor [265], where rGO acted as the active material for sensing changes in gas concentration.

2.7 Summary

In conclusion, various SHM technologies have been explored for composite structures in the aerospace sector. While optical fiber and piezoelectric transducer sensors exhibit relatively high technology readiness levels (TRLs), their integration with composites remains challenging. In contrast, carbon-based nanomaterials offer excellent compatibility with composites, making them strong candidates for embedded or surface-mounted sensing applications.

Over the past decade, piezoresistive carbon-based sensors have emerged as a promising solution for strain measurement in composites, owing to their lightweight nature, design flexibility, material compatibility, and excellent sensitivity. This field has gained increasing attention with the advancement in the synthesis and processing of conductive nanomaterials, such as carbon-based nanoparticles. Their incorporation into composites has proven both practical and effective.

The dimensionality of carbon nanomaterials, 0D (*e.g.*, CB), 1D (*e.g.*, CNTs, CNFs), and 2D (*e.g.*, graphene), plays a critical role in defining the electromechanical performance of piezoresistive sensors. For instance, CNTs and CNFs typically exhibit a downward drift in resistance under strain with linear responses, while CB often shows an upward drift with nonlinear behavior. Several studies have investigated the sensing mechanisms of each material and demonstrated that hybridizing different dimensionalities can combine their strengths, leading to tunable and enhanced sensor performance.

One key enabler of such hybrid systems is the formulation of printable inks using appropriate binders and dispersing agents. Notably, surfactants such as CNC and Triton X-100 have enabled the dispersion of hydrophobic nanomaterials into aqueous inks while also tailoring rheological properties to suit specific printing methods.

With the ability to control the sensor pattern during fabrication, researchers have also focused on how geometry, such as line length, width, thickness, and overall shape, affects sensor performance. Studies have shown that increasing the sensing length or decreasing the width can improve sensitivity, though often at the expense of reliability. As a result, considerable attention has been paid to optimizing sensor geometry, including the design of multidirectional strain sensors and novel omnidirectional architectures, in comparison to traditional grid patterns.

Advances in ink formulation have also expanded the range of deposition techniques available for integrating sensors with composite substrates. Methods range from simple approaches like direct coating to more controlled techniques such as screen printing on intermediate substrates, followed by transfer to the composite. Other reported techniques include laser engraving and direct spraying. However, these methods often involve multiple fabrication steps and sometimes require adhesive bonding, which adds complexity and limits integration to geometrically simple surfaces. Moreover, subsequent treatments, such as thermal curing, may be necessary to enhance performance and durability.

Recent studies have demonstrated the multifunctionality of printed sensors, showing that they can be tailored to mitigate temperature variations during strain sensing or even simultaneously sense strain, temperature, and humidity. Despite the progress in strain sensing, temperature sensing in composites is still relatively underdeveloped, although promising results have been shown using hybrid nanomaterial sensors with self-compensating behaviors.

Finally, the combination of the piezoresistive properties of carbon nanomaterials with their design flexibility has enabled wireless sensing through printed antennas. These antennas, often printed on flexible substrates, can monitor frequency shifts corresponding to mechanical deformation. While some research has explored integrating antenna-based strain sensors with composites, these have typically used conventional materials like copper, which pose integration challenges. Transitioning to carbon-based wireless sensors could provide a more seamless solution for smart composite structures.

3. OBJECTIVES AND APPROACH

3.1 Objectives

The use of FRP composites has steadily increased due to their exceptional performance characteristics in aerospace industry, including high strength-to-weight ratios and resistance to environmental degradation. To ensure the safety and durability of these materials, SHM systems—comprising one or more integrated sensors—are increasingly employed to track the condition of composite structures. However, existing monitoring technologies often fail to meet critical requirements such as *compatibility* with composite structures, *ease of integration*, and *reduced system complexity*.

This thesis addresses these challenges by leveraging the piezoresistive and electrical properties of carbon nanomaterials for sensor integration with GFRPs. The primary objective was to enhance the functionality and performance of these sensors for SHM applications and ensure their effective integration into aircraft structures. To achieve this, optimal integration methods were first established, followed by an evaluation of the performance of the carbon-based sensors, including both piezoresistive and antenna-type sensors. Their behavior was then tested in laboratory-scale setups designed to assess compatibility with composite structures and simulate real-world conditions.

To systematically address the research problem, the objectives of this thesis are outlined as follows:

- Development of carbon-based inks: Formulating carbon-based inks for use in various printing techniques, which were investigated for their suitability and effectiveness in sensor integration.

- Carbon nanomaterial impact: Study the influence of different nanomaterials (*e.g.,* carbon nanotubes, carbon black) on sensor response under multiple stimuli, including strain, temperature, and impact.

- Investigation of printing methods: Exploring and optimizing various printing techniques, such as screen printing and other advanced deposition methods, to determine their effectiveness in fabricating strain sensors on composite substrates.
- Geometrical pattern influence: Analyzing how the geometry of strain sensors affects their electromechanical performance, particularly under application-oriented conditions such as varying strain levels.
- Assessing sensor performance: Investigating the effect of different carbon nanomaterials (*e.g.*, CNTs, CB, etc.) on sensor performance under various stimuli, including strain, temperature, and impact. Additionally, printing of antenna will be assessed for their sensing capabilities.

The broader impact of work defined within this thesis is the driving motivation, summarized as follows.

- Decrease of aircraft downtime**:** Depending on the size of the aircraft, the NDT of an aircraft takes a considerable time; therefore, in-flight strain data that the proposed sensors can collect can decrease the frequency of these inspections, lowering the downtime of the aircraft. Eventually, condition-based maintenance can be an option.
- Real-time evaluation of the structural components for real-time countermeasures**:** due to the real-time nature of the data, the pilot (and/or auto-pilot) can be advised to perform preventative measures to delay/eliminate structural failure of the aircraft.
- Lighter SHM systems**:** Decreasing the weight allows higher fuel loads, lower fuel consumption, and many more critical advantages to aircraft (weight is one of the most important parameters affecting the aircraft's flight capabilities).
- Ease of application, highly flexible, and on-demand solution**:** A sensor tailored to the specific needs of each structural component and/or mission simplifies the SHM system considerably, and ease of application allows quick sensor replacement without allowing human operator risk.
- The outcome of this thesis will lay the groundwork for future technological advancements and the localization of emerging technologies in several key

areas. Advancing toward smart skin technologies, this research contributes to the foundational development of multi-sensor systems and smart skin applications for aerospace structures. The methodologies and technologies developed in this thesis may also find broader applications in industrial and technological domains, including medical diagnostics and wearable health monitoring systems.

3.2 Materials

CB (purity of 95% and size of 148 nm), CNF (purity of 96% and outside diameter ranges 190–590 nm), and silver paint (99% purity) were purchased from Nanografi (Turkey). CNTs (95% purity, 6–9 nm diameter, and 5 µm length) were purchased from Sigma-Aldrich (United States of America). Other CNTs (90% purity, < 9 nm diameter, and 1 µm length) were purchased from Nanocyl. Additional CNTs (99 wt% MWNTs, < 20 nm) were purchased from NanoIntegris (USA), and CNTs (95 wt% MWNTs, 5–15 nm diameter, and 10–50 µm length) were purchased from Cheaptube (USA). Graphene ink with total solid content of around 10 wt.% dispersed in water was purchased from Graphene-Wear (lateral size 1000±500 nm and thickness ~10±5 nm). Triton-X 100 (TX-100) was purchased from Sigma-Aldrich (United States of America) and CNCs (NCV-100, diameter of 8 nm and length of 150 nm) were purchased from CelluForce (Canada). Isopropyl alcohol (IPA) was supplied by Carlo Erba Reagents (Germany). All materials were used without further purification. The abbreviation and physical properties of the carbon nanomaterials are provided in Table 3.1.

Table 3.1 : Purity, diameter, and length of various type of CNTs, CNFs, CB used in this study.

Nanomaterials	Abbreviation	Purity (%)	Diameter (nm)	Length (µm)	Source	Grade
Carbon nanotubes	CNTSA	95	6–9	5	Sigma-Aldrich	Research grade
	CNTCT	95	5–15	10–50	Cheap Tube	Industrial grade
	CNTNI	99	<20	–	NanoIntegris	Industrial grade
	CNTNC	90	<9	1	Nanocyl	Industrial grade
Carbon nanofibers	CNF	96	190–590	–	Nanografi	Industrial grade
Carbon black	CB	95	148	-	Nanograf	Industrial grade

Based on the provided data, CNTs generally have higher aspect ratios (length-to-diameter ratios) compared to CNF. The CNTs from Sigma-Aldrich (CNTSA) have a diameter range of 6-9 nm and a length of 5 µm, yielding an aspect ratio of approximately 556-833. The CNTCT from Cheap Tube, with a diameter range of 5-15 nm and a length of 10-50 µm, has an aspect ratio ranging from 667 to 10,000. CNTNI from NanoIntegris , with a diameter of < 20 nm and unspecified length, likely has an even higher aspect ratio, as nanotubes typically have lengths far exceeding their diameters. CNTNC from Nanocyl, with a diameter of < 9 nm and a length of 1 µm, has an estimated aspect ratio of about 111, which is still quite high. On the other hand, CNFs from Nanografi, with a diameter range of 190-590 nm and unspecified length, have a significantly lower aspect ratio due to the much larger diameter in comparison to the typical lengths of CNTs. The order of aspect ratios, from highest to lowest, is as follows: CNTNI (NanoIntegris), CNTCT (Cheap Tube), CNTSA (Sigma-Aldrich), CNTNC (Nanocyl), and CNF (Nanografi).

To avoid confusion while reading, the abbreviation *CNTs* is used interchangeably to refer to carbon nanotubes in general, without specifying a particular type or commercial source.

3.3 Ink Compositions and Properties

As discussed at the end of section 2.2, formulating carbon-based inks for printing applications requires selecting solvents and surfactants to optimize dispersion stability, surface tension, and printability. CNCs were chosen for their exceptional ability to disperse and stabilize CNTs and other carbon nanomaterials in aqueous solutions, owing to their high surface charge and covalent bonding potential. TX-100 acts as a critical surfactant, reducing surface tension, improving ink wettability, and enhancing dispersion stability. The solvent ratio, particularly the water/IPA mixture, plays a key role in tuning ink properties. For instance, a 70/30 water-to-IPA ratio effectively lowers surface tension and mitigates defects such as the coffee-ring effect, ensuring better uniformity [154–156]. Additionally, varying the concentration of carbon nanomaterials impacts rheology and printing performance. By systematically evaluating these factors, the formulation process ensures a refined balance between dispersion stability, surface tension, and printability, producing inks suited for precise, high-quality printing applications.

3.3.1 Direct coating: Developing CNTSA-based inks and their characterization

This section details the formulation and application of CNTSA/CNC inks for direct coating method, aiming to develop sensors with varying CNTSA/CNC compositions. By systematically adjusting the CNTSA-to-CNC ratio, this study examines how ink composition influences the electromechanical properties of the sensors, as shown in Table 3.2. The preparation process involves optimizing ink dispersion, ensuring uniform coating, and evaluating the stability of the printed layers. The coated sensors undergo electromechanical testing to assess conductivity, strain sensitivity, and overall performance. These findings provide insight into the role of CNTSA/CNC content in sensor functionality, aiding the development of tunable, high-performance sensing materials.

Table 3.2 : Formulation details of CNTSA/CNC inks used for the direct coating method.

Ink code	Total weight percentage (wt.%) of CNTSA and CNC	CNTSA/CNC weight ratio (wt.%:wt.%)	Water/IPA ratio	Purpose of study
CNTSA/CNC_0.0:4.0	4.0	0.0:4.0	100/0	Preparing sensors with various CNTSA/CNC content and studying their influence on electromechanical properties.
CNTSA/CNC_0.1:0.1	0.2	0.1:0.1	100/0	
CNTSA/CNC_0.5:0.5	1.0	0.5:0.5	100/0	
CNTSA/CNC_0.8:0.4	1.2	0.8:0.4	100/0	
CNTSA/CNC_0.8:0.8	1.6	0.8:0.8	100/0	
CNTSA/CNC_0.8:4.0	4.8	0.8:4.0	100/0	

3.3.2 Screen printing: Developing carbon-based inks and their characterization

As highlighted in the previous chapter, surface tension and rheological behavior are critical factors affecting the printability and quality of aqueous-based inks. If an ink's surface tension exceeds the substrate's surface energy, it can lead to poor wettability and reduced printing resolution [154,266]. Interactions between surfactants, binders, and solvents significantly influence ink dispersion and print performance.

To address these challenges, ink development focused on three key aspects:

- Assessing how total ink concentration impacts printability and quality,
- examining the combined influence of TX-100, CNC, and IPA on the dispersion, wettability, and printability of CB- and CNF-based inks,

- and evaluating the specific role of TX-100 in the printability of hybrid inks.

As detailed in Table 3.3, the ink formulation was optimized to achieve these objectives by adjusting total content and tailoring the solvent-to-surfactant ratio to minimize surface tension mismatches with the substrate. Seven carbon-based inks were prepared for printability testing and sensor fabrication, including CNTSA, CNTNC, CNF, CB, CB/CNTSA-6, CNTNC-6, and CB/CNF-6.

Table 3.3 : Composition details of carbon-based inks used for the screen printing method.

	Carbon nanomaterials			Surfactant		Solvent mixture	
Ink code	**CB (wt.%)**	**CNT (wt.%)**	**CNF (wt.%)**	**CNC (wt.%)**	**TX-100 (wt.%)**	**Water/IPA ratio**	**Purpose of study**
CNTSA	-	0.0	-	6.0	-	100/0	Assessing the effect of total ink concentration on printability and quality in an aqueous medium
	-	0.5	-	0.5	-	100/0	
	-	3.0	-	3.0	-	100/0	
	-	6.0	-	6.0	-	100/0	
	-	8.0	-	8.0	-	100/0	
CNTCT	-	4.0	-	4.0	-	100/0	Assessing the effect of total ink concentration and industrial carbon types on the printability in aqueous and water/IPA mediums.
	-	4.0	-	4.0	-	70/30	
	-	6.0	-	6.0	-	100/0	
	-	6.0	-	6.0	-	70/30	
CNTNI	-	6.0	-	6.0	-	70/30	
	-	8.0	-	4.0	-	70/30	
CNTNC	-	2.0	-	2.0	-	70/30	
	-	4.0	-	2.0	-	70/30	
	-	6.0	-	2.0	-	70/30	
CNF	-	-	3.0	0.0	3.0	100/0	Studying the combined influence of TX-100, CNC, and IPA on the dispersion wettability and printability of CB and CNF-based inks.
	-	-	3.0	0.0	6.0	100/0	
	-	-	2.0	2.0	0.0	70/30	
	-	-	4.0	4.0	0.0	70/30	
CB	3.0	-	-	0.0	3.0	70/30	
	3.0	-	-	0.0	3.0	100/0	
	6.0	-	-	0.0	6.0	70/30	
	6.0	-	-	0.0	6.0	100/0	
	9.0	-	-	0.0	9.0	70/30	
	9.0	-	-	0.0	9.0	100/0	
	4.0	-	-	4.0	0.0	100/0	
	4.0	-	-	4.0	0.0	70/30	
	4.0	-	-	4.0	2.0	70/30	
	4.0	-	-	4.0	4.0	70/30	
	4.0	-	-	4.0	6.0	70/30	
	10.0	-	-	4.0	6.0	70/30	
CB/CNTSA-0	4.0	2.0	-	4.0	0.0	70/30	Evaluating the impact of TX-100 on the printability of hybrid inks.
CB/CNTSA-3	4.0	2.0	-	4.0	3.0	70/30	
CB/CNTSA-6	4.0	2.0	-	4.0	6.0	70/30	
CB/CNTSA-9	4.0	2.0	-	4.0	9.0	70/30	
CB/CNTNC-6	4.0	2.0	0.0	4.0	6.0	70/30	
CB/CNF-0	4.0	0.0	2.0	4.0	0.0	70/30	
CB/CNF-3	4.0	2.0	-	4.0	3.0	70/30	
CB/CNF-6	4.0	2.0	-	4.0	6.0	70/30	
CB/CNF-9	4.0	2.0	-	4.0	9.0	70/30	

3.3.3 Spray printing: Developing carbon-based inks and their characterization

In this section, the preparation and evaluation of various carbon-based inks designed for spray printing applications are detailed. The main goal was to develop ink formulations that maintain stable dispersions and sprayable for consistent and reproducible spray deposition. Achieving high-quality spray coatings requires careful adjustment of the ratios between carbon nanomaterials, surfactants, and solvents. By optimizing the solvent-surfactant balance and adjusting the overall ink concentration, it is possible to enhance ink wettability, achieve better substrate coverage, and minimize defects commonly associated with spray printing, such as spillover and non-uniform coating.

The preparation of carbon-based inks follows a systematic approach to ensure homogeneous dispersion, stability, and optimized rheological properties. Industrial-friendly materials such as CNTNC and CB were selected for a spray printing method suitable for large-scale applications. CNF was not considered due to the mediocre performance of its CNF sensor prepared using screen printing method. The compositions of the prepared inks are summarized in Table 3.4, where different formulations of CNTNC-based, CB-based, and CB/CNTNC hybrid inks are listed along with their respective component ratios. Here, the printability and operational limits of carbon-based inks in spray printing applications were examined. The study evaluates ink formulation, viscosity, and printing uniformity.

Table 3.4 : Composition details of carbon-based inks used for spray printing.

Ink code	**Carbon nanomaterials**		**Surfactant**		**Solvent mixture**	**Purpose of study**
	CB (wt.%)	**CNT- (wt.%)**	**CNC (wt.%)**	**TX-100 (wt.%)**	**Water/IPA ratio**	
CNTNC_sprayed	0.0	0.0	0.0	0.0	70/30	Investigating the printability and operational limits of CNT-based inks in spray printing applications.
	0.0	0.25	0.25	0.25	70/30	
	0.0	0.5	0.5	0.5	70/30	
	0.0	0.75	0.75	0.75	70/30	
	0.0	1.0	1.0	1.0	70/30	
	0.0	1.25	1.25	1.25	70/30	
CB_ sprayed	5.0	0.0	2.0	3.0	70/30	Assessing the printability of CB and CB/CNTNC-based inks.
	5.0	0.0	2.0	3.0	90/10	
	5.0	0.0	2.0	3.0	50/50	
	10.0	0.0	6.0	4.0	80/20	
CB/CNTNC_sprayed	1.0	0.5	1.0	1.5	70/30	

3.4 Stability of Carbon Nanostructures in Various Solvent Medium

Understanding the dispersion mechanisms of carbon nanostructures, primarily CNTs, is essential for selecting a suitable medium for the developed novel inks. When considered for industrial applications, such inks need to be stable for long duration of shelf lives hence, the stability check for various times is essential to understand for scale-up studies as well. In here, IPA, ethanol, acetone, and distilled water (DI-water) were selected as potential solvents due to their affordability. CNTs sourced from Nanocyl (referred to as CNTNC) and Sigma-Aldrich (referred to as CNTSA) were dispersed at a weight ratio of 0.5% in the selected solvents. The dispersions were kept on the shelf for four weeks, after which their stability was evaluated.

Results showed that both IPA and ethanol enabled stable CNT dispersions, with CNTNC and CNTSA exhibiting dispersed characteristics and no visible phase separation, as shown in Figure 3.1. In contrast, dispersions in DI-water displayed poor quality, with significant phase separation. Although acetone provided reasonable dispersion for CNTSA, it failed to disperse CNTNC effectively and, more critically, is known to degrade the epoxy matrix of composite coupons. Therefore, acetone was eliminated as a solvent option.

Despite ethanol's good dispersion capability, it was also excluded due to its higher volatility compared to IPA, which can lead to faster evaporation rates during the ink formulation and printing process, potentially affecting ink stability and uniformity. Consequently, IPA was selected as the most suitable dispersion medium. DI-water was deemed the least favorable, as CNTs could not be adequately dispersed in it.

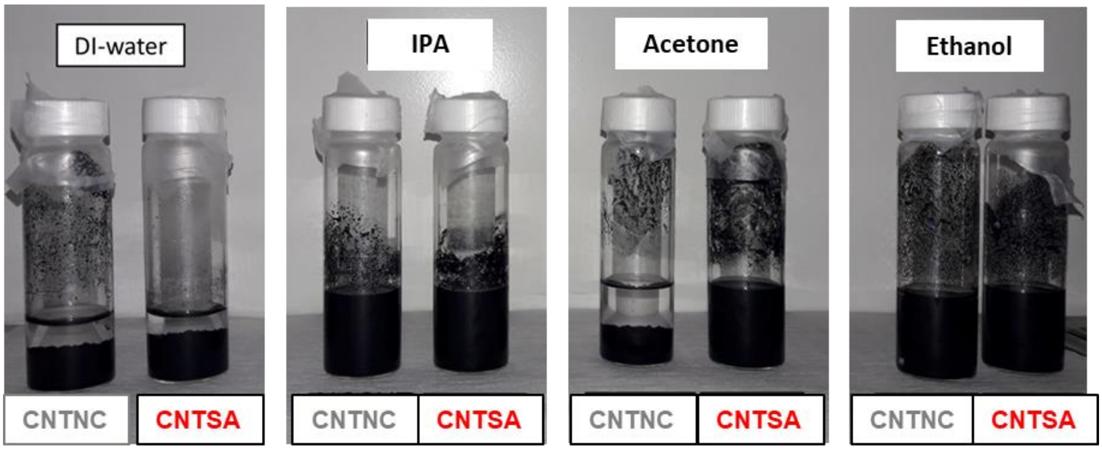

Figure 3.1 : After four weeks, carbon nanotubes' stability in water with and without surfactants.

Microscopic images of the as-prepared inks were analyzed to investigate the dispersibility of carbon nanostructures, both with and without surfactants, in an aqueous medium. Figure 3.2 shows that both CNC and TX-100 surfactants improved the dispersibility of the carbon nanostructures. The effectiveness of the surfactants varied depending on the type of carbon nanostructure. TX-100 was slightly more effective in dispersing CBs compared to CNC. Overall, TX-100 was the most efficient in separating the carbon nanostructures, while CNTNC proved the most difficult to disperse effectively.

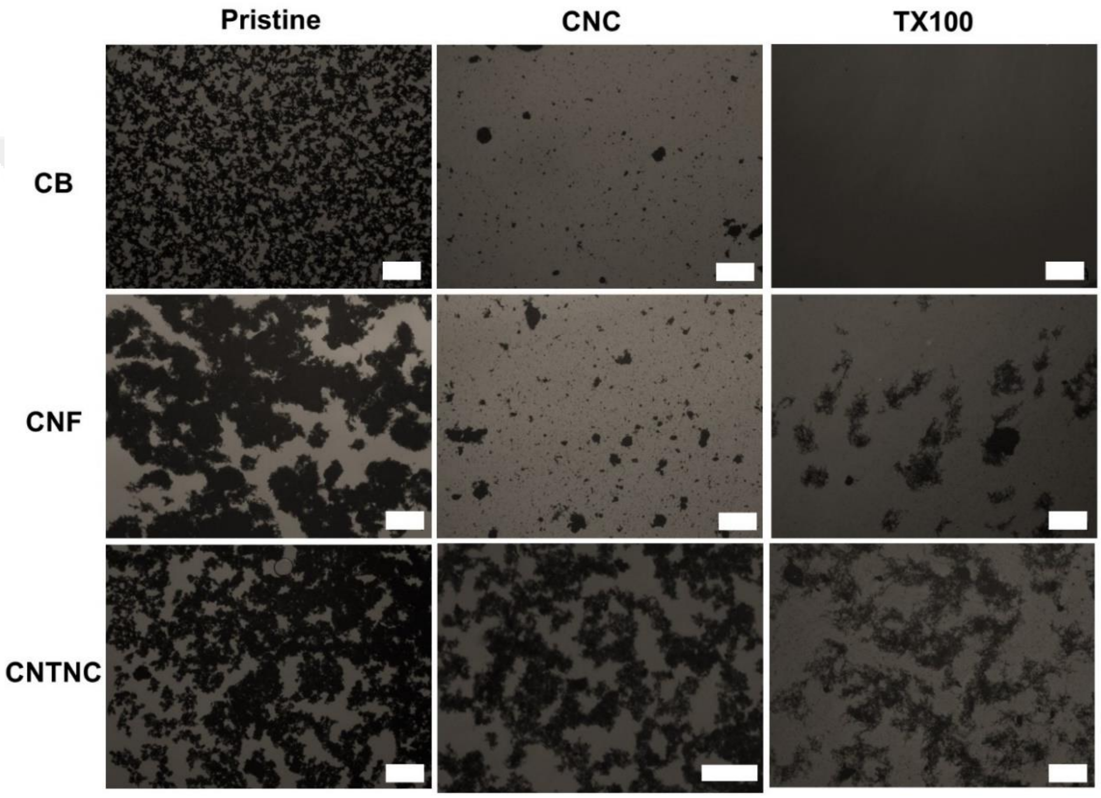

Figure 3.2 : Matrix of microscopic images of carbon nanostructures with and without surfactants (scale bar: 500 μm). Columns, from left to right, correspond to: pristine (without surfactant), CNC addition, and TX-100 addition. Rows, from top to bottom, correspond to: CB (first row), CNF (second row), and CNTNC (third row).

3.5 Rheological Analysis

The rheology of ink is governed by viscosity, shear-thinning and thixotropic behaviors, complex modulus, and cohesiveness. Rheological properties were investigated using a rheometer (Discovery Hybrid Rheometer 2, TA Instruments) equipped with parallel plates, as demonstrated in Figure 3.3. First, 0.5 ml of the tested ink was mounted on the stationary plate, and a 1 mm gap between the fixed and rotary plates was set. The shear viscosity was measured using a steady-state flow sweep test with shear rates ranging from 0.1 to 1000 s^{-1}. Before testing, a pre-shear rate of 0.1 s^{-1} was applied for 30 seconds [267], followed by a rest period of 120 seconds.

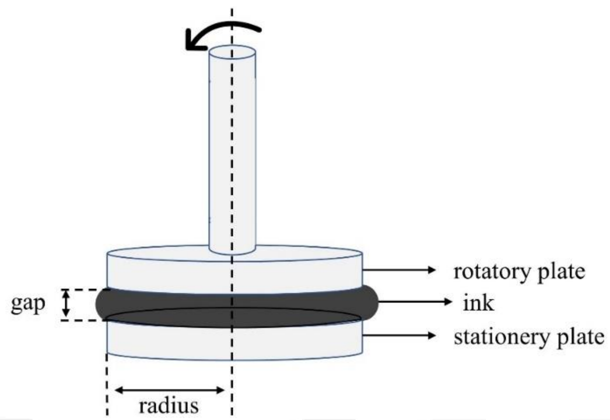

Figure 3.3 : Schematic of the parallel plate rheometer used for measuring the rheological properties of the inks.

The viscoelastic properties of the inks were investigated under oscillatory stresses between 0.1 and 1000 Pa at a frequency of 1 Hz. Initially, a pre-shear rate of 0.1 s^{-1} was applied for 30 seconds, and then the test was conducted by applying a sinusoidal stress (σ) using.

$$\sigma = \sigma_0 \sin(\omega t) \quad (3.1)$$

where σ_0, ω and t are stress amplitude, angular frequency, and time, respectively [268]. The shear strain (γ) subsequently can be measured using.

$$\gamma = \gamma_0 \sin(\omega t + \delta) \quad (3.2)$$

where γ_0 and δ are maximum strain and phase shift, respectively [268]. The ratio of the applied stress to strain equals the complex modulus (G^*):

$$G^* = \sigma/\gamma \quad (3.3)$$

The complex modulus can also be expressed as in.

$$G^* = G' + i \cdot G'' \quad (3.4)$$

where G' and G'' are the storage and loss moduli, respectively.

The screen-printing process was simulated in time-dependent steady-state mode [268] and consisted of three stages. Stage I mimics the resting period of the ink droplet, during which the droplet is subjected to a small shear rate of 0.1 s^{-1} for 120 seconds. In Stage II, the movement of the force applied to the ink droplet is simulated by applying a shear rate of 100 s^{-1} for 60 seconds. Stage III simulates the recovery period after the ink has been deposited on the substrate surface, where a small shear rate of 0.1 s^{-1} was applied for 120 seconds. The test was repeated five times, and the average of at least three measurements for viscosity and recovery rates was reported.

Similarly, the simulation of the screen-printing process during time-dependent oscillatory mode under three different stages was also carried out, as previously reported [267]. In Stages, I and III, a stress of 1 Pa was enough to simulate resting and recovery after printing. During Stage II, a stress of 1000 Pa was applied. These stress values were obtained after conducting the oscillatory test described earlier.

A strain sweep test was also conducted to determine the linear viscoelastic region. Next, a frequency sweep test in the 0.1 to 628 rad/sec range was performed to measure the complex viscosity. All tests were carried out at room temperature.

3.6 GFRPs Fabrication and Their Characteristics

In this section, the preparation and characterization of GFRP composites were described, which serve as the substrate for subsequent ink deposition and testing.

The weight ratio of resin/hardener is 100:25. Plain woven E-Glass fabric (200 g/m^2 areal density) was purchased from Hexcel (USA). All materials were used as received without further purification.

Five bidirectional glass fiber plies were used to fabricate all the composites in this study. The GFRP laminates were prepared using vacuum infusion. 4:1 weight ratio of resin to hardener was thoroughly mixed and degassed for ten minutes before infusing into the vacuum bag. All the GFRP composites were cured at room temperature for 24 hours. Before subsequent use, the as-prepared GFRP composites were cut into 25×250 mm^2 as coupons matching the size recommendation in ASTM D3039 standard.

A tensile test was conducted on neat GFRPs using a Universal Testing Machine (UTM) (AGS-X, Shimadzu) equipped with a 50 kN load cell, following the ASTM D3039 standard. Briefly, a fabricated coupon (25 × 250 mm^2) was mounted between the grips (without using tabs) at a distance of 150 mm, with the crosshead speed set to 2 mm/min. Figure 3.4a shows tensile stress-strain curves for GFRPs, and Figure 3.4b shows the digital image of coupons after testing. The linearity of the stress-strain curves dropped after approximately 0.75% strain, indicating the initiation of damage.

The ultimate tensile strength (UTS) and elastic modulus of the GFRPs were found to be 315 ± 30 MPa and 2.0 ± 0.2 GPa, respectively.

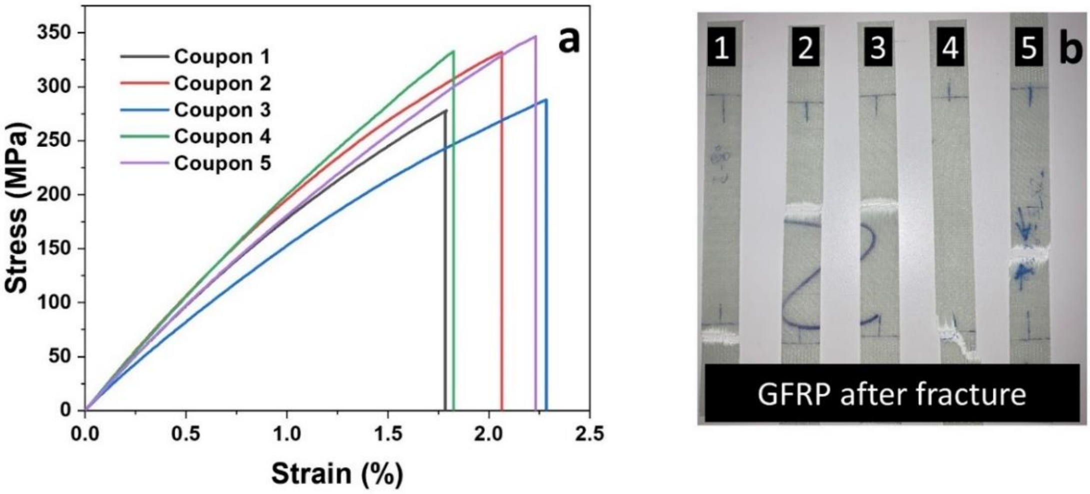

Figure 3.4 : a) Stress-strain graph of five GFRP coupons using ASTM D3039 standard and b) digital image of the five coupons after failure.

Table 3.5 summarizes physical and mechanical properties of the fabricated GFRPs. The calculated glass fiber volume fraction of five batches was 42.5 ± 1.5%, while the calculated void content (air bubbles) of three batches was 2.4 ± 1.1%. These results indicate the consistent physical properties of the GFRPs.

Table 3.5 : Physical and mechanical properties of GFRPs.

Glass fiber volume fraction (%)	Void content (%)	Ultimate Tensile Strength (MPa)	Elastic modulus (GPa)
42.5 ± 1.5	2.4 ± 1.1	315 ± 30	2.0 ± 0.2

The specific surface energy of the GFRP substrate can reach values as high as 37 mN/m [161]. Wenzel et al. suggest that the physical condition of a rough surface increases the actual surface area within a measured unit compared to a smooth surface [269]. This increase in the surface area enhances the intensity of surface energy, which proportionally alters the solid's wetting behavior while not affecting the specific surface energy values. This relationship aligns with fundamental principles of wetting action.

Therefore, the surface was sanded using sanding paper to minimize significant surface features and further increase the surface area, facilitating improved wettability and promoting better ink adhesion during the screen and spray printing processes.

3.7 Design and Description of Sensor Patterns

The existing literature lacks in-depth research on the influence of geometric patterns on piezoresistive response. Hence, four distinct geometric patterns were designed using a CAD program, as detailed in Table 3.6. These patterns were tailored with attention given to their individual shape and total length. To enable comparative analysis between the patterns, the sensing width of each pattern was standardized to 0.75 mm. Additionally, for consistency, the inner circles in the o-line and omnidirectional designs remained constant with a radius of 3 mm. Each pattern was designed to ensure it possesses a unique electrically conductive path, represented by the sensor's total length, and distinctive physical geometry. The total electrically conductive paths and other geometric properties are outlined in Table 3.6.

Table 3.6 : Geometric properties of the sensors.

Geometry	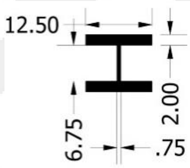 Line	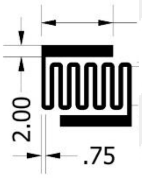 Grid	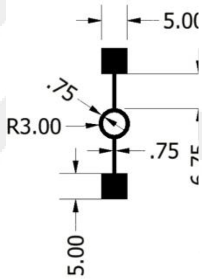 O-line	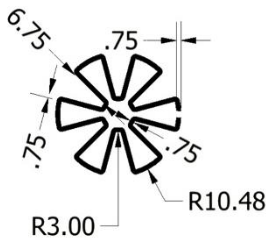 Omnidirectional
Sensor length (mm)	~7	~84	~23	~120
Printed Coverage Area (mm^2)	~5.1	~106.3	~10.1	~297.6
Number of legs	1	11	2	12

According to the ASTM D3039 standard, the total length of a strain sensor should be long enough to encompass the length of the repeating unit [69]. Therefore, a sensing length of 6.75 mm was sufficient to cover the repeating unit of the composites, maximizing sensitivity and being compact enough to fit onto GFRP coupons cut according to ASTM D3039 dimensions. Additionally, to maintain symmetry in the grid sensor’s electrode area design, the number of sensing legs needed to be odd; therefore, an 11-leg was chosen. Similarly, to ensure symmetry in the design of the omnidirectional pattern for the potential of multi-directional sensing, the maximum number of legs that fit on the GFRP coupon is 12.

3.8 Integration of Strain Sensor onto GFRPs

Various printing methods will be employed to achieve proper integration of carbon nanomaterials with GFRPs and to maintain flexibility in the sensors' performance by controlling their geometrical dimensions.

3.8.1 Direct coating application method

This method is simple and efficient. After depositing the ink onto the surface of the GFRP, a roller is used to uniformly spread and coat the surface through a striking motion. The sample is then dried at 40 °C for 10 minutes. Silver paste is applied to attach copper pieces, enabling electrical connection with the source meter. Figure 3.5 provides a summary of the ink processing and printing steps.

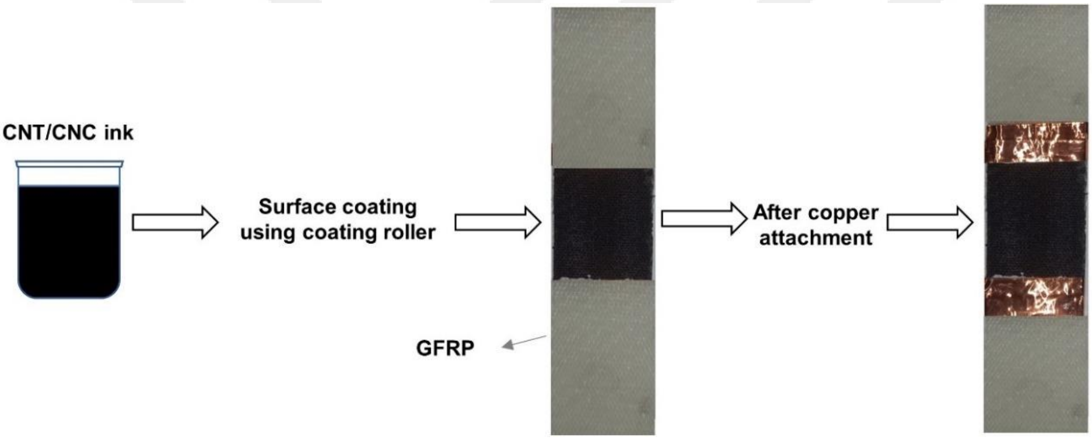

Figure 3.5 : Overview of the roller coating method for applying the final ink formulation onto GFRPs, followed by drying and electrode attachment using silver paste for electrical connections.

3.8.2 Screen printing method

Screen printing is an ancient technique that originated in China nearly 1000 years ago [287]. It is widely used for printing on various substrates, ranging from textiles to circuit boards. In this method, the desired pattern, such as the sensor's geometry, is transferred onto a substrate through a mesh stencil, allowing ink to pass through open areas while blocking it elsewhere, ensuring a precise and consistent print. The mesh, typically made from synthetic fibers like polyester, is stretched over a rigid frame. This study used Mesh T120, supplied by Sefar (Switzerland). A squeegee is then used to force ink across the mesh, allowing it to pass through the open pores and imprint the pattern onto the substrate beneath. Figure 3.6 summarizes the method.

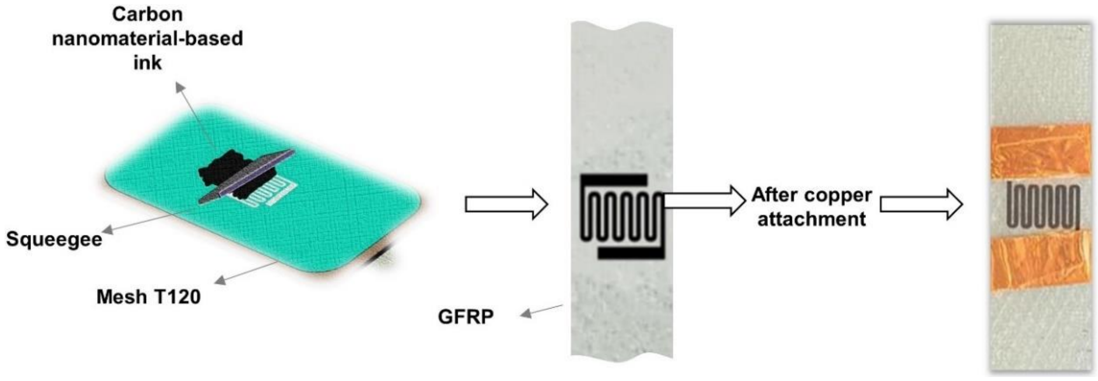

Figure 3.6 : Schematic representation of the screen printing process, showing ink transfer through a mesh stencil with a squeegee to form sensor patterns on GFRPs.

3.8.3 Spray printing method

Spray printing is a versatile method for depositing thin films and uniform coatings onto substrates, making it particularly attractive for the aerospace industry due to its scalability and ability to conform to complex geometries. To enable spray printing, a custom spray printing setup was developed using a commercial airbrush, as shown in Figure 3.7. Uniform film deposition was achieved by adjusting parameters such as air pressure, nozzle-to-substrate distance, spray duration, and ink viscosity.

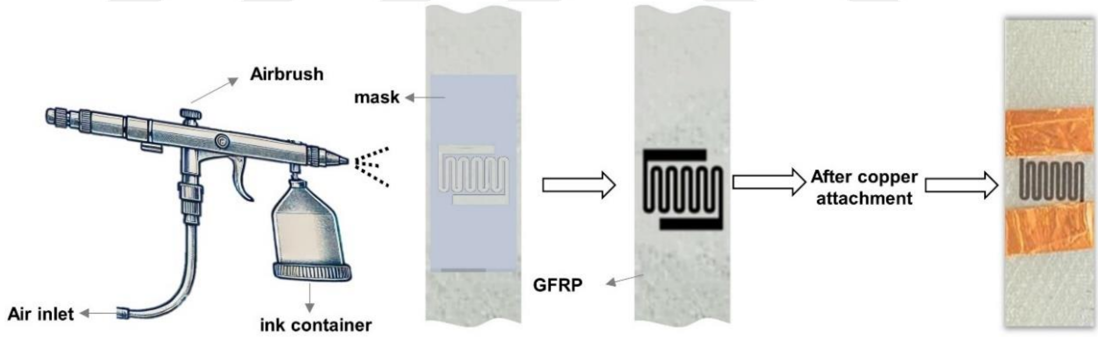

Figure 3.7 : Schematic representation of the spray printing process, showing ink transfer through a mask to form sensor patterns on GFRPs.

3.9 Printing Quality and Morphological Characterization

The quality of the printed patterns was analyzed visually using a microscope to evaluate overall print uniformity and feature clarity. Additionally, the line width of the printed sensors was measured using ImageJ software, with at least 10 measurements taken to calculate the average.

The morphology of the printed sensors was characterized using scanning electron microscopy (SEM) (FEI-Qanta FEG250, USA). Additionally, selected sensors printed on GFRP substrates were cut using a sharp tool, and their cross-sections were imaged with SEM to measure the sensor thickness.

3.10 Electrical and Electromechanical Testing and Setup

3.10.1 Electrical measurements

After successfully printing the carbon-based sensors, connecting them to electrical cables to interface with the source meter is essential. Copper foils (0.1 mm thickness) were attached to the designated electrode areas using silver paint. To ensure proper curing of the silver paint, the host coupons were placed in a furnace at 40°C for 16 hours.

Electrical resistance was measured in DC mode using a Keithley 2400 with a two-probe configuration. The sampling frequency for electrical resistance was 1 Hz. The test lasted 300 seconds, during which electrical stability was assessed.

3.10.2 Electromechanical performance in tensile and cyclic tests

Some of the developed strain sensors required a stabilization period while under a voltage difference. Therefore, for the sake of consistency, after the voltage difference was applied and before mechanical testing, all strain sensors were allowed to be under constant voltage for a brief time (50 seconds) to reach stabilization. The electrical resistance sampling frequency was 1 Hz.

The piezoresistive behavior of the printed sensors was studied by conducting electromechanical tests. The electromechanical setup, shown in Figure 3.8, consists of a UTM (AGS-X, Shimadzu, 50 kN load cell), extensometer (Epsilon, Model 3542, 50 mm gauge length), and Keithley (2400 series) [270]. The resistance change during the tests was calculated using.

$$\frac{\Delta R}{R_0}\% = \frac{R_i - R_0}{R_0} * 100 \tag{3.5}$$

where R_i and R_0 are instantaneous and initial resistances, respectively [270].

The influence of the applied strain rate was investigated by conducting six single-cycle tests between 2 and 12 mm/min with 2 mm/min increments in each cycle with an elongation of 0.15 mm, corresponding to 0.3% strain.

The reliability of the sensors was evaluated during tensile cyclic tests, conducted in two phases: the first 50 cycles within the elastic region and the subsequent 50 cycles within the plastic region, at a strain rate of 6 mm/min [270]. Using the same samples for both phases allowed a direct comparison of sensor behavior under different strain conditions. Based on the reproducible results, the 50-cycle test was found to be sufficiently long to capture changes between various patterns, as supported by Arana et al. [27]. Each test was repeated five times to ensure a reliable dataset, and the average was calculated.

Residual resistance after the first cycle was calculated and identified as the damage following the initial loading [271]. This parameter was used to differentiate between various carbon nanofillers and sensor types.

Sensitivity or gauge factor, was determined by calculating the slope of the resistance change to strain as follows:

$$GF = \frac{\Delta R}{\varepsilon R_0} \tag{3.6}$$

where ε is the strain. Linearity is assessed through a linear fit's coefficient of determination (R^2), which quantifies the relationship between the electrical signal and the applied load [90,170]. Moreover, during monotonic tensile tests, the strain rate was selected as 2 mm/min, consistent with ASTM D3039.

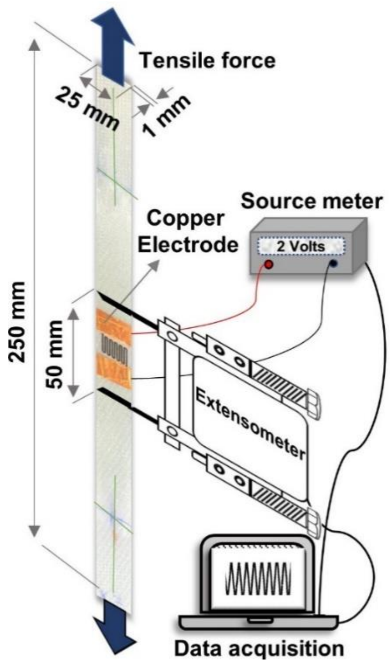

Figure 3.8 : Testing setup for electromechanical performance under tensile and cyclic loading.

3.10.3 Electromechanical performance in four-pint bending test

To evaluate the performance of the screen-printed sensors under tension and compression forces, separate 4-point bending tests were conducted on GFRP coupons with sensors printed directly on their surfaces. The tests were performed using the same UTM machine equipped with a 50 kN load cell, while resistance changes were measured using a Keithley 2400.

Figure 3.9 illustrates the testing procedure in four-point bending following ASTM D7264 standard. The bending setup included outer supports spaced 150 mm apart, and inner loading points spaced 50 mm apart. Maximum strain was calculated using the following equation according to ASTM D7264 standard

$$\varepsilon = \frac{4.36\delta h}{L^2} \tag{3.7}$$

where δ, h, and L are mid-span deflection, thickness of the GFRP, and support span.

With a thickness of approximately 1 mm, a support span of 150 mm, and a displacement of 11 mm, the resulting strain is approximately 0.2%. At this strain, ten consecutive cycles were repeated at a strain rate of 12 mm/min. In the compression test, the sensor was placed on the compressive side, while in the tension test, the sensor was positioned on the tensile side of the GFRP coupon, as illustrated in Figure 3.9b-c.

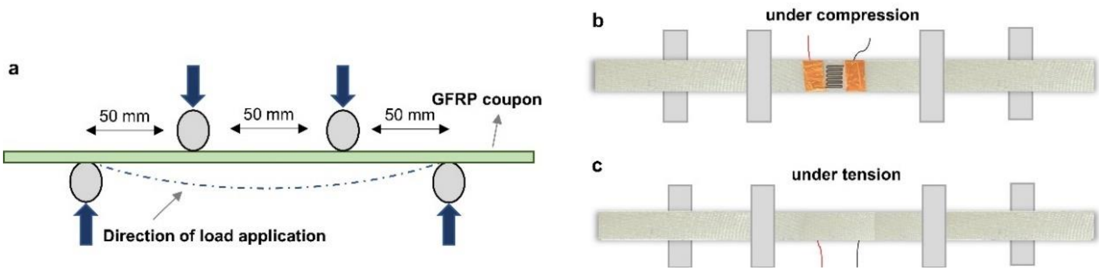

Figure 3.9 : a) Four-point bending test setup. b) Position of the coupon when the sensor experiences compression and c) position when it experiences tension forces.

3.10.4 Multifunctional and thermal exposure testing approach

The temperature sensing performance of the sensors was measured inside a custom-designed setup consisting of a Four Point Probe Model FPP 470 heating bed, thermal camera Optris PI 400i, and Keithley 2400 (applied voltage was 2.1 V). The temperature coefficient of resistance (TCR) was calculated using equation 3.8, and the average of at least three samples was reported.

$$TCR = \frac{\Delta R}{R_0 T} \tag{3.8}$$

Impact testing was conducted by dropping a stainless-steel ball (covered with an insulator layer) with a specific weight and diameter from inside a tube of a particular height and appropriate diameter. The voltage was supplied using Keithley 2400 in bias mode at a frequency of 50 (or every 20 ms). A similar test approach has been reported in the literature [272–274].

3.11 Antenna Performance: Simulation, Setup, and Testing

Electromagnetic simulations were carried out using CST Microwave Studio. The dielectric properties of the GFRP substrate were defined with a relative permittivity (ε) of 5 and a dielectric loss tangent of 0.04. The dielectric thickness, corresponding to the GFRP laminate, was set to approximately 1 mm. Since the electrical conductivity of dielectric materials like GFRP is frequency-dependent and part of the complex permittivity, it was not assigned as a fixed value but rather implicitly represented through the specified permittivity and loss tangent values.

The antenna sensor testing setup consists of a UTM, an extensometer, and a Vector Network Analyzer (VNA) (N5230A PNA series, 10 MHz- 40GHz), as demonstrated in Figure 3.10. To accommodate the time required for the VNA to complete its scan, the strain was applied incrementally in 0.2% steps to the antenna sensor. Each increment was held for 70 seconds to allow for thorough VNA scanning. This procedure was repeated six steps, up to a maximum strain of 1.2%.

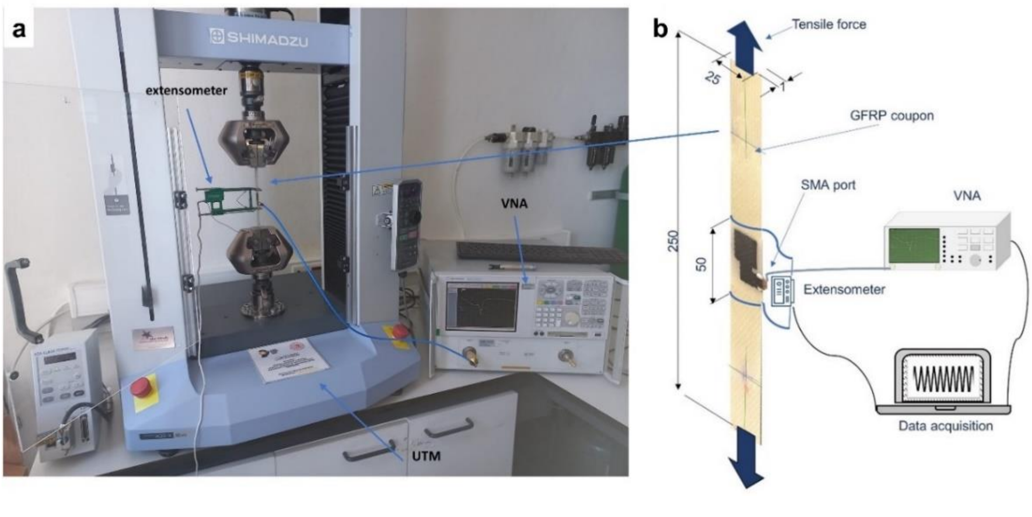

Figure 3.10 : a) Digital image and b) schematic of the testing setup for an antenna sensor.

The sensitivity of the sensor was evaluated using equation 3.9

$$\text{Sensitivity} = \frac{\Delta S_{11}}{S_{11,0}\,\varepsilon} \tag{3.9}$$

where S_{11} is reflection coefficient. $S_{11,0}$ equals the value of the S_{11} parameter at a specific frequency at 0% strain, and ε is strain.

Another bending test was carried out as illustrated in Figure 3.11a. with the corresponding digital image of the bent GFRP coupon shown in Figure 3.11b. A preliminary study revealed that when the antenna and its host composite were bent over a radius smaller than 7 mm, delamination occurred at the SMA connector interface. This resulted in signal loss and unreliable measurements. Therefore, in this work, three measurements were conducted using radii of 7 mm, 8 mm, and ∞ (flat/unbent condition).

The induced surface strain due to bending can be calculated using the following equation:

$$\varepsilon = \frac{y}{R} \tag{3.10}$$

where y is the distance from the neutral axis to the outer surface, and for a symmetrical cross-section, y = t/2 y, with t being the thickness of the coupon. R is the radius of curvature. As shown in Equation 3.10, decreasing the radius of curvature leads to increased surface strain.

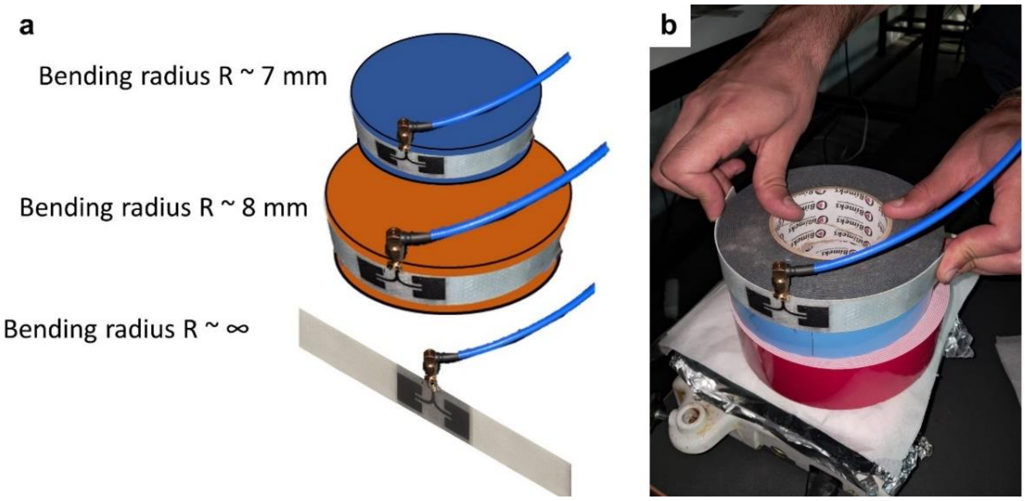

Figure 3.11 : a) Schematic illustration of patch antennas printed onto GFRP coupons placed on circular objects with radii of 7 mm, 8 mm, and ∞ (flat/unbent condition). b) Digital image showing the patch antenna printed on a GFRP coupon mounted on a circular object with a 7 mm radius.

4. PRINTABILITY OF CARBON-BASED INKS

This section discusses the printing quality of various carbon nanomaterial-based inks applied through coating, screen printing, and spray printing methods. The ink formulations were systematically varied to improve printing quality. Printing quality was evaluated both visually and using a light microscope, focusing on factors such as ink bleeding, resolution, surface coverage, and line width.

4.1 Coating: A Direct Application of CNTSA/CNC-Based Inks onto GFRPs and their Characterization

In this study, various CNTSA/CNC ink formulations were prepared with different CNTSA/CNC content and water/IPA ratios to investigate their influence on the overall ink characteristics and printability. The formulations were designed with varying total weight percentages of CNTSA and CNC, as well as specific CNTSA/CNC weight ratios, detailed in Table 4.1. The primary aim was to study the impact of these variations on the ink's behavior, such as viscosity, dispersion stability, and printability.

Table 4.1 : Composition details of CNTSA/CNC inks ink formulations used for the direct coating method.

Total weight percentage (wt.%) of CNTSA* and CNC	CNT/CNC weight ratio (wt.%:wt.%)	Water/IPA ratio
4.0	0.0:4.0	100/0
0.2	0.1:0.1	100/0
1.0	0.5:0.5	100/0
1.2	0.8:0.4	100/0
1.6	0.8:0.8	100/0
4.8	0.8:4.0	100/0

*CNTSA: The CNTs was purchased from Sigma Aldrich with high quality.

To elucidate rheological interactions between CNTSA and CNC in aqueous inks, it is essential first characterize the behavior of CNC aqueous solutions independently. A 4.0 wt.% CNC solution, corresponding to the highest CNC concentration employed in CNTSA/CNC inks, was tested, with results summarized in Table 4.1. Three distinct rheological regimes were identified. At low shear rates (<1 s^{-1}), viscosity decreased with increasing shear rate, indicating shear-thinning behavior (Figure 4.1a). This was followed by a plateau region at intermediate shear rates, and a second decline in viscosity was observed at higher shear rates. Such rheological behavior is characteristic of liquid crystal solutions [275] and has been reported in CNC aqueous solutions in earlier studies [39–42] .

Upon hybridization with CNTs, a significant increase in viscosity was observed. This increase was attributed to enhanced solid network formation [280]. Furthermore, varying the CNC concentration from 0.4 to 4.0 wt.% at a fixed CNTSA concentration of 0.8 wt.% resulted in a progressive increase in viscosity. This trend is consistent with previous studies [279], where higher CNC concentration promoted more pronounced solid-like behavior due to denser CNC rod interactions.

To further investigate the hybrid nature of CNTSA/CNC inks, shear viscosity measurements were performed at a fixed angular frequency of 0.1 rad/s for three different CNTSA:CNC ratios (0.1:0.1, 0.5:0.5, and 0.8:0.8 wt.%:wt.%). A sharp increase in shear viscosity was observed at the 0.8:0.8 wt.%:wt.% ratio (total solid content of 1.6 wt.%), indicating enhanced network formation, as shown in Figure 4.1b. Experimentally, inks with viscosities lower than that of the 0.5:0.5 wt.%:wt.% formulation were unsuitable for coating or printing processes, likely due to insufficient network formation with low viscosity as a baseline threshold.

The storage (G′) and loss (G″) moduli of CNTSA/CNC inks with weight ratios of 0.5:0.5 and 0.8:0.8 were evaluated across an angular frequency range of 0.1–100 rad/s (Figure 4.1c). Both formulations exhibited similar G′ and G″ trends, reinforcing their solid-like behavior [281]. G′ increased with angular frequency, a characteristic response commonly reported for CNTSA and CNC dispersions [277,278,281–283]. At low frequencies, the solid-like characteristic intensified with increasing concentration with the 0.8:0.8 ink exhibiting a G′ of 44 Pa compared to 20 Pa for the 0.5:0.5 ink. Similar concentration-dependent enhancements have been observed in CNT-based polymeric dispersions [281,282]. Conversely, G″ displayed a different pattern. At low angular frequencies (0–1 rad/s), G″ decreased before increasing beyond 1 rad/s, suggesting a notable increase in elastic behavior at lower frequencies.

Finally, the shear viscosity of CNTSA/CNC ink with only 0.5:0.5 wt.%:wt.% ratio was compared to its complex viscosity. Complex viscosity was determined through an amplitude sweep test followed by a frequency sweep test over 0.1–100 rad/s. As shown in Figure 4.1d, complex viscosity values were higher than shear viscosity, indicating that CNTSA/CNC inks did not conform to the Cox-Merz rule, which typically applies to very low-concentration CNC and CNT-based solutions [277,284].

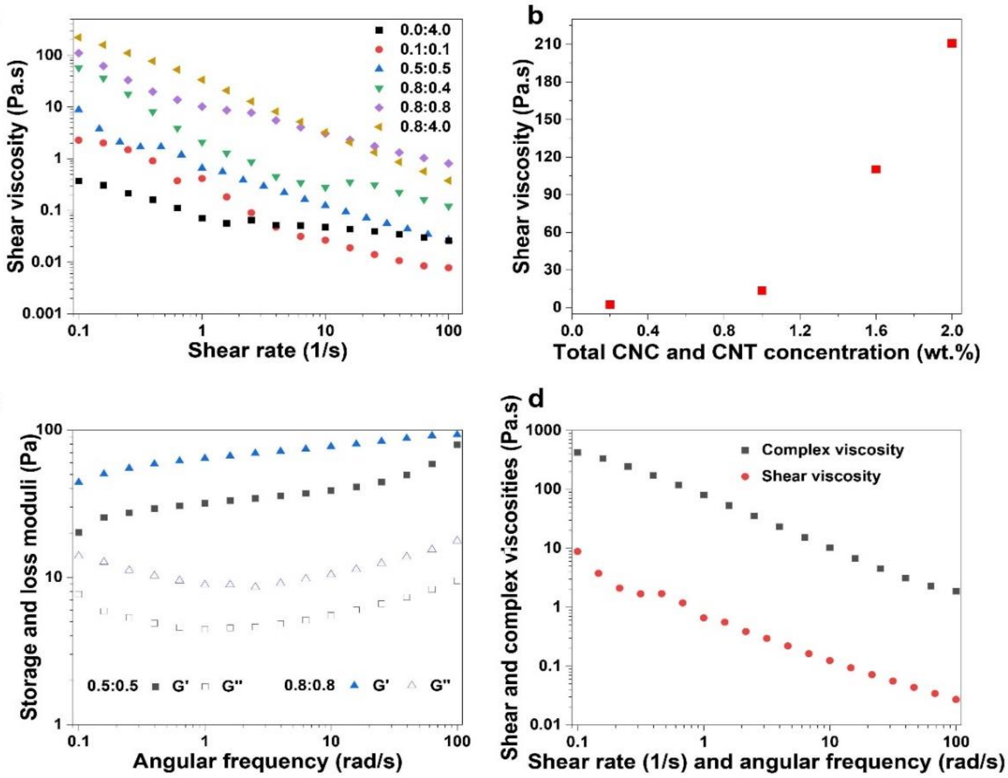

Figure 4.1 : a) Shear viscosity as a function of shear rate for different CNTSA/CNC ink compositions, b) shear viscosity as a function of total CNTSA and CNC concentration by fixing CNTSA-to-CNC ratio at 1:1 (angular frequency of 0.1 rad/s), c) storage (G′) and loss (G′′) moduli as a function of angular frequency for 0.5:0.5 and 0.8:0.8 inks, and d) comparison between shear and complex viscosities for 0.5:0.5 ink.

Figure 4.2 presents micrographs of CNTSA/CNC coating at varying compositions, in which CNTSA and CNC were mixed in different ratios. Bright spots in CNT buckypapers are typically associated with surfactants or foreign particles [285,286]; however, in the present study, these bright spots were attributed to excess CNCs. The CNTSA/CNC_0.5:0.5 composition exhibited the fewest bright spots, suggesting that CNCs were adequately dispersed along individual CNTs (Figure 2a). When the CNTSA content was fixed at 0.8 wt.% and the CNC content increased from 0.4 to 4.0 wt.%, the frequency of bright spots was risen compared to lower CNC compositions.

Additionally, the shape of these bright spots changed with increasing CNC content, as shown in Figure 4.2b. In CNTSA/CNC_0.8:0.4, the spots appeared mostly as isolated bright points. However, as CNC concentration increased, these spots became more elongated and linear, aligning with the curvature of CNTs (Figure 4.2e-d).

Furthermore, the surface morphology of the sensors displayed a porous structure, which varied with CNC composition. As CNC content increased, the frequency and apparent size of pores decreased. Previous studies have reported the porous nature of pure CNT buckypapers [287,288], as similar trends observed in here. Additionally, higher CNC concentrations reduced CNT entanglement and bundling (Figure 4.2b-d), suggesting that CNCs effectively separate CNTs even after coating process and drying from an aqueous medium on composite surfaces.

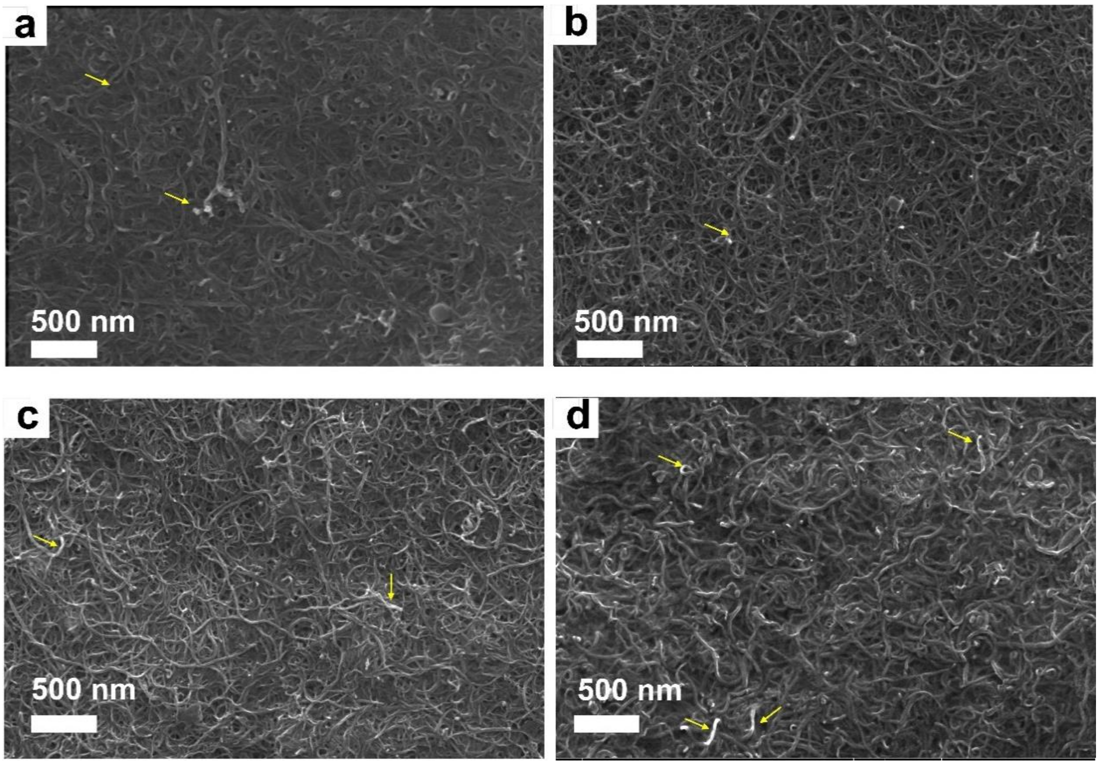

Figure 4.2 : Surface morphology of developed strain sensors at different CNTSA/CNC compositions: a) 0.5:0.5, b) 0.8:0.4, c) 0.8:0.8, and d) 0.8:4.0. (yellow arrows show bright regions which were attributed to CNCs)

In summary, CNTSA/CNC-based inks exhibited shear thinning behavior, and their rheological properties could be tailored by adjusting the total solid content through varying the CNT:CNC ratio. Additionally, upon coating the surfaces of GFRPs with the inks, good adhesion was observed to the surface, paving the way for the application of more precise methods such as screen and spray printing. These methods offer enhanced control over the printed areas, enabling the creating of specific, well-defined patterns directly onto the GFRP surfaces.

4.2 Screen printing: A Facile Method of Applying Carbon-Based Inks onto GFRPs and their Characterizations

In this section, the formulation and characterization of various carbon-based inks intended for screen printing applications are described. The primary objective is to optimize ink formulations to achieve stable dispersions, wettability, and desirable rheological properties, all of which are essential for effective and reproducible printing. The formulation process involves systematically adjusting the ratios of carbon nanomaterials, surfactants, and solvents to achieve optimal printability and uniform deposition on substrates. By tailoring the solvent-to-surfactant ratio and modifying the total ink concentration, it is possible to enhance ink wettability, reduce surface tension mismatches with substrates, and minimize common defects such as the coffee-ring effect.

4.2.1 CNTSA/CNC-based inks

The CNTSA supplied by Sigma-Aldrich (CNT) have a diameter range of 6-9 nm and a length of 5 µm, yielding an aspect ratio of approximately 556-833. The inks were formulated with progressively increasing CNSAT/CNC content, ranging from 0.5 wt.% to 8.0 wt.%. This approach aimed to optimize printing by adjusting the initial loading of components, using only an aqueous medium. The goal was to investigate how higher solid contents influence ink texture, viscosity, and shear-thinning behavior, key factors for ensuring consistent pattern deposition during screen printing. The composition details of the prepared CNTSA/CNC-based inks are provided in Table 4.2.

Table 4.2 : Ink compositions of CNT/CNC ink formulations for screen printing method.

Carbon nanomaterials CNTSA (wt.%)	Surfactant CNC (wt.%)	Solvent mixture Water/IPA ratio
0.0	6.0	100/0
0.5	0.5	100/0
3.0	3.0	100/0
6.0	6.0	100/0
8.0	8.0	100/0

The ink texture of the four CNTSA/CNC inks is shown in Figure 4.3. By increasing the CNTSA/CNC content, the ink texture shifted from liquid-like to paste-like. This shift in texture increased the viscosity of the ink, as illustrated in Figure 4.3a. Under high shear rates, all the inks showed shear thinning properties, an important trait of ink used for the screen printing method, allowing the ink to easily penetrate the mesh and enable effective printing [289]. This behavior was attributed to the alignment of the CNTSA and CNCs and the disruption of entanglement of CNTSA/CNC particles [290]. As depicted in Figure 4.3b, printing these inks on GFRPs using a T120 screen mesh resulted in excessive ink spreading for CNTSA/CNC inks with ratios of 0.5:0.5 and 3.0:3.0. However, paste-like inks with higher content ratio resulted in successful print, although the high viscosity of the 8.0:8.0 ink content led eventually to mesh clogging. Owens et al. also reported printing with paste-like aqueous inks using a direct printing method [197]. Nonetheless, after printing, the printed pattern does not require additional treatment, such as curing at high temperatures, which is typically a necessary step for polymer-based inks [137].

Somalu et al. discussed that ink network strength and adequate viscoelastic properties are essential in defining the printability of an ink [291]. Therefore, oscillatory tests were conducted to evaluate the viscoelastic properties of the inks. The complex modulus, which measures the ink's resistance to deformation, was plotted as a function of the applied stress, as shown in Figure 4.3c. Results showed that the higher the CNTSA/CNC content, the higher the complex modulus becomes. The linear region, where the complex modulus remains unchanged, is referred to as a linear viscoelastic region (LVR) [292]. Ink with a CNTSA/CNC weight ratio of 0.5:0.5 exhibited a linear response within a small stress range, indicating a weak structure. As the CNTSA/CNC content increased, however, the inks exhibited longer linear viscoelastic behavior over a wider stress range. This dependency of viscoelasticity on the initial content of the CNTSA/CNC was attributed to the interaction between CNTSA and CNCs. This interaction could be a combination of high aspect ratio CNT-CNT interactions [197] and repulsion of the highly charged surface of CNC particles [293]. Moreover, within the LVR region, the $\mathrm{G''/G'}$ ratio has been employed as an indicator of the cohesiveness of an ink [294]; the lower the ratio, the higher the cohesive is the ink [295]. As calculated and shown in Figure 4.3, $\mathrm{G''/G'}$ ratios of 6.0:6.0 and 8.0:8.0 CNTSA/CNC inks were higher than that of 3.0:3.0 CNTSA/CNC ink, indicating improved cohesion. This increased cohesion may have suppressed ink bleeding but also led to void formation. The similar values of G''/G' ratios for 6.0:6.0 and 8.0:8.0 CNTSA/CNC inks, as outlined in Table 4.3, imply saturation in viscoelastic properties. On the other hand, CNC suspension (0.0:6.0 CNT/CNC ink) showed weaker network strength compared with 6.0:6.0 CNT/CNC ink, indicating the critical role of CNT particles in increasing viscoelastic properties.

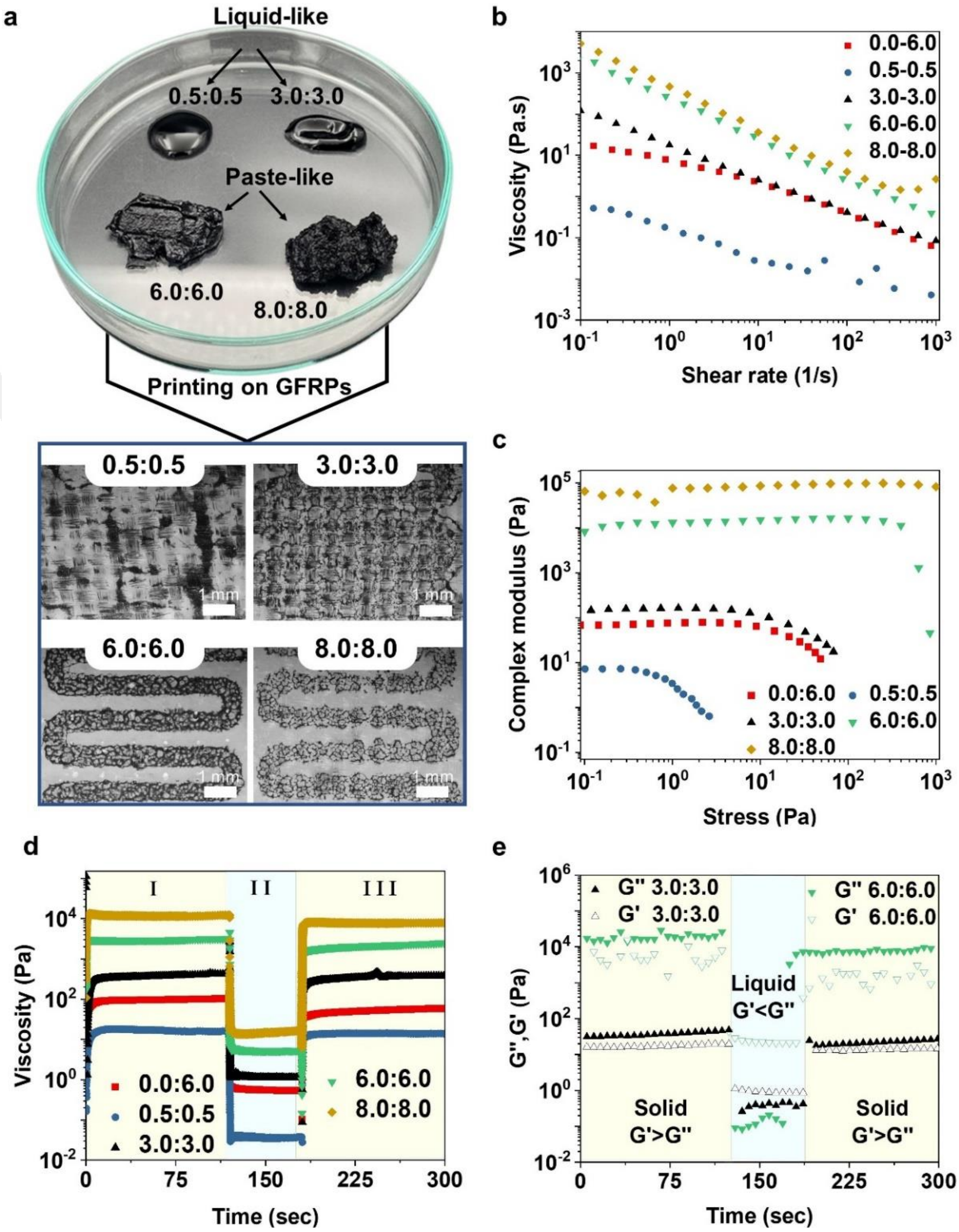

Figure 4.3 : a) Image of ink texture in Petri dishes showing the transition from liquid-like (0.5:0.5, 3.0:3.0) to paste-like (6.0:6.0, 8.0:8.0) textures of CNTSA/CNC-based inks and corresponding microscopic images depict printed patterns on GFRP substrates (scale bar: 1 mm). b) Steady-state viscosity measurements for various CNTSA/CNC inks. c) Oscillatory test results, highlighting variations in viscoelastic properties across different ink concentrations. d) The viscosity changes during the screen printing process simulation. e) The viscoelastic properties during the screen printing simulation for inks with ratios 3.0:3.0 and 6.0:6.0.

Thixotropic behavior is the ink's ability to recover its structure after printing, which can be deduced from the screen printing simulation test [290]. Therefore, the screen-printing process simulation was conducted in time-dependent steady state mode and divided into three stages: (I) resting before printing, (II) printing, during which stress is applied to the ink, and (III) recovery after printing. All inks showed thixotropic behavior, as illustrated in Figure 4.3d. Their shear viscosity recovery rates were calculated and are summarized in Figure 4.3. On average, during the first 100 seconds after printing, inks with high CNTSA/CNC content exhibited lower recovery rates than inks with lower CNTSA/CNC content, favoring appropriate printing conditions [137]. To differentiate between the roles of CNCs and CNTSA in the recovery rate, the thixotropic behavior of a CNC suspension with a ratio of 0.0:6.0 (without CNTSA) was analyzed. The recovery rate of the CNC suspension was 52 ± 8%, indicating that the addition of CNTSA, as in the 6.0:6.0 CNTSA/CNC ink with a higher recovery rate of 77 ± 6%, facilitated an increase in the recovery rate. The recovery rate of the initial viscosity of CNC-based aqueous suspension is not due to the entanglement of the rod-like crystalline particles (low aspect ratio) but due to their surface charges [143,293], which explains the recoverability of the CNC suspension. Therefore, the fibrillated nature and high aspect ratio of the CNTSA are more likely to form a stronger network compared to the absence of CNTSA, resulting in enhanced rheological properties. Thixotropic behaviors for CNC suspensions [293] and CNT-based inks [296] have been reported. Furthermore, as shown in Figure 4.3e, the simulation of the screen-printing process in time-dependent oscillatory mode also demonstrates that, after printing, CNTSA/CNC inks also recover their viscoelastic properties.

Table 4.3 : Rheological properties of CNTSA/CNC prepared inks.

CNTSA/CNC (wt.%/wt.%)	LVR (Pa)	G''/G'*	Shear viscosity** (Pa·s)	Recovery rate after 10 sec (%)***	Recovery rate after 100 sec (%)****
0.0:6.0	0.1-6	0.47 ± 0.02	83 ± 19	44 ± 5	52 ± 8
0.5:0.5	0.1-0.6	0.34 ± 0.03	16 ± 1	81 ± 4	87 ± 4
3.0:3.0	0.1-5.0	0.34 ± 0.02	290 ± 104	56 ± 9	92 ± 7
6.0:6.0	1.0-251.0	0.21 ± 0.02	2855 ± 404	53 ± 4	77 ± 6
8.0:8.0	1.0-631.0	0.22 ± 0.02	11165 ± 1666	72 ± 6	68 ± 5

* G''/G' ratio calculated as the average values across the corresponding LVR for at least two identical samples
** taken after 100 seconds in Stage I
*** data taken from Stage III after 10 seconds
**** data taken from Stage III after 100 seconds

The five printed layers of CNTSA/CNC used to prepare CNTSA-based sensors formed a conformal coating that closely adhered to the composite's rough topography, as shown in Figure 4.4a. Increasing the number of printed layers filled the voids created after each printing step. Figure 4.4b shows the cross-section of the five-layer sensor printed on GFRP composite, with a thickness of 17 ± 2 μm.

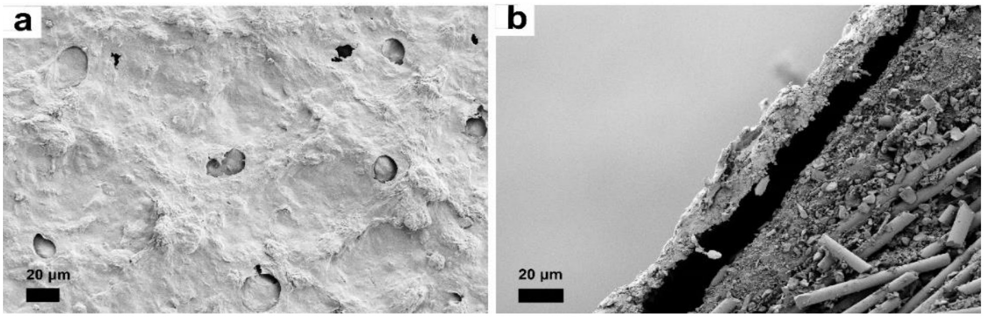

Figure 4.4 : a) Five printed layers of CNTSA/CNC used to prepare CNTSA-based sensors formed a conformal coating that adhered closely to the composite's rough topography, and b) cross section of host composite and the five-layer printed CNTSA-based sensor.

4.2.2 Industrial-grade multisource CNT/CNC-based inks

To assess scalable and cost-effective sensing applications, the study focused on industrial-grade CNTs that offer practical alternatives to high-purity, lab-grade materials like those from Sigma-Aldrich. These CNTs, CNTCT, CNTNI, and CNTNC, were selected not only for their affordability but also for their diverse physical properties, which allow for a meaningful comparison in terms of ink formulation, dispersion behavior, and print performance. Their suitability for large-scale use makes them particularly relevant for real-world applications.

By systematically varying the CNT/CNC ratios and adjusting the water/IPA mixtures, the inks were optimized to achieve an optimal balance between print quality and conductivity, as shown in Table 4.4.

Table 4.4 : Ink compositions of industrial-grade multisource CNTCT/CNC, CNTNI/CNC, and CNTNC/CNC ink formulations for screen printing method.

Carbon nanomaterials	Carbon nanomaterials (wt.%)	CNC (wt.%)	Solvent mixture Water/IPA ratio
CNTCT	4.0	4.0	100/0
	4.0	4.0	70/30
	6.0	6.0	100/0
	6.0	6.0	70/30
CNTNI	6.0	6.0	70/30
	4.0	4.0	70/30
CNTNC	2.0	2.0	70/30
	2.0	2.0	70/30
	2.0	2.0	70/30

The print quality of the CNTCT/CNC inks was evaluated under two different solvent conditions: pure water (100/0) and a water/IPA mixture (70/30). For the CNTCT/CNC 4.0:4.0 formulation, the use of pure water resulted in poor print quality with noticeable defects and irregularities, as shown in Figure 4.5a. However, when the solvent ratio was adjusted to water/IPA ratio of 70/30, a significant improvement in print quality was observed, as shown in Figure 4.5b. Despite this enhancement, the electrical resistance remained relatively high at 250 kΩ after printing five layers, indicating that CNTCT exhibits high sheet resistance even under improved printing conditions.

Similarly, the 6.0:6.0 formulation, with and without the addition of IPA, exhibited results comparable to the 4.0:4.0 formulation, as shown in Figure 4.5c-d. In both cases, the CNT:CNC ratio was kept constant as 1:1. The addition of IPA led to a noticeable improvement in print quality for the 6.0:6.0 formulation; however, after printing five layers, its electrical resistance remained significantly high at 4 MΩ, highlighting the challenges associated with achieving lower resistance with CNTCT.

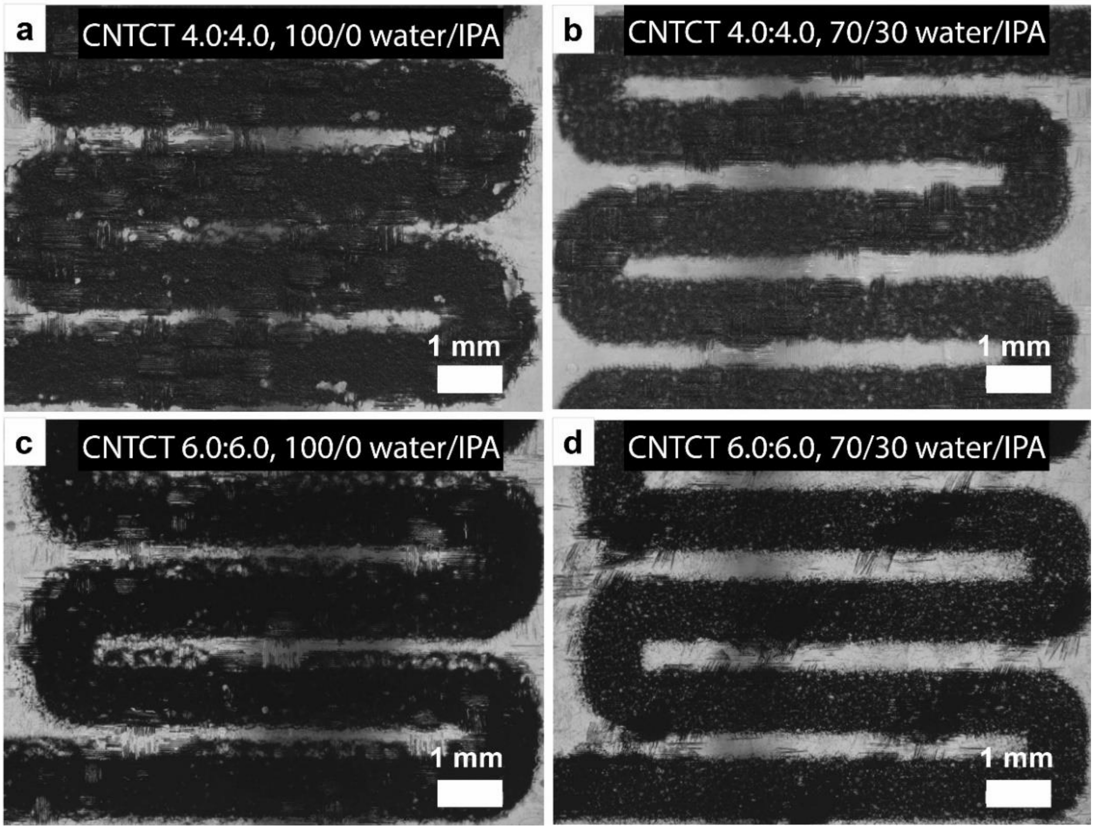

Figure 4.5 : Light microscope images of printed CNTCT/CNC 4.0:4.0 at a water/IPA ratio of a) 100/0 and b) 70/30, along with CNTCT/CNC 6.0:6.0 at a water/IPA ratio of c) 100/0 and d) 70/30.

For CNTNI-based formulations supplied by NanoIntegris, a water/IPA ratio of 70/30 was used, as it provided better dispersion and printability than pure water, as shown in earlier results. After printing ten layers, as shown in Figure 4.6a, the initial formulation with a 6.0:6.0 CNTNI/CNC ratio produced poor electrical performance, with unmeasurable resistance even. This indicates that the conductive network formed by CNTNI under these conditions was insufficient to achieve measurable conductivity. To improve electrical performance, the CNTNI ratio was doubled relative to CNC, reaching a total concentration of 8.0:4.0 wt.%/wt.%, as shown in Figure 4.6b, in opposed to the 1:1 ratio in earlier CNT types. While this adjustment maintained acceptable printability, the electrical resistance remained high at 276 kΩ after five layers, underscoring the difficulty of achieving adequate conductivity with CNTNI.

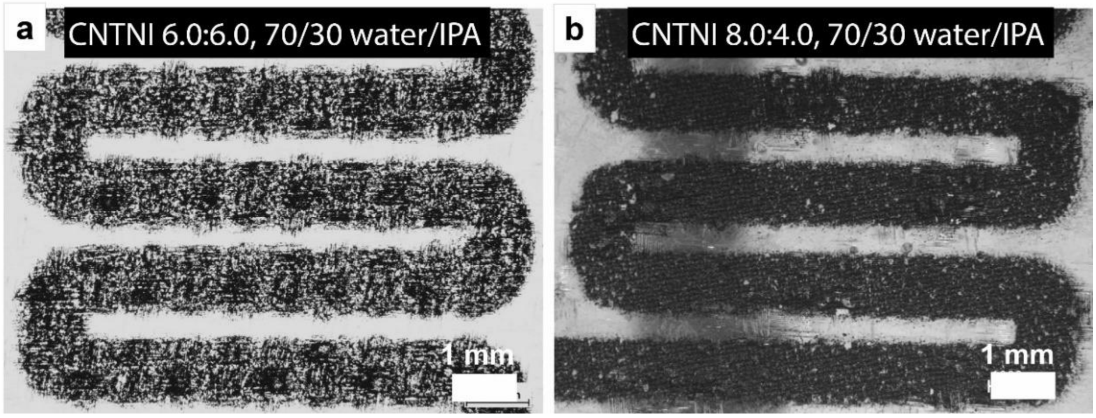

Figure 4.6 : Light microscope images of printed CNTNI at a water/IPA ratio of 70/30 with formulations of a) 6.0:6.0 and b) 8.0:4.0.

CNTNC, supplied by Nanocyl, was dispersed in a water/IPA (70/30) medium using CNCs to assess its printability. This solvent ratio was selected based on previous findings that demonstrated its effectiveness in improving print quality and reducing surface tension-related defects. CNTNC/CNC concentrations were prepared, 2.0:2.0, 4.0:4.0, and 6.0:6.0. Figure 4.7a, the ink texture followed a clear trend: similar to earlier findings, increasing the total concentration caused a shift from a liquid-like consistency to a more paste-like one, with increase in viscosity as shown in Figure 4.8a.

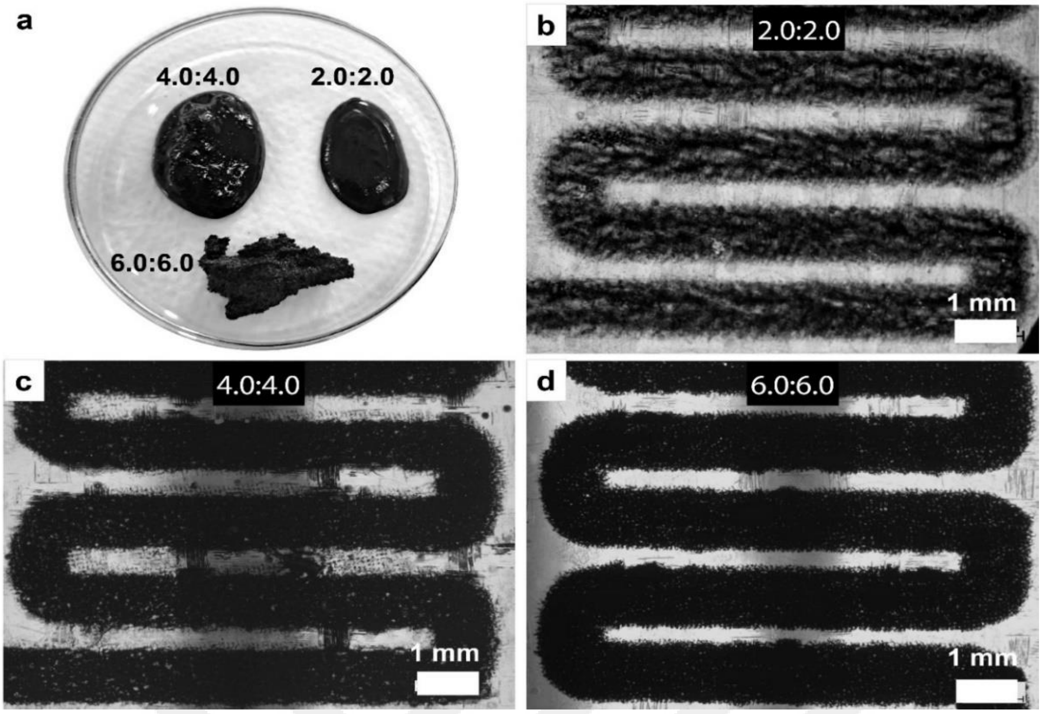

Figure 4.7 : a) Ink texture of printed CNTNC/CNC at various concentrations. Light microscope images of printed CNTNC/CNC at a water/IPA ratio of 70/30 with formulations b) 2.0:2.0, c) 4.0:4.0, and d) 6.0:6.0.

All CNTNC/CNC inks were printable, as shown in Figure 4.7b-d. This good printability across various concentrations is attributed to the enhanced wettability resulting from the addition of the water/IPA mixture, as supported by earlier results reported herein and previous studies [154–156].

Figure 4.8b shows the viscosities of inks prepared using a fixed CNT/CNC ratio of 4.0:4.0 with selected CNT types, tested under steady-state conditions. It is evident that by varying the water/IPA ratio from 100/0 to 70/30, the ink's viscosity increased, regardless of the supplier of the CNT and the used weight ratio. Also, the content of each CNT supplier yielded different viscosities even when the CNT/CNC ratio was kept constant. This is associated with the CNC dispersion in CNT particles as a result of hydrophobic interactions and covalent bonds [142,148,149]. Due to the imperfections found in the side walls of CNTs, which can create hydrophilic regions [149], only the tips of the CNC interact with the sp^2 carbon lattice. Additionally, recent research indicates that the tips of CNCs are more prone to adhering to the side walls of CNTs rather than achieving perfect alignment, owing to the formation of a covalent bond between defects in the CNTs and hydroxyl groups on the CNTs [142]. Considering these findings and recognizing potential variations in surface characteristics and chemical structure among suppliers of CNTs, CNC particles are likely to interact differently with each of the CNT types, resulting in different rheological behaviors.

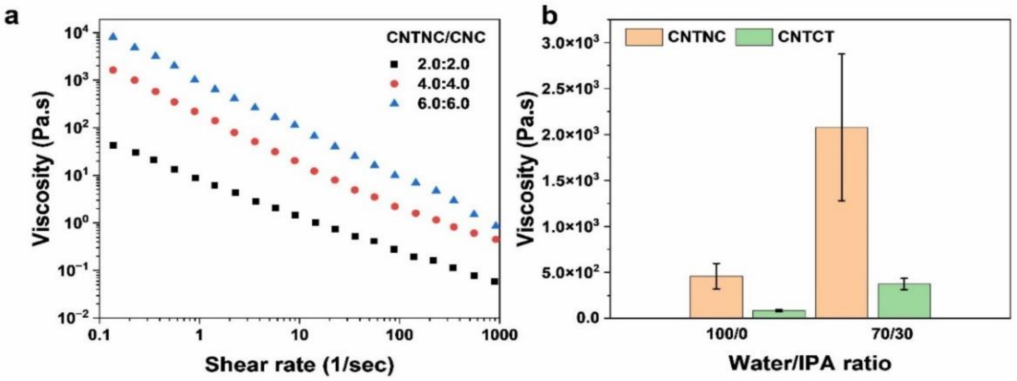

Figure 4.8 : Shear viscosity as function of shear rate for three CNTNC/CNC inks a) and b) average viscosities for 4.0/4.0 CNTCT/CNC and CNTNC/CNC before and after addition of IPA.

As presented in Figure 4.9, the CNTNC/CNC 6.0:6.0 (water/IPA 70/30) ink formulation has a thick texture, which hinders its applicability, although there is still penetration in the mesh. Therefore, the viscosity of CNTNC/CNC 6.0:6.0 (water/IPA 70/30) 9610 ± 2702 Pa·s is considered to be at a maximum limit at which the ink's viscosity is acceptable. Moreover, at such high viscosities, the screen printing mesh tends to clog, thus reducing the number of prints using that mesh.

Figure 4.9 : CNTNC/CNC 6.0:6.0 (water/IPA 70/30) before and after steady state test.

4.2.3 CNF-based inks

The development of CNF-based inks aimed to optimize printability by reducing surface tension and enhancing wettability, particularly at moderate concentrations.

Similar to the formulation process for CB-based inks, distilled water and a water/IPA mixture (70/30) were utilized as solvents, while TX-100 and CNC were incorporated as surfactants to improve dispersion stability, as shown in Table 4.5.

Table 4.5 : Composition details of CNF/TX-100 and CNF/CNC ink formulations prepared for screen printing method.

Carbon nanomaterials	Surfactant		Solvent mixture
CNF (wt.%)	**CNC (wt.%)**	**TX-100 (wt.%)**	**Water/IPA ratio**
3.0	0.0	3.0	100/0
3.0	0.0	6.0	100/0
2.0	2.0	0.0	70/30
4.0	4.0	0.0	70/30

First, an attempt was made to develop CNF-based inks using TX-100 as a surfactant. By keeping the CNF weight ratio to 3.0 wt.% and varying TX-100 ratio between 3-6 wt.%, the inks were not printable and yielded low dispersibility, as demonstrated in Figure 4.10. To disperse CNFs in an aqueous medium, TX-100 weight ratio needs to exceed that of the CNF by 13 to 40-fold, and even at such high ratios, TX-100 disperses CNFs for short period before sedimentation takes a place [297], explaining the poor print resolution and low dispersibility of CNF/TX-100 based inks. Consequently, due to difficulty of TX-100 to effectively disperse CNF particles TX-100 as a sole surfactant was discontinued.

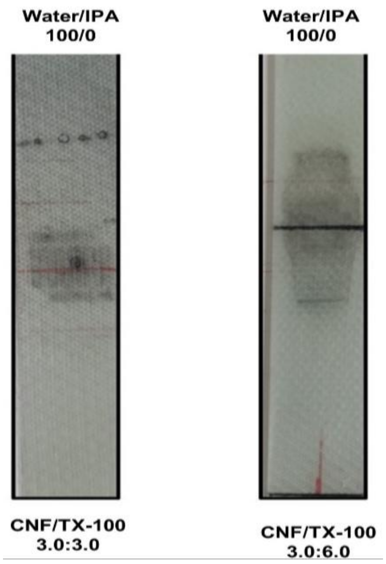

Figure 4.10 : Visual comparison of CNF-based inks printed with varying TX-100 ratios (3.0:3.0 and 3.0:6.0 wt.%) (water/IPA: 100/0).

To reduce the surface tension of the CNF/CNC ink, a water/IPA solvent with a 70/30 ratio was used. Two CNF/CNC ratios were tested, as detailed in Table 4.5. Figure 4.11shows that increasing the total CNF/CNC ratio resulted in more uniform printing, leading to a better-established electrical network. The line width did not vary significantly with the increase in CNF/CNC content from 2.0:2.0 to 4.0:4.0, changing only from 956±47μm to 935±45μm. Increasing the printing layer for CNF/CNC ink with weight ratio of 4.0:4.0 decreased the electrical resistance from 312 ± 76 kΩ to 62 ± 15 kΩ. CNF-based sensors with two printed layers were prepared using CNF/CNC ink with a weight ratio of 4.0:4.0 for further testing.

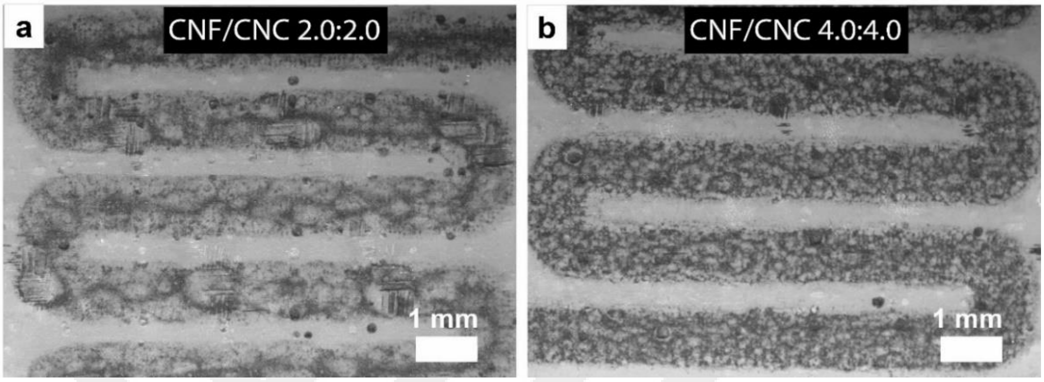

Figure 4.11 : Light microscope images of printed CNF/CNC-based ink with a corresponding ratio of a) 2.0:2.0 and b) 4.0:4.0 wt.%.

Rheological results of water/IPA (70/30) CNF/CNC-based ink with weight ratio of 4.0:4.0 is shown in Figure 4.12. The complex modulus remains unchanged and showed a linear response over a stress range as demonstrated in Figure 3a. Within the linear region, the calculated G''/G' ratio was equal to 0.36 ± 0.03. When the ink was subjected to forces mimicking those forces applied during screen printing process, the shear viscosity recovered 35 ± 5% and 42 ± 4% after ten and 100 seconds, respectively. This recovery rate was associated with the CNF particles' ability to entangle and disentangle before and after application of force. The moderate recovery rate value explains the large line width compared with initial line width.

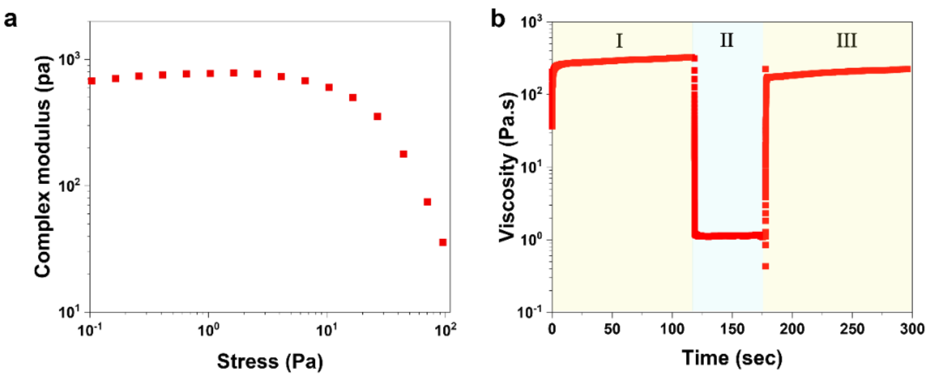

Figure 4.12 : Rheological characterization of CNF/CNC-based ink (4.0:4.0 ratio): a) complex modulus vs. applied stress and b) screen printing simulation.

Figure 4.13 shows the surface morphology of two layers printed using CNF/CNC ink with a weight ratio of:4.0:4.0. In Figure 4.13a, the surface roughness is notable and, in fact, much notable than CB-based sensor discussed in the previous section. This surface roughness was attributed to the ability of CNFs to readily agglomerate and form big aggregates as demonstrated in Figure 4.13a at higher magnification. Along with the CNF aggregates, CNFs formed conductive paths through CNCs. Nonetheless, the measured diameter of the CNF/CNC particles was 116 ± 41 μm.

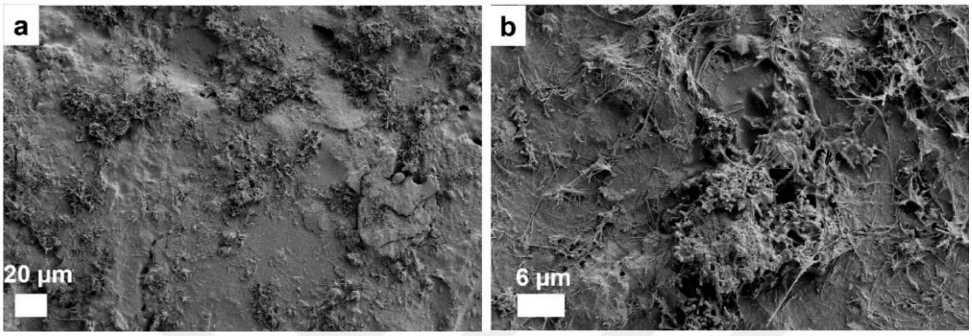

Figure 4.13 : SEM images showing the surface morphology of a CNF-based sensor printed with a CNF/CNC ratio of 4.0:4.0 using two printed layers. a) Lower magnification (1K) reveals rough surface features with evident CNF aggregates. b) Higher magnification (5K) highlights a network of entangled CNFs and CNCs.

4.2.4 CB-based inks

In this study, a range of CB-based ink formulations was prepared to investigate their impact on print quality. The formulations were systematically modified by adjusting the CB and CNC content, TX-100 concentration, and solvent composition. Table 4.6 presents the compositions of the prepared inks, outlining the range of parameters examined to optimize the printing process.

Table 4.6 : Composition details of CB/TX-100, CB/CNC, and CB/CNC/TX-100 ink formulations for screen printing method.

Carbon nanomaterials	Surfactant		Solvent mixture
CB (wt.%)	**CNC (wt.%)**	**TX-100 (wt.%)**	**Water/IPA ratio**
3.0	0.0	3.0	70/30
3.0	0.0	3.0	100/0
6.0	0.0	6.0	70/30
6.0	0.0	6.0	100/0
9.0	0.0	9.0	70/30
9.0	0.0	9.0	100/0
4.0	4.0	0.0	100/0
4.0	4.0	0.0	70/30
4.0	4.0	2.0	70/30
4.0	4.0	4.0	70/30
4.0	4.0	6.0	70/30
10.0	4.0	6.0	70/30

To enhance the dispersibility of CB particles, TX-100 was incorporated as a surfactant to improve wettability and promote uniform dispersion. Initial tests revealed that using TX-100 alone was insufficient for achieving successful printing on GFRP substrates, even when high CB/TX-100 weight ratios such as 9.0:9.0 were employed. As shown in Figure 4.14, while TX-100 improved wettability, it did not significantly modify the ink's rheological properties, resulting in poor print quality. However, adding IPA as a co-solvent notably enhanced printability, although it still fell short of enabling proper printing. This improvement was particularly evident at the CB/TX-100 ratio of 9.0:9.0, where IPA reduced the ink's spreading after printing.

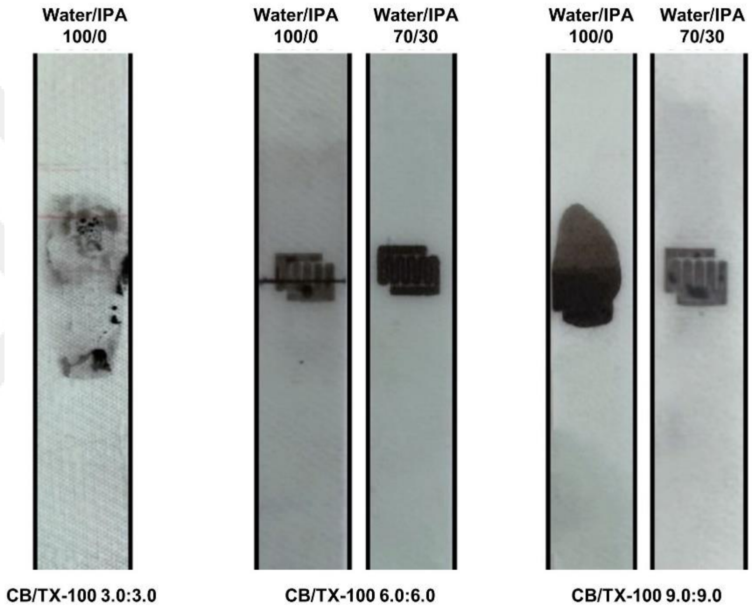

Figure 4.14 : Printing results of CB/TX-100 inks with various TX-100 concentrations and solvent mixtures. The samples include, left to right: CB/TX-100 3.0:3.0 (water/IPA 100/0), CB/TX-100 6.0:6.0 (water/IPA 100/0), CB/TX 6.0:6.0 (water/IPA 70/30), CB/TX 9.0:9.0 (water/IPA 100/0), and CB/TX-100 9.0:9.0 (water/IPA 70/30).

During ink preparation, to avoid high concentration and potential gelation of the CNC suspension, the highest CNC ratio kept at 4.0 wt.%. In an aqueous medium, Figure 4.15 shows that by altering the CB/CNC weight ratio up to 4.0:4.0, resulted in unsuccessful printing. However, by reducing the surface tension of the CB/CNC ink with a weight ratio of 4.0:4.0 after the addition of IPA, a significant improvement in printing was seen. The improvement in printability was attributed to the wettability and higher boiling point of IPA compared with water which facilitated accelerated drying of the ink and, in turn, minimizing spillover [154,155]. In the direction of printing, despite the improvement in printing, ink bleeding was observed.

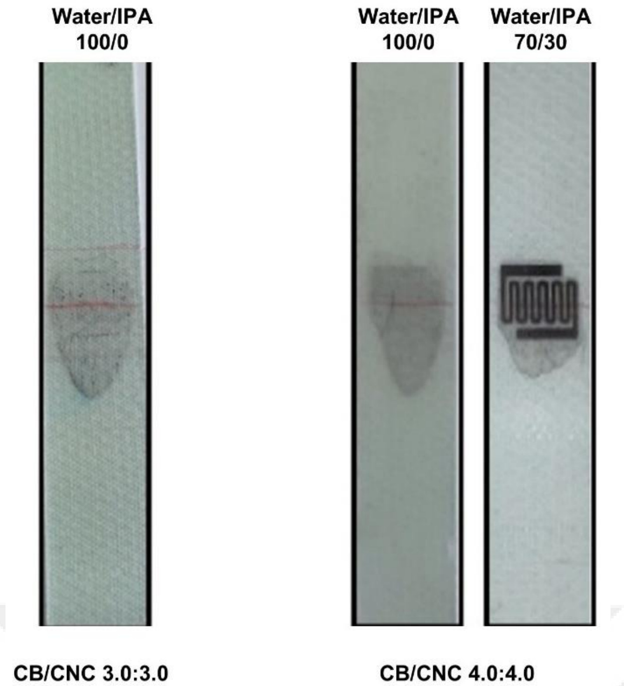

Figure 4.15 : Printing results of CB/CNC inks with various CNC concentrations and solvent mixtures. The samples include, left to right: CB/CNC 3.0:3.0 (W/IPA 100/0), CB/CNC 4.0:4.0 (water/IPA 100/0), and CB/CNC 4.0:4.0 (water/IPA 70/30).

The ink bleeding observed was attributed to insufficient wetting, poor drying, and/or poor rheological properties. To address the issue of ink bleeding, TX-100 was added to the ink formulation CB/CNC 4.0:4.0 at various ratios (2, 4, and 6 wt.%) to improve rheological properties and further enhance printability. Interestingly, ink bleeding observed in the direction of printing lessened at a TX-100 ratio of 2.0 wt.%, as depicted in Figure 4.16a-b. Further increase in the TX-100 ratio resulted in diminishing ink bleeding as demonstrated in Figure 4.16b-c. The improvement in printing condition was attributed to improved wettability and potential improvement in rheological properties, which are discussed shortly. However, the addition of TX-100 displayed a bubble texture and foam-like appearance, resulting in surface defects after printing. During ink preparation, the mixing of TX-100 yielded a foam appearance. Kolb et al. and Patist et al. discussed that the foamy behavior in CB/TX-100-based solution is the result of micelles formulation, which are formed after TX-100 has reached the critical micelle concentration [298,299]. These micelles consist of clusters where the hydrophilic polyethylene oxide (PEO) chains of TX-100 are aligned with water molecules, while the hydrophobic aromatic hydrocarbon groups cluster together or may interact with methyl groups in IPA. After printing, these clusters burst as water evaporates and leave surface defects. Nonetheless, irrespective of the bubble texture, at TX-100 wt.% of 6.0, the best printing resolution was obtained.

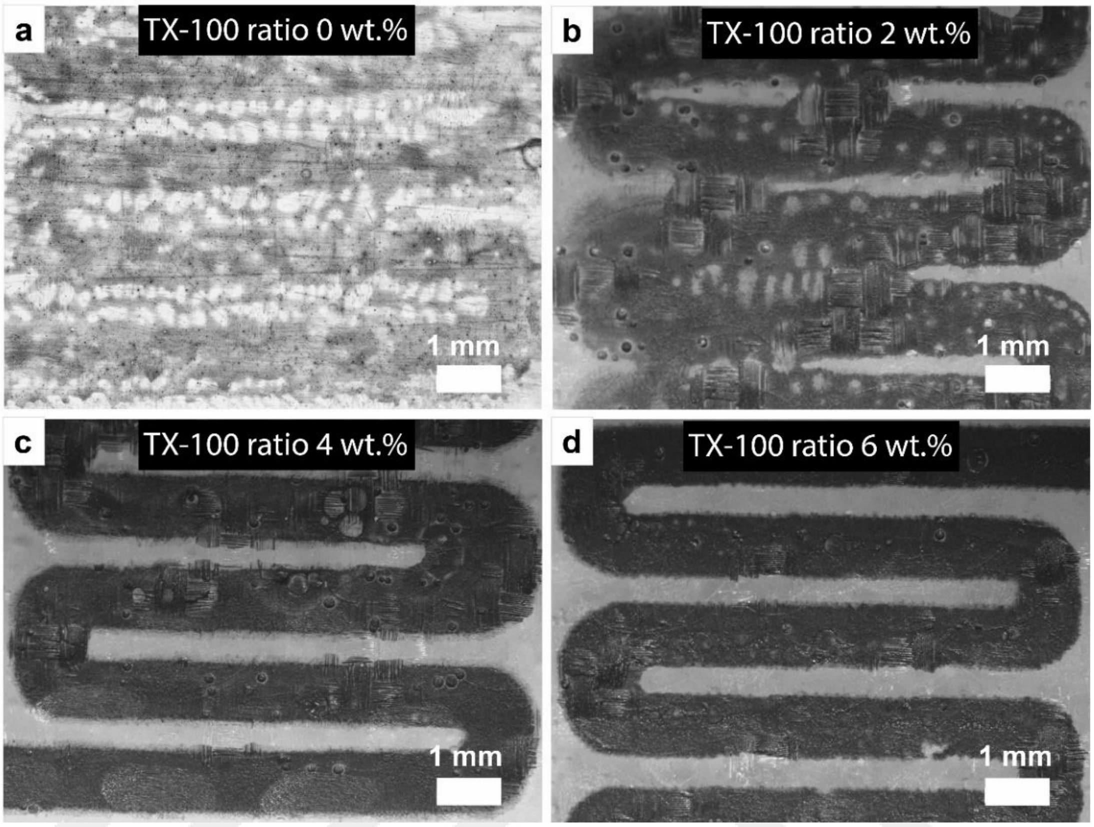

Figure 4.16 : Light microscope images of printed CB/CNC-based ink with a TX-100 ratio of a) 0, b) 2, c) 4, and d) 6 wt.%.

The initial resistance of the first layer print of CB/CNC/TX-100 ink with ratio of 4.0:4.0:6.0 was ~23 MΩ, which is considered to be unacceptably high. To decrease the initial resistance of the ink, the CB ratio increased from 4.0 to 10.0 wt.%. This led to a significant decrease in resistance down to 464 ± 38 kΩ. This improvement in initial resistance is attributed to the evident increase in CB content and possibly to a thicker print layer resulting from the higher viscosity [300,301], as discussed in the rheology measurement section below. Figure 4.17a shows the first layer print of CB/CNC/TX-100 ink with a ratio of 10.0:4.0:6.0. By increasing the CB content, the line width increased from 964 ± 37 µm to 1023 ± 34 µm for inks with CB weight ratios of 4.0 and 10.0, respectively. Although increasing the CB ratio slightly reduced the formation of micelles and the resulting surface defects, eliminating these defects remained challenging. In Figure 4.17b, by increasing the printing layer to two, the CB/CNC content increased, and voids in the surface decreased, leading to a reduction in electrical resistance to 194 ± 64 kΩ. Increasing the printing layer led to an increase in line width to 1137 ± 32 μm. Under these acceptable conditions, CB-based sensors were fabricated and prepared for further testing.

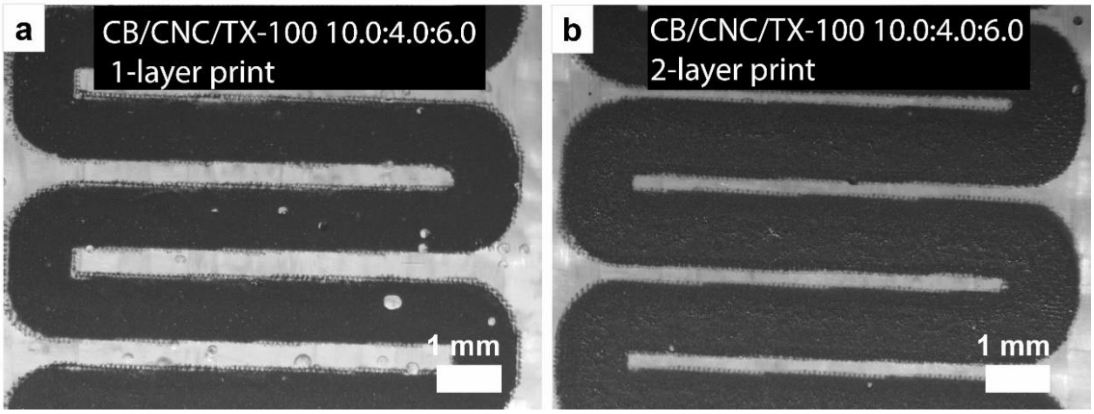

Figure 4.17 : Light microscope images of printed CB/CNC/TX-100 with a weight ratio of 10.0:4.0:6.0 after a) one-layer and b) two-layer print.

To shed a light on any potential improvement in rheological properties after the addition of TX-100 and its relatively resolution, the CB/CNC/TX-100-based inks subjected to rheological evaluation. The complex modulus, which measures the ink's resistance to deformation, decreased as the TX-100 ratio increased, as illustrated in Figure 4.18a. This decrease could be attributed to the disentanglement of the large CB aggregates, leading to a better dispersion [302]. Inks with increasing TX-100 ratios require less force to disrupt the ink's network and force the ink into the printing mesh. The linear region, where the complex modulus remains unchanged, is referred to LVR [292]. CBs are composed of stacked graphene sheets, forming a composite of both amorphous and crystalline carbon substructures [303]. TX-100 stabilizes CBs primarily through its hydrophobic alkyl chains, which interact with the hydrophobic surfaces of CB. Additionally, steric stabilization occurs due to the repulsion between the adjacent hydrophilic polyethylene glycol (PEG) chains of TX-100. While TX-100 provides stability through these mechanisms, π-π stacking interactions with the π-electron system of CBs are less likely to play a significant role [304].

As calculated and shown in Figure 4.18b, the addition of TX-100 increased G''/G' ratio, an indicator of cohesiveness. This is an indication that TX-100 favors more liquid-like ink consistently, resulting in a less cohesive ink and, in turn, facilitating screen printing process [268,295].

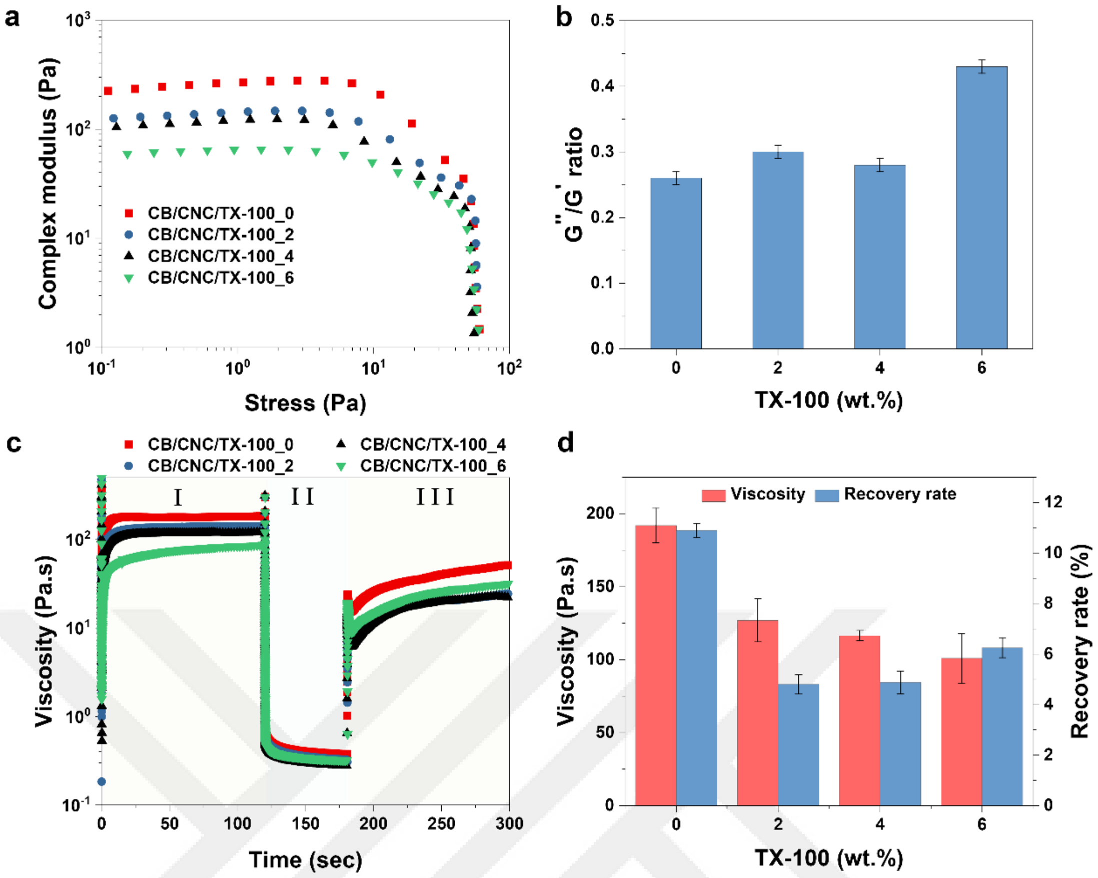

Figure 4.18 : Influence of TX-100 on a) complex modulus, b) G′′/G′ ratio, c) screen printing simulation, and d) viscosity and recovery rate.

Screen printing simulation results are summarized in Figure 4.18c-d. Shear viscosity significantly dropped after the addition TX-100 which was attributed to the enhanced dispersibility discussed earlier [302,305]. No significant decrease in viscosity was noted when the TX-100 ratio reached 4 and 6 w.%, indicating saturation. The decrease in viscosity after addition of TX-100 led to a decrease in recovery rate after ten seconds. This pattern decrease in recovery rate is similar after 100 seconds, as calculated in Table 4.7. Even after 100 seconds, the recovery rate values for CB/CNC/TX-100 inks are considerably small in consideration for using in screen printing method [137]. Associating this result with printability results shown in Figure 4.17, it becomes clear that the improvement seen at TX-100 ratio of 4.0 wt.% and higher was not due to recovery rate but perhaps due to the reduction in surface tension [306,307]. The low recovery rate also explains the large line width after successful printing which is associated with low printing resolution [134]. The overall low recovery rate was associated with low aspect ratio of the spherical CBs [301] which prompts disaggregation at a particular shear force but when the force is lifted the ink's reformation of the original structure is slow, and recoverability of CNCs [143,293].

Table 4.7 : Rheological and printing properties of the developed CB/CNC/TX-100 inks.

CB/CNC/TX-100 content	Shear viscosity (Pa·s)	Viscosity recovery rate after 10 sec (%)	Viscosity recovery rate after 100 sec (%)	G′′/ G′ ratio	R_0 (kΩ)
4.0:4.0:0.0	192 ± 112	11 ± 0	26 ± 1	0.26 ± 0.01	-
4.0:4.0:2.0	127 ± 15	5 ± 0	12 ± 2	0.30 ± 0.01	-
4.0:4.0:4.0	117 ± 4	5 ± 1	13 ± 1	0.28 ± 0.01	-
4.0:4.0:6.0	101 ± 17	6 ± 0	17 ± 0	0.43 ± 0.01	~23000
10.0:4.0:6.0	349 ± 5	12 ± 1	38 ± 2	0.18 ± 0.03	464 ± 38

Figure 4.19a illustrates that increasing the CB/CNC/TX-100 content from 4.0:4.0:6.0 to 10.0:4.0:6.0 leads to a notable increase in shear viscosity. This increase is attributed to the higher solid content of CB particles in the ink formulation. The recovery rate of the ink after 10 seconds and 100 seconds improved significantly, rising from 6 ± 0 and 17 ± 0 to 12 ± 1 and 38 ± 2, respectively, as shown in Figure 4.19b. This indicates enhanced structural recovery after deformation. However, the G″/G′ (loss modulus to storage modulus) ratio decreased from 0.43 ± 0.01 to 0.18 ± 0.03. This reduction suggests an increase in the cohesive strength of the ink, indicating a more solid-like behavior due to the stronger interactions between CB and CNC particles at higher concentrations.

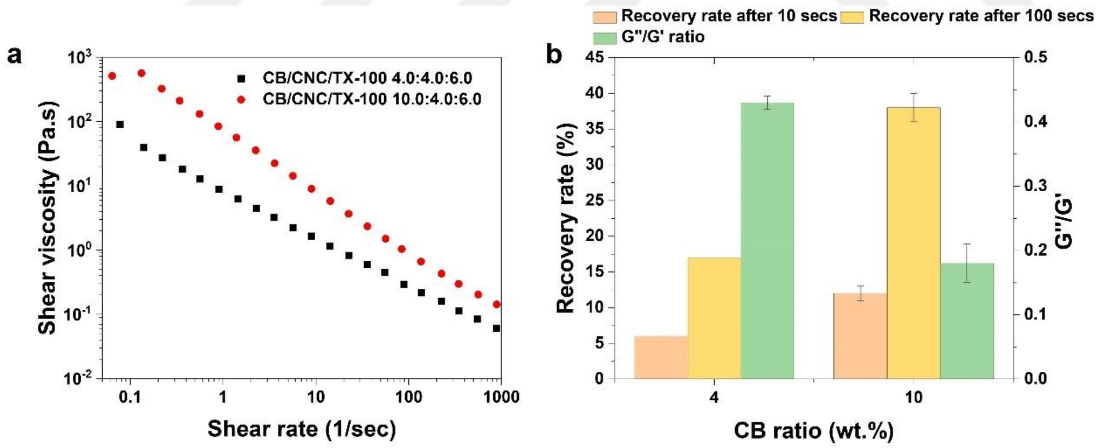

Figure 4.19 : a) Shear viscosity as a function of shear rate for CB/CNC/TX-100 inks with compositions of 4.0:4.0:6.0 and 10.0:4.0:6.0, b) comparison of recovery rates after 10 seconds and 100 seconds along with G″/G′ ratio for CB/CNC/TX-100 inks with CB ratios of 4.0 wt.% and 10.0 wt.%.

Having established the rheological properties and recovery characteristics of the CB/CNC/TX-100 inks, it is essential to further investigate the surface morphology of the optimized ink formulation (10.0:4.0:6.0). Analyzing the surface morphology will provide valuable insights into the distribution of conductive particles, the homogeneity of the printed pattern, and potential defects that may influence electrical performance.

Figure 4.20a presents the surface morphology of two layers printed using CB/CNC/TX-100 ink, formulated with a weight ratio of 10.0:4.0:6.0. In Figure 4.20b, the bubble-like texture is prominently visible, which is attributed to the burst micelles formed during the printing process, as discussed earlier. At a higher magnification, the distribution of CB and CNC particles becomes evident. CB particles are observed to form continuous conductive paths facilitated by the CNCs, demonstrating effective particle dispersion. The average diameter of the CB/CNC particle clusters was measured to be 75 ± 13 nm.

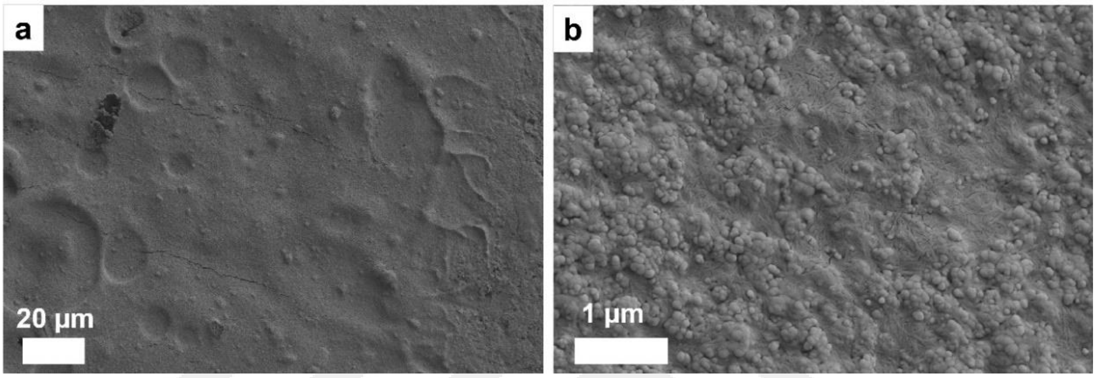

Figure 4.20 : SEM images showing the surface morphology of the0020CB-based sensor (10.0:4.0:6.0 ink formulation) at two different magnifications: a) Low magnification (1K) highlighting surface roughness and irregularities, and b) High magnification (50K) revealing a densely packed network of CB particles with interconnected structures that contribute to electrical conductivity.

For comparison, the individual CB particle diameter was measured using SEM images of the as-received CB powder, as shown in Figure 4.21. These measurements indicate a smaller average particle diameter of 46 ± 12 nm for the unprocessed CB particles.

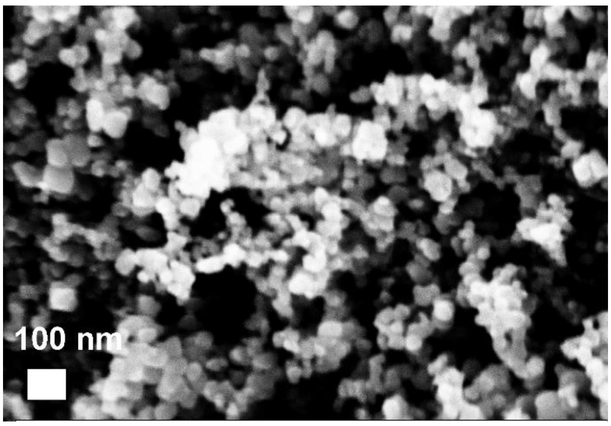

Figure 4.21 : SEM image of CB particles.

In conclusion, the optimization of CB/CNC/TX-100 inks through controlled adjustments of CB concentration, TX-100 ratio, and solvent composition successfully improved printability and reduced electrical resistance. Despite some surface defects associated with micelle formation, the formulation with a 10.0:4.0:6.0 ratio demonstrated the most consistent performance, achieving acceptable electrical properties and suitable morphology for further sensor fabrication.

The subsequent section will focus on CNF-based inks, evaluating their formulation, printability, and performance characteristics.

4.2.5 CB/CNTSA-based inks

Hybrid carbon nanomaterial-based sensors combine the advantages of different nanomaterials to achieve enhanced electromechanical performance. Herein, CB was hybridized with CNTSA in the ink formulation to study the effect of this combination on sensor performance.

In the previous section, the addition of TX-100 into CB/CNC-based inks stabilizes it. In this work, the influence of TX-100 on CB/CNTSA/CNC hybrid-based ink is investigated. TX-100 stabilizes CNTs through π-π stacking interactions between its benzene ring and the π-electron system of CNTs. The hydrophobic alkyl chains of TX-100 likely adsorb along the length of the CNT surface rather than wrapping around its circumference. Additionally, steric stabilization occurs due to the repulsion between adjacent hydrophilic PEG chains of TX-100 [308].

The CNC and CB-to-CNTSA ratios was kept constant at 4.0 and 4.0:2.0 wt.%, respectively. It was argued that since the CB has lower aspect ratio than CNTSA, its weight ratio was kept double that of CNTSA. In the previous chapters, the addition of IPA to water-based inks enhanced printability by reducing surface tension and wettability and accelerating drying. The addition TX-100 influenced the printing quality and rheology, depending on the filler type. Therefore, in the study, the water/IPA ratio kept constant at 70/30 and TX-100 was varied, as detailed in Table 4.8. To assess the printability of developed ink, the inks were printed on surface of GFRPs.

Table 4.8 : Composition details of CB/CNTSA-based inks with varying TX-100 concentrations for screen printing method.

Carbon name	Carbon nanomaterials		Surfactant		Solvent mixture
	CB (wt.%)	CNTSA (wt.%)	CNC (wt.%)	TX-100 (wt.%)	Water/IPA ratio
CB/CNTSA-0	4.0	2.0	4.0	0.0	70/30
CB/CNTSA-3	4.0	2.0	4.0	3.0	70/30
CB/CNTSA-6	4.0	2.0	4.0	6.0	70/30
CB/CNTSA-9	4.0	2.0	4.0	9.0	70/30

Figure 4.22 shows printing results of the prepared CB/CNTSA-based inks with various TX-100 ratios. TX-100 at ratios of 0 and 3 wt.%, ink bleeding was observed. This excessive ink bleeding could cause potential short circuit, leading to low initial resistance. However, as the TX-100 ratio increased to 6 and 9 wt.%, ink bleeding dimensioned. Akindoyo et al. observed similar improvement in printing with the addition of TX-100 to CNTSA-based inks, likely due to a reduction in surface tension [307].

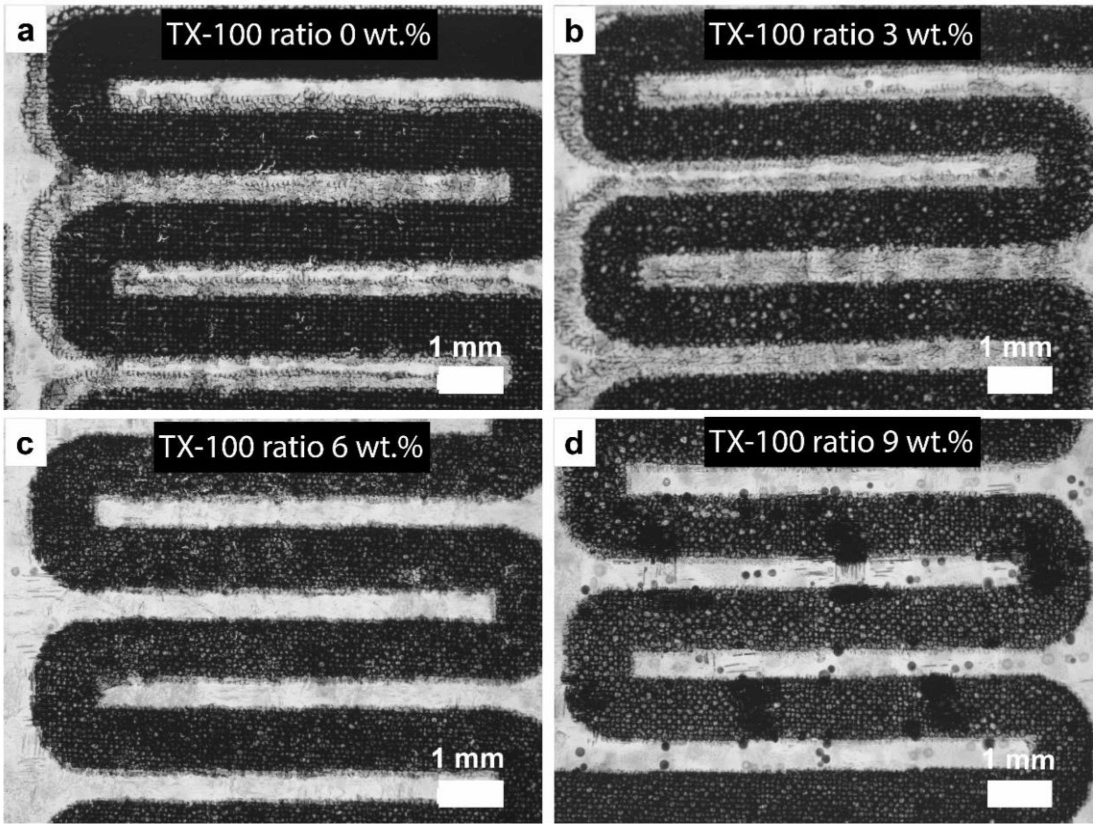

Figure 4.22 : Light microscope images of printed CB/CNTSA/CNC/TX-based ink with varying TX-100 ratios of a) 0, b) 3, c) 6, and d) 9 wt.%.

As discussed previously, TX-100 stabilizes CBs through hydrophobic interactions and steric effects. Additionally, TX-100 stabilizes CNTs via π-π stacking interactions with the CNTs' π-electron system and adsorption along the CNT surface. The hydrophobic alkyl chains of TX-100 likely adsorb along the length of the CNT surface rather than wrapping around its circumference [308]. Additionally, steric stabilization occurs due to the repulsion between adjacent hydrophilic PEG chains of TX-100. As a result, TX-100 effectively stabilizes the CB/CNTSA hybrid ink, improving printability and reducing ink bleeding.

As calculated and shown in Table 4.9, the line width remained relatively unchanged with increasing TX-100 ratio, indicating that maybe by increasing the TX-100 ratio from 6 to 9 wt.% unaffected rheological behavior of the ink.

To understand the role of TX-100 in printing, the inks rheological properties were evaluated. The complex modulus decreased as the TX-100 ratio increased, similar to CB-based inks with varying TX-100 ratios, as illustrated in Figure 4.23a. This decrease could be attributed mainly to the disentanglement of CB/CNTSA, CNTSA, and CB aggregates, leading to a better dispersion [302,309]. Inks with increasing TX-100 ratio requires less force to disrupt the ink's network and force the ink into the printing mesh. Within the LVR region, as calculated and shown in Figure 4.23b, the addition of TX-100 increased G''/G' ratio; the lower the ratio the higher the cohesive is the ink [295]. This is an indication that the addition of TX-100 favors more liquid-like ink consistently, resulting in a less cohesive ink and, thus, facilitating screen printing process [268,295].

Screen printing simulation results are summarized in Figure 4.23c-d. Shear viscosity significantly dropped after the addition TX-100 which was attributed to the enhanced dispersibility discussed earlier [302], similar to results of CB-based inks with varying TX-ratios. No significant decrease in viscosity was noted when the TX-100 ratio reached 4 and 6 w.%, indicating saturation. However, unlike CB-based inks with varying TX-100 ratios, the decrease in viscosity after addition of TX-100 led to an increase in recovery rate after ten and 100 seconds, as calculated in Table 4.9. Even after 100 seconds, the recovery rate values for CB/CNC/TX-100 inks are considerably larger than value of CB-based inks, which explains why CB/CNTSA-based inks results in finer line width compared with CB-based inks. Associating this result with printability results shown in Figure 4.22, it becomes clear that the improvement seen at TX-100 ratio of 4.0 wt.% and higher was due to recovery rate and reduction in surface tension [306,307]. The overall moderate recovery rate was mainly associated with presence of the high aspect ratio CNTs [296] and to a less degree to the low aspect ratio CB and CNC particles [143,293].

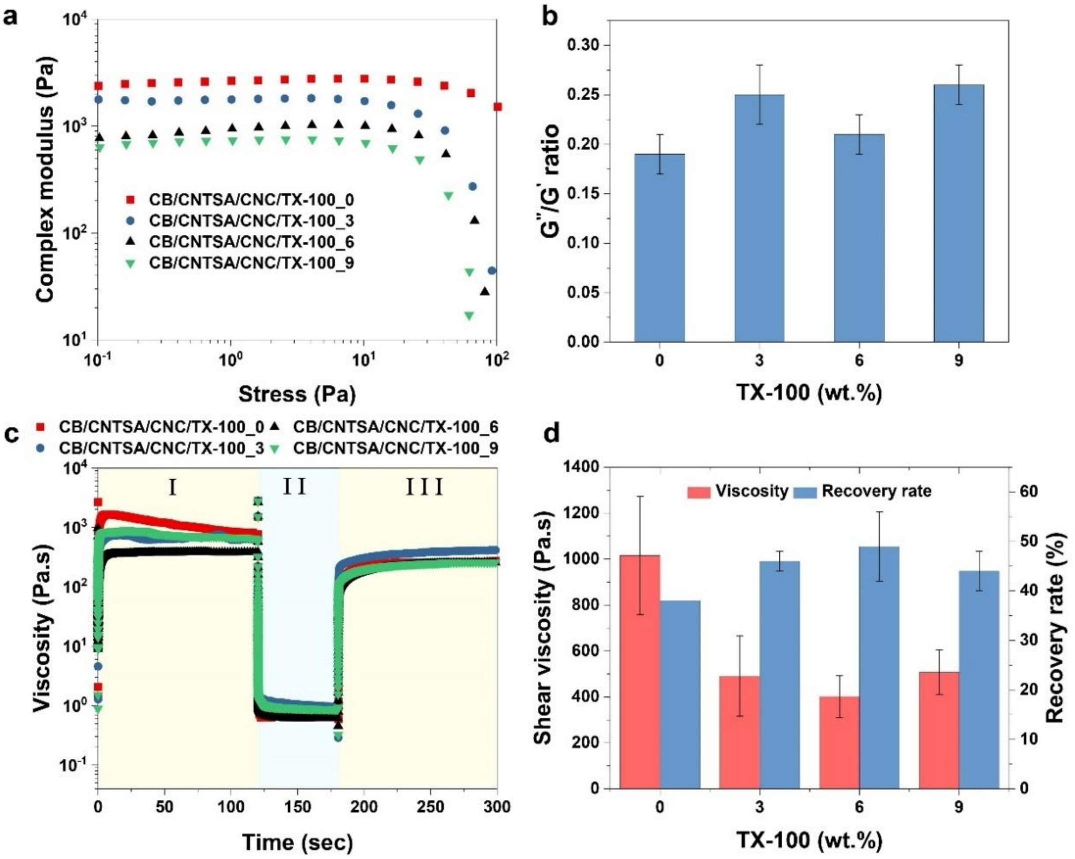

Figure 4.23 : Influence of CB/CNTSA/CNC/TX-100 ink formation with varying TX-100 concentrations (0, 3, 6, and 9 wt.%) on a) complex modulus, b) G''/G'ratio, c) screen printing simulation, and d) viscosity and recovery rate.

Table 4.9 : Rheological and printing properties of the CB/CNTSA-based inks.

Ink content	Shear viscosity (Pa·s)	Viscosity recovery rate after 10 sec (%)	Viscosity recovery rate after 100 sec (%)	G''/G' ratio	Line width (mm)	R_0 (kΩ)
CB/CNTSA-0	1016 ± 257	38 ± 0	44 ± 10	0.19 ± 0.02	964 ± 26	156 ± 72
CB/CNTSA-3	491 ± 175	46 ± 2	67 ± 5	0.25 ± 0.03	934 ± 38	416 ± 43
CB/CNTSA-6	402 ± 92	49 ± 7	71 ± 13	0.21 ± 0.02	994 ± 52	575 ± 69
CB/CNTSA-9	507 ± 97	44 ± 4	71 ± 13	0.26 ± 0.02	985 ± 23	356 ± 51

Figure 4.24a shows the surface morphology of two layers printed using CB/CNTSA/CNC/TX-100 ink with a weight ratio of 4.0:2.0:4.0:6.0 at two different magnifications. Due to the higher ratio of CB compared to CNTSA, the distribution of CB particles within the sensor is more apparent in Figure 4.24b. The CNTSA, with their high aspect ratio, are interwoven within the CB and CNCs, forming a network that enhances both the structural integrity and conductive pathways of the printed layers.

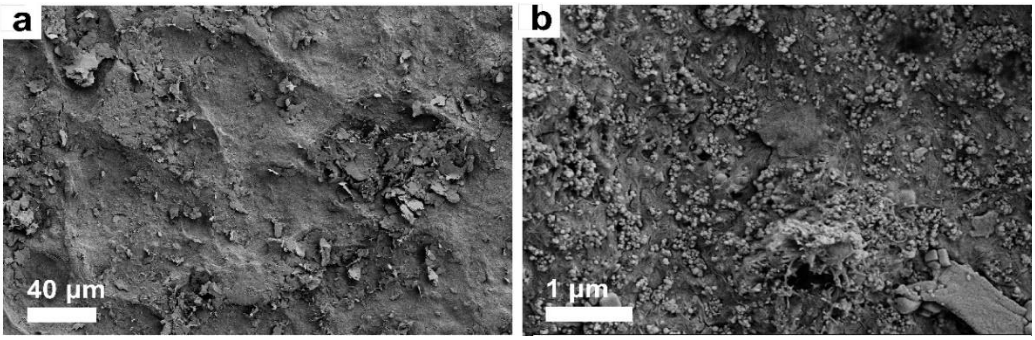

Figure 4.24 : Morphology of two-layer CB/CNTSA-based sensor under two magnifications: a) 1K and b) 50K.

4.2.6 CB/CNTNC-based inks

In this section, the formulation of hybrid CB/CNTNC inks was examined for the fabrication of printed sensors. This hybrid approach is expected to contribute to more reliable and sensitive sensor applications.

Since CNTCT and CNTNI potentially exhibit lower sheet resistance, they were not considered for hybridization with carbon black, as their conductivity might not be sufficiently enhanced by the addition of carbon black. Instead, a CB/CNTNC/CNC/TX-100 formulation with a weight ratio of 4.0:2.0:2.0:6.0 in a water/IPA (70/30) medium was developed, which proved sufficient to achieve acceptable printing quality. This CB/CNTNC composition closely resembles the successfully developed CB/CNTSA-based ink discussed earlier, maintaining a balance between printability and conductivity. As shown in Figure 4.25, two layers of the ink were successfully printed onto GFRP, demonstrating good adhesion and uniform coverage.

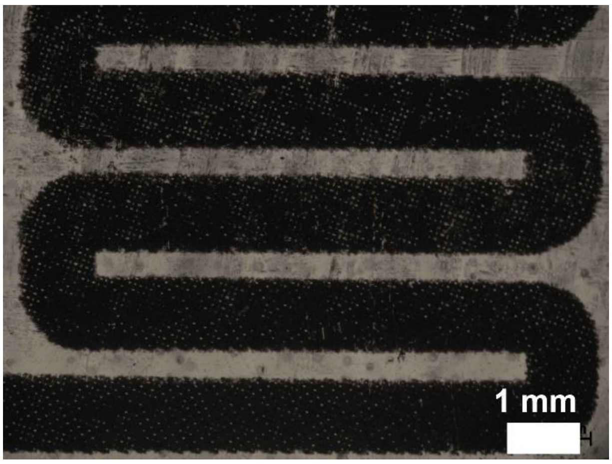

Figure 4.25 : Light microscope images of printed CB/CNTNC/CNC/TX-based ink with a TX-100 ratio of 4.0:2.0:2.0:6.0.

Additionally, the viscosity of the ink, presented in Figure 4.26, highlights its shear thinning behavior, which is crucial for ensuring consistent deposition and layer formation during the printing process.

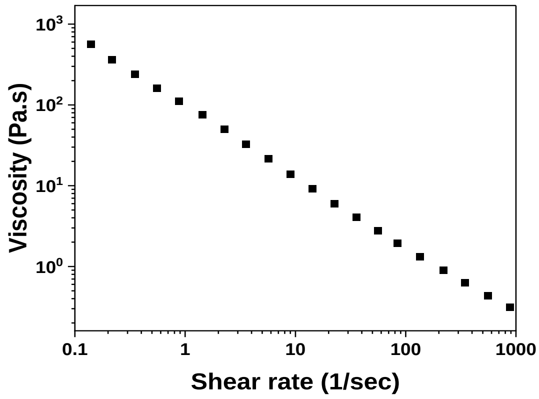

Figure 4.26 : Shear viscosity of CB/CNTNC-based ink with a TX-100 ratio of 4.0:2.0:4.0:6.0 in a water/IPA ratio of 70/30.

4.2.7 CB/CNF-based inks

This section examines the formulation of hybrid CB/CNF inks for fabricating printed sensors. This hybrid approach is expected to yield more reliable and sensitive sensors compared to those made with CNF alone.

Similar to the development of CB/CNTSA-based inks, the CNC and CB-to-CNF ratios kept constant at 4.0 and 4.0:2.0 wt.%, respectively. In the previous sections, the addition of IPA to water-based inks enhanced printability by reducing surface tension and wettability and accelerating drying, whereas the addition TX-100 influenced the printing quality and rheology. Therefore, in this work, the water/IPA ratio was kept constant at 70/30, while the TX-100 concentration was varied, as detailed in Table 4.10, following the development approach used for the CB/CNTSA-based ink.

Table 4.10 : Composition details of CB/CNF/CNC ink formulations with varying TX-100 concentrations.

Carbon name	Carbon nanomaterials		Surfactant		Solvent mixture
	CB (wt.%)	CNF (wt.%)	CNC (wt.%)	TX-100 (wt.%)	Water/IPA ratio
CB/CNF-0	4.0	2.0	4.0	0.0	70/30
CB/CNF-3	4.0	2.0	4.0	3.0	70/30
CB/CNF-6	4.0	2.0	4.0	6.0	70/30
CB/CNF-9	4.0	2.0	4.0	9.0	70/30

Figure 4.27 shows the printing results of CB/CNF-based inks with varying TX-100 ratios. Unlike CB/CNTSA-based inks, minimal ink bleeding occurred even before the

addition of TX-100, possibly due to the formation of large CNF aggregates, which may have hindered ink flow during printing. At TX-100 ratios of 3 wt.% and higher, this slight ink bleeding disappeared. As discussed earlier, TX-100 alone could not effectively disperse CNFs. Therefore, the slight improvement observed after adding TX-100 is likely due to the interaction between CB and TX-100, as well as TX-100's ability to modify the ink's surface tension. Furthermore, as shown in Table 4.11, the line width remained relatively unchanged with increasing TX-100 ratio, indicating that further increase in the TX-100 ratio unaffected rheological behavior of the ink.

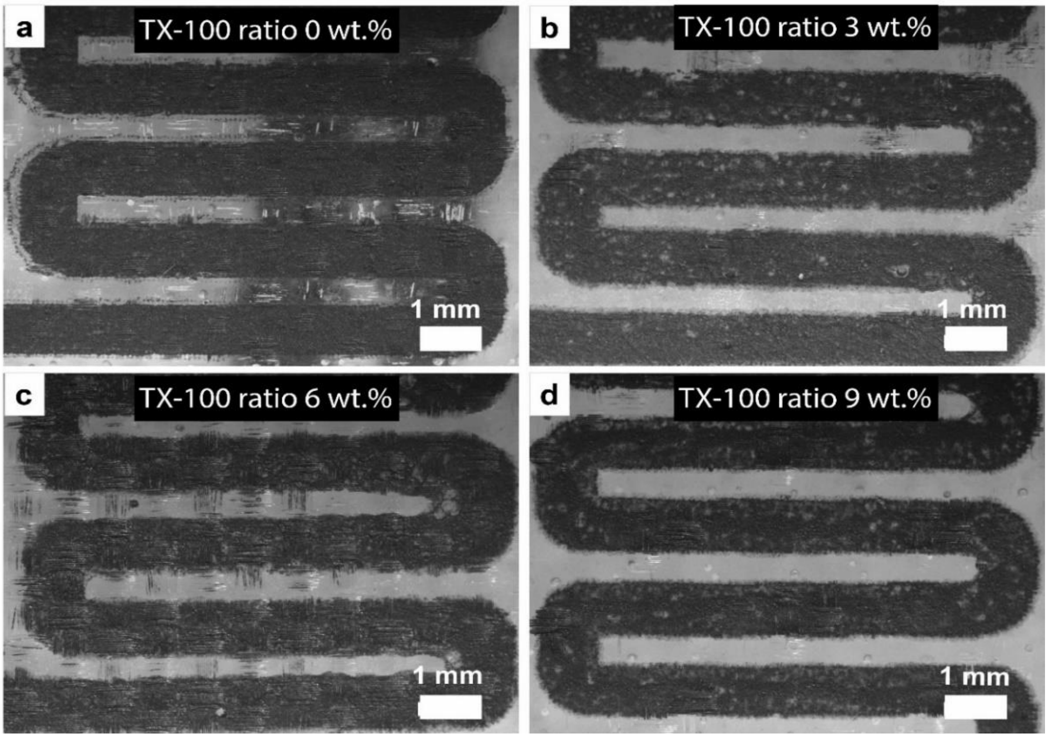

Figure 4.27 : Light microscope images of printed CB/CNF/CNC/TX-based ink with TX-100 ratios of a) 0, b) 3, c) 6, and d) 9 wt.%.

The electrical resistance of CB/CNF-based sensors with varying TX-100 ratios exhibited different behavior compared to CB/CNTSA-based sensors. At TX-100 ratios of 0 and 3 wt.%, the measured electrical resistance of the single-layer CB/CNF-based sensors overlapped, indicating that the slight increase in TX-100 had minimal impact on the conductive pathway. However, further increases in TX-100 led to a rise in electrical resistance, as detailed in Table 4.11. The interactions between CB and CNF, as well as between CNF and TX-100, likely played a significant role in determining the electrical resistance after the addition of TX-100. It has been reported that excess TX-100 can increase electrical resistance by forming isolating layers between conductive particles [310,311].

Table 4.11 : Rheological and printing properties of the CB/CNF-based inks.

Ink content	Shear viscosity (Pa·s)	Viscosity recovery rate after 10 sec (%)	Viscosity recovery rate after 100 sec (%)	G''/G' ratio	Line width (mm)	R_0 (kΩ)
CB/CNF-0	578 ± 57	18 ± 5	46 ± 7	0.20 ± 0.03	896 ± 29	312 ± 76
CB/CNF-3	258 ± 85	26 ± 6	41 ± 10	0.44 ± 0.03	937 ± 48	279 ± 55
CB/CNF-6	278 ± 10	30 ± 2	53 ± 9	0.40 ± 0.01	977 ± 33	313 ± 50
CB/CNF-9	293 ± 37	38 ± 3	67 ± 5	0.40 ± 0.03	924 ± 45	782 ± 64

To better understand the interactions between CB and CNF, as well as between CNF and TX-100, rheological properties were evaluated. The complex modulus decreased notably at a TX-100 ratio of 3 wt.%, as shown in Figure 4.28a. This decrease could be attributed to the disentanglement of CB and CB/CNF, and to a lesser extent, the disentanglement of CNFs. However, further increases in the TX-100 ratio resulted in only a slight decrease in complex modulus. Within the LVR region, as calculated and shown in Figure 4.28b, the addition of TX-100 increased the G''/G' ratio, indicating that TX-100 promotes a more liquid-like ink consistency. This results in a less cohesive ink, thereby facilitating the screen printing process [268,295].

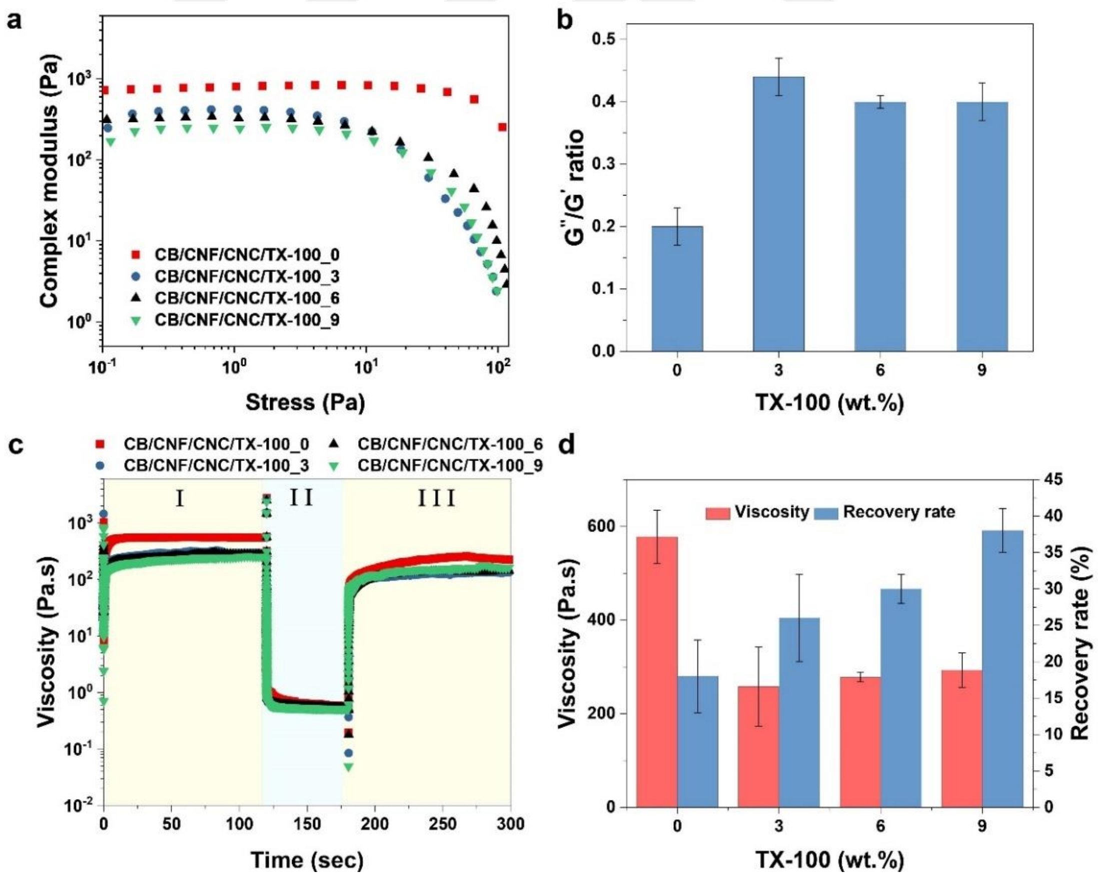

Figure 4.28 : Influence of CB/CNF/CNC/TX-100 ink formation with varying TX-100 concentrations (0, 3, 6, and 9 wt.%) on: a) complex modulus, b) G''/G' ratio, c) screen printing simulation, and d) viscosity and recovery rate.

Screen printing simulation results are summarized in Figure 4.28c. Shear viscosity dropped significantly after the addition of TX-100, which was attributed to the enhanced dispersibility discussed earlier [302], similar to the behavior observed in CB/CNT-based inks with varying TX-100 ratios. No significant decrease in viscosity was noted once the TX-100 ratio reached 3 wt.%, suggesting saturation. However, as with CB/CNT-based inks, the reduction in viscosity after the addition of TX-100 led to an increase in recovery rate after 10 and 100 seconds, as calculated in Table 4.11. On average, the recovery rate values for CB/CNF-based inks were lower than those for CB/CNT-based inks. Associating these results with the printability outcomes shown in Figure 4.27, it becomes evident that the improvement seen at the TX-100 ratio of 3.0 wt.% persisted at higher ratios due to the enhanced recovery rate and reduced surface tension [306,307]. The overall moderate recovery rate was mainly attributed to the presence of high-aspect-ratio CNFs [296], and to a lesser extent, the lower-aspect-ratio CB and CNC particles[143,293].

The resistance of the CB/CNF single-layer print increased with the addition of TX-100, as shown in Table 4.11. The difference in aspect ratio between CNTs and CNFs could explain why TX-100 decreased resistance in CB/CNT-based inks but increased it in CB/CNF-based inks. The higher aspect ratio of CNTs allows for better percolation and improved conductive pathways, whereas the lower aspect ratio of CNFs may lead to increased interparticle spacing, disrupting conductivity.

Figure 4.29a illustrates the surface morphology of two layers printed using CB/CNF/CNC/TX ink with a weight ratio of 4.0:2.0:4.0:6.0. Similar to the CB/CNTSA-based sensor, the CB/CNF-based sensor effectively covers the surface of the host GFRP composite. In Figure 4.29b, CNFs are visible within the CB and CNC matrix, indicating their integration into the printed structure. This distribution suggests the role of CNFs in reinforcing the network formed by CB and CNC particles within the sensor.

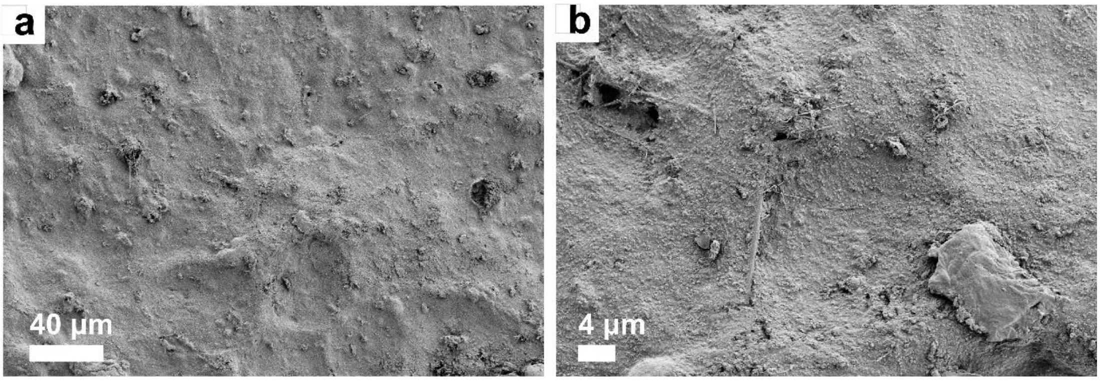

Figure 4.29 : Morphology of two-layer CB/CNF-based sensor under two magnifications: a) 1K and b) 5K.

4.3 Spray Printing: Viscosity Limits, Print Quality, and Characterization

In this section, the formulation and characterization of three different carbon-based inks, CNTNC, CB, and CB/CNTNC hybrid inks, are presented for spray printing applications. The primary goal is to develop ink systems with optimized droplet formation to achieve uniform coatings on GFRPs. Spray printing requires precise control over ink properties such as viscosity (influenced by solid content), volatility (determined by the solvent mixture), and particle dispersion (managed by surfactants) to prevent issues like nozzle clogging, uneven coverage, or overspray. To address these challenges, the ink formulations were systematically adjusted by varying the ratios of carbon nanomaterials, surfactants, and solvents. Through this fine-tuning, the sprayability and coating uniformity of each ink were enhanced, enabling controlled deposition with minimal defects across the substrate surface.

4.3.1 CNTNC/CNC-based inks

In order to assess the sprayability of CNTNC-based inks, CNTNC was dispersed in water/IPA mixture using CNC and TX-100 as co-surfactants.

In the initial phase of this study, various CNTNC-based ink formulations were prepared and evaluated in terms of their rheological properties and sprayability. The primary goal was to determine an optimal composition that achieves both good printability and desirable electrical performance. For this, several ink compositions were tested with varying CNTNC, CNC, and TX-100 concentrations while maintaining a fixed water/IPA (70:30) solvent ratio. Seven inks were spray-printed as detailed in Table 4.12.

Table 4.12 : Composition details of CNTNC/CNC ink formulations used for spray printing.

Carbon nanomaterials	Surfactant		Solvent mixture
CNTNC (wt.%)	CNC (wt.%)	TX-100 (wt.%)	Water/IPA ratio
0.25	0.25	0.25	70/30
0.5	0.5	0.5	70/30
0.75	0.75	0.75	70/30
1.0	1.0	1.0	70/30
0.75	0.75	0	70/30
0.75	0.75	0.25	70/30
0.75	0.75	0.5	70/30

The influence of CNTNC/CNC/TX-100 ink concentration on printing quality using a line pattern is shown in Figure 4.30. Results indicate that increasing the ink concentration improved print quality. At 0.25:0.25:0.25 wt.%, the printed lines exhibited irregularities and poor uniformity. As the concentration increased to 0.50:0.50:0.50, overall printing quality improved, though some irregularities remained. However, at 0.75:0.75:0.75 and 1.00:1.00:1.00, the printed structures became more uniform, making these formulations promising candidates for further investigation.

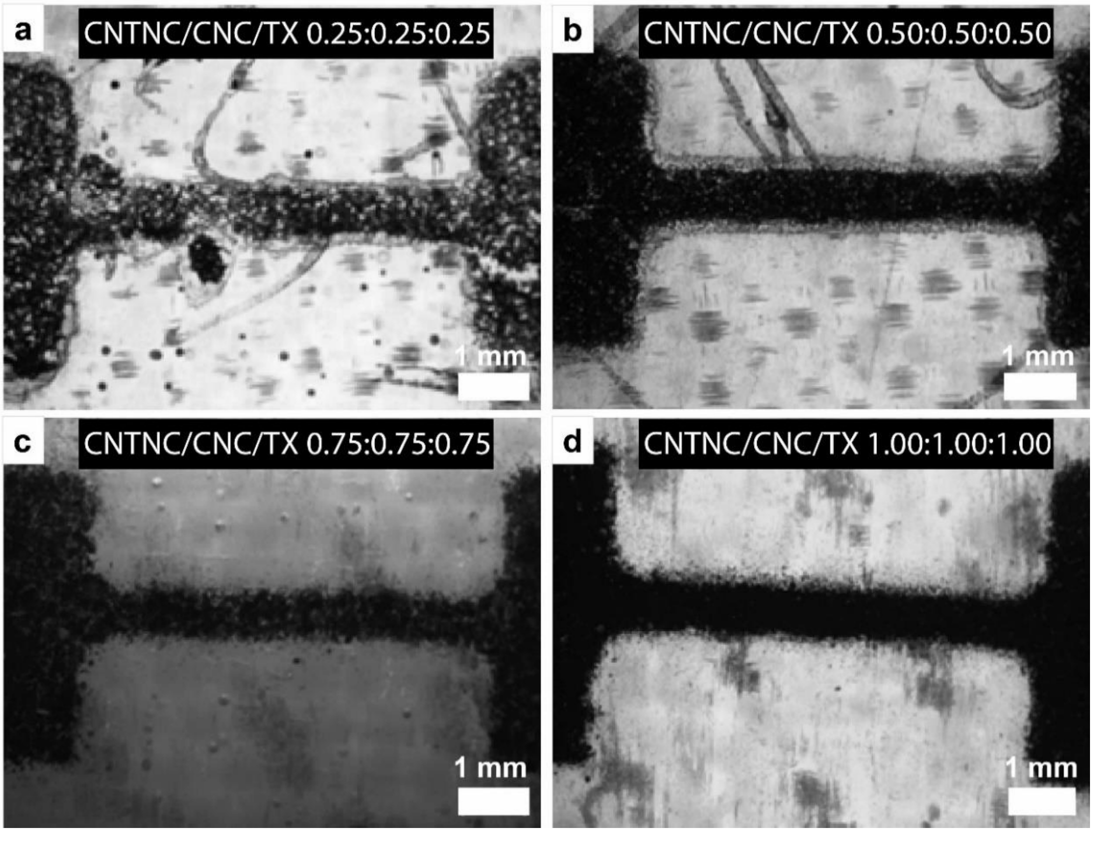

Figure 4.30 : Light microscope images of printed CNTNC/CNC/TX-based inks in two layers with total ratios of a) 0.25:0.25:0.25, b) 0.50:0.50:0.50, a) 0.75:0.75:0.75, and a) 1.00:1.00:1.00.

All the inks exhibited shear-thinning behavior, as shown in Figure 4.31. This behavior is beneficial for spray printing, as it allows the ink to flow more easily under shear stress. As the total CNTNC/CNC/TX-100 concentration increased, the viscosity also increased, with measured values of 7.52 ± 1.24, 27.39 ± 4.81, 43.41 ± 9.12, and 111.82 ± 12.93 Pa·s. The 0.75:0.75:0.75 wt.% ink was selected for further evaluation as it achieved a good balance between printability and uniformity.

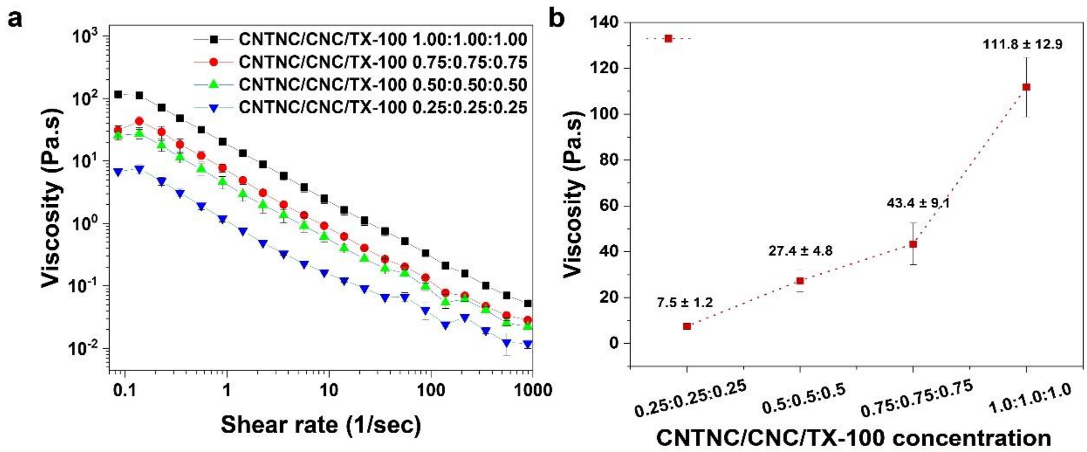

Figure 4.31 : a) Shear viscosity as a function of shear rate for different CNTNC/CNC/TX-100 formulations: 1.00:1.00:1.00, 0.75:0.75:0.75, 0.50:0.50:0.50, and 0.25:0.25:0.25 wt.%. b) Average viscosity values of the same ink formulations were measured at a shear rate of 1 s^{-1} as a function of solid content.

To further improve printing quality, the concentration of TX-100 was varied from 0.00 to 0.75 wt.. in CNTNC/CNC ink with a ratio of 0.75:0.75. Corresponding printed inks in five layers are shown in Figure 4.32. Since TX-100 played a key role in modifying the viscosity and stability of the ink, a systematic variation of its content was conducted to investigate its effect on rheological behavior and spray printing performance. A grid pattern was selected for this evaluation, as it was more challenging to print due to the lines being close to each other, requiring more precise control over the deposition process.

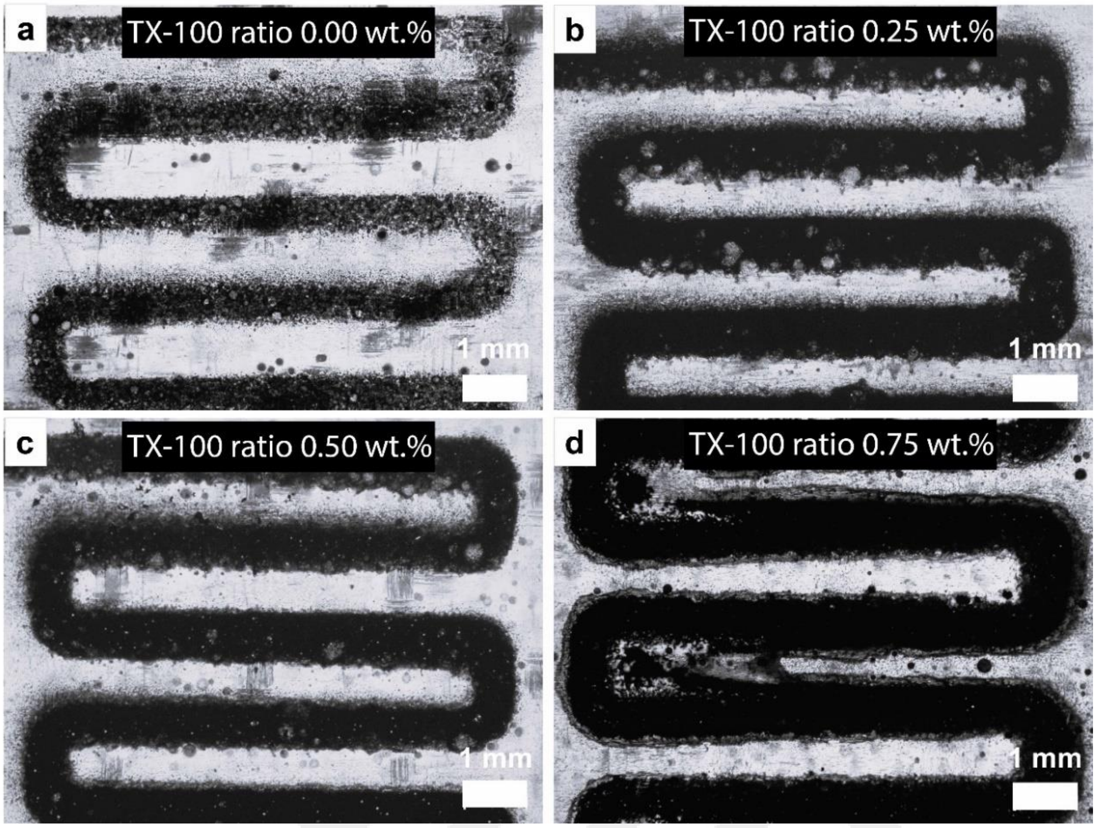

Figure 4.32 : Light microscope images of CNTNC/CNC ink at a 0.75:0.75 ratio, showing the effect of TX-100 addition on printability at the following ratios: a) 0.00, b) 0.25, c) 0.50, and d) 0.75 wt.%.

As the concentration of TX-100 increased, a clear improvement in print quality and uniformity was observed. At 0.00 wt.% TX-100, the printed pattern exhibited significant surface defects, including discontinuities and irregular deposition, indicating inadequate wetting and dispersion stability. Introducing TX-100 at 0.25 wt.% improved the print quality slightly, though visible voids and non-uniformities persisted. Increasing the TX-100 concentration to 0.50 wt.% resulted in a more consistent deposition with fewer voids and enhanced uniformity, although some imperfections remain. The highest TX-100 concentration (0.75 wt.%) resulted in excessive ink spreading, leading to irregular edges and reduced printing resolution. Reducing the TX-100 concentration to 0.5 wt.% improved the uniformity of the printed structures, with smoother edges and fewer defects.

Electrical resistance measurements further supported these observations. Before the addition of TX-100 (0.00 wt.%), the printed structures exhibited a high resistance of 329 ± 168 kΩ, indicating poor conductivity. With the introduction of TX-100 at 0.50 wt.%, resistance decreased drastically to 15 ± 6 kΩ, while at 0.25 wt.%, it further improved to 14 ± 2 kΩ. This significant reduction in resistance was attributed to enhanced dispersion and improved connectivity of conductive pathways. This reduction is attributed to the enhanced dispersibility of CNTNCs, improving network formation [310,311]. Orrill et al. argued that although TX-100 has a much higher resistivity than individual CNTs, the reduction in electrical resistance in CNT-based films after adding TX-100 was due to the increased contact area between adjacent CNTs facilitated by the TX-100 molecules [312]. Hence, given the poor electrical performance and structural inconsistencies at 0.00 wt.%, this condition was eliminated from further evaluation. Based on these findings, a TX-100 concentration of 0.50 wt.% was selected for further testing.

The effect of TX-100 concentration on the viscosity of CNTNC/CNC/TX-100-based inks was systematically investigated to determine the optimal formulation for spray printing applications. As shown in Figure 4.33, increasing the concentration of TX-100 progressively decreased the viscosity of the ink, ranging from 81.9 ± 8.4 Pa·s at 0 wt.% TX-100 to 43.4 ± 9.1 Pa·s at 0.75 wt.% TX-100. This reduction in viscosity can be attributed to the surfactant's ability to improve dispersion and lower surface tension, enhancing the ink’s flow characteristics. TX-100 with weight ratio of 0.5 wt.% was identified as the most favorable concentration, achieving a balance between printability, viscosity control, and ink stability essential for achieving high-quality printed patterns.

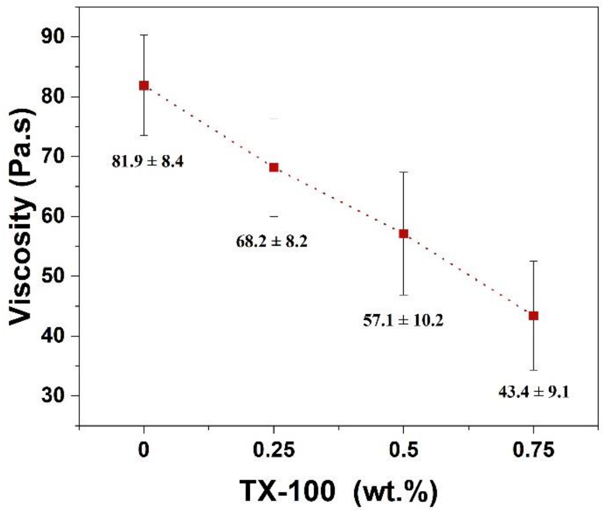

Figure 4.33 : Influence of varying TX-100 on shear viscosity measured at a shear rate of 1 s^{-1}.

In addition to modifying the TX-100 concentration, mask thickness was assessed as another key parameter influencing print uniformity, and electrical resistance of the spray-printed grid patterns. By adjusting the mask thickness, the deposition rate and overall film morphology were controlled to optimize the printed structures.

In the initial phase of our experiments, spray printing was performed using a 0.4 mm thick mask. However, it was observed that this thin mask did not adhere well to the composite substrate, leading to significant ink spreading and poor pattern definition. Due to poor contact between the mask and the substrate, the ink likely spread beyond the intended boundaries, resulting in inconsistent deposition and reduced print quality. To address this issue, additional masks with thicknesses of 0.8 mm, 1.2 mm, 1.6 mm, and 2.0 mm were fabricated and tested using the CNTNC/CNC-TX-100 0.75:0.75:0.5 ink formulation. The printing quality for each mask is summarized in Figure 4.34. The 0.4 mm mask resulted in the lowest print quality, with substantial ink spreading. After testing the thicker masks, it was found that there was minimal improvement in print quality beyond the 1.2 mm mask. Therefore, the 1.2 mm mask was selected for further experiments, ensuring better repeatability in results and providing a more consistent foundation for preparing sensors for electromechanical testing.

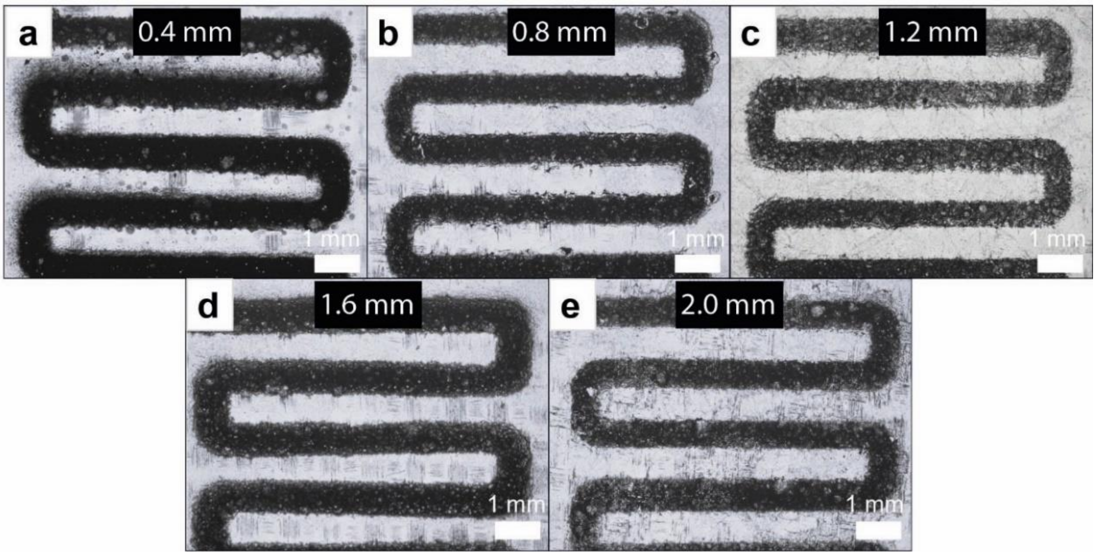

Figure 4.34 : Influence of mask thickness on spray-printed grid patterns applied in five layers. The patterns were printed using varying mask thicknesses: a) 0.4 mm, b) 0.8 mm, c) 1.2 mm, d) 1.6 mm, and e) 2.0 mm.

The effect of layer count on electrical resistance was analyzed for the 0.75:0.75:0.5 ink formulation. As shown in Figure 4.35, resistance progressively decreased with increasing layers. However, beyond the eighth layer, the reduction in resistance becomes negligible, with only minor variations observed. This suggests that the conductive pathways have reached saturation, where further deposition no longer significantly improves electrical properties. At this stage, excessive layering may lead to unnecessary material consumption, longer processing times, and potential mechanical instability. Based on these findings, an eight-layer deposition is identified as the optimal balance between electrical performance and fabrication efficiency for CNT-based inks.

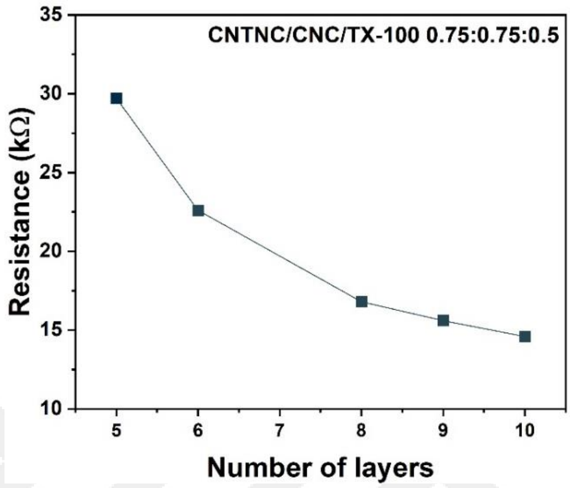

Figure 4.35 : Effect of layer count on electrical resistance for the CNTNC/CNC/TX-100 0.75:0.75:0.5 ink formulation.

The light microscope image in Figure 4.36 confirms that the optimized parameters produce printed structures with well-defined edges, uniform deposition, and minimal defects. To assess the reproducibility of the fabrication process, five sensors were manufactured, and their average electrical resistance was measured at 15.5 ± 1.5 kΩ. Using the optimized deposition strategy, line, grid, and omnidirectional patterns were successfully fabricated for electromechanical testing and evaluation.

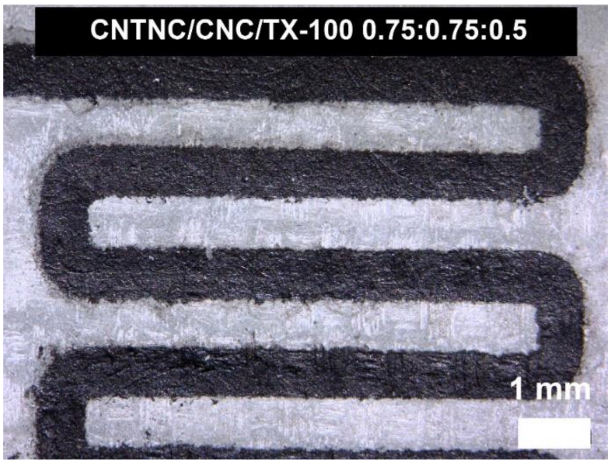

Figure 4.36 : Light microscope image of the spray-printed sensor using an 8-layer CNTNC/CNC/TX-100 0.75:0.75:0.5 ink formulation, exhibiting well-defined edges, uniform deposition, and minimal defects.

4.3.2 CB-based inks

To assess the sprayability of CB-based inks, CB was dispersed in a water/IPA mixture using CNC and TX-100 as co-surfactants. This section focuses on the development, formulation, and characterization of these CB-based inks.

Various formulations of CB-based inks were prepared to investigate the effect of surfactant concentration (TX-100 and CNC), solvent composition (water/IPA ratio), and solid content (CB ratio) on the printability and rheological properties of the ink. The decision to work with these specific concentrations was driven by preliminary experiments. The formulations are detailed in Table 4.13.

Table 4.13 : Composition details of CB/CNC-based inks used for spray printing.

Carbon nanomaterials	Surfactant		Solvent mixture
CB (wt.%)	**CNC (wt.%)**	**TX-100 (wt.%)**	**Water/IPA ratio**
5.0	2.0	3.0	70/30
5.0	2.0	3.0	90/10
5.0	2.0	3.0	50/50
10.0	4.0	6.0	80/20

When the 5.0:2.0:3.0 (CB/CNC/TX-100 wt.%) ink was applied in eight layers, the printed patterns showed spreading and poor edge definition, as seen in Figure 4.37a. After adjusting the water/IPA ratio to 90/10 while maintaining the same solid content, the formulation still resulted in spreading and failed to produce a well-defined pattern on the substrate under identical spray printing conditions, as shown in Figure 4.37b.

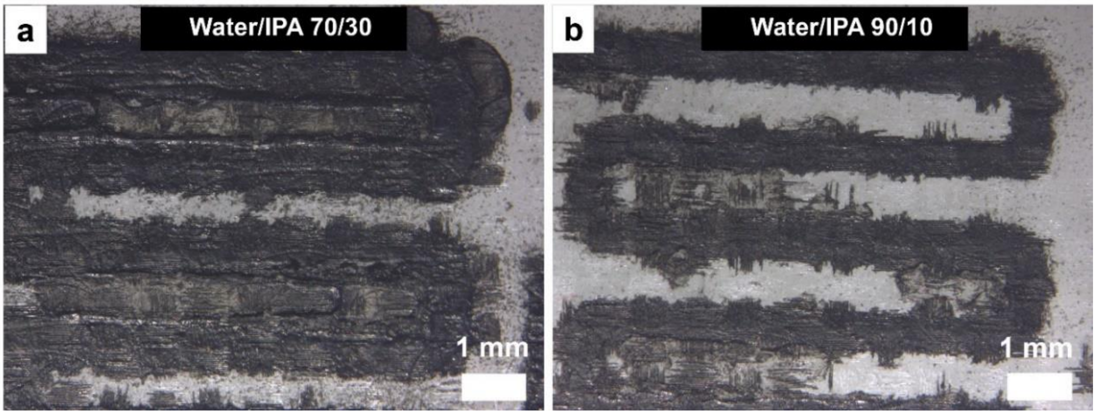

Figure 4.37 : Light microscope images of spray-printed CB/CNC/TX-100 inks (5.0:2.0:3.0 wt.%) using a 1.6 mm mask and 8-layer deposition: a) prepared in 70:30 water/IPA, and b) prepared in 90:10 water/IPA.

To improve print transfer, the water/IPA ratio was adjusted to 50/50 while maintaining the same solid content (5.0:2.0:3.0). This change resulted in improved print quality with acceptable resolution, as seen in Figure 4.38. However, post-print electrical characterization revealed that the resistance remained unacceptably high, reaching up to 800 kΩ after eight printed layers.

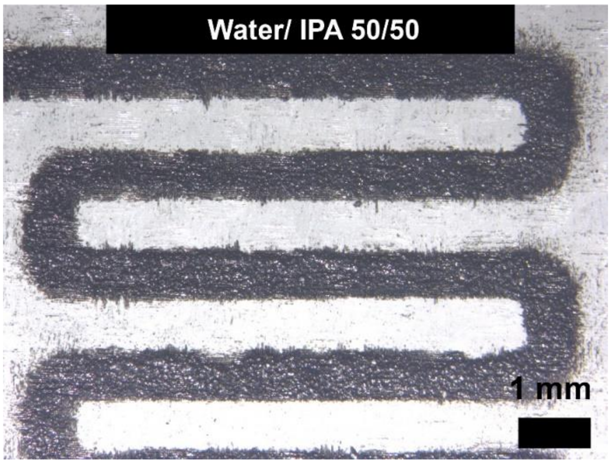

Figure 4.38 : Light microscope image of the spray-printed sensor using an 8-layer CB/CNC/TX-100 10.0:2.0:3.0 and 50/50 water/IPA ratio formulation.

To address this issue, both the solid content and solvent ratio were re-optimized. A final ink formulation of 10.0:4.0:6.0 (CB/CNC/TX-100 wt.%) was prepared in an 80/20 water/IPA mixture. As shown in Figure 4.39, this formulation yielded consistent printing. The printed structures exhibited good pattern definition and adequate conductivity. The use of water/IPA was effective in enabling sharper pattern edges and reducing ink bleeding.

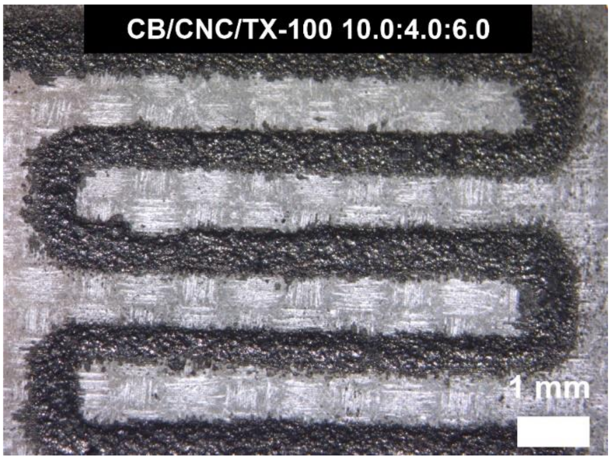

Figure 4.39 : Light microscope image of the spray-printed sensor using CB/CNC/TX-100 10.0:4.0:6.0 and 80/20 water/IPA ratio formulation.

Following the initial printability evaluations, a layer-by-layer optimization study was conducted using the 10.0:4.0:6.0 (CB/CNC/TX-100 wt.%) ink dispersed in an 80/20 water/IPA medium. Spray printing was performed, with even-numbered layer counts ranging from 6 to 16 layers. The electrical resistance of the printed patterns was measured after each deposition cycle to assess the effect of layer number on conductivity, as seen in Figure 4.40. These results indicate that while the majority of the resistance drop occurred within the first few additional layers, resistance values began to stabilize at around 14 layers, suggesting that 16 layers may represent a saturation point for electrical performance under these conditions. Using the optimized deposition strategy, line, grid, and omnidirectional patterns were successfully fabricated for electromechanical testing and evaluation.

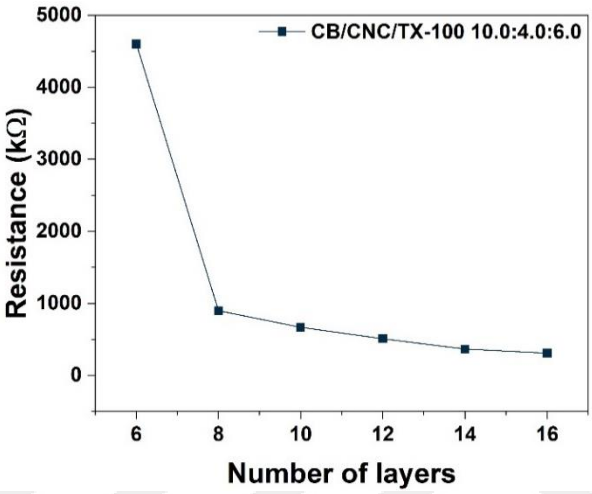

Figure 4.40 : Effect of layer count on electrical resistance for the CB/CNC/TX-100 10.0:4.0:6.0 ink formulation.

4.3.3 CB/CNTNC-based inks

In order to assess the sprayability of hybrid inks, CB/CNTs were dispersed in water/IPA mixture using CNC and TX-100 as co-surfactants.

Based on previous findings, only one ink formulation, the hybrid CB/CNTNC-based ink, was sufficient to achieve successful printing. In the following section, the hybrid ink formulation consisting of CB/CNTNC/CNC/TX-100 at a ratio of 1.0:0.5:1.0:1.5 was evaluated. This formulation was derived by reducing the component ratios used in the screen-printing inks by one-fourth, aiming to maintain similar solid ratios. The ink was spray-printed using the grid pattern and exhibited well-defined features with minimal defects, as shown in Figure 4.41.

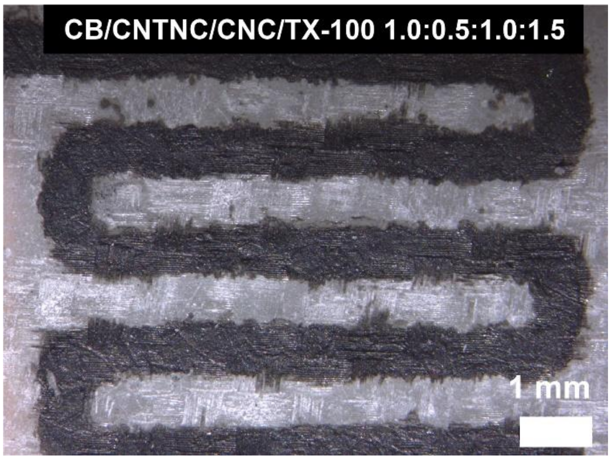

Figure 4.41 : Light microscope image of the spray-printed sensor using CB/CNTNC/CNC/TX-100 1.0:0.5:1.0:1.5 (wt.%) and water/IPA 80/20 ratio formulation.

The shear viscosity behavior of the hybrid ink is shown in Figure 4.42, displaying the expected shear-thinning behavior.

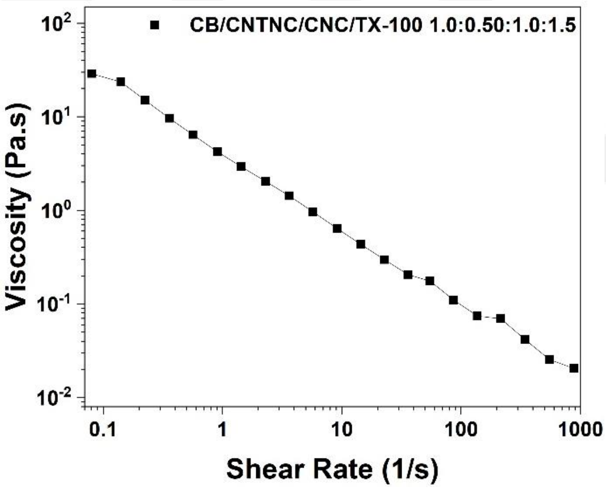

Figure 4.42 : Shear viscosity of the hybrid CB/CNT/CNC/TX-100: 1.0:0.50:1.0:1.5 ink formulation.

To optimize the initial resistance of the grid pattern, Figure 4.43 illustrates the relationship between the number of deposited layers and the measured electrical resistance for the hybrid ink formulation CB/CNTNC/CNC/TX-100 (1.0:0.5:1.0:1.5). The resistance decreased with an increasing layer count, indicating that the initial layers contribute most effectively to establishing conductive pathways. After reaching 6 layers, the rate of resistance reduction became more gradual and eventually plateaued around 8 layers. Beyond this point, further increase in the number of layers (10 and 12 layers) did not significantly improve conductivity. Based on these findings, the optimal layer deposition for the hybrid ink formulation appeared to be around 8 layers. Using this deposition strategy line, grid, and omnidirectional patterns were successfully fabricated.

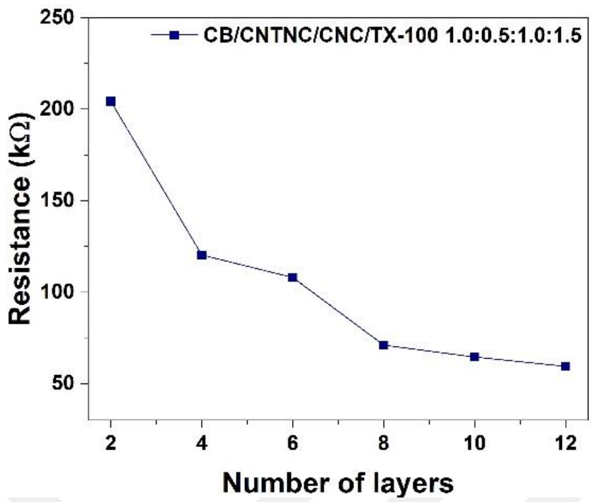

Figure 4.43 : Electrical resistance of printed CB/CNTNC/CNC/TX-100 with a ratio of 1.0:0.5:1.0:1.5 as a function of the number of layers.

4.4 Overview of Printing Methods and Sensor Abbreviations for Further Testing

Three different printing methods were considered: coating, screen printing, and spray printing. Coating with a roller tool onto GFRPs was not optimal due to limited control over printing quality, despite the simplicity of the method. Additionally, no specific geometry could be printed. In contrast, screen printing provided better control over sensor geometry, allowing for the printing of various carbon-based inks after optimization. However, a drawback of this method is that multiple layers may be required to achieve acceptable electrical resistance, which could result in the printed line width being larger than the original design. The spray printing method, on the other hand, mitigates this issue by using a mask, ensuring that the line width stays closer to the original design. Additionally, spray printing is scalable and can be easily integrated into the aerospace industry. Figure 4.44 shows a comparison between the CNTNC-based sensors printed using the screen and spray printing methods, highlighting the difference in line width.

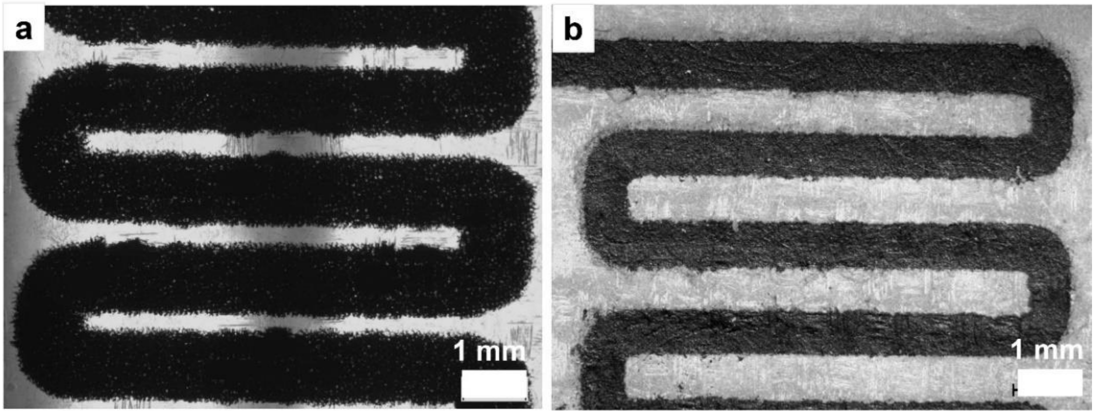

Figure 4.44 : Comparison of CNTNC-based sensors printed using a) screen and b) spray printing methods, highlighting differences in line width.

Another key difference between screen and spray printing lies in the viscosity requirements of the inks. Screen-printable inks typically have significantly higher viscosities than those used for spray printing, as the screen printing process requires the ink to maintain its shape and stay within the patterned areas of the mesh during transfer. In contrast, spray-printable inks require lower viscosities to ensure proper atomization and uniform deposition during the spraying process. This distinction is illustrated in Figure 4.45.

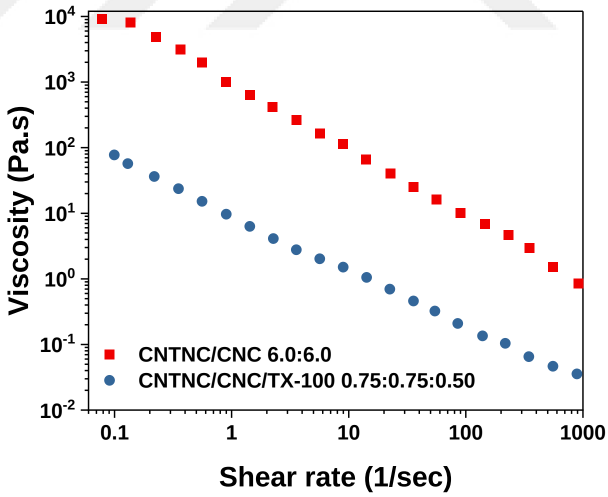

Figure 4.45 : Comparison of ink viscosity of CNTNC inks used for screen spray printing methods.

Using the developed and printable inks, various carbon nanomaterial-based sensors were printed. Table 4.14 presents the solid content and abbreviations of the printed sensors, categorized by the printing method used.

Table 4.14 : Solid content and abbreviations of the printed carbon nanomaterial-based sensors using the developed printable inks, categorized by printing method.

Printing method	Sensor name	Solid content (wt.%)						Surfactants (wt.%)
		CNTSA	CNTNC	Graphene	CNF	CB	CNC	TX-100
Coating	CNTSA/CNC_0.5:0.5	0.5	0.0	0.0	0.0	0.0	0.5	0.0
	CNTSA/CNC_0.8:0.4	0.8	0.0	0.0	0.0	0.0	0.4	0.0
	CNTSA/CNC_0.8:0.8	0.8	0.0	0.0	0.0	0.0	0.8	0.0
	CNTSA/CNC_0.8:4.0	0.8	0.0	0.0	0.0	0.0	4.0	0.0
Screen printing	CNTSA	6.0	0.0	0.0	0.0	0.0	6.0	0.0
	CNTNC-2	0.0	2.0	0.0	0.0	0.0	2.0	0.0
	CNTNC-6	6.0	0.0	0.0	0.0	0.0	6.0	0.0
	Graphene	0.0	0.0	10.0*	0.0	0.0	6.0	0.0
	CB	0.0	0.0	0.0	0.0	10.0	4.0	6.0
	CB/CNTSA-6	2.0	0.0	0.0	0.0	4.0	2.0	0.0
	CB/CNTNC-6	0.0	2.0	0.0	0.0	4.0	4.0	6.0
	CB/CNF-6	0.0	0.0	0.0	2.0	4.0	4.0	6.0
Spray printing	CNTNC_sprayed	0.0	0.75	0.0	0.0	0.0	0.75	0.5
	CB_sprayed	0.0	0.0	0.0	0.0	10.0	4.0	6.0
	CB/CNTNC_sprayed	0.0	0.5	0.0	0.0	1.0	1.0	1.5

* According to the manufacturer.

5. ELECTROMECHANICAL ANALYSIS OF CARBON-BASED SENSORS

5.1 Electrical Properties

5.1.1 Electrical properties of non-patterned sensors: A direct application onto GFRPs

Conductive paths formed by CNTs can be categorized into two types: i) overlapping contacts and ii) in-plane contacts [189]. Overlapping contacts encompass all possible tunneling junctions between two CNTs; however, expect tip-to-tip contacts, which belong to the in-plane contacts. Previously, it was demonstrated that CNCs attach to the sidewall of an MWCNT [146,148]. By considering the large aspect ratio of CNTs (length to diameter ratio, which is more significant than 650 in this study), it is attributed that CNCs are less likely to attach to the tips of a CNT. As a result, the presence of CNCs alters the number of overlapping contacts without disturbing in-plane contacts, and CNCs affect the resistance of the CNT/CNC hybrid network (notice not the intrinsic resistance of individual CNT) by altering the tunneling distance.

Through this approach, a series of sensors with varying CNTSA/CNC compositions were prepared to investigate their impact on the conductive paths and resistance characteristics. The compositions used in the fabrication of these sensors were as detailed in Table 4.14.

The potential of the developed CNTSA/CNC piezoresistive strain sensors were initially studied for their electrical properties and stabilities in the unloading state where no strain or force was applied. First, after subjecting the sensors to different voltages ranging from -10 to 10 V, current-voltage curves were plotted. As shown in Figure 5.1a, all the developed sensors showed linear behavior; ohmic behavior. This desired behavior reflects the sensors' ability to resist constantly when under a wide range of voltages, which is a crucial property for a strain sensor. The initial resistance of CNTSA/CNC_0.8:4.0, 310 ohms, the sensor was almost threefold larger than CNTSA/CNC_0.8:0.4 and CNTSA/CNC_0.8:0.8 with initial resistances of 112 and

108 ohms, respectively. This was attributed to the ability of CNCs to physically decrease the number of available tunneling junctions and increase tunneling distance. This claim is also supported by the morphology analysis carried out in the previous section in a qualitative fashion.

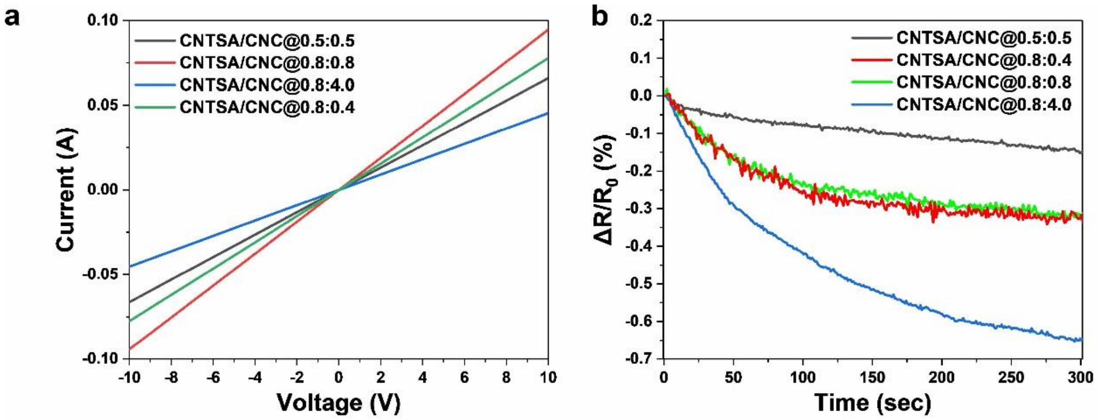

Figure 5.1 : a) Current-voltage curves for the developed sensors and b) electrical stability of the developed sensors in unloading state for a period of time at room temperature.

The stability of sensors was evaluated by applying a constant voltage, 2.1 V as demonstrated in Figure 5.1b. Resistance change as a function of time was plotted for the developed sensors. CNTSA/CNC_0.5:0.5 sensors showed negligible change in resistance, while CNTSA/CNC_0.8:4.0 showed the most significant resistance change over the same period. At room temperature, CNTSA/CNC_0.5:0.5 reached almost immediate stability. However, CNTSA/CNC_0.8:4.0 reached near stability only after 200 seconds.

Furthermore, it was noted that the recorded resistance change was negative, demonstrating that the sensors' conductivity increased after the voltage difference application. Such an increase in conductivity after applying voltage difference has been reported for CNT-based nanocomposite sensors in an earlier report [313]. The increase in conductivity due to applied voltage difference was attributed to the promotion of electron tunneling among adjacent CNT particles, which, in turn, led to a decrease in tunneling resistance, increasing conductivity [314]. The rise in temperature in an individual CNT, as a result of Joule heating, when electric current is applied, supplied sufficient energy for electrons to tunnel between adjacent particles. On the other hand, the stable state of CNTSA/CNC_0.5:0.5 under constant voltage difference was attributed to the ideal number of tunneling junctions between CNTs which promoted negligible change resistance.

Next, the stability of CNTSA/CNC_0.5:0.5 and CNTSA/CNC_0.8:4.0 were also tested at elevated temperatures. Figure 5.2 shows that changes in resistances at room temperature and 40 ˚C for CNTSA/CNC_0.5:0.5 sensors were almost identical. Although the initial resistance dropped when the temperature was elevated, the rate of resistance change was the same, which demonstrates the sensor's ability to function at such an elevated temperature with no difference in performance. The drop in initial resistance was attributed to the enhanced contact between adjacent CNTs because electrons possessed enough energy to jump between neighbor CNTs at a rate similar to when the sample was only subjected to Joule heating. For CNTSA/CNC_0.8:4.0, however, after the sensor was subjected to high temperature, stability was reached faster than when the resistance change was measured at room temperature. This faster stability case was attributed to the enhanced tunneling junctions between adjacent CNTs, which facilitated the electrons to possess enough energy to jump between CNTs faster.

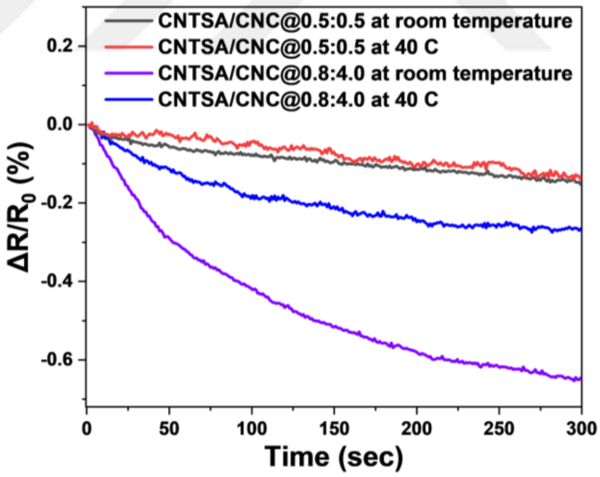

Figure 5.2 : Resistance change during unloading at two different temperatures, room temperature and 40 °C, for CNTSACNC@0.5:0.5 and CNTSACNC@0.8:4.0.

Since a CNC is attached to a CNT at its defect points, mainly sidewalls, not the tip of the CNT (*e.g.*, oxygen presence), and not by creating a new defect nor by altering the nature of the outermost layer of the CNT, it is proposed that CNC does not add additional elastic scattering to electrons when a voltage difference is applied to an individual CNT. Therefore, under applied voltage difference, electrons are only elastically scattered due to the existing defects [315] despite the attraction between

CNCs and the CNT. It was concluded that CNC provides electrical stability when a CNT is subjected to voltage differences. Also, the CNT to CNC ratio plays a role in determining the degree of stability.

It is worth reporting that a preliminary study was carried out to determine whether or not an electrical resistance sampling frequency of 1 Hz was enough to capture the intrinsic changes occurring on the strain during mechanical testing. Using CNTSA/CNC_0.5:0.5 sensors as a reference, cyclic tests were performed by varying electrical resistance sampling frequencies at 1 and 20 Hz. Figure 5.3 shows that by increasing the sampling frequency from 1 to 20 Hz for cyclic tests, the accuracy of the test did not change, emphasizing that 1 Hz was enough to capture the intrinsic changes occurring on the strain during mechanical tests.

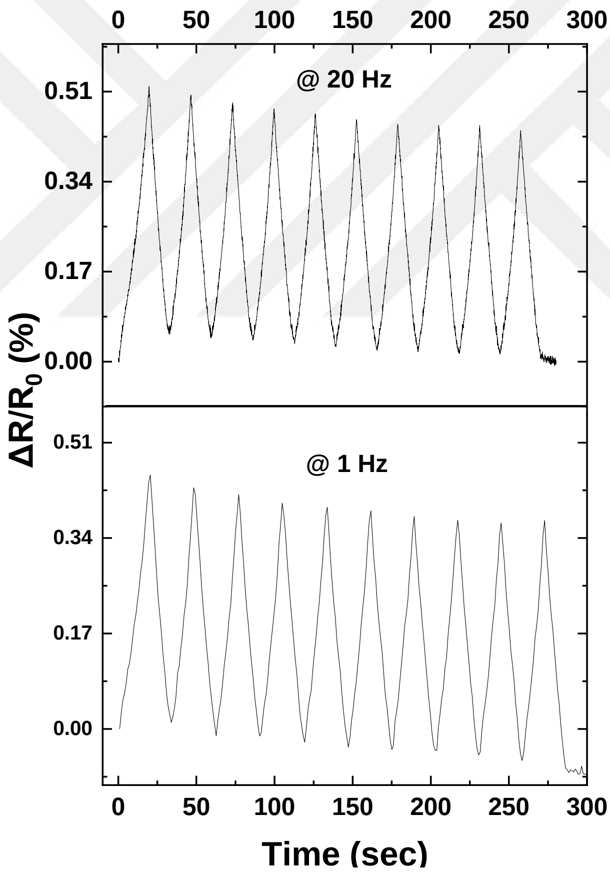

Figure 5.3 : Comparison of cyclic tests at different electrical resistance sampling frequencies (1 Hz and 20 Hz) using CNTSA/CNC_0.5:0.5 sensors.

Based on these discussions, an analytical approach for CNTSA/CNC-based coated onto GFRPs were studied.

The contact resistance between CNTs is usually much higher than the intrinsic resistance of a CNT [183], thus, the resistance of CNT composites can be approximated as

$$R = \frac{M}{N}\frac{h^2 t}{d^2 e^2 \sqrt{2m\chi}} \exp\left[4\frac{\pi t}{h}\sqrt{2m\chi}\right] \quad (5.1)$$

where M, N, h, t, d, e, m, and χ denote number of CNTs in a conductive path, the number of conductive paths, Planck's constant, average tunneling distance, the diameter of CNT, electron charge, the mass of electron, and work function of a CNT, respectively. The attachment of CNCs to a CNT was shown not to increase the intrinsic resistance of a CNT (See section 3.3 Electromechanical analysis), which further justifies ignoring intrinsic resistance in equation 5.1. However, equation 5.1 does not consider the effect of hybridization on the available tunneling junctions. So, by considering the effective length of a CNC and a constant related to the initial content of CNC, the following modification was suggested

$$\frac{M}{N}\frac{d^2}{Z(d+2l_{eff}^{CNC})^2} \quad (5.2)$$

where l_{eff}^{CNC} is the effective length of a CNC, and Z is a constant which depends on the number of CNCs, *i.e.*, concentration and/or agglomeration. l_{eff}^{CNC} is the projection of actual CNC length on the axis, perpendicular to MWCNT, best illustrated in Figure 5.4. l_{eff}^{CNC} was calculated as $l_{eff}^{CNC} = l^{CNC}\sin(ß)$ where l^{CNC} is the average length of a CNC rod, and ß is the average angle between a CNC rod and a CNT, which depends on the surface charge of the CNC and defect sites on the CNT [149]. In this work, as was recently demonstrated that CNCs attach with their tips on MWCNT rather than a perfect alignment [142], therefore, the average ß was accepted to be 45° without considering any other parametric studies.

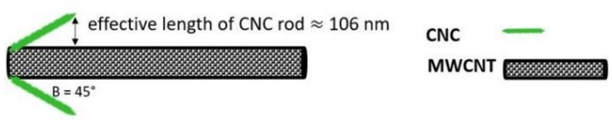

Figure 5.4 : Illustration of the effective length of a CNC rod.

Equation 5.1 can be rewritten to define the resistance as below

$$R = \frac{M}{N}\frac{h^2 t}{Z(d+2l^{CNC}\sin(ß))^2 e^2 \sqrt{2m\chi}} \exp\left[4\frac{\pi t}{h}\sqrt{2m\chi}\right] \quad (5.3)$$

To emphasize the effect of CNC on initial tunneling distance, equation 5.3 was arranged as the following

$$t_0 = \frac{h}{e^2\sqrt{2m\chi}} W\left(e^2\sqrt{2m\chi}\frac{N}{M}\frac{Z\left(d+2l^{CNC}\sin(ß)\right)^2}{h^2}\rho_0\right) \tag{5.4}$$

where $W(x)$ and ρ_0 are the Lambert function [183] and resistivity, respectively. Equation 5.4 shows that the initial tunneling resistance is proportional to the length of the CNC rod, the angle between a CNC and a CNT, and the content of the CNCs. These three parameters affect the tunneling junctions between CNTs.

In literature, change in average tunneling distance, t, has a linear relation with strain. However, in the case of CNT/CNC, it was suggested that change in average tunneling distance has nonlinear relation with strain as the following

$$t = t_0(1 + E\varepsilon^B) \tag{5.5}$$

where ε is strain, and B is constant and is related to the initial CNC content. E is a constant and can be calculated using equation 5.6

$$E = cos^2 a - v\, sin^2 a \tag{5.6}$$

where v is Poisson's ratio which was taken to be 0.31 [316,317] and a is the angle between the direction of strain and tunneling distance [88]. For random orientation of CNTs, the value of a is assumed to be constant during the tensile test and evaluated to be $a = sin^{-1}\frac{\pi}{4}$ [88,187]. The final value of E was calculated to be 0.345.

Change of resistance can be calculated as the following [174].

$$\frac{\Delta R}{R_0} = \frac{R_t}{R_0} - 1 = \left(\frac{\mathrm{t}}{t_0}\right)\exp\left[\frac{4\pi\sqrt{2m\chi}}{h}(t - t_0)\right] - 1 \tag{5.7}$$

It should be emphasized that the terms Z, l^{CNC}, and sin(ß) do not appear in equation 5.7 because they are constants and do not depend on the change in strain. Rearranging equation 5.5 and combining it with equation 5.7, the resistance change was calculated as below

$$\frac{\Delta R}{R_0} = (1 + E\varepsilon^B)\exp\left[\frac{4\pi\sqrt{2m\chi}}{h}t_0 E\varepsilon^B\right] - 1 \tag{5.8}$$

Plugging the value of the constants in equation 5.8 (See Table 5.1), the related calculation is revised as below:

$$\frac{\Delta R}{R_0} = (1 + 0.345\varepsilon^B)\exp[1.58t_0\varepsilon^B] - 1 \quad (5.9)$$

Table 5.1 : Constants and parameters used in modeling.

Constants	h	e	m	χ*	d	l^{CNT}	l^{CNC}
Value	6.62 ×10^{-34}	1.602 ×10^{-19}	9.109 ×10^{-31}	0.2	7.5	5000	150
Unit	Joule-second	Coulombs	Kg	eV	nm	nm	nm

*in absence of polymer matrix, the barrier height was assumed to be 0.2 eV [186,318,319] and to be constant with increase or decrease of CNC.

5.1.2 Electrical properties of patterned sensors: influence of printing layers and applied voltage on stability

In DC mode, many studies only reported the I-V curve as the only tool to test the electrical stability of a piezoresistive strain sensor or to simply measure the initial resistance of the sensor [134,320–322]. Generally, the applied voltage ranges from 0.5 up to 17 V [33,201,323,324]. Only a few efforts have studied the influence of the applied voltage on electromechanical stability of piezoresistive sensor [325,326]. Therefore, a detailed investigation of the sensor's electrical properties was conducted.

To investigate the influence of thickness on sensor performance, the o-line pattern was printed with a total of ten layers using a 6.0:6.0 CNTSA/CNC ink formulation. Resistance was measured after each layer. As shown in Figure 5.5, the decrease in resistance became less significant beyond the fourth layer, suggesting diminishing returns in electrical network improvement with additional layers. This highlights the point at which the electrical network becomes well-established, making further layers unnecessary for improving performance. The decrease of electrical resistance was attributed to enhanced electrical networking and increased CNTs with each additional layer [327]. Similar results were obtained for other patterns as shown in Figure 5.6.

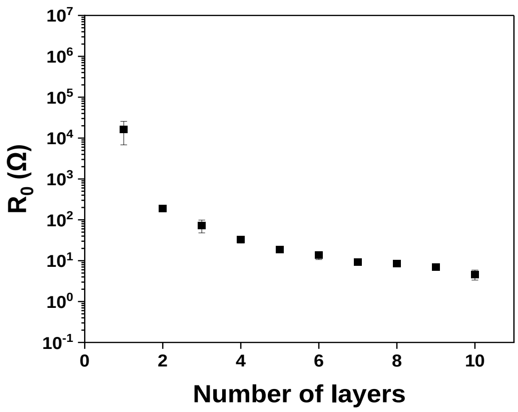

Figure 5.5 : Resistance measurements of a 6.0:6.0 CNTSA/CNC ink formulation printed in o-line patterns with a total of ten layers.

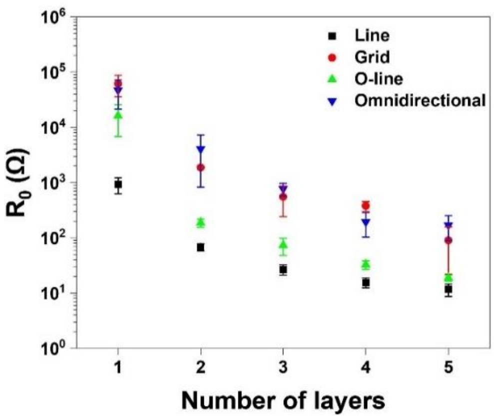

Figure 5.6 : Resistance measurements of a 6.0:6.0 CNTSA/CNC ink formulation printed in line, grid, o-line, and omnidirectional patterns with a total of five layers.

To compare the different patterns discussed in this study, it was necessary to determine the optimal number of printed layers for electrical stability. The grid pattern was chosen to assess electrical stability as a function of the number of printed layers, which ranged from one to five. Figure 5.7a-b shows that electrical signal noise decreased with more printed layers. This improvement in electrical stability corresponded to an improvement in the linearity of the sensors during tensile loading tests, as shown in Figure 5.8a. The one-layer sensor had poor linearity (not calculable), while the five-layer sensor showed the highest linearity.

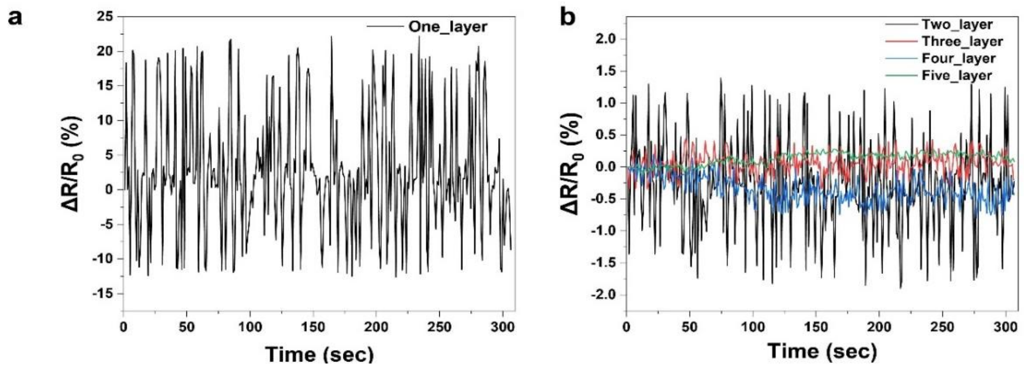

Figure 5.7 : a) Electrical stability of one-layer grid sensor and b) electrical stability of two-, three-, four-, and five-layer grid sensors.

To determine the optimal applied voltage, it was varied between 2 and 32 V, and the electrical stability (b), heat generation (Figure 5.8c), and electromechanical behavior (Figure 5.8d) of the five-layer sensor were analyzed. The findings show that the five-layer sensor maintained stability at low voltages but displayed reduced stability at higher voltages due to heat generated from Joule heating [328–330], which impacted linearity, leading to drifting in electrical resistance despite the applied load. Consequently, the five-layer sensor was identified as the optimal design, balancing electrical stability, minimal noise, and improved linearity at lower voltages, such as 2 V.

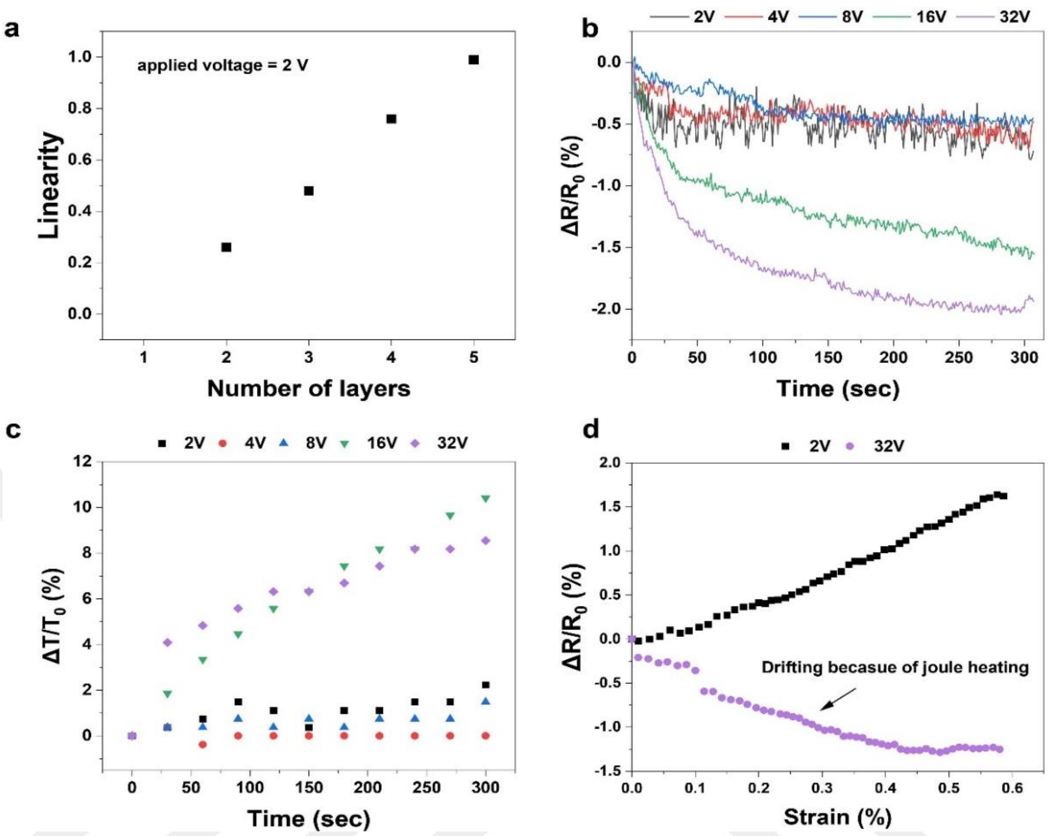

Figure 5.8 : a) Linearity of electrical signal in monotonic tensile tests as a function of printed layer number. Five-layer grid sensor under influence of various voltages: b) electrical stability, c) temperature changes, and d) monotonic tensile tests recorded.

Furthermore, Figure 5.9 illustrates the electrical stability of the five-layer print of the four different patterns at 2 V. All five-layer patterns showed stable electrical response during the 300 seconds.

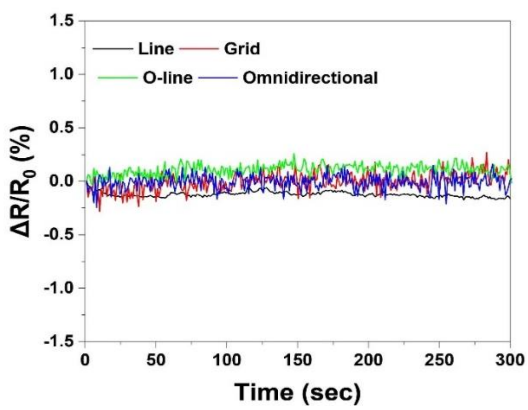

Figure 5.9 : Corresponding electrical stability of five-layer sensors with various patterns at a voltage of 2 V.

5.2 Performance evaluation of CNTSA/CNC-based strain sensors coated onto GFRP

All the performance evaluation of carbon-based sensors was studied by electromechanical testing. Initially, the high-quality CNTs from Sigma Aldrich were studied to determine the compositional analysis for prepared inks. Hence the CNT/CNC at different ratios were studied to achieve the optimal content to be applied as a direct coating onto GFRPs.

5.2.1 Optimizing the CNTSA/CNC formulized inks and their performance analysis

A representative tensile strain graph is shown in Figure 5.10, and other mechanical properties are summarized in Table 3.5. The elastic region of the vacuum-infused GFRP composite was found to extend up between 0.6-0.7 % strain, beyond which a a slight deviation from linearity was observed. This region, extending up to around 1.4% strain, suggests the onset of nonlinear or plastic deformation behavior.

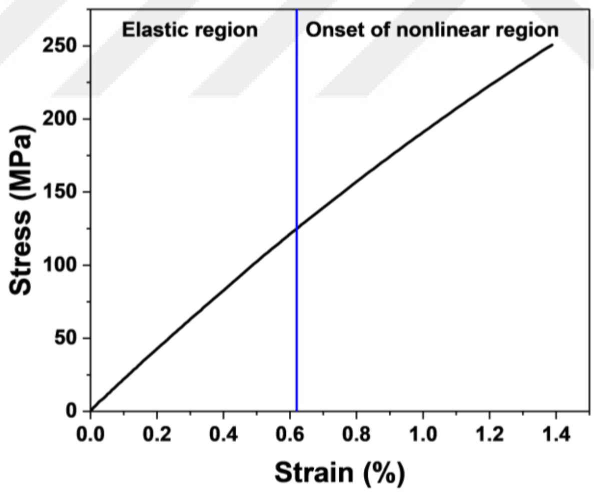

Figure 5.10 : Stress-strain curve of the GFRP coupon under tensile loading.

Four sensors, CNTSA/CNC_0.5:0.5, CNTSA/CNC_0.8:0.4, CNTSA/CNC_0.8:0.8, and CNTSA/CNC_0.8:4.0, at different CNTSA/CNC compositions were selected to be tested for their tensile piezoresistive properties. The piezoresistive behavior was studied under both elastic and plastic deformations. Depending on the CNTSA/CNC composition, different responses were observed. CNTSA/CNC_0.5:0.5 and CNTSA/CNC_0.8:0.8 sensors captured and matched the elastic region of the composite, demonstrating the feasibility of coating application, , as shown in Figure

5.11a-b. The linearity of the sensors, R^2, under the elastic region, was high, as tabulated in Table 5.2. CNTSA/CNC_0.5:0.5 showed a higher gauge factor than CNTSA/CNC_0.8:0.8; 1.0 and 0.7, respectively. The difference between the sensitivity of these two sensors was attributed to the composition of CNTSA/CNC in CNTSA/CNC_0.5:0.5, which is close to the rheological percolation threshold. Similar results were identified in the literature, and it was shown that sensitivity was higher at percolation load, and as the CNT loading increased sensitivity dropped [186,331,332].

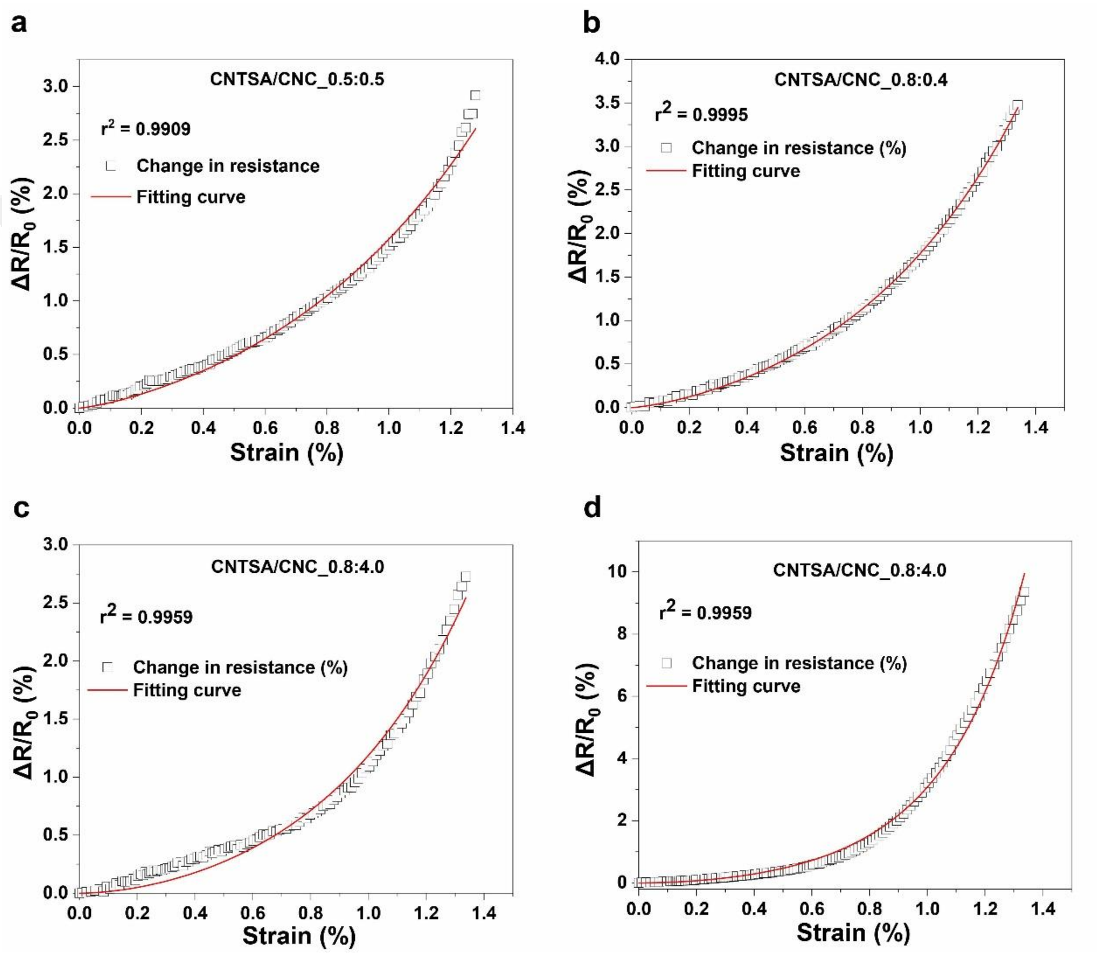

Figure 5.11 : Experimental and theoretical tensile piezoresistive behavior of a) CNTSA/CNC_0.5:0.5, b) CNTSA/CNC_0.8:0.4, c) CNTSA/CNC_0.8:0.8, and d) CNTSA/CNC_0.8:4.0.

When the CNT ratio was fixed at 0.8 wt.%, and the CNC ratio was increased from 0.4 to 4.0 wt.%, CNTSA/CNC_0.8:0.4, CNTSA/CNC_0.8:0.8, and CNTSA/CNC_0.8:4.0 showed distinct piezoresistive behaviors. Initially, CNTSA/CNC_0.8:0.4 and CNTSA/CNC_0.8:4.0 could not capture the entire elastic region of the composite, as shown in Figure 5.11b-c. Only to around 0.30% strain high linearity was maintained. Also, as the CNC composition increased, gauge factors for the elastic region decreased from 0.9 to 0.5. However, an inverse pattern was seen for the calculated maximum gauge factor in the plastic region (1.20-1.35% strain). CNTSA/CNC_0.8:4.0 had the highest gauge factor of 22.2. In literature, at least for the elastic region of CNT nanocomposites, it has been established that the sensitivity increases as CNT load decreases [333] which is the opposite trend we observed as the CNT amount decreased by increasing the CNC loading. This was reconciled as follows.

The conductive network paths in the presence of a high load of CNC subjected to an external strain was thought to mimic that of aligned CNT conductive network paths. To demonstrate, when a plain aligned CNT conductive network is subjected to a strain in the direction of the alignment, the increase in tunneling distance is lower than when the aligned CNT network is subjected to a strain in the transverse direction [334], which leads to lower gauge factors in the alignment direction. Although, in our case, the CNTs were randomly aligned, the dominant contribution in a change in tunneling distance in the network of CNT in the presence of high loads of CNC (*e.g.* CNTSA/CNC_0.8:4.0) was mainly limited to in-plane tunneling. In other words, in-plane contacts aligned with the direction of strain (while relative tunneling distances of in-plane contacts transverse to the applied strain would decrease) exhibit the same change in tunneling distance as aligned CNT contacts. Therefore, in-plane tunneling becomes dominant at high CNC loadings (e.g., CNTSA/CNC_0.8:4.0). This behavior can be quantified by equation 5.10 [335].

$$\mathrm{GF} = (1 + 2v) + \frac{\Delta R}{R_0 \varepsilon} \quad (5.10)$$

The equation describes the influence on the gauge factor as a result of geometrical changes and resistance changes due to changes in tunneling resistance. The geometrical gauge factor was calculated to be 1.62 (for Poisson's ratio of 0.31), which suggests that the piezoresistive change of CNTSA/CNC sensors seen in the elastic region (0-0.6%) could be attributed to mainly geometrical changes. In plastic region, the piezoresistive change could be attributed to a pronounced change in tunneling distance amongst CNT particles [186]. As can be observed in Table 5.2, as CNC content increased gauge factors in plastic region increased. Since a change in piezoresistive in plastic region was attuited to a change in tunneling distance, the increase in gauge factors with increase of CNC content could be presented to the imbalances in CNT network [186,336]. But in here, since CNTs aren't dispersed in a typical polymer matrix here, these imbalances were likely caused by varying CNT contact types formed with different CNC content. This could mean overlapping contacts dominate at low CNC loads, while in-plane contacts become more prevalent at high CNC loads.

The fitting procedure after applying equation 5.9 was performed and resulted in a good match between theoretical and experimental comparison. Using equation 5.9, the average initial tunneling distance, t_0, for the developed sensors was determined, and the results are summarized in Table 5.2. It is important to note that the modeling effort herein emphasizes the relation between the approximated average initial tunneling distance and CNC content rather than the actual or absolute values of tunneling distance. Table 5.2 shows that when the CNT content was constant (0.8 wt.%), approximated tunneling distance for 7 for CNTSA/CNC_0.8:0.4 and CNTSA/CNC_0.8:4.0 increased from 0.4 up to 0.7, respectively. Since the CNCs tend to attach to sidewalls of CNTs rather than to their tips, the increase in average tunneling distance was regarded as an increase in overlapping contacts, while in-plane tunneling distance remained unchanged. We concluded that the tunneling distance is a function of CNC content.

Table 5.2 : Properties and characteristics of the CNTSA/CNC strain sensors coated on GFRPs.

Given name	Gauge factor*		Max. gauge factor* 1.20-1.35% strain [r^2]	Average tunneling distance, t_0, (nm)**	B**
	0-0.30% strain [R^2]	0-0.60% strain [R^2]			
CNTSA/CNC_0.5:0.5	1.0 [0.997]	1.0 [0.997]	7.7 [0.975]	0.4	1.3
CNTSA/CNC_0.8:0.4	0.9 [0.991]	-	6.3 [0.998]	0.4	1.4
CNTSA/CNC_0.8:0.8	0.7 [0.996]	0.7 [0.996]	6.4 [0.993]	0.3	1.8
CNTSA/CNC_0.8:4.0	0.5 [0.998]	-	22.2 [0.999]	0.7	1.9

* Gauge factors were calculated for linear regions
** tunneling distance and B were best fitting results based on equation 5.9.

The value of B also increased with rising CNC content, suggesting that the nonlinear relationship between average tunneling distance and strain becomes more pronounced as the CNC content increases. To gain further insights, change in tunneling distance and tunneling distance as function of strain was plotted using equation 5.5. Figure 5.12a shows that at any strain value (below 1%), at the lower CNC content, the change in tunneling is achieved higher. This relation suggests that the movements of CNTs are impaired by the CNCs. This impairment could be attributed to CNCs occupying the available tunneling junctions on a CNT. With the assumption that CNCs tend to attach to the side of walls of a CNT rather than to its ends, B can be interpreted as an indirect indication of CNT-CNT interaction under strain in the presence of CNCs. Hence, higher B values for elastic regions yield a low sensitivity under strain; for example, CNTSA/CNC_0.8:4.0 has the lowest gauge factor (between 0-0.30% strain). In plastic regions, when permanent deformation occurs, B and the initial average tunneling distance determine the sensor's sensitivity. For example, although the tunneling distance change in CNTSA/CNC_0.8:4.0 was smaller compared to other sensors, its initial average tunneling distance of approximately 0.7 nm was closer to the cutoff distance (1.40–1.80 nm) [174,176] than those of the other sensors, as shown in Figure 5.12b.

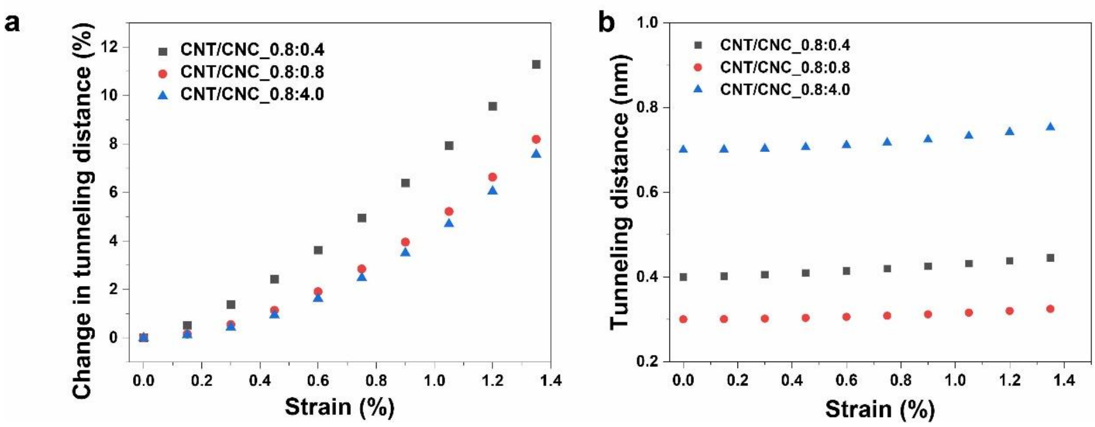

Figure 5.12 : a) Change in tunneling distance and b) tunneling distance as a function of strains at various CNC compositions.

Based on the previous findings and premises developed in this work and the accumulated knowledge from the literature, it is concluded that the effect of highly loaded CNCs on the CNTs conductive paths diminishes the required routes for electron transfer, as demonstrated in Figure 5.13. Hence, it is shown that at low loads of CNCs, both in-plane and overlapping contacts are responsible for electron tunneling. At high loads of CNCs, however, mainly in-plane contacts are responsible for electron tunneling. Therefore, an applied strain invokes higher changes in average tunneling distance in a medium where CNC loads are lower than in a medium where CNC loads are high. It is worth reporting that the good reproducibility of the results was emphasized through the average values of gauge factors, B values, and the initial tunneling distances of three identical sensors for each of the developed sensors (See Table 5.2).

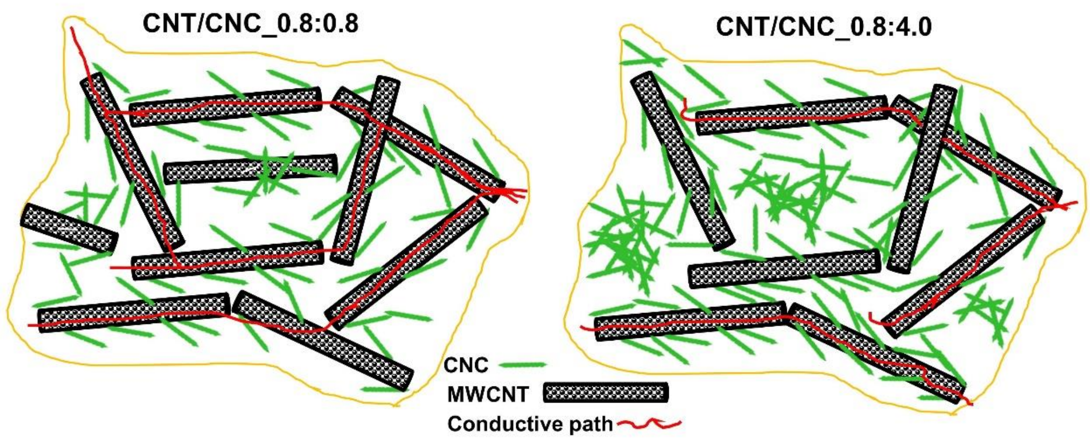

Figure 5.13 : Schematic showing the effect of CNCs, at low and high loads, on the type of CNT contacts and conductive paths.

5.2.2 Reliability assessment

To demonstrate the feasibility and durability of the CNTSA/CNC sensors as an application for structural health monitoring systems, a reliable performance test was carried out in elastic region (at 0.60% strain). CNTSA/CNC_0.8:0.8 was subjected to 250 tensile cycles with a crosshead speed of 6 mm/min. As demonstrated in Figure 5.14, the negative piezoresistive behavior of the sensor, which was previously seen in [166,199], was attributed to three main reasons: i) permanent changes in the CNT conductive network [199], ii) Poisson effect [93,337], and iii) mechanical hysteresis [70]. Our attribution to the decrease in resistance during cyclic loading, however, could be related mainly to the continuous reconstruction of CNT conductive pathways. As discussed in supporting information, although mechanical hysteresis has an effect on cyclic loading, its effect was not continuously dominant after the first few cycles. To better exploit this phenomenon in strain sensing for practical applications, the mechanism of this behavior is yet to be fully understood which requires further investigation. Nonetheless, after 250 cycles the CNTSA/CNC composite on the surface of GFRP composite remained intact demonstrating the feasibility of coating CNTSA/CNC on surface of composites and the durability of the coated layer. Further in-depth discussion and comparison between sensors' performance are provided in supporting information.

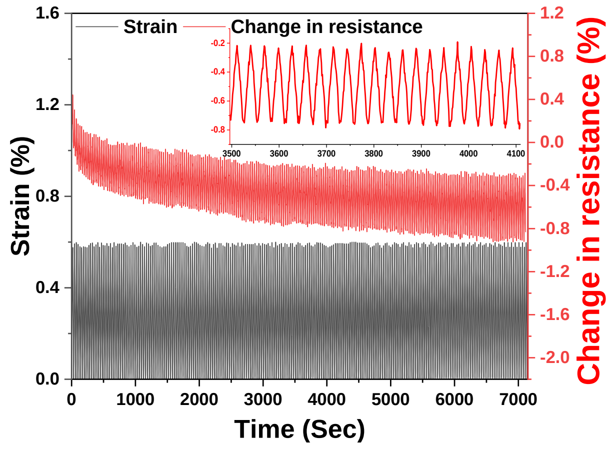

Figure 5.14 : Piezoresistive behavior as a function of time for a total of 250 cycles for CNTSA/CNC_0.8:0.8 at a strain of 0.60%. Inset figure shows enlarged portion of resistance change at time interval between 3500 and 4120 second.

Coating the surface of GFRPs with CNTSA/CNC demonstrated the applicability of sensing capabilities of the approach. Controlling the total solid content also plays a critical role in determining the sensor's electromechanical performance. However, this simple coating method using a roller coating tool does not allow precise control over the printed pattern. Therefore, screen and spray printing methods were employed to achieve more precise control over the printed pattern.

5.3 Influence of Geometrical Pattern on Strain Sensors' Performance

In this section, screen-printed CNTSA sensors were used to study the influence of strain rate and geometrical pattern on their reliability, sensitivity, and linearity.

5.3.1 Strain rate influence and sensor performance of CNTSA-based sensors

The CNTSA/CNC-based ink with a 6.0:6.0 content ratio, formulated for the screen printing method, was used to fabricate the sensors in this study. The influence of the applied strain rate test involved six single-cycle tests to investigate the influence of applied strain rates, ranging from 2 to 12 mm/min in 2 mm/min increments, with an elongation of 0.15 mm (corresponding to 0.3% strain). Cyclic tensile testing consisted of 50 cycles at 0.6% strain, followed by an additional 50 cycles at 1.2% strain.

The piezoresistive response of CNT-based nanocomposite polymers typically depends on the applied strain rate. To investigate this effect on CNTSA/CNC sensors, a strain rate test was conducted. Figure 5.15 shows the piezoresistive response of the sensors under increasing strain rates tested at 0.3% strain, where all sensors exhibited similar behavior and their response appeared independent of the strain rate. In CNT-based nanocomposites, high strain rates exacerbate signal drifting and result in shoulder peak during unloading. This dependency is usually attributed to the mobility of the polymer chain within the nanocomposite, which influences the relative position of the carbon nanomaterials [338,339], and the type of interaction between the polymer matrix and carbon nanomaterial [340]. In contrast, the CNTSA/CNC sensors' independence from strain rate can be attributed to the absence of a polymer matrix.

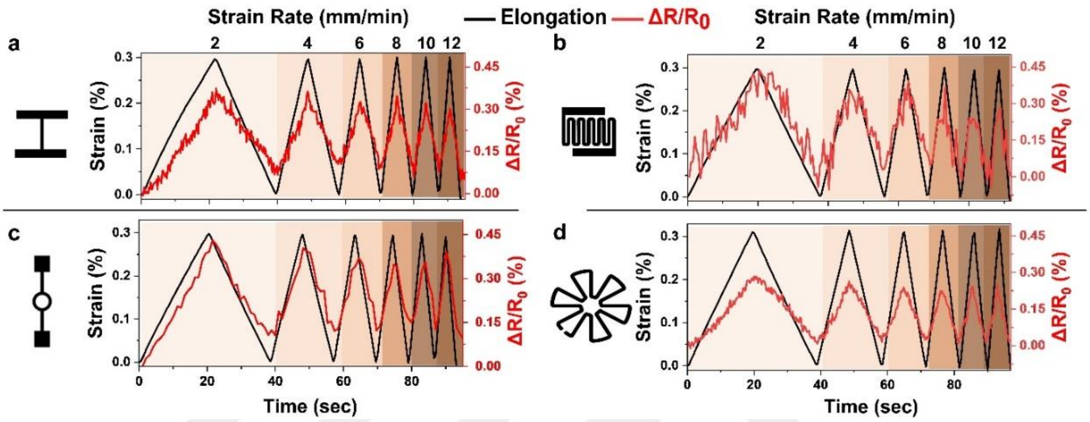

Figure 5.15 : Single cyclic tensile strain rates for a) line, b) grid, c) o-line, and d) omnidirectional.

Influence of geometrical pattern on reliability, sensitivity, and linearity of CNTSA-based sensors

The electromechanical characteristics of a strain sensor, specifically sensitivity, reliability, and linearity, were evaluated by testing printed sensors on the GFRP surface under cyclic loading. The sensors underwent 50 tensile cycles at 0.6% strain and an additional 50 cycles at 1.2% strain.

The impact of cyclic loading on the electrical network was investigated by assessing the surface morphology using SEM. Figure 5.16a shows the surface morphology of the CNTSA/CNC sensor after being subjected to 50 tensile loading cycles at 0.6% strain. The sensor's electrical network exhibited no noticeable damage compared to its state before loading (see Figure 4.4). However, after additional 50 cycles at 1.2% strain, cracks were visible, as shown in Figure 5.16b. In the cracked regions, CNT strands were observed bridging the two sides of the crack, as detailed in the higher magnification image shown in Figure 5.16c. Imaging a surface crack at higher magnification using a secondary electron detector revealed the inner network of the CNTSA/CNC sensor, as shown in Figure 5.16d. The dense internal structure of the electrical network extends out of plane, resulting from the multiple printed layers, with visible bridging CNTs.

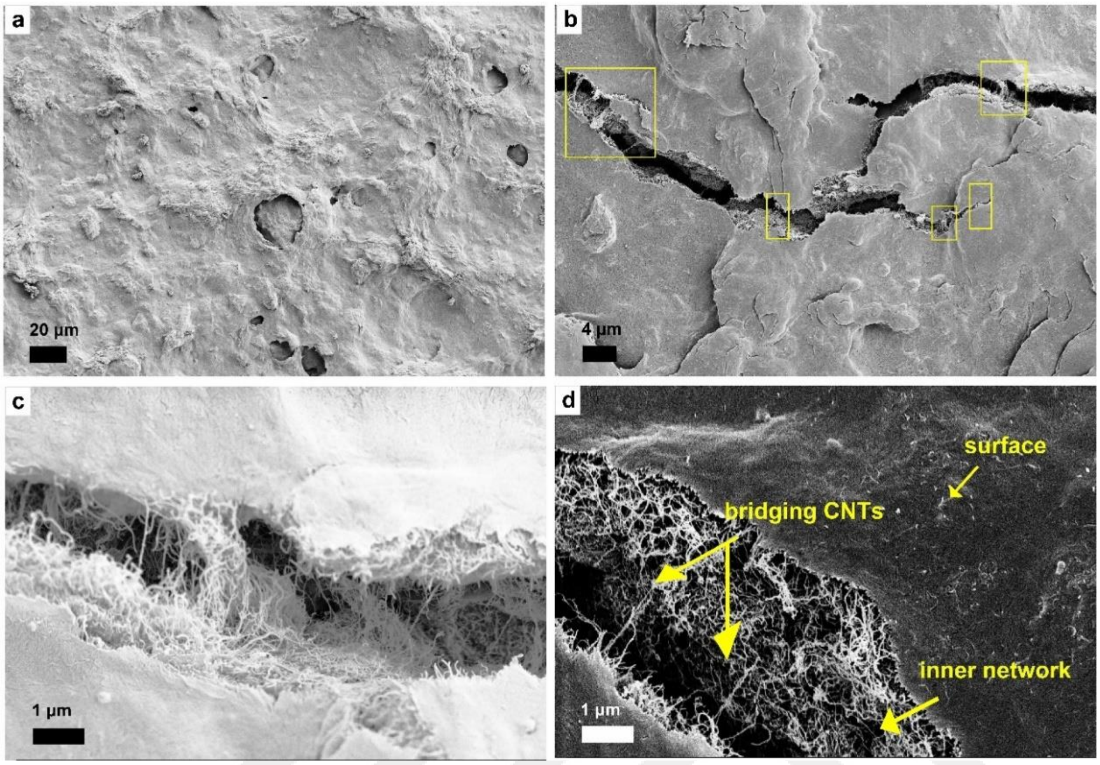

Figure 5.16 : Surface morphology of 6.0:6.0 CNTSA/CNC sensor after loading at a) 0.6% and b) 1.2% strain (Yellow rectangles indicate regions where the stretched CNT network bridges cracks). c) High-magnification view of the stretched CNT network highlighted in the far-right yellow rectangle of (b) c) Secondary electron microscopy image of a surface crack at higher magnification, revealing the dense inner network of the CNTSA/CNC sensor, with bridging CNTs extending out of the plane due to the multilayered printing.

Figure 5.17 illustrates the representative results for all patterns, with a focus on the first ten cycles. It shows that the sensors exhibited varying behaviors depending on the applied strain and geometric pattern.

To understand the differences in sensor behavior, the electromechanical properties were quantified in terms of signal reliability (maximum and minimum peaks), sensitivity, and linearity, as shown in Figure 5.18a-b. At 0.6% strain, all sensors exhibited a slight decrease in maximum resistance change on average, indicating a downward drift, as shown in Figure 5.18a. However, at 1.2% strain, the peak intensity increased notably, highlighting a strain-dependent response with a slight upward drift. The line and o-line sensors showed the highest peak intensity at both strain levels, while the grid and omnidirectional sensors had lower peak intensities. The slight downward drift at 0.6% strain was attributed to the rearrangement and alignment of CNTs [341], with no apparent visible damage (see Figure 5.16a), whereas the upward drift at 1.2% strain was attributed to damage in the electrical network (see Figure 5.16b).

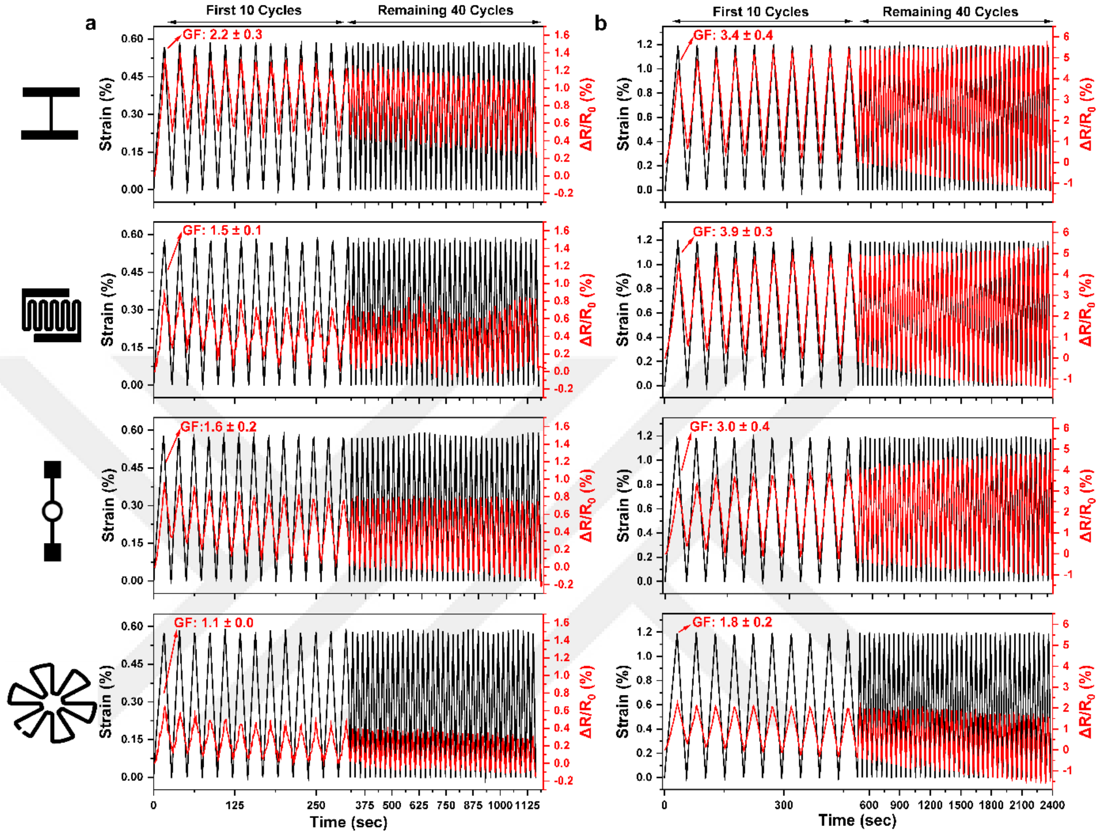

Figure 5.17 : Electromechanical cyclic behavior at a) 0.6% and b) 1.2% strains. The first ten cycles are shown in the first half of the x-axis, with the remaining 40 cycles represented in the second half of the axis to highlight the initial phase of loading.

Interestingly, the omnidirectional pattern exhibited an opposite trend at 1.2% strain, with a decrease in maximum resistance change. This could be due to transverse strains aligning with segments of the omnidirectional pattern that run parallel to these strains. The alignment may cause local compression of the conductive pathways, thereby reducing resistance. This compression could counteract the effect of the applied tensile load, resulting in more complex piezoresistive behavior and ultimately decreasing the sensor’s sensitivity to strain.

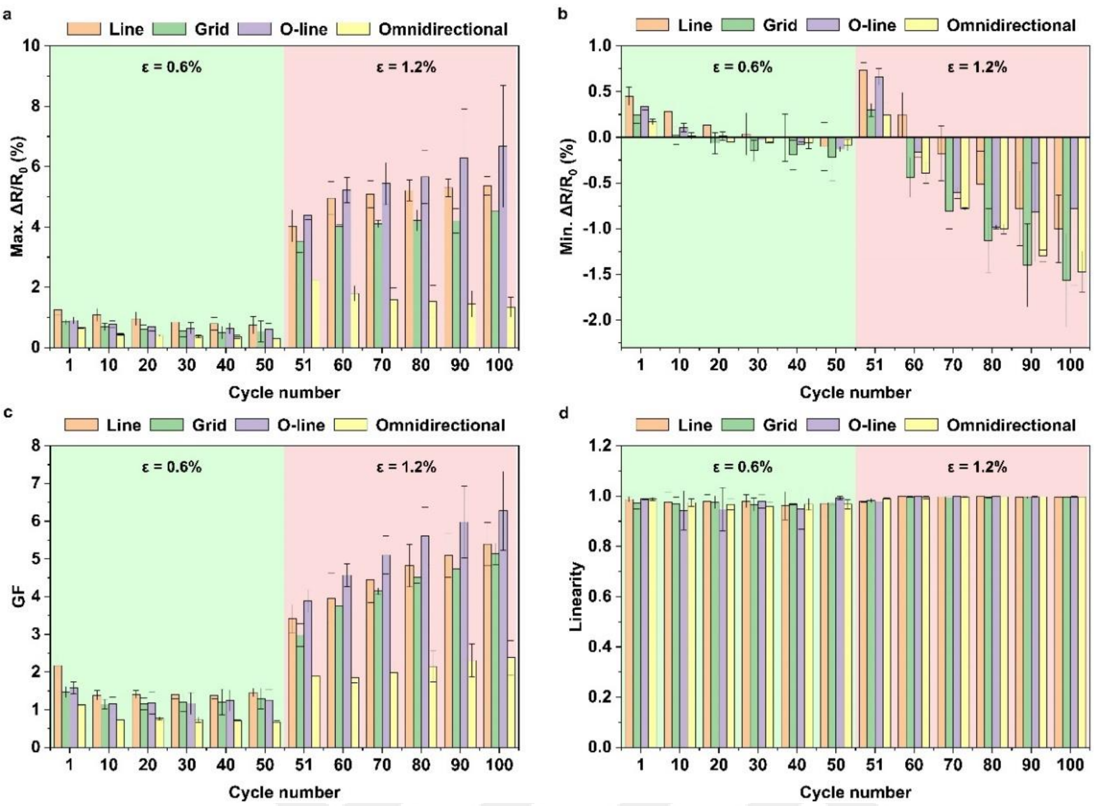

Figure 5.18 : a) Maximum and b) minimum resistance change as a function cycle number, c) average GFs, and d) average linearity as a function of cycle number.

The minimum resistance change was influenced greatly by the cycle number and applied strain than by the geometric pattern, as shown in Figure 5.18b. As the cycle number increased, minimum resistance change decreased, with greater decrease at higher strains. The printed CNTSA/CNC sensor patterns responded differently than CNT-based nanocomposites under cyclic loading [341]. In CNT-based nanocomposites, high strains cause both minimum and maximum resistance changes to drift downward, often accompanied by shoulder peaks, a behavior linked to the viscoelastic properties and creep within the nanocomposites. Since the printed CNT/CNC sensors lack a polymer matrix, the observed drift in the minimum resistance change was attributed to the alignment of the CNT particles [87,88], which is particularly evident for CNTs near damage locations (see Figure 5.16c). The applied strain likely also influenced the rate of CNTSA alignment, leading to the differences observed in the drift of minimum resistance change at 0.6% and 1.2%. It is important to note that the observed downward drifts are unlikely caused by Joule heating, since its effects were only observed at high voltages, as discussed earlier.

Under repetitive loading, such as fatigue testing, composites can experience self-heating, especially at high frequencies above 5 Hz. This effect is influenced by factors including loading conditions, stacking sequence, geometry, and material properties [342,343]. While surface discontinuities on GFRPs can lead to lower temperature rises, particularly with smaller discontinuities, longer testing durations generally result in higher temperatures [342]. However, at 0.6% strain in which a cycle lasts 29 seconds, indicating a lower frequency than the frequencies linked to self-heating, it was concluded that self-heating had minimal impact on the results.

Al-Bahrani et al. evaluated the degree of damage in CNT-based sensors by measuring residual resistance after sudden impact loads [271]. Similarly, the residual resistance changes after the first cycle were quantified and presented in Table 5.3 to be interpreted as a damage occurred in the sensor's electrical network. Line and o-line sensors showed larger damages compared with grid and omnidirectional sensors. However, due to signal drifting in subsequent cycles, the apparent damages diminished, indicating a dependency on history loading, likely related to the potential alignment of CNTs, as discussed earlier.

In Figure 5.18c, the average GF is plotted as a function of the cycle number. At 0.6% strain, the calculated average GF values of the first cycles of the line, grid, o-line, and omnidirectional are 2.2 ± 0.3, 1.5 ± 0.1, 1.6 ± 0.2, and 1.1 ± 0.0, respectively. This data indicates that GF was found to be inversely proportional to the sensor length (see Table 3.6). The higher sensitivity of the line and o-line sensors compared to the grid and omnidirectional sensors may be due to their smaller coverage areas (see Table 3.6). The line sensor is the most sensitive because its entire length aligns with the direction of the applied load, whereas, for example, grid sensor extends perpendicularly.

After the first cycle, the GF values dropped but remained unchanged for all sensors. The initial drop in GF values was due to the damage observed at the end of the first cycle. Unlike previous studies that found GF drifting correlated with electrical signal drift in both CNT-based self-sensing nanocomposites [341] and grid pattern printed on Kapton film [27], this study did not observe such a correlation. At 1.2% strain, sensor sensitivities also depended on the geometric pattern. However, the GFs of the sensors increased with the number of cycles. This continuous rise in GFs was attributed to the growing difference between the maximum and minimum resistance changes. The maximum resistance change increased due to the accumulated damage inflicted on the sensors at the end of each cycle, while the minimum resistance change decreased due to the progressive alignment of CNTs with each cycle [87,344].

Table 5.3 : Summary of electromechanical properties of CNTSA-based sensors with different pattern designs under varying strain conditions.

Geometric pattern	**R_0 (kΩ)**	**0.6% strain**			**1.2% strain**	
		Damage after 1st cycle (%)	**GF***	**Linearity***	**GF***	**Linearity***
Line	2.6 ± 0.9	0.45 ± 0.10	2.2 ± 0.3	0.99 ± 0.01	3.4 ± 0.4	0.98 ± 0.01
Grid	54.0 ± 26.0	0.23 ± 0.09	1.5 ± 0.1	0.97 ± 0.02	3.0 ± 0.4	0.98 ± 0.01
O-line	10.3 ± 4.2	0.34 ± 0.04	1.6 ± 0.2	0.99 ± 0.01	3.9 ± 0.3	0.97 ± 0.01
Omnidirectional	43.2 ± 5.1	0.17 ± 0.03	1.1 ± 0.0	0.99 ± 0.01	1.8 ± 0.2	0.98 ± 0.02

* Average values calculated for the corresponding first cycle.

Figure 5.18d shows the linearity of the sensor patterns as a function of cycle number. All sensors, regardless of geometry and applied strain, exhibited high linearity and remained unaffected by the number of cycles. Even under high strains and formation of cracks, the sensors kept their linearity intact. This contrasts with nanocomposite-based sensors, which are often negatively impacted by the viscoelastic properties inherent to the polymer matrix. At 0.6% strain, the observed linearity was attributed to the abundance of CNTs within the network [345]. However, as cracks develop at 1.2% strain, the bridging CNTs (see Figure 5.16c-d) become strained, resulting in a linear change in their resistance, and thus, maintaining the highly linear response [346].

Ultimately, these findings provide valuable insights into the relationship between geometric patterns, initial resistance, and the electromechanical response of CNTSA/CNC sensors. Contrary to previous studies suggesting that increasing initial resistance by extending the length of CNTSA-based nanocomposite sensors enhances sensitivity [27,31,36], the presented results indicate the opposite trend: sensors with lower initial resistance, such as the line and o-line sensors, exhibited greater resistance changes and sensitivities compared to longer sensors, such as grid and omnidirectional. The factors that play a more decisive role in determining the sensor's electromechanical response than its initial resistance are: 1) the total area covered by the sensor (see Table 3.6), 2) whether the sensor’s length aligns with the direction of the applied load (*e.g.*, o-line sensor) or extends perpendicular to it (*e.g.*, grid), and 3) whether segments of the sensor are parallel to transverse strains (*e.g.*, omnidirectional). Furthermore, the initial resistance significantly impacts the piezoresistive response only when comparing sensors with similar geometric patterns (*e.g.*, five- vs ten-layer o-line sensors). Other factors, such as transverse sensitivity, length-to-width ratio, and the printing method, may also influence the sensor's piezoresistive performance [40].

Next, to compare the performance between research-grade and industrial-grade materials, the performance of CNTs supplied by Nanocyl and CNF-based sensors was assessed.

5.1 Influence of Industrial-Grade CNTNC and CNF on Strain Sensors Performance

As part of the further exploration of commercially available 1D nanomaterials, different CNT types (CNTCT, CNTNI, and CNTNC) and CNF were considered. However, CNTCT and CNTNI electrical resistance was found to be inadequate for reliable sensing applications, leading to their exclusion from subsequent testing.

Hence, the focus now shifts to CNTNC-based sensors. Compared to the previously used CNT, CNTNC exhibits a slightly lower purity (90%) with a shorter length (1 µm) while maintaining a comparable diameter (<9 nm). These differences in morphology and purity are expected to influence the conductive network and overall sensor performance. To examine these effects, two CNTNC/CNC-based sensors were printed using two ink formulations, 2.0:2.0 and 6.0:6.0, abbreviated as CNTNC-2 and CNTNC-6, respectively (see Table 4.14 for more information). Grid, line, and omnidirectional sensors were printed from CNTNC-2, while only grid and line sensors were produced from CNTNC-6. The omnidirectional pattern was difficult to print using the 6.0:6.0 formulation due to inhomogeneous deposition, as the high concentration of the ink made it challenging to handle and process; hence, it was not printed. The CNF sensor printed using the grid pattern was the only CNF-based sensor pattern considered for evaluation. CNTNC-2, CNTNC-6, and CNF sensors were subjected to cyclic loading at 0.6% strain. Sensor reliability, sensitivity, and linearity were assessed.

5.1.1 Electromechanical performance of CNTNC-2 line, grid, and omnidirectional sensors

Figure 5.19shows representative cyclic test results for line, grid, and omnidirectional CNTNC-2 sensors.

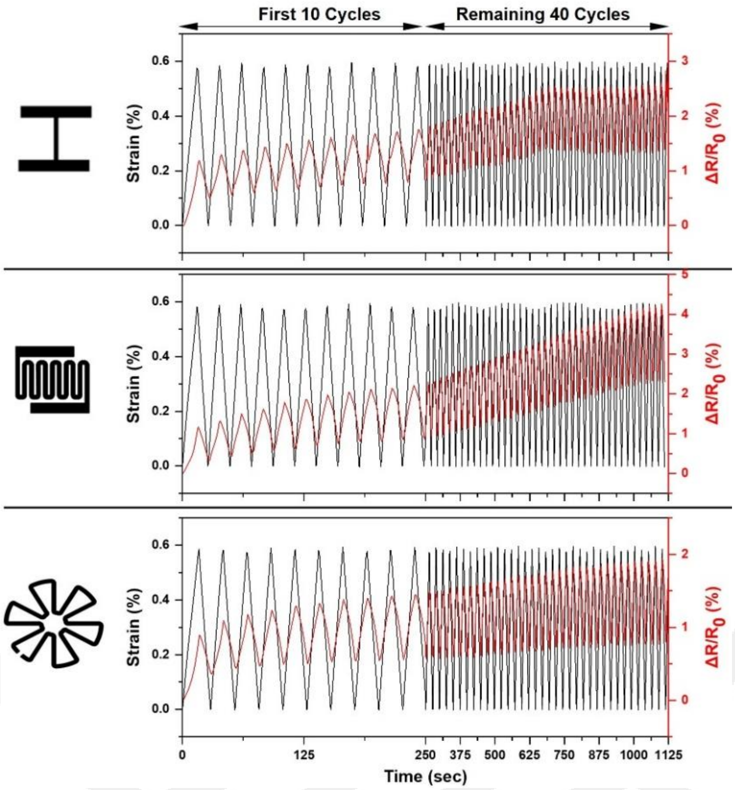

Figure 5.19 : Representative cyclic loading test for line, grid, and omnidirectional CNTNC-2 sensors. The first ten cycles are shown in the first half of the x-axis, with the remaining 40 cycles represented in the second half of the axis to highlight the initial phase of loading.

Figure 5.20a shows that all CNTNC-2 sensor patterns exhibited an increasing maximum resistance change with the number of cycles. In other words, the sensors demonstrated unreliable performance. While previously reported CNT sensors showed a downward drift, the upward drift observed in CNTNC-2 sensors is attributed to differences in the electrical network, influenced by purity.

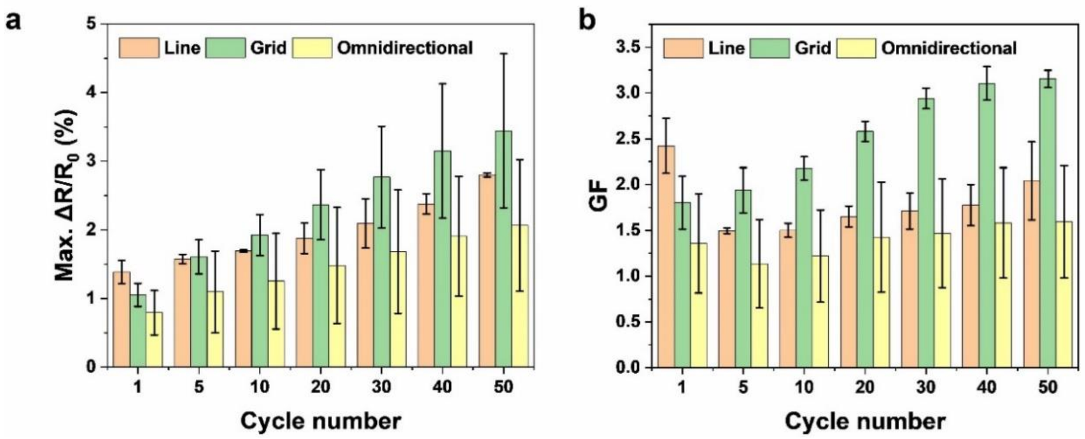

Figure 5.20 : a) Maximum resistance change as a function cycle number and b) gauge factor as a function cycle number for the line, grid, and omnidirectional CNTNC-2 sensors.

This increase in maximum resistance change resulted in an increasing trend in sensitivity, as shown in Figure 5.20b. In other words, the gauge factor increased with the number of cycles, unlike previously reported CNT sensors. However, the gauge factor values in the first cycle of line, grid, and omnidirectional sensors decreased with an increase in the conductive path, 2.4 ± 0.3, 1.8 ± 0.3, and 1.4 ± 0.5m respectively, a trend similar to CNT sensors.

The linearity of CNTNC-2 sensors exhibited high consistency regardless of the geometrical pattern, as shown in Figure 5.21.

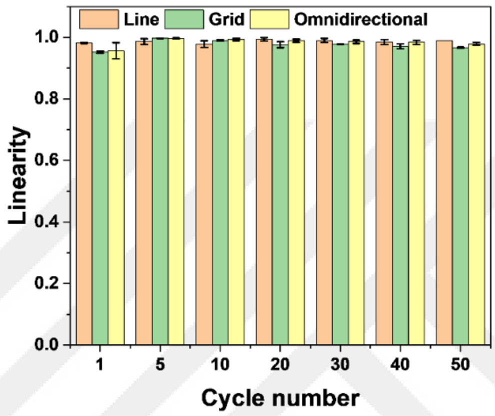

Figure 5.21 : Linearity of line, grid, and omnidirectional CNTNC-2 sensors.

5.1.2 Electromechanical performance of CNTNC-6 line and grid sensors

Figure 5.22 presents representative cyclic test results for line and grid CNTNC-6 sensors, which exhibited similar behavior to the previously reported CNTNC-2 sensors, an upward drifting in resistance change.

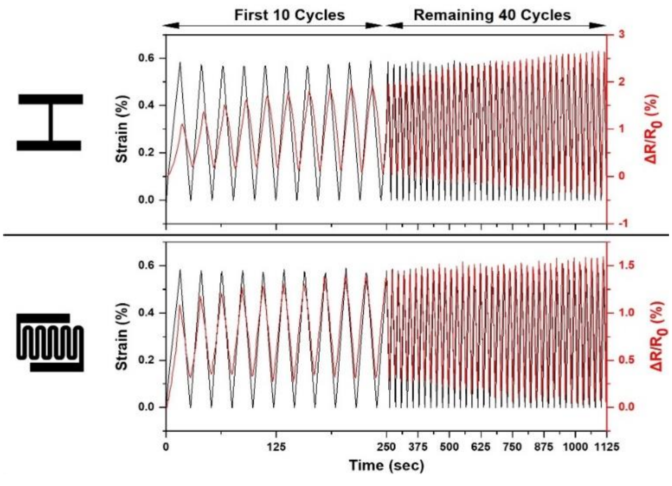

Figure 5.22 : Representative cyclic loading test for line and grid CNTNC-6 sensors. The first ten cycles are shown in the first half of the x-axis, with the remaining 40 cycles represented in the second half of the axis to highlight the initial loading phase.

Despite the difference in the CNTNC and CNC concentrations in the prepared inks used for printing, both line and grid CNTNC-6 sensors exhibited similar behavior to CNTNC-2 sensors, as shown in Figure 5.23a. This suggests that filler concentration does not directly influence the overall electrical response. Additionally, both CNTNC-2 and CNTNC-6 sensors exhibited an increase in maximum resistance change with cycle number, reinforcing the unreliability observed in CNTNC sensors. Overall, the long-term stability of CNTNC-2 and CNTNC-6 sensors remains a concern due to the continuous increase in resistance change over cycles. The gauge factor trends in CNTNC-6 sensors also followed a similar increasing pattern with cycling, line, and grid CNTNC-6 sensors exhibiting a sensitivity of 2.2 ± 0.5 and 1.7 ± 0.2, respectively, as shown in Figure 5.23b. The gauge factor values also tended to increase with the increase of the cyclic number.

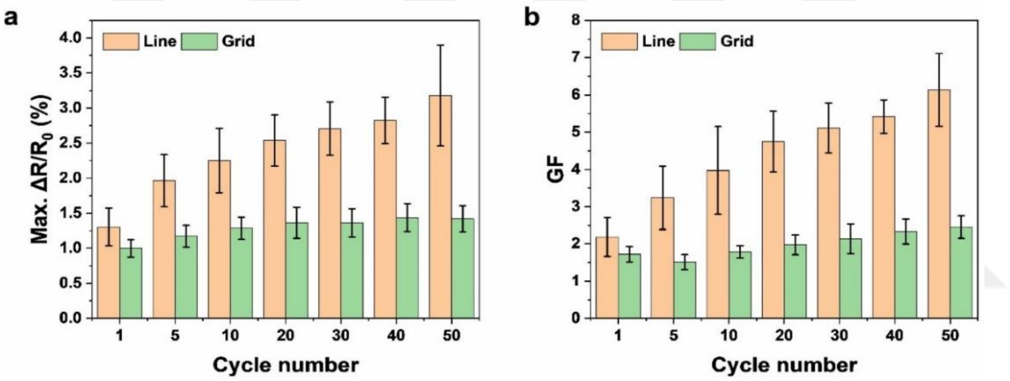

Figure 5.23 : a) Maximum resistance change as a function cycle number and b) gauge factor as a function cycle number for the line and grid, CNTNC-6 sensors.

The linearity of CNTNC-6 was high and comparable to that of CNTNC-2 sensors, as shown in Figure 5.24. Despite the differences in CNTNC/CNC loading during printing, both sensor types demonstrated excellent linear responses across various geometrical patterns, including line and grid configurations.

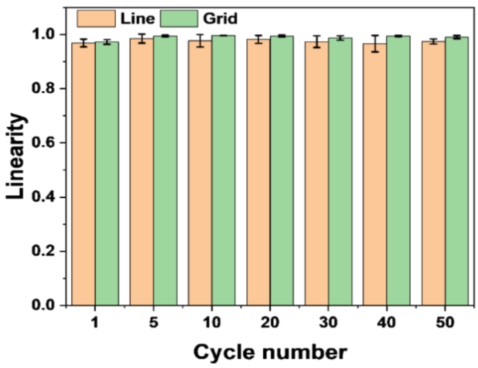

Figure 5.24 : Linearity of line and grid CNTNC-6 sensors.

5.1.3 Electromechanical performance of CNF grid sensor

CNF grid sensor was subjected to cyclic loading at a strain of 0.6% strain similar to the testing condition of CNTNC sensor reported above. Figure 5.25 shows representative cyclic test result for grid CNF sensor, showing a steep downward drifting in resistance change.

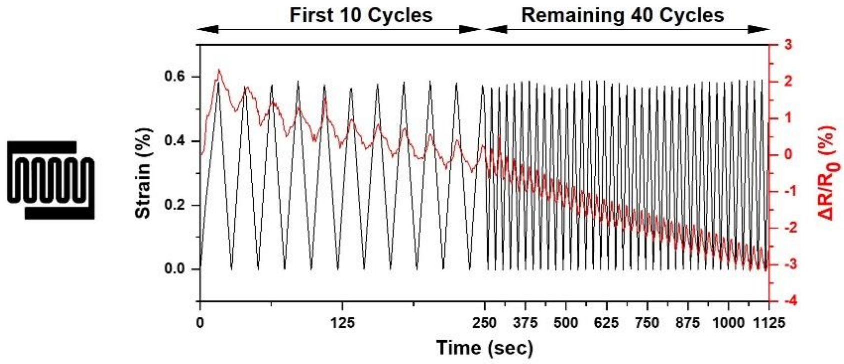

Figure 5.25 : Representative cyclic loading test for grid CNF sensor. The first ten cycles are shown in the first half of the x-axis, with the remaining 40 cycles represented in the second half of the axis to highlight the initial loading phase.

The sensor exhibited a steep downward drift in maximum resistance change, as demonstrated in Figure 5.26a. Paleo et al. reported signal drift for CNF-based nanocomposite sensor although less severe than reported herein [101].

The damage after the first cycle is 0.89±0.34%, suggesting a small damage. The relatively high aspect ratio of CNFs creates a fibrillated and entangled network, forming a robust electrical structure [117]. Similar to CNTs, when this interlocked network is strained without sustaining significant damage, the positions of the intertwined nanoparticles shift and overlap, leading to minimal changes in the electrical network and, consequently, lower sensitivity.

The CNF grid sensor demonstrated a sensitivity of 3.8 ± 0.8. Under tensile force, the gauge factor of CNF sensor was slightly higher compared to their nanocomposite counterparts [101,102]. Similar to CNTSA, gauge factor values dropped as cycle number increased, as shown in Figure 5.26b.

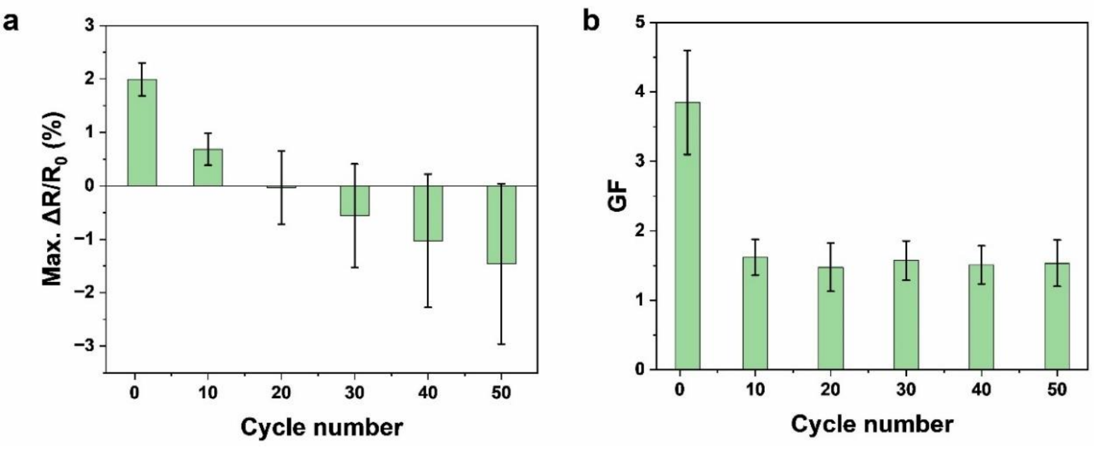

Figure 5.26 : a) Maximum resistance change as a function of cycle number and b) gauge factor as a function of cycle number for the grid CNF sensor.

CNF sensors demonstrated an excellent linear response, as shown in Figure 5.27. Linear response has been reported for CNF-based sensors [102,347]. Studies showed that good linearity for CNF-based nanocomposite strain sensors [101] can be achieved above percolation threshold at high filler loads [345]. For example, CNF-based polypropylene nanocomposite subjected to four-point bending loading demonstrated a linearity as high as 0.96 [101].

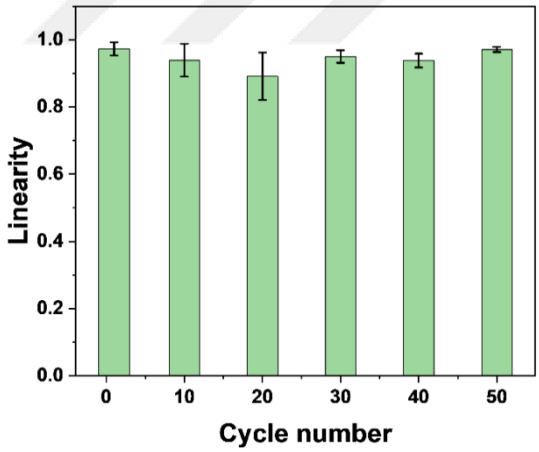

Figure 5.27 : Linearity of grid CNF sensor.

With these findings established, the next phase of the study shifts focus to a 0D conductive material: carbon black.

5.2 Influence of Geometrical Pattern on Reliability, Sensitivity, and Linearity of CB-Based Sensors

Unlike 1D nanomaterials, which have a high aspect ratio and form percolation networks through entanglement, CB consists of nearly spherical particles that create conductive pathways via particle-to-particle contact and are considered to have an aspect ratio of 1. To investigate how this morphological difference influences sensor performance, CB-based sensors were fabricated and tested using the four pattern geometries, allowing for a comparison of both the effect of nanostructure and the influence of pattern geometry on sensor performance.

Figure 5.28 presents representative cyclic test results for the line, grid, o-line, and omnidirectional CB sensors. All sensors showed minimal changes in resistance across the 50 cycles.

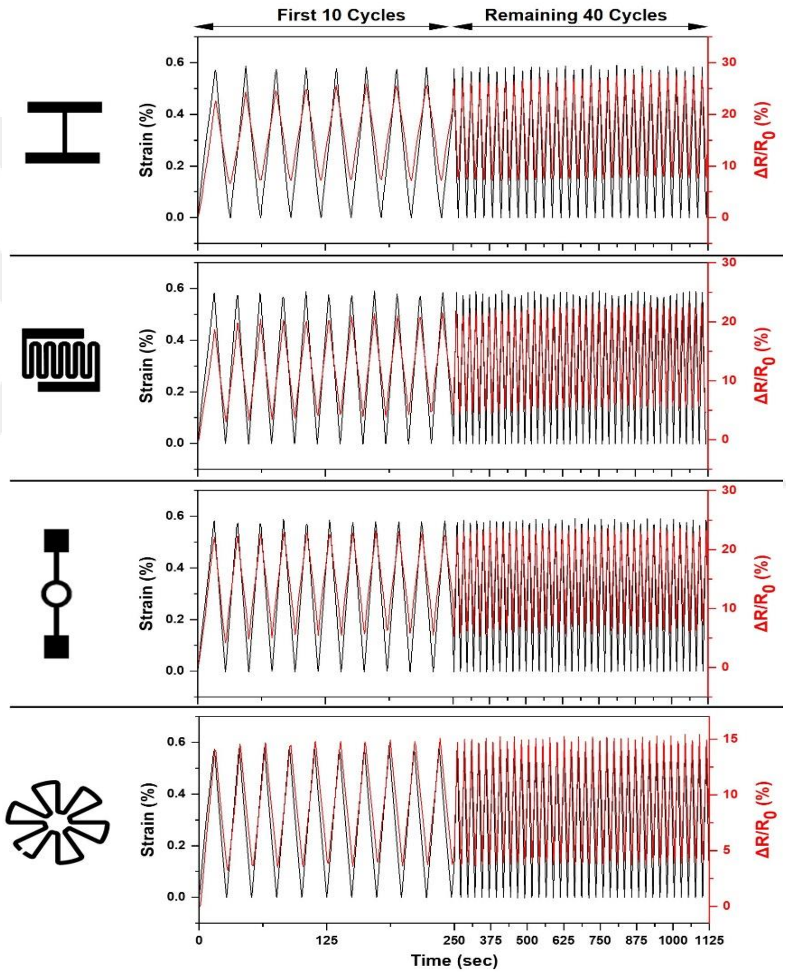

Figure 5.28 : Representative cyclic loading test for line, grid, o-line, and omnidirectional CB sensors. The first ten cycles are shown in the first half of the x-axis, with the remaining 40 cycles represented in the second half of the axis to highlight the initial loading phase.

By evaluating the average maximum resistance change, the CB sensor exhibited a slight upward drift, attributed to the spherical nature of CB particles [117], as shown in Figure 5.29a. However, this slight upward drift was significantly less severe than that observed in CB-based nanocomposites under tensile loading [117].

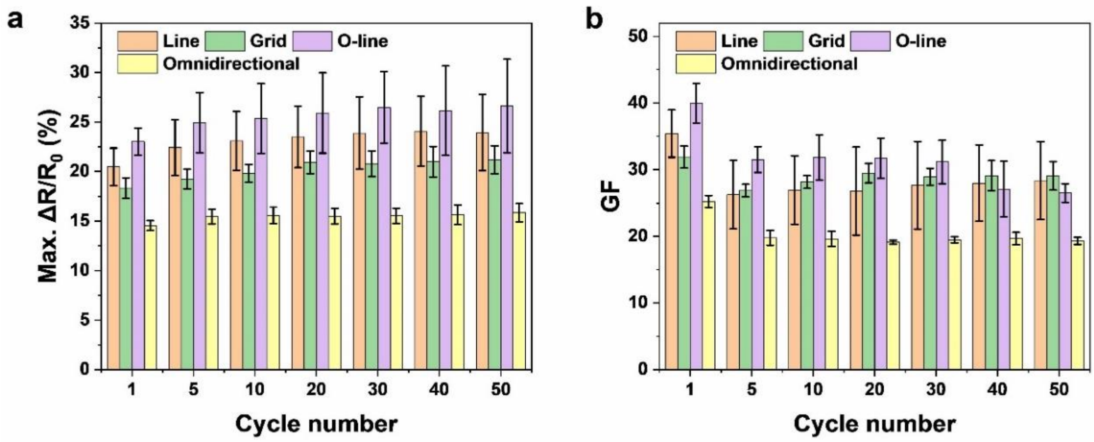

Figure 5.29 : a) Maximum resistance change as a function of cycle number and b) gauge factor as a function of cycle number for the line, grid, o-line, and omnidirectional CB sensors.

The extent of damage varied depending on the geometrical pattern, as detailed in Table 5.4. The damage levels for line, grid, o-line, and omnidirectional sensors were 6.4 ± 0.6%, 2.9 ± 0.5%, 5.4 ± 1.7%, and 3.5 ± 0.4%, respectively. Similar to previously reported CNTSA sensors, those with shorter conductive paths, such as line and o-line patterns, exhibited the highest damage. In contrast, sensors with longer conductive paths, such as grid and omnidirectional designs, demonstrated lower damage levels. Nonetheless, damage after the first cycle has also been reported for CB nanocomposites [117]. Unlike CB nanocomposites, which tend to accumulate damage after each cycle due to the inherent viscoelastic properties of the polymer matrix [117,348–350], the damage observed in the CB sensors after the first cycle remained unchanged over 50 cycles (as demonstrated in the representative results in Figure 5.28). This stability may be attributed to the absence of a polymer matrix within the CB network.

Table 5.4 : Summary of electromechanical properties of CB-based sensors with different pattern designs.

Geometric pattern	R_0 (kΩ)	0.6% strain		
		Damage after 1st cycle (%)	GF*	Linearity*
Line	20.8 ± 6.1	6.43 ± 0.60	35.4 ± 3.6	1.00 ± 0.00
Grid	194.1 ± 63.6	2.95 ± 0.52	31.9 ± 2.0	1.00 ± 0.00
O-line	51.3 ± 0.7	5.42 ± 1.67	40.3 ± 3.0	1.00 ± 0.0
Omnidirectional	271.7 ± 31.8	3.45 ± 0.35	25.2 ± 0.9	1.00 ± 0.0

* Average values calculated for the corresponding first cycle.

The CB sensor exhibited high sensitivity across all geometries, as demonstrated in Table 5.4, with single-line patterns (line and o-line) demonstrating higher values than multi-line patterns (grid and omnidirectional). These sensitivity values are much higher than those of CNT and CNF sensors previously reported. This finding is consistent with the literature, where CB nanocomposite sensors typically show higher sensitivity compared to CNT nanocomposite sensors [117]. This is attributed to the low aspect ratio of CB, which makes it less likely to reorient under strain, leading to the immediate breakdown of conductive pathways.

All sensors exhibited a drop in GF values after the first cycle as shown in Figure 5.29b. The drop is attributed to the damage seen at the end of the first cycle. However, the GF values remained stable across the subsequent 50 cycles. Unlike the sensitivity of CB nanocomposite sensors reported in the literature, which tends to increase with the number of cycles due to accumulated damage [117], the GF values of the CB sensors in this study remained relatively unchanged after the first cycle, showing less dependency on cycling. This behavior is attributed to the abundance of CB particles within the electrical network.

The most surprising result is the near-perfect linear response across 50 cycles for all CB sensors, as shown in Figure 5.30. This excellent linearity contrasts with literature reports on CB-based nanocomposite sensors [117,118,351] which typically describe nonlinear responses. In fact, the linearity of CB-based nanocomposites is generally considered inferior to that of CNT-based counterparts [352]. We believe the abundance of CB particles within the CB/CNC network and absence of polymer matrix played a critical role in maintaining a linear response under loading. While the relative positions of adjacent CB particles may change rapidly, their abundance likely helps preserve a consistent and linear variation.

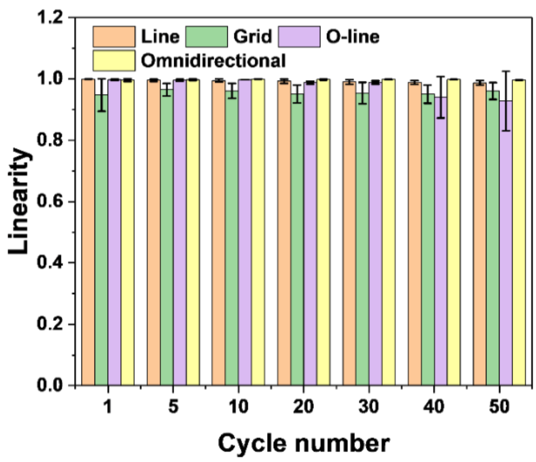

Figure 5.30 : Linearity of line, grid, o-line, and omnidirectional CB sensors.

The findings highlight the complex relationship between geometric patterns, initial resistance, and the electromechanical response of CB sensors, similar to CNTSA sensors reported earlier. Contrary to previous studies suggesting that increased initial resistance enhances sensitivity, it was found that sensors with lower initial resistance, such as those with line and o-line patterns, exhibited greater resistance changes and sensitivities. This trend was consistent across both CNTSA and CB sensors. Additionally, the initial resistance notably impacts the piezoresistive response only when comparing sensors with different numbers of printed layers using the same geometric pattern.

Next, graphene-based grid sensor performance was evaluated in a similar approach.

5.3 Influence of Graphene on Strain Sensor Performance

In this section, graphene ink supplied by Graphene-Wear was printed onto GFRPs using a grid pattern. By assessing the electromechanical performance of the graphene grid sensor, its behavior can be compared with other types of nanomaterial-based sensors to evaluate relative performance and characteristics.

The host composites were subjected to cyclic loading at 0.6% strain for 50 cycles. Figure 5.31 shows representative cyclic test result for grid graphene sensor.

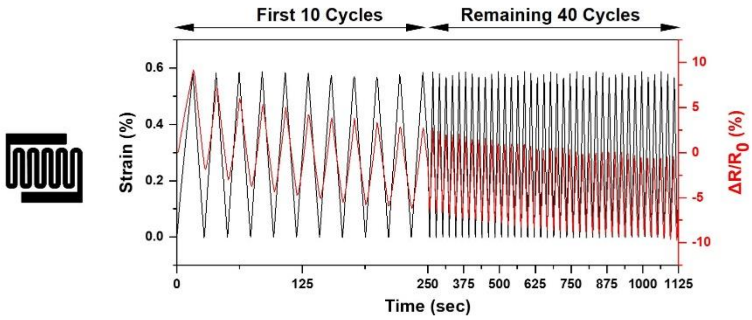

Figure 5.31 : Representative cyclic loading test for grid graphene sensor. The first ten cycles are shown in the first half of the x-axis, with the remaining 40 cycles represented in the second half of the axis to highlight the initial loading phase.

The sensor exhibited a significant downward drift in its electrical signal, as quantified by the maximum resistance change shown in Figure 5.32a. This behavior has been previously reported for graphene-based strain sensors under cyclic testing [353]. We speculate that the decrease may be due to the gradual alignment of graphene sheets and/or unfolding of graphene wrinkles [354]. Despite this drift, the sensor demonstrated a high initial gauge factor of 16.9 ± 1.5 during the first cycle. Notably, after the first cycle, the sensitivity remained stable, as shown in Figure 5.32b.

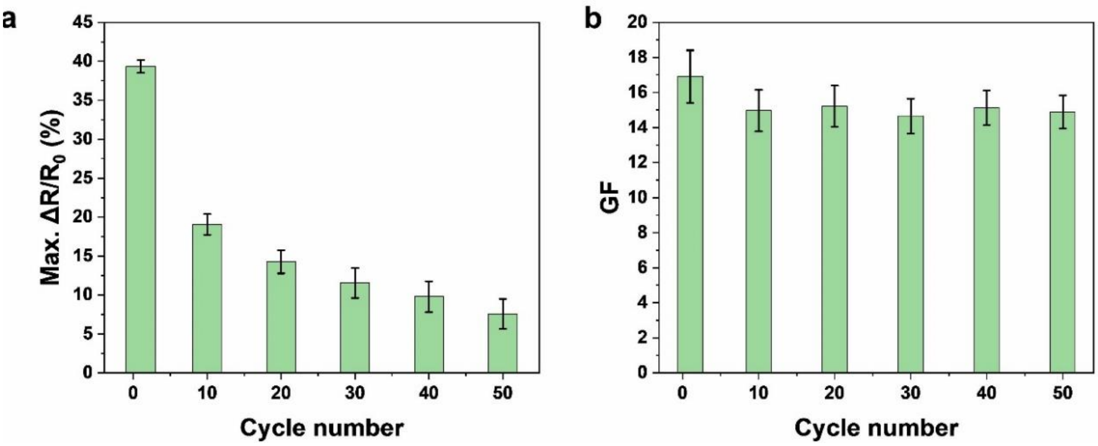

Figure 5.32 : a) Maximum resistance change as a function of cycle number and b) gauge factor as a function of cycle number for the grid graphene sensor.

Figure 5.33 shows that the grid graphene sensor exhibited a near-perfect linear response, a result similar to that reported for graphene-based sensors [353].

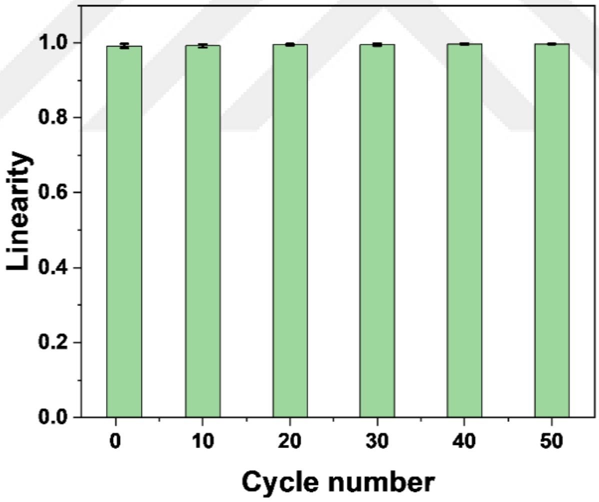

Figure 5.33 : Linearity of grid graphene sensor.

5.4 Influence of the Synergetic Effect of Hybrid Nanomaterials on Strain Sensors Performance

Earlier results showed that CNT and CNF sensors exhibited a downward drift in electrical signal, while CNTNC sensors exhibited an upward drift, making them less suitable for real-world applications due to their unreliable electrical response. In contrast, CB sensors demonstrated more promising performance, despite the slight upward drift.

Rather than comparing multiple geometries, the study now concentrates on optimizing sensor performance through hybrid formulations. Using the grid geometry, various hybridized nanomaterials were explored to assess their sensing capabilities. Hybrid sensor formulations were developed by combining CB with CNTSA, CNTNC, and CNF, resulting in CB/CNTSA-6, CB/CNTNC-6, and CB/CNF-6 sensors (see Table 4.14 for more information). These hybrid compositions were selected for their synergistic effects. The goal was to enhance the overall performance of the standalone sensors. The following provides a comparative analysis of these grid-based sensors.

The three hybrid CB/CNTSA-6, CB/CNTNC-6, and CB/CNF-6 sensors and their hosts were subjected to tensile loading at 0.6% strain for 50 cycles. Representative cyclic loading results are shown in Figure 5.34.

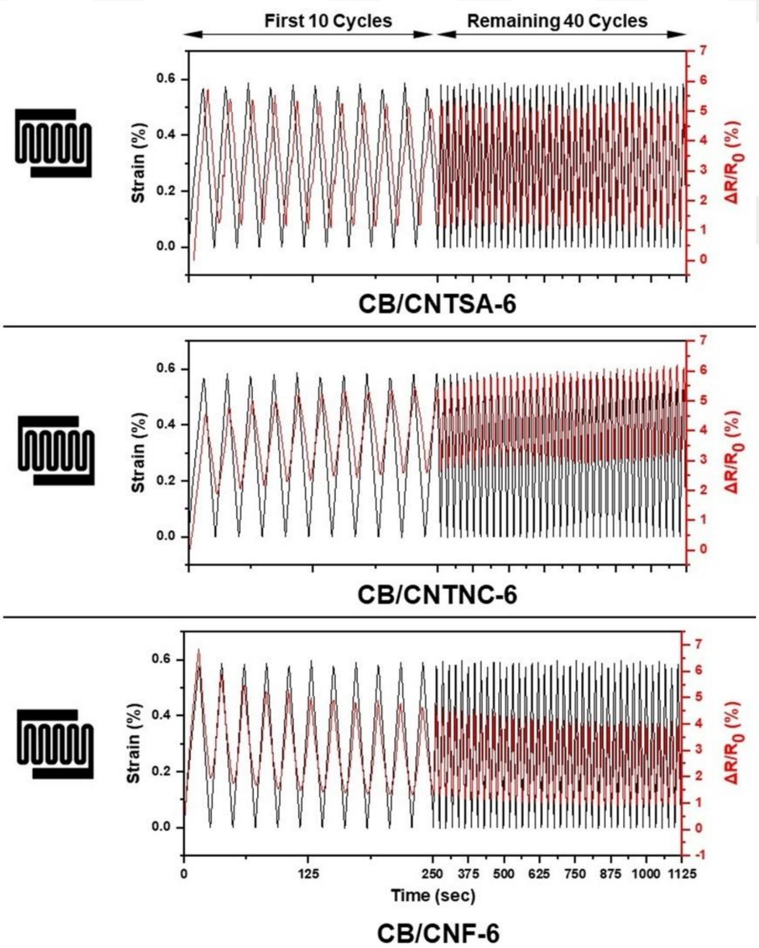

Figure 5.34 : Representative cyclic loading test for CB/CNTSA-6, CB/CNTNC-6, and CB/CNF-6 grid sensors. The first ten cycles are shown in the first half of the x-axis, with the remaining 40 cycles represented in the second half of the axis to highlight the initial loading phase.

These hybrid formulations showed improved reliability, as illustrated in Figure 5.35a. This enhancement in performance was attributed to the synergistic effect of fibrillar and spherical nanoparticles, which contributed to a more stable conductive network under strain. Among the hybrid sensors, CB/CNTSA-6 exhibited highly reliable performance, while CB/CNF demonstrated significant improvement in drift compared to the standalone CNF sensor. Similar reliable performance for CB/CNT-based nanocomposites was also reported by Huang et al. [118]. Although CB/CNTNC-6 showed improved reliability compared to the standalone CNTNC sensor, the maximum resistance change continued to increase as the cycle number increased, indicating a limitation in the stability of this particular hybrid.

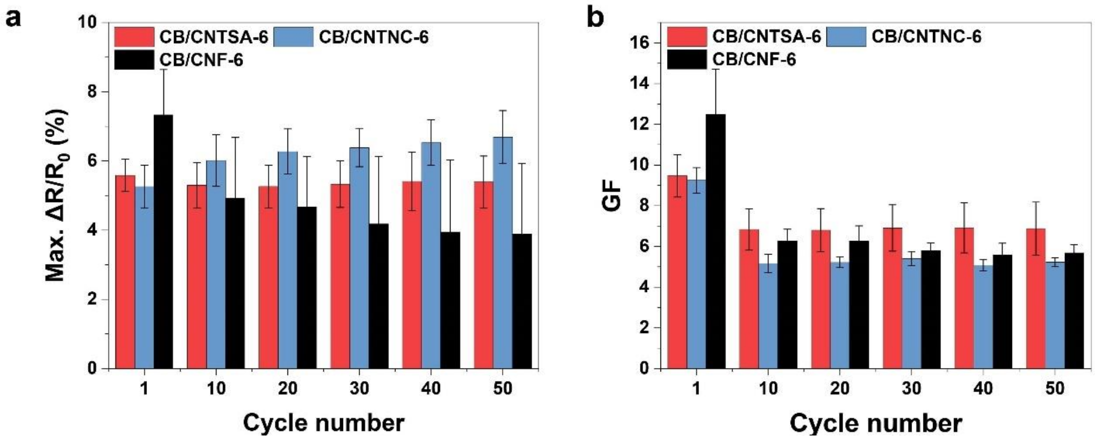

Figure 5.35 : a) Maximum resistance change as a function cycle number and b) gauge factor as a function cycle number for the grid CB/CNTSA-6, CB/CNTNC-6, and CB/CNF-6 grid sensors.

CB/CNTSA-6, CB/CNTNC-6, and CB/CNF-6 exhibited sensitivities of 9.5 ± 1.0, 9.2 ± 0.6, and 12.5 ± 2.2, respectively, which was in line with the anticipated results, higher than the standalone CNTSA, CNTNC, and CNF sensors but lower than the CB sensor. Previous studies have reported improved gauge factor values after hydrazination [205,355]. For example, Zhang et al. found that increasing the CB ratio in CB/CNT nanocomposite strain sensors led to a corresponding increase in sensitivity [355].

The mid-range sensitivities suggest that the sensing mechanisms of both fibrillar and particulate components are involved. In [124,356], transmission electron microscopy (TEM) images revealed three distinct contact nodes in the CB/CNT hybrid system: CNT-CNT, CNT-CB, and CB-CB. The authors concluded that CB particles bridge potential gaps in the network, resulting in a synergistic effect.

The gauge factor values for all hybrid sensors remained relatively unchanged after the first cycle, as shown in Figure 5.35b, demonstrating less dependence on the cycle number and indicating stable sensor performance over repeated loading. It is worth highlighting that the CB/CNTNC-6 sensor exhibited no change in sensitivity after the first cycle, unlike the standalone CNTNC-2 and CNTNC-6 sensors, where sensitivity increased with subsequent cycles. This further emphasizes the stability of the CB/CNTNC-6 hybrid formulation.

All hybrid sensors also exhibited high linearity, as shown in Figure 5.36. This consistency in linearity across both hybrid and single-component sensors highlights the stable and predictable electrical behavior of these materials, making them highly suitable for precise strain-sensing applications. The hybridization of CB with CNTs and CNF appears to preserve the linearity observed in the individual components.

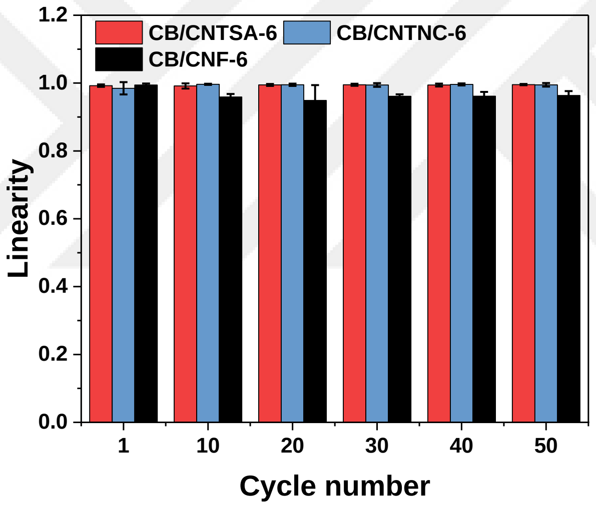

Figure 5.36 : Linearity of CB/CNT-6, CB/CNTNC-6, and CB/CNF-6 grid sensors.

5.5 Summary of the Influence of Geometrical Pattern and Carbon Nanomaterial Type on Strain Sensing Performance

The damage observed at the end of the first cycle quantifies the residual resistance, serving as an indicator of how much the sensor's conductive network is altered during initial loading. The gauge factor represents the sensor's sensitivity to strain, the higher the value, the greater the sensitivity. Our results showed that, regardless of the nanofiller type (0D, such as CB, or 1D, such as CNTSA), the damage after the first cycle and gauge factor values were closely correlated with the sensor pattern, which is quantified by the total length or conductive path, allowing for a simplified comparison.

Sensor length depended on the geometry, with the length increasing in the following order: line, o-line, grid, and omnidirectional geometries (see Table 3.6 for more information).

Our findings show that the degree of damage and gauge factor values in CNTSA and CB sensors is influenced by the geometric pattern, particularly the total length of the conductive path, introducing an additional design consideration for optimizing strain sensor performance. Figure 5.37a presents the damage after the first cycle and the gauge factor calculated for the first cycle as a function of the sensor's total conductive path length for CNTSA sensors. On average, both the damage and gauge factor values decreased as the sensor length increased.

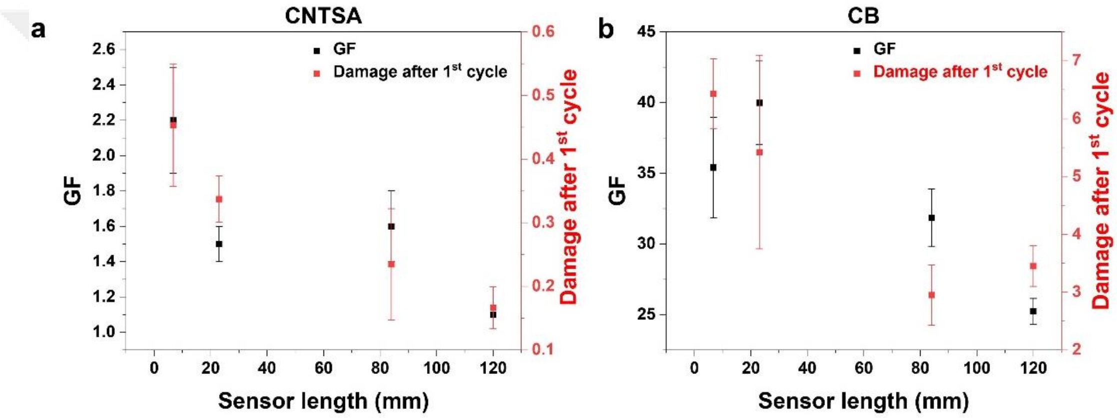

Figure 5.37 : Average gauge factor of the first cycle and damage after the first cycle as a function of total conductive path length for a) CNTSA and b) CB sensors.

Similarly, for CB sensors, the damage after the first cycle and the gauge factor calculated for the first cycle depended on the sensor length, as shown in Figure 5.37b. This suggests that the influence of sensor length on strain sensor performance is independent of the type of carbon nanomaterials used.

Next, a comparison and summary of carbon nanomaterial-based sensors are provided, focusing solely on the material performance using the grid pattern geometry.

The value of the gauge factor and the extent of damage varied significantly depending on the type of carbon filler used, as shown in Figure 5.38a. Fibrillated fillers as in CNTSA and CNF sensors, exhibited relatively low levels of damage, with CNTSA showing a damage value of 0.36 ± 0.28% and CNF at 0.89 ± 0.34%, suggesting that these materials maintain greater structural integrity under strain. These results are consistent with those reported in previous studies on CB [117], CNT [27], and CNF nanocomposites [101]. In contrast, spherical particles like CB showed the highest damage after the first cycle, with a value of 2.95 ± 0.52%. This behavior indicates that CB-based networks are more prone to disruption when subjected to tensile loading. Unlike CB nanocomposites, which tend to accumulate damage after each cycle due to the inherent viscoelastic properties of the polymer matrix [117,348–350], the damage observed in the CB sensor after the first cycle remained unchanged over 50 cycles which increases severity of local damages under cyclic loading. Graphene, on the other hand, exhibited a negative damage value of -0.71 ± 0.78%, indicating rapid change in its electrical network after its first cycle.

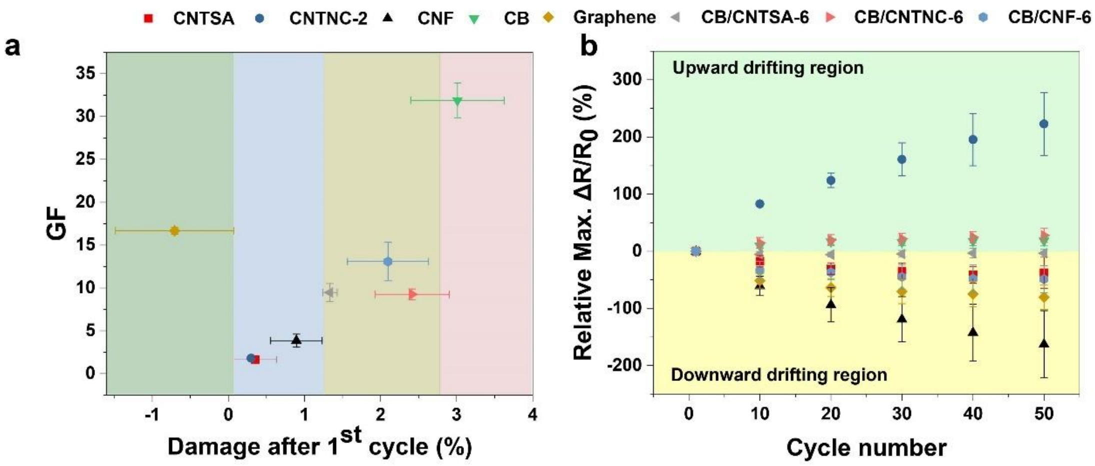

Figure 5.38 : a) Gauge factor (GF) as a function of residual resistance after the first cycle. Sensor types are color-coded as follows: dark red for 0D material-based sensors (*e.g.*, CB), steel blue for 1D material-based sensors (*e.g.*, CNTSA, CNF), dark green for 2D material-based sensors (*e.g.*, graphene), and olive for hybrid sensors combining 0D and 1D materials. b) Relative resistance change as a function of cycle number. Values below zero indicate downward drifting, while values above zero indicate upward drifting. The sensor pattern: grid.

Hybrid sensors demonstrated intermediate damage values, bridging the gap between the fibrillated and spherical particle extremes. For instance, the CB/CNTSA-6 hybrid sensor exhibited a damage value of 1.65 ± 0.37%, while the CB/CNF-6 hybrid had 1.65 ± 0.62%. This intermediate damage values were due to the synergistic effect of fibril and spherical nanoparticles Notably, the damage in the CB/CNTSA-6 hybrid sensor remained unchanged throughout 50 cycles.

The observed damage value correlates directly with the gauge factor of the sensors, with higher gauge factors being associated with greater damage. For instance, the CB sensor exhibited a significantly higher gauge factor of 31.89 ± 1.65, corresponding to its higher damage value, while CNTSA sensors, with a lower gauge factor of 1.5 ± 0.1, exhibited less damage.

As a result, the damage after the first loading cycle emerges as a useful parameter for differentiating the performance of sensors with various carbon fillers, highlighting its importance as an additional design consideration when selecting the carbon filler type and sensor geometry.

Figure 5.38b presents the relative resistance change for various grid sensors, including CNTSA, CNTNC-2, CNF, CB, Graphene, CB/CNTSA-6, CB/CNTNC-6, and CB/CNF-6. An increase in the relative resistance change indicates upward drifting, whereas a decrease reflects downward drifting over time. Among these, the CNTNC-2 sensor exhibited the most severe upward drift. CB-based sensors also showed upward drifting, although to a much lesser extent. In contrast, the CNTSA sensor demonstrated downward drift, but this effect was significantly more pronounced in the CNF and graphene sensors. Interestingly, when CB and CNF were hybridized in the CB/CNF-6 sensor, the drifting behavior was notably reduced, though not entirely eliminated. Similarly, hybrid sensors such as CB/CNTSA-6 and CB/CNTNC-6 exhibited improved signal stability and more reliable performance compared to their standalone counterparts, highlighting the benefits of material hybridization in mitigating drift and enhancing sensor reliability.

5.6 Performance of electromechanical properties of spray-printed sensors

In this section, sensors prepared using spray printing methods were subjected to tensile loading at 0.6% strain for 50 cycles to evaluate their performance. This evaluation focuses on understanding how well the spray-printed sensors handle mechanical strain and maintain functionality under repeated loading, providing insights into the effectiveness and potential of the spray printing approach for sensor fabrication. Three carbon nanomaterials were considered: CNTNC, CB, and CB/CNTNC. Three patterns were assessed: line, grid, and omnidirectional.

5.6.1 CNTNC-based sensors

Using line, grid, and omnidirectional geometries, CNTNC_sprayed sensors and their hosts were subjected to a tensile loading at 0.6% strain for 50 cycles. Representative cyclic loading results are shown in Figure 5.39.

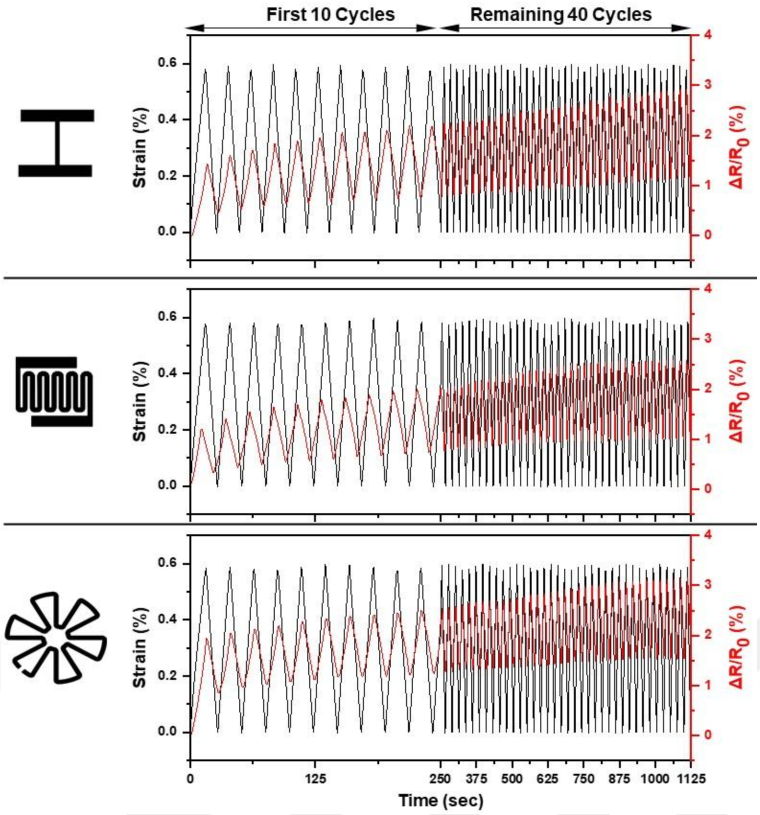

Figure 5.39 : Representative cyclic loading test for line, grid, and omnidirectional CNTNC_sprayed sensors. The first ten cycles are shown in the first half of the x-axis, with the remaining 40 cycles represented in the second half of the axis to highlight the initial loading phase.

Figure 5.40a shows that, irrespective of the pattern, all CNTNC_sprayed sensor designs exhibited an increasing maximum resistance change with the number of cycles, indicating unreliable performance over time. Similarly, screen-printed CNTNC-2 and CNTNC-6 sensors followed the same trend, displaying progressive drift during cyclic loading. The gauge factor of these sensors also increased with increase of cycle number, as shown in Figure 5.40b. Specifically, the line, grid, and omnidirectional patterns demonstrated sensitivities of 2.5 ± 0.3, 2.1 ± 0.6**,** and 3.5 ± 0.3, respectively, in their first cycle.

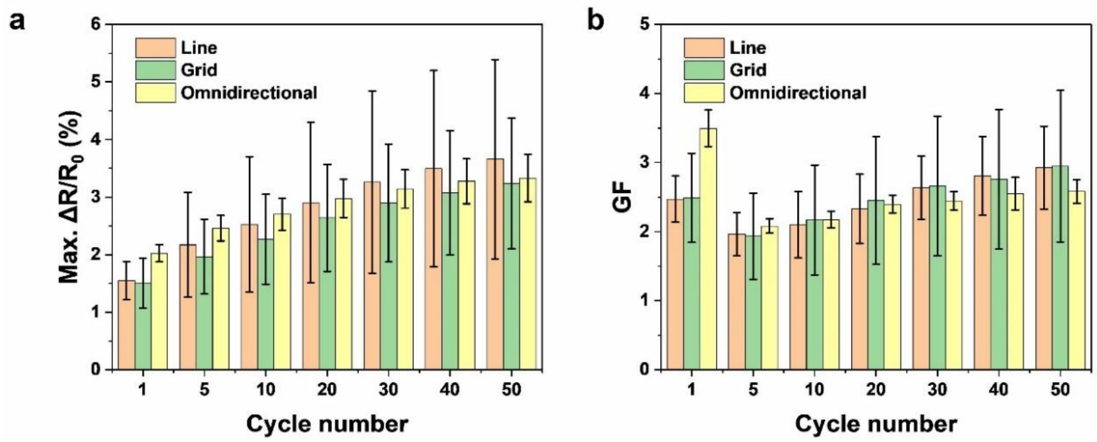

Figure 5.40 : a) Maximum resistance change as a function cycle number and b) gauge factor as a function cycle number for the line, grid, and omnidirectional CNTNC_sprayed sensors.

Figure 5.41 shows that all CNTNC_sprayed sensors exhibited good linear response. Similar results were reported earlier for CNTNC-based screen printed sensors.

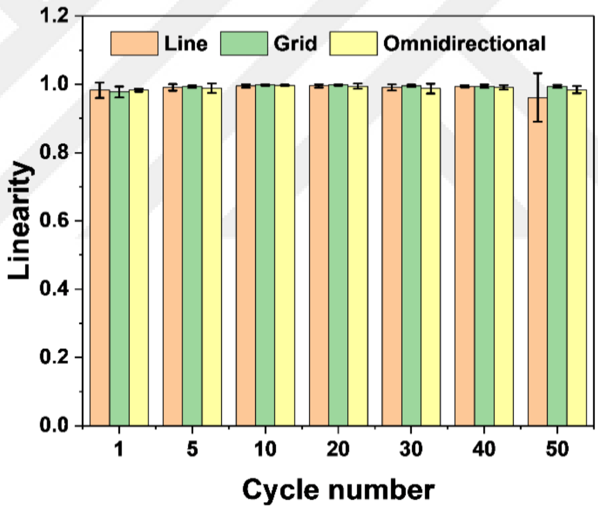

Figure 5.41 : Linearity of line, grid, and omnidirectional CNTNC_sprayed sensors.

5.6.2 CB-based sensors

Using line, grid, and omnidirectional geometries, CB _sprayed sensors and their hosts were subjected to a tensile loading at 0.6% strain for 50 cycles. Representative cyclic loading results are shown in Figure 5.42.

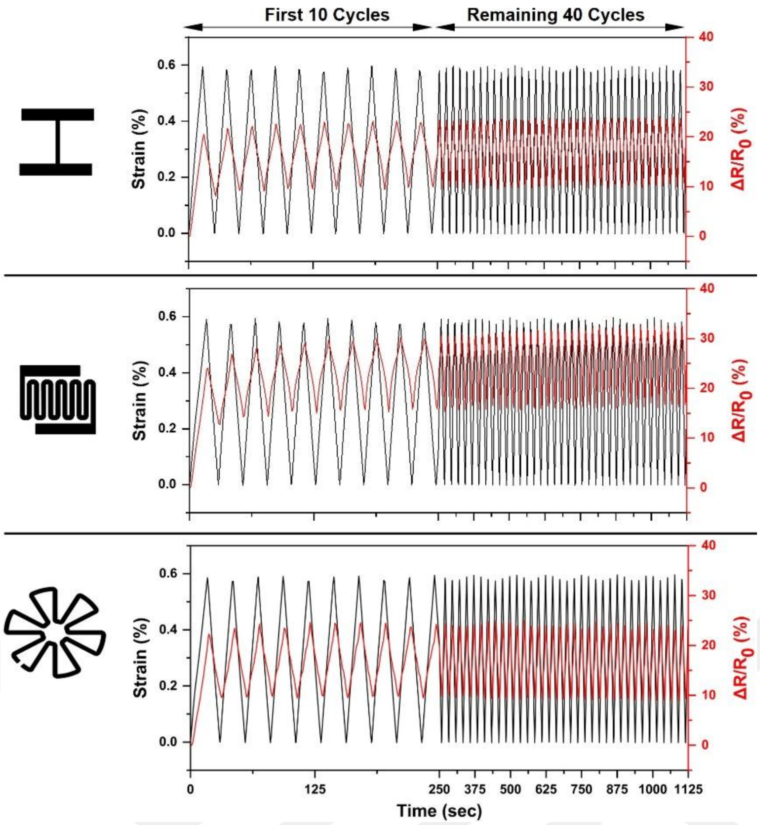

Figure 5.42 : Representative cyclic loading test for line, grid, and omnidirectional CB _sprayed sensors. The first ten cycles are shown in the first half of the x-axis, with the remaining 40 cycles represented in the second half of the axis to highlight the initial loading phase.

Figure 5.43a shows that line and grid CB_sprayed sensors exhibited an increasing maximum resistance change with the number of cycles, indicating unreliable performance, unlike omnidirectional sensor which showed a more reliable behavior. However, after an initial drop in the gauge factor during the first cycle for all sensors, the values increased in subsequent cycles for line and gird sensors. The value of gauge factor of the omnidirectional after the first cycle remained relatively unchanged. This behavior was consistent with the trend observed in CB sensors fabricated using the screen-printing method. The gauge factor values during the first cycle for the line, grid, and omnidirectional sensors were 40.7 ± 1.0, 40.0 ± 1.0, and 38.7 ± 1.4 respectively.

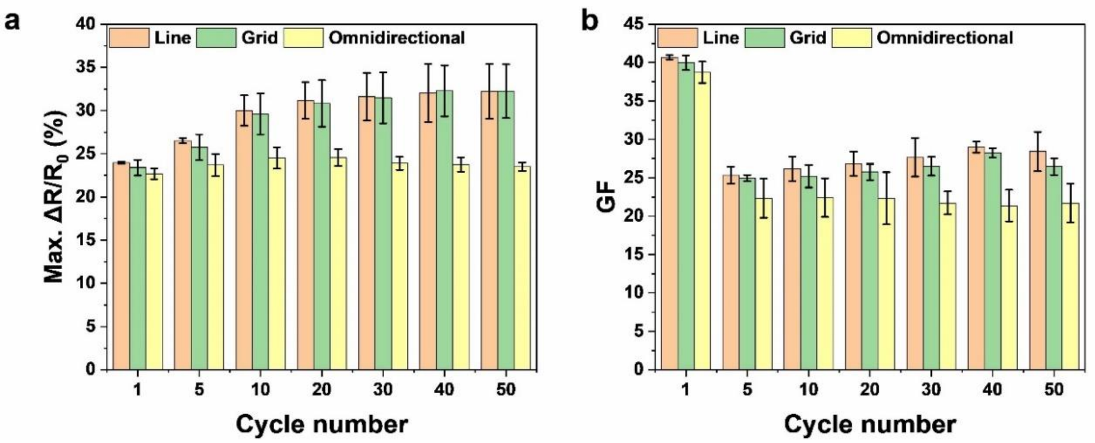

Figure 5.43 : a) Maximum resistance change as a function cycle number and b) gauge factor as a function cycle number for the line, grid, and omnidirectional CB_sprayed sensors.

Figure 5.44 shows that all CB sensors exhibited good linear response during the first five cycles. However, linearity for line and grid dropped after the tenth cycle, unlike the results reported earlier for CB sensors printed using the screen printed method. Difference between results was attributed to difference between fabrication quality of the sensors.

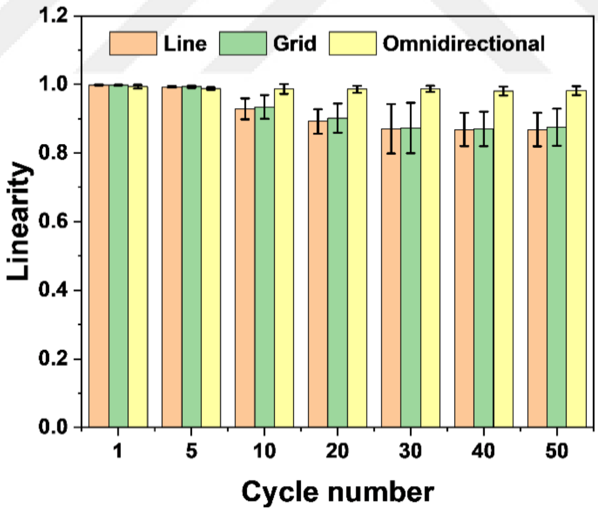

Figure 5.44 : Linearity of line, grid, and omnidirectional CB_sprayed sensors.

5.6.3 CB/CNTNC-based sensors

Using line, grid, and omnidirectional geometries, CB/CNTNC_sprayed sensors and their hosts were subjected to a tensile loading at 0.6% strain for 50 cycles. Representative cyclic loading results are shown in Figure 5.45.

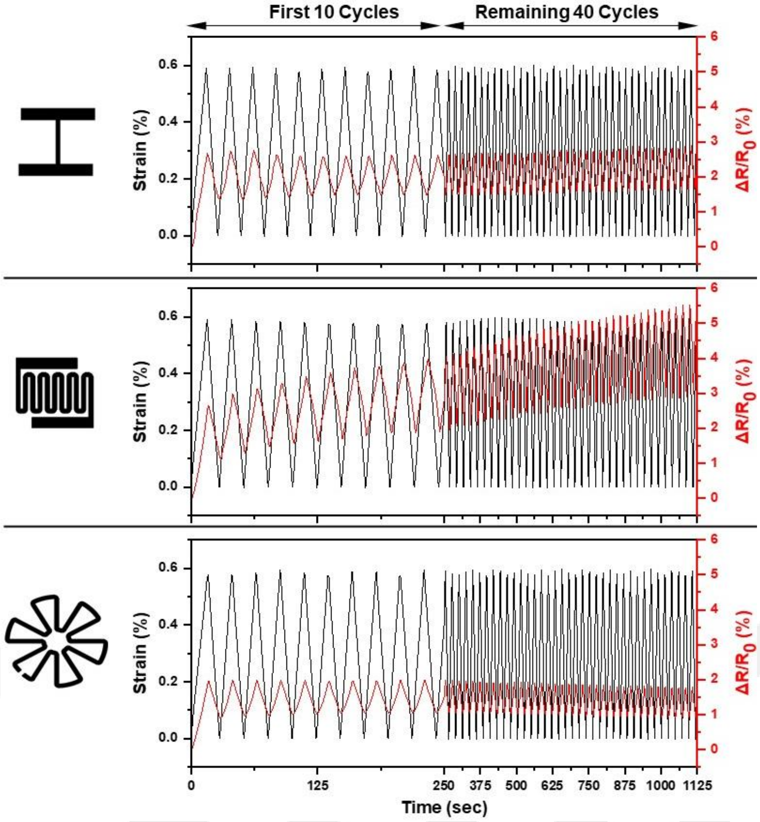

Figure 5.45 : Representative cyclic loading test for line, grid, and omnidirectional CB/CNTNC_sprayed sensors. The first ten cycles are shown in the first half of the x-axis, with the remaining 40 cycles represented in the second half of the axis to highlight the initial loading phase.

Figure 5.46a shows that both line and grid sensor designs exhibited upward drifting, indicating a gradual increase in baseline resistance over repeated cycles. In contrast, the omnidirectional pattern showed no noticeable drifting, suggesting superior signal stability over time. The gauge factor of the grid sensor increased with the number of cycles, whereas the gauge factors for the line and omnidirectional sensors remained relatively unchanged, as shown in Figure 5.46b. Despite the observed drifting, the line and grid sensors demonstrated higher initial gauge factors, 4.5 ± 0.2 for both, compared to the omnidirectional sensor, which exhibited a gauge factor of 3.3 ± 0.6.

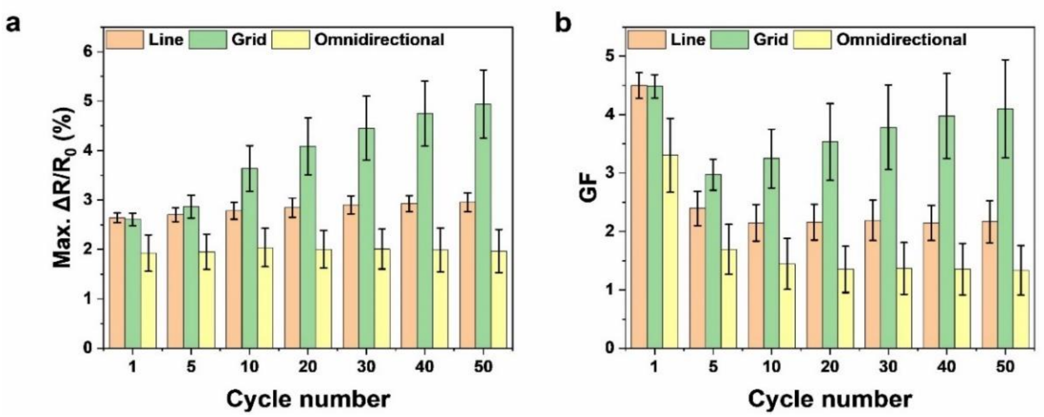

Figure 5.46 : a) Maximum resistance change as a function cycle number and b) gauge factor as a function cycle number for the line, grid, and omnidirectional CB/CNTNC_sprayed sensors.

Figure 5.47 shows that all CB/CNTNC_sprayed sensors exhibited good linear response. Similar results were reported earlier for CB/CNTNC-based sensors printed using screen printing method.

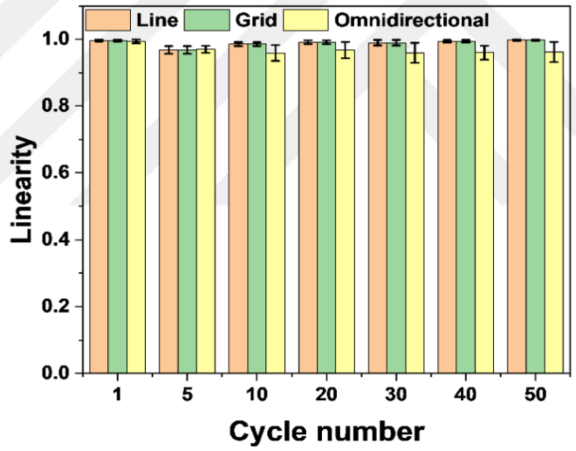

Figure 5.47 : Linearity of line, grid, and omnidirectional CB/CNTNC_sprayed sensors.

5.6.4 How does the printing method shape sensor performance?

Figure 5.48 presents the average gauge factor of screen printed CB and spray printed CB_sprayed sensors as a function of their corresponding average resistance. The results indicate that the screen-printed CB sensor exhibited a significantly wider printed trace compared to the CB-sprayed sensor. This broader geometry resulted in a lower average resistance, which corresponded to a decrease in sensitivity. These observations underscore the importance of printing resolution and trace geometry, as they directly influence both the electrical resistance and the electromechanical response of the sensors.

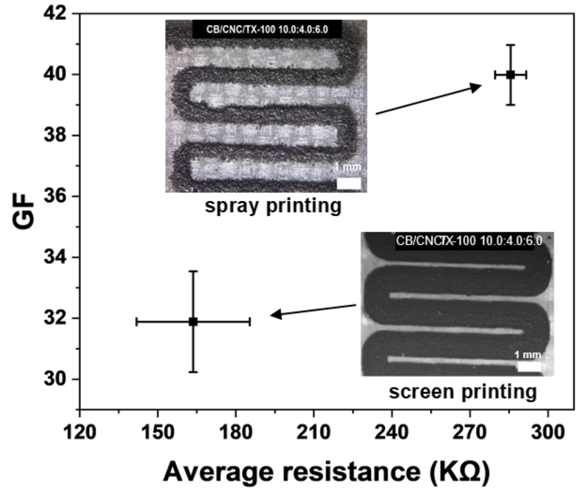

Figure 5.48 : Gauge factor of CB and CB_srpayed sensors as a function of their corresponding average resistance

5.7 Electromechanical Tests of Additional Studies on Hybrid Sensors

5.7.1 Tensile and compressive loading response with four-point bending tests

Screen printed CB sensors, identified as the most sensitive and generally reliable despite a slight upward drift, and CB/CNTSA-6 sensors, noted for their high reliability with mid-range sensitivity, were freshly prepared using a grid pattern. Their GFRP hosts were subjected to tensile loading (one set of sensors) or compressive loading (a separate fresh set) during four-point bending tests at 0.2% strain. Figure 5.49 presents representative cyclic results (10 cycles) of the CB and CB/CNTSA-6 grid sensors under both tension and compression at 0.2% strain. Under both loads, the CB sensors showed larger response compared with CB/CNTSA-6 sensors, as anticipated.

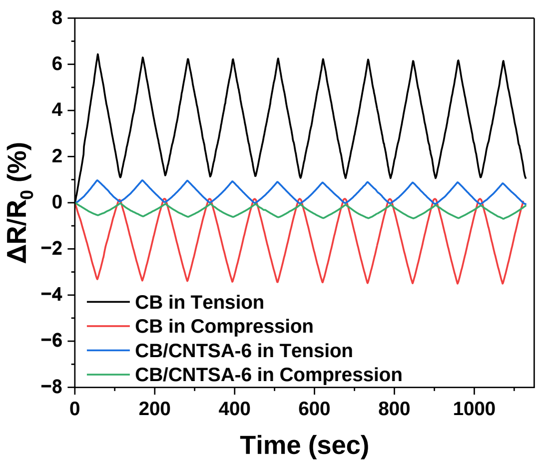

Figure 5.49 : Representative cyclic response (10 cycles) of CB and CB/CNTSA-6 grid sensors under tensile and compressive loading at 0.2% strain, subjected to four-point bending.

The observed difference in resistance change between tension and compression for both the CB and CB/CNTSA-6 sensors can be attributed to the distinct behaviors of the conductive network under these loading conditions. Specifically, during tensile loading, the resistance change was higher and positive, indicating an increase in resistance. This is expected as the conductive pathways in the sensor are stretched, leading to an increase in the resistive elements' distance, causing a decrease in conductivity.

Conversely, under compressive loading, the resistance change was lower and negative. This behavior can be explained by the increase in charge density when the conductive network is compressed. As the material is compressed, the conductive particles and charge carriers are forced closer together, which can enhance conductivity and cause the observed decrease in resistance change [357].

The gauge factors obtained for the two sensors further emphasize the differences in sensitivity between tensile and compressive loading. The CB/CNTSA-6 sensor exhibited a GF of 4.3 ± 0.6 under tension and 3.2 ± 1.1 under compression, while the CB sensor showed a significantly higher GF of 25.8 ± 2.0 in tension and 15.0 ± 0.15 in compression. The higher GF in tension for both sensors suggests that they are more sensitive to strain under tensile forces, which aligns with the anti-symmetric behavior typically observed in CNT-based nanocomposites [54,358].

This enhanced sensitivity under tension could be due to the better alignment of the conductive pathways within the sensor material during elongation. As the material stretches, the conductive particles align more favorably, improving the resistance change and overall sensor response. On the other hand, the lower GF in compression indicates that the conductive pathways are less responsive to strain under compressive forces, likely because compression reduces the movement or reorientation of the conductive pathways, limiting the resistance change.

Despite these differences in behavior, all sensors exhibited excellent linearity across the test conditions, indicating that the relationship between strain and resistance remained consistent and predictable under both tensile and compressive loading.

5.7.2 Multidirectional sensing performance of omnidirectional sensor

The versatility and resilience of the printed sensors were evaluated under cyclic loading applied at varying orientations, reflecting potential real-world application scenarios. Screen-printed CNTSA-based omnidirectional patterns were printed on GFRP substrates at three different angles, 0°, 45°, and 90°, and subjected to 50 tensile cycles at 0.6% strain, consistent with the test conditions described earlier. Figure 5.50 presents the first ten cycles for a clearer comparison. The results indicate that the orientation of the omnidirectional sensors had no significant impact on their performance, demonstrating their multidirectional sensing capability.

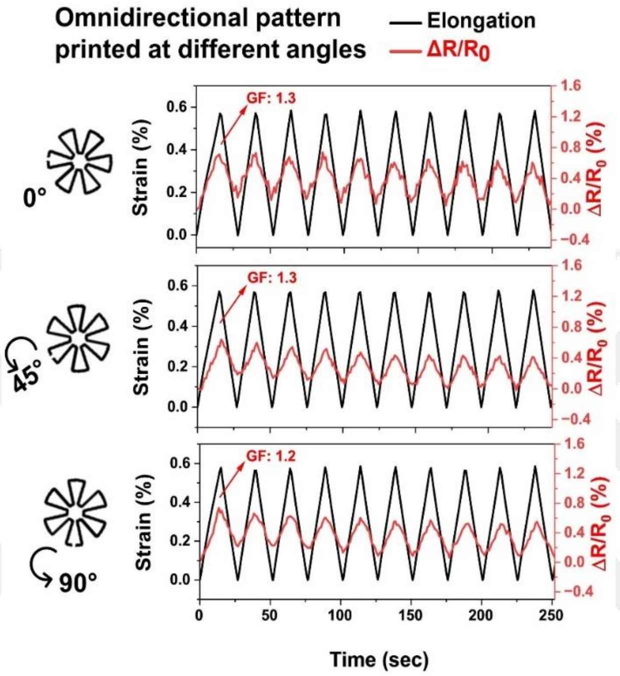

Figure 5.50 : Omnidirectional sensors printed at different angles and subjected to cyclic loading at 0.6% strain.

Figure 5.51 shows the 50 tensile cycles for omnidirectional sensors printed at different angles. Results show that the direction of the omnidirectional sensors had no impact on the sensor’s performance during the 50 cycles.

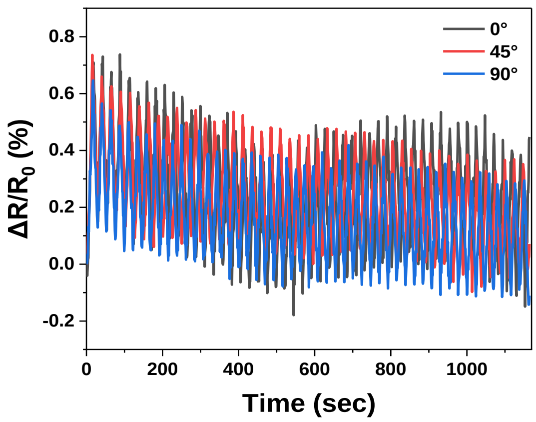

Figure 5.51 : Omnidirectional sensors printed at different angles and subjected to cyclic loading at 0.6% strain for 50 cycles.

5.7.3 Directionality and transverse sensing characteristics of omnidirectional and grid-based sensors

The transverse sensitivity ratio is defined as the gauge factor in the transverse direction divided by the gauge factor in the longitudinal direction, expressed as a percentage. Ideally, this ratio should be minimal, as grid-pattern sensors are engineered for optimal performance when aligned with the applied load direction, hence their unidirectional design feature. For instance, commercial metal strain gauges typically exhibit transverse sensitivity ratios below 1% [359]. However, achieving zero transverse sensitivity for carbon-based strain sensors is challenging due to material properties and manufacturing challenges [359]. Therefore, understanding and minimizing transverse sensitivity is crucial for accurate strain measurements, particularly in high-precision applications, such as in aerospace industry.

At least three identical screen-printed sensors of CNTNC-2, CB, and CB/CNTNC-6, using grid pattern, were prepared and tested to compare their response between the transverse and longitudinal directions under a tensile loading at a strain of 0.6%. Figure 5.52 illustrates the orientation of the grid sensors on GFRP coupons, aligned in both transverse and longitudinal directions, with the applied tensile load indicated by the blue arrows.

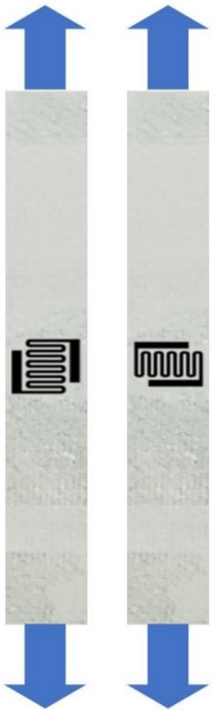

Figure 5.52 : Grid sensors printed onto GFRP coupons in transverse and longitudinal directions relative to the applied tensile load shown in blue arrows.

Figure 5.53 presents the longitudinal and transverse strain responses of CNTNC-2, CB, and CB/CNTNC-6 grid sensors under a tensile strain of 0.6%. The CNTNC-2 sensor demonstrated a relatively consistent response across both orientations, with a gauge factor of 1.8 ± 0.3 in the longitudinal direction and 1.4 ± 0.0 in the transverse direction. This corresponds to a transverse sensitivity of 78%, suggesting an almost isotropic behavior and minimal directional dependence in strain sensing.

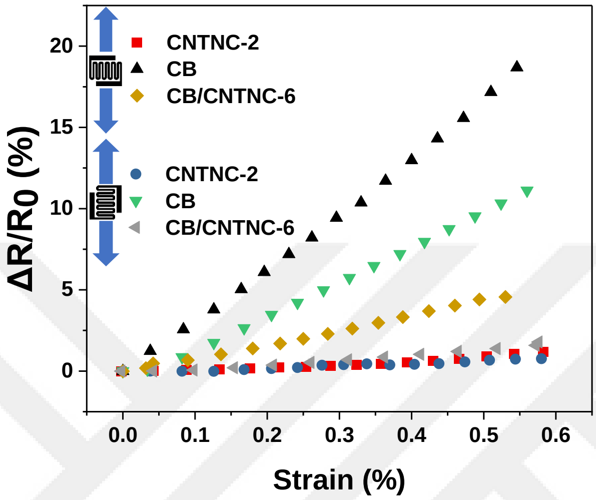

Figure 5.53 : Longitudinal and transverse strain response of CNTNC-2, CB, and CB/CNTNC-6 grid sensors.

The CB sensor exhibited a more directionally dependent response, with the gauge factor decreasing from 31.9 ± 1.7 in the longitudinal direction to 19.0 ± 0.7 in the transverse direction. This yields a transverse sensitivity of 60%, indicating that while the sensor maintains notable performance in both directions, it is more effective when aligned with the strain direction.

The CB/CNTNC-6 hybrid sensor showed the most pronounced directional sensitivity, with a gauge factor of 9.3 ± 0.6 in the longitudinal orientation and 3.8 ± 1.5 in the transverse, resulting in a transverse sensitivity of 41%. This suggests a strong dependence on alignment with the loading direction, potentially due to anisotropy in the distribution or interaction of the CB and CNT components within the grid structure. The transverse sensitivity values of all sensors are summarized in Figure 5.54.

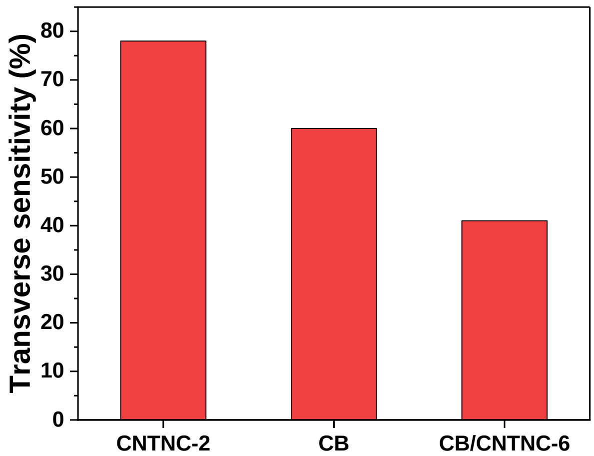

Figure 5.54 : Transverse sensitivity values of CNTNC-2. CB, and CB/CNTNC-6 grid sensors.

5.7.4 Influence of thickness on CNTA sensors

In addition to the geometric pattern and applied load, the thickness of the sensor plays a significant role in determining the electromechanical response. However, studies on the effect of thickness on the piezoresistive response of CNTSAS sensors have yielded conflicting results. Some studies suggest that increasing thickness improves sensitivity [26,327,360,361], while others report the opposite [38,162,362]. To investigate this further, a ten-layer CNTSA o-line sensor was printed onto GFRPs and subjected to tensile cyclic loading at 0.6% strain. The performance of the ten-layer sensor was then compared with the results obtained from the five-layer sensor, which was discussed earlier. Increasing the number of layers from five to ten resulted in a significant reduction in electrical conductivity, from 130 S/m to 49 S/m, and a decrease in the average initial resistance from 10.3 kΩ to 5.5 kΩ. Furthermore, both sensitivity and damage after the first cycle were found to be thickness-dependent. Thicker sensors (ten layers) exhibited lower sensitivity (1.2 ± 0.1) and less damage (0.15 ± 0.02) compared to the thinner five-layer sensors. The increased CNTSA density in the thicker sensors created more conductive paths, which reduced the sensor's sensitivity while also minimizing damage [183].

5.7.5 500-Cycle durability assessment of CB sensors

Since the CB sensor demonstrated good performance at a strain of 0.6% in previous tests, a lower strain level of 0.3% was selected for the 500-cycle tensile test to assess the sensor's long-term reliability and performance stability under less extreme conditions. A freshly prepared CB sensor integrated into its host composite was subjected to this test. Figure 5.55 shows that the sensor exhibited reliable performance across the 500 cycles, with no significant drifting. The sensitivity of the sensor was as high as 17.2 during the first cycle, indicating excellent initial responsiveness. This finding confirms that the CB sensor maintains consistent performance even under repeated cyclic loading at 0.3% strain, demonstrating its suitability for long-term applications in various sensing environments.

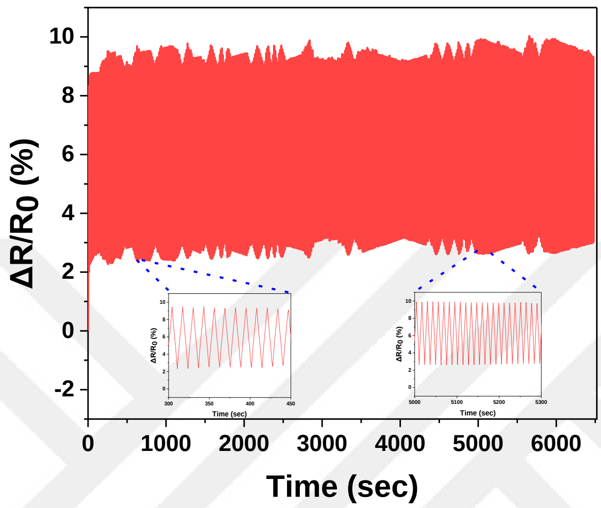

Figure 5.55 : Reliability of CB sensor performance over 500 cycles. The first inset on the right shows a magnification of cycles between 300 and 450, while the second inset on the left highlights cycles between 5000 and 5500.

5.8 Multifunctionality of Carbon-Based Strain Sensors

Temperature variations can affect sensor measurements in SHM applications, making it crucial to monitor temperature [204]. To showcase the multifunctionality of our sensors, the temperature-sensing performance of the grid pattern was assessed using various carbon nanostructures. Screen-printed CNTSA, CNF, CB, CB/CNTSA-6, and CB/CNF-6 based sensors were subjected to a variation in temperature, and TCR was calculated. Three samples of each sensor type were tested over a temperature range of 25 °C to 60 °C. Figure 5.56a shows the resistance change as a function of temperature, with all sensor types exhibiting good linearity and a negative temperature coefficient.

Figure 5.56b illustrates the average TCR for each sensor type. Among the tested sensors, the CNTSA-based sensor exhibited the highest sensitivity, with a TCR of -0.36 ± 0.04 %/°C, followed by the CNF-based sensor with a TCR of -0.21 ± 0.04 %/°C. Notably, the CNT-based sensor showed significantly higher sensitivity compared to previously reported CNT buckypaper, CNT buckypaper/composite [363], and CNT-based nanocomposite grid patterns [364]. The negative temperature coefficient commonly observed in CNT-based sensors is attributed to their semiconductive charge transport properties [205].

In contrast, CB-based sensors exhibited the lowest TCR values. At elevated temperatures, the thermal energy likely enhances the mobility of electrons within the CB network, facilitating the formation or strengthening of conductive pathways between CB particles and reducing the overall resistance [365]. Similarly, hybrid sensors such as CB/CNTSA-6 and CB/CNF-6 displayed sensitivity levels comparable to CB-based sensors. This indicates that hybridization had minimal impact on enhancing sensitivity, likely because electron transfer is primarily confined to CB domains, limiting the influence of temperature changes on electrical resistance.

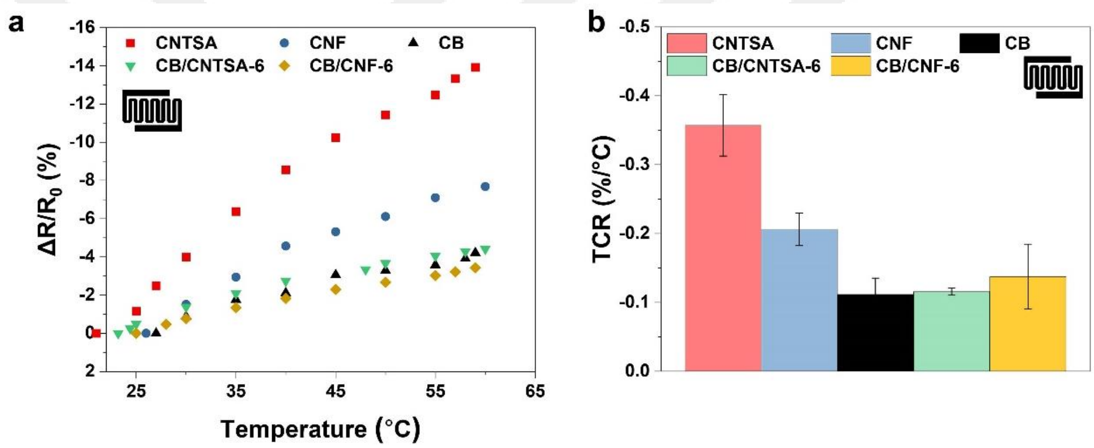

Figure 5.56 : a) Resistance change of carbon-based sensors as a function of temperature, and b) temperature coefficient of resistance for grid geometry for the same carbon-based sensor type.

Varying the sensor length by using the o-line pattern, which is shorter than the grid pattern, resulted in lower sensitivities for both CNTSA and CB-based sensors, as shown in Figure 5.57. This indicates that the conductive path of the sensor plays a crucial role in its performance under temperature variations. For both CB and CNTSA sensors, the grid pattern demonstrated higher TCR values compared to their o-line counterparts.

Interestingly, Buga et al. reported that sensor design has minimal impact on the TCR of sensors. [366]. This discrepancy can be attributed to the significant differences in the initial resistances of the o-line and grid sensors in this study compared to the sensors evaluated in [366].

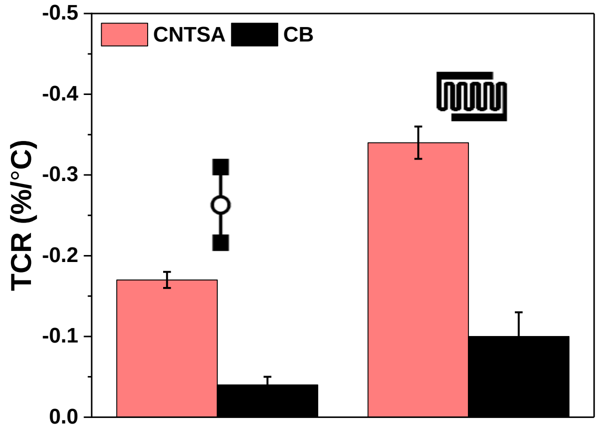

Figure 5.57 : Temperature coefficient of resistance for CNTSA and CB-based sensors using o-line and grid patterns.

The impact from foreign objects, bird strikes, or hail is common in the aerospace industry; thus, a sensor capable of registering it and providing information about its severity of the impact is highly sought-after. The impact test was carried out by dropping a stainless-steel ball (36 g) from 185 cm height onto the sensors to investigate if they are also sensitive to impact damage, as demonstrated in Figure 5.58a. To estimate the energy of the impact, during the test, the air drag was assumed to be negligible on the potential energy used [272]. The percentage resistance change versus time data is provided in Figure 5.58b. The calculated impact energy was approximately 0.6 J. Initial results demonstrate strong potential for screen-printed CNTSA, CNF, CB, CB/CNTSA-6, and CB/CNF-6 sensors to detect and measure impacts on composite structures. Among them, the CB sensor showed the highest resistance change, highlighting its high sensitivity to such impact energy. The hybrid sensors, CB/CNTSA-6 and CB/CNF-6, exhibited moderate sensitivity, while the standalone CNTSA and CNF sensors showed the lowest sensitivity levels.

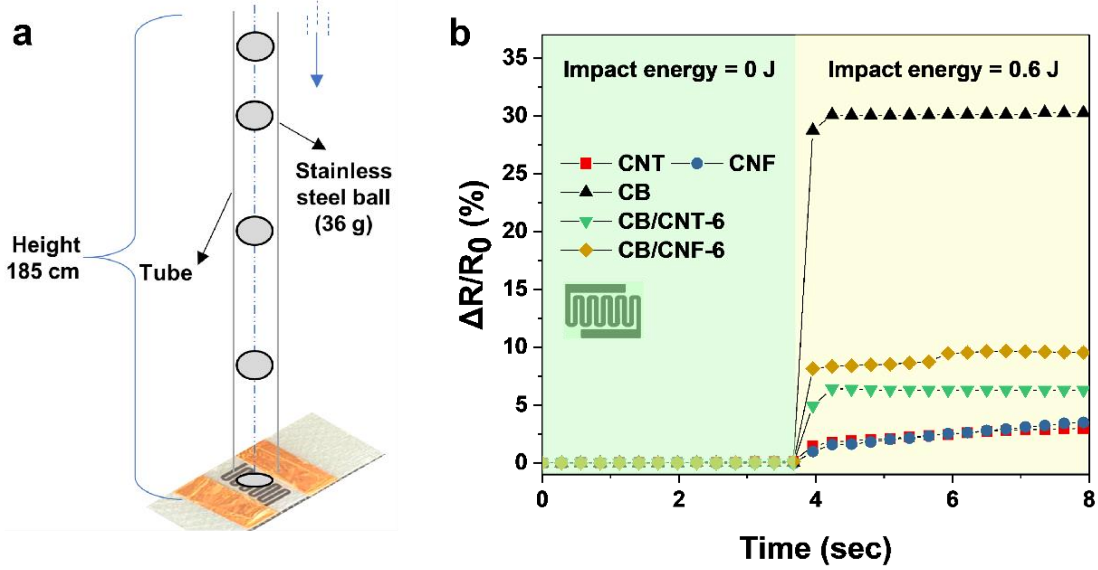

Figure 5.58 : a) Schematic showing the details of the impact testing and b) resistance change before and after grid carbon-based sensors subjected to impact of 0.6 J.

6. PERFORMANCE CHARACTERISTICS OF CARBON-BASED ANTENNA PATCH STRAIN SENSORS

6.1 Introduction

The integration of sensing and wireless communication capabilities into structural materials represents a promising frontier in SHM, especially for aerospace and civil applications. Traditional strain sensors, though widely used, often require wired data acquisition systems, limiting their scalability, real-time responsiveness, and applicability in complex or remote environments. As a result, there has been increasing interest in the development of multifunctional, structurally integrated sensors capable of both detecting mechanical deformation and enabling wireless interrogation.

Among emerging solutions, antenna-based strain sensors have gained attention due to their ability to transduce mechanical strain into shifts in electromagnetic response, which can be remotely detected via radio frequency interrogation. By leveraging changes in the antenna’s geometry or material properties under strain, such systems can enable passive or semi-passive wireless sensing platforms. However, challenges remain in achieving robust mechanical integration with structural substrates, maintaining antenna performance under deformation, and simplifying fabrication processes for large-scale or complex geometries.

In this context, carbon-based materials offer unique advantages due to their tunable electrical properties, flexibility, and compatibility with scalable printing techniques. When printed onto fiber-reinforced polymer composites, these materials can serve as the conductive elements of patch antennas while also mechanically conforming to the host structure.

This chpater presents an initial step toward integrating sensing and communication functionalities within structural materials by developing a carbon-based antenna patch strain sensor directly printed onto GFRPs, with the long-term goal of enabling real-time monitoring through enhanced responsiveness and remote interrogation. Herein, carbon-based antenna strain sensors were directly printed onto GFRPs, leveraging their structural integration and electromagnetic responsiveness. The GFRP substrate, approximately 1 mm thick, served as the dielectric layer for the antenna. To evaluate the antenna's behavior, the reflection coefficient (S_{11}) was measured using a VNA, an instrument that characterizes the reflection and transmission of radio frequency devices like antennas. While the VNA primarily provides information on impedance matching and reflection, it does not fully capture radiation efficiency or detailed antenna patterns. S_{11} represents the amount of power reflected from the antenna back to the source and serves as a key parameter for assessing impedance matching as well as potential radiation or absorption characteristics. In this study, impedance matching between the antenna and the VNA was not explicitly optimized through additional matching networks; instead, standard VNA calibration was performed, and the antenna was connected via an SMA port to the VNA. The S11 parameter was measured to identify the resonant frequency and evaluate basic reflection characteristics. More detailed characterizations, including the antenna's radiation pattern, electromagnetic field polarity, and overall radiated power, have not yet been conducted and are planned for future research. These measurements are crucial for thoroughly assessing the antenna's performance in wireless strain sensing applications and will be addressed in subsequent studies.

To begin the investigation, reflection behavior under static conditions was examined, followed by the analysis of strain-induced shifts in resonance. These results provide initial insights into the feasibility of using printed antenna structures as wireless strain sensors. In addition to uniaxial strain evaluations, Section 6.2 builds on this by exploring the performance of two antenna designs, including a mirrored variant, and examining their response under bending forces to simulate more complex mechanical deformations.

6.2 Reflection Behavior and Strain Sensitivity of Screen-Printed CNTSA/CB-Based Antenna Sensors

This subsection begins the detailed investigation into the performance of the carbon-based antenna strain sensors. Specifically, we focus on the reflection behavior and strain sensitivity of antenna patterns fabricated using the screen-printing method with CNTSA/CB-6 ink directly applied onto GFRP substrates. The design and dimensions of the patch antenna is shown in Figure 6.1.

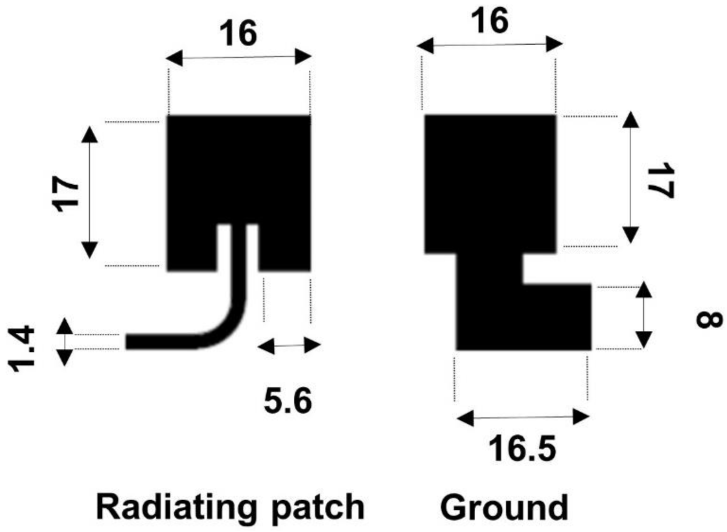

Figure 6.1 : Dimensions of radiating patch and ground plane (in mm).

To test the signal reflection characteristics of the antenna sensor, the VNA was configured with an intermediate frequency (IF) bandwidth of 50 Hz. The measurement range was set between 6 GHz and 8 GHz, divided into 2001 points, resulting in a frequency step size of 1 MHz. This frequency range was selected because the antenna's resonant frequency falls within it, and it lies within the microwave spectrum, overlapping with frequency bands commonly studied in radar and communication research. Averaging was turned off during the measurements to preserve the raw data.

Figure 6.2 illustrates the performance of the CB/CNT-based antenna sensor under monotonic strain conditions. Specifically, Figure 6.2a shows the variation of the S_{11} parameter (return loss) as a function of frequency for increasing levels of applied strain. For better clarity and visualization, selected strain values are presented in the plot.

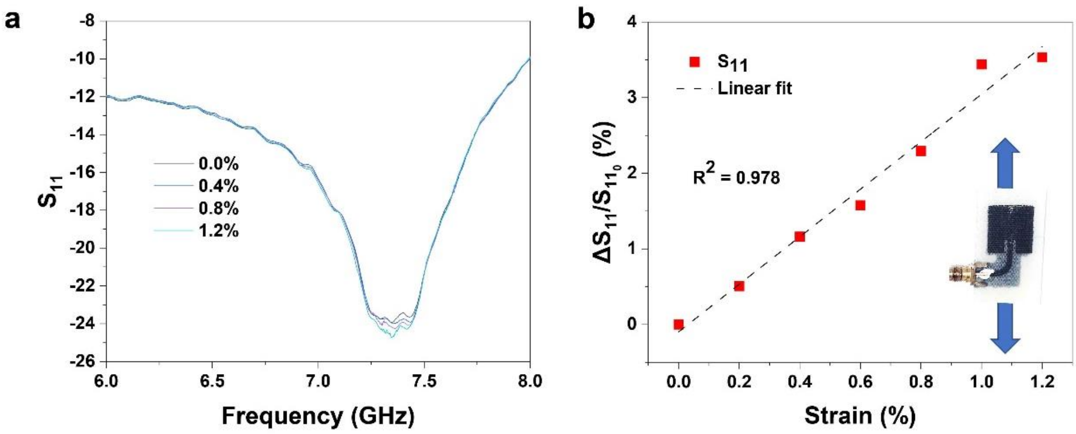

Figure 6.2 : a) Frequency response of the printed antenna at various strain values and b) change in S_{11} parameter value as a function of the applied strain.

The S_{11} data was extracted and averaged over the frequency range of 7.3 to 7.35 GHz to minimize noise and focus on the region of interest. This averaged S_{11} data was subsequently used to compute the change in the S_{11} parameter, which is plotted as a function of strain in Figure 6.2b. Additionally, the inset figure in Figure 4b provides a schematic representation of the direction of the applied force relative to the radiating patch of the antenna. The results demonstrate that the CNT/CB-based antenna sensor exhibited a linear response to the applied strain, indicating its potential for accurate and predictable strain sensing applications. Using equation 3.9, the calculated sensitivity was as high as 3.1 which is larger than conventional metallic strain gauges.

It should be emphasized that the frequency changed only minimally, as previously demonstrated in Figure 6.2a. However, in the literature, frequency shifts under strain have been observed in printed antennas. For instance, Mahmoud et al. reported a frequency shift under strain and quantified the sensitivity of their silver-based printed sensor as the change in frequency divided by strain [367]. We believe that the minimal frequency shift in our case is due to the lower conductivity of the printed CNTSA/CB-based sensor. Additionally, the measured S_{11} value was approximately –24 dB, indicating a significant return loss. This suggests that while the antenna efficiently absorbs power at the resonant frequency, a considerable amount of energy may still be dissipated due to the inherent material losses in the conductive network.

To investigate the effect of sampling size on the frequency measurements, the same CNTSA/CB-based antenna sensor was re-evaluated under adjusted test conditions. For this experiment, the sweeping parameters of the VNA were modified. The VNA was configured with an IF bandwidth of 20 Hz, covering a frequency range of 1 GHz to 18 GHz, with a total of 1701 points. This adjustment resulted in a step size of 10 MHz. Averaging was disabled during the measurements to maintain the raw data integrity.

By reducing the number of sampling points, the measurement time was significantly decreased. However, the IF bandwidth was lowered to 20 Hz to ensure higher measurement accuracy despite the fewer samples. This trade-off was necessary to minimize noise and maintain reliable detection of resonant frequency shifts, even with a coarser frequency resolution. While this setting limited the frequency granularity, it provided a good balance between speed and measurement fidelity, enabling clearer interpretation of strain-induced frequency variations.

Figure 6.3a presents the results of repeated tests conducted on the antenna sensor under slightly higher strain levels, reaching up to 1.4%. Similar to the previous experiment, the S_{11} parameter data was extracted and averaged over the frequency range of 7.3 to 7.35 GHz. The sensor's performance, as depicted in Figure 6.3b, remained highly linear, with a coefficient of determination (R^2 value) of 0.984. This demonstrates the antenna sensor's consistent and reliable response to strain, even with adjustments to the sampling and measurement parameters. The calculated sensitivity of the antenna sensor reached a maximum value of 4.1, representing an improvement compared to the first test. This increase in sensitivity can likely be attributed to the slightly higher strain applied during this test compared to the previous experiment.

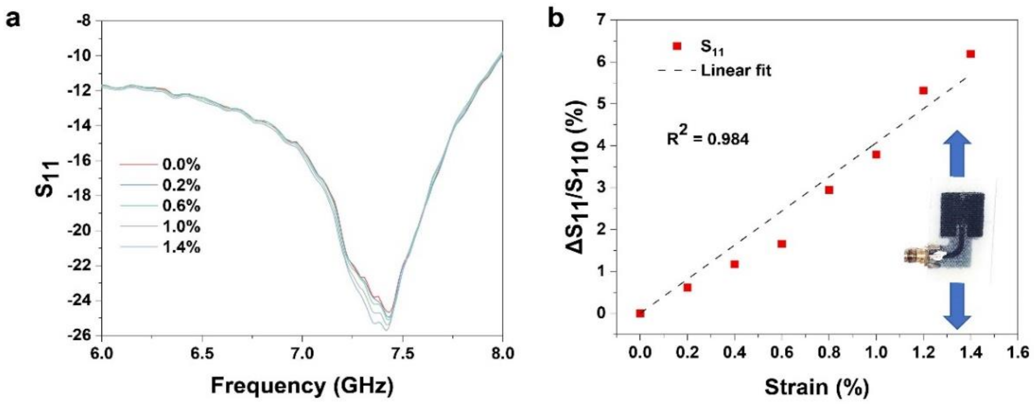

Figure 6.3 : Retesting of the strain sensors antenna a) frequency response of the printed antenna at various strain values and b) change in S_{11} parameter value as a function of the applied strain.

In summary, our investigations demonstrated that the CNTSA/CB-based antenna strain sensor exhibited a highly linear response to applied strain, achieving sensitivities as high as 4.1, surpassing conventional metallic strain gauges. While the reflection coefficient indicated efficient power absorption, we observed only a minimal frequency shift under strain, which we attribute to the lower conductivity of the printed carbon-based material. It is important to note that monitoring antenna performance through frequency shift is generally considered a more robust and reliable method for sensing applications than relying solely on S_{11} changes, as frequency is inherently less susceptible to external noise and connection variations. To address this limitation and significantly enhance the antenna's sensitivity to frequency shifts, the subsequent section focuses on substantially improving the electrical conductivity of the conductive network. This will be achieved by transitioning to the exclusive use of

CNTs for their superior conductivity and by employing spray printing to enable higher material deposition and the formation of more effective conductive pathways.

6.3 Signal Reflection and Bending Response of Spray-Printed CNTNC-Based Antenna Sensors

6.3.1 Antenna design and simulation results

Building on the findings from Section 6.1, this section delves into an advanced approach for developing carbon-based antenna strain sensors. To overcome the conductivity limitations identified previously, we shifted to spray-printing CNTNC-based ink onto GFRP substrates, enabling significantly greater material deposition and, consequently, improved electrical conductivity. We designed and fabricated two distinct patch antenna variants (both featuring an enlarged ground plane for enhanced electrical conductivity and uniformity) to thoroughly compare their performance, as illustrated in Figure 6.4a-b. In both designs, the ground patch was enlarged to cover the entire surface of the GFRP laminate. Additionally, the radiation patch in the second design featured a symmetric geometry, as detailed in, as shown in Figure 6.4b. This symmetry was primarily introduced to simplify its electromagnetic modeling and to potentially offer more predictable resonant behavior, making the design process more straightforward.

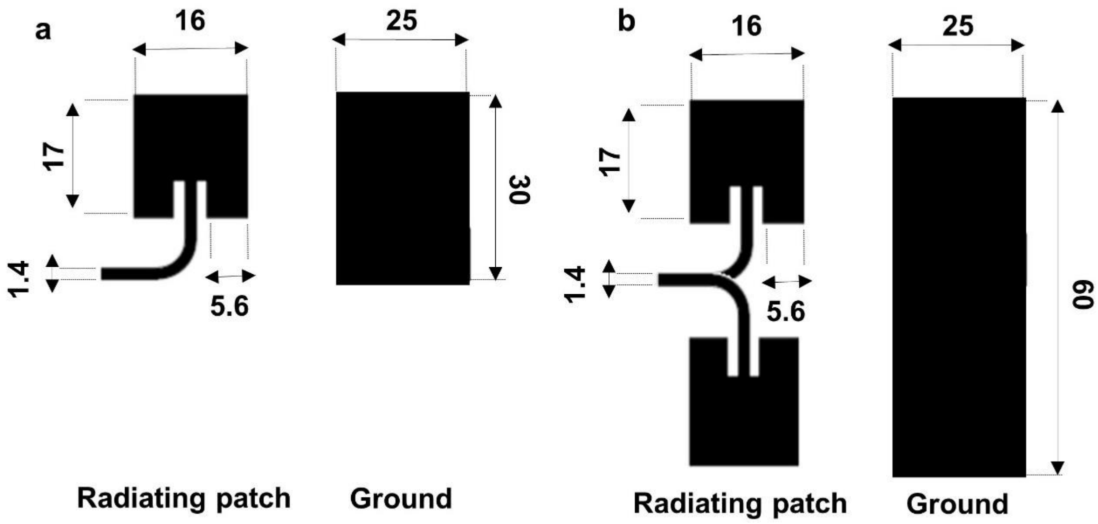

Figure 6.4 : Dimensions of the radiating patch and ground plane (in mm) for a) the original antenna design and b) the symmetric patch design, where the radiating structure is mirrored.

Based on the simulated S-Parameters (S_{11}) presented in Figure 6.5, a detailed analysis of the reflection characteristics for the first design and the second symmetric antenna design is possible. This figure illustrates the magnitude of the reflection coefficient in dB across a broad frequency range, providing insights into their impedance matching and resonant behavior.

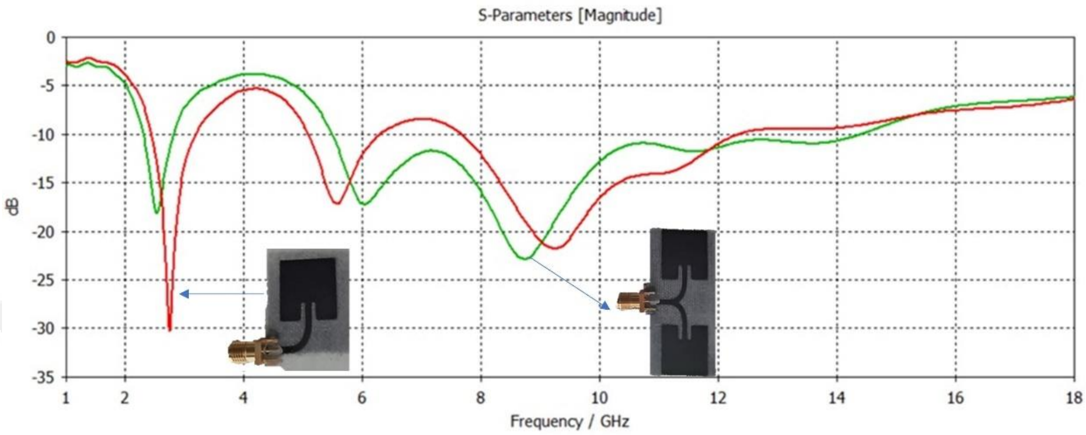

Figure 6.5 : Simulated S-Parameters (magnitude of S_{11} in dB) as a function of frequency (GHz) for the two antenna designs.

Upon examination, both antenna designs exhibit multi-band resonant characteristics, indicating their potential for operation across several distinct frequency bands. The first design (single-leaf) demonstrates a significantly deep primary resonance around 3.0 GHz, reaching approximately -30 dB. This deep dip signifies good impedance matching at this frequency, implying that nearly incident power is transferred to the antenna. Additional, albeit shallower, resonances are also observable for this design at higher frequencies, 5.5 and 9.0 GHz.

In contrast, the second symmetric antenna design (double-leaf) shows its deepest resonance around 9 GHz, with a return loss of approximately -23 dB. While this still represents good impedance matching, it is less pronounced than the primary resonance of the first design. The symmetric design also exhibits several other shallow resonant frequencies across the spectrum, including notable dips around 2.5 GHz and 6.0 GHz.

The differences in the resonant frequencies, depths, and bandwidths between these two designs underscore the impact of their respective geometries, particularly the introduction of the symmetric radiation patch in the second design and the enlarged ground plane common to both. These simulated results are crucial as they provide a theoretical foundation for understanding the electromagnetic behavior of these spray-printed carbon-based antenna sensors, with the observed variations in impedance matching and resonant characteristics informing the interpretation of their subsequent experimental performance.

6.3.2 Antenna fabrication and experimental validation

Following the theoretical insights gained from the simulations, the designed antenna patterns were actualized through spray printing onto GFRP substrates using the CNTNC-based ink. This fabrication process allowed for direct integration of the sensors onto the structural components, leveraging the improved conductivity discussed earlier. After spray-printing the radiating patch onto one surface of the GFRP substrate and allowing it to dry, as shown in Figure 6.6, the ground layer was printed onto the opposite side. Subsequently, their S_{11} was measured under measured under a no-strain condition to establish their baseline electromagnetic performance.

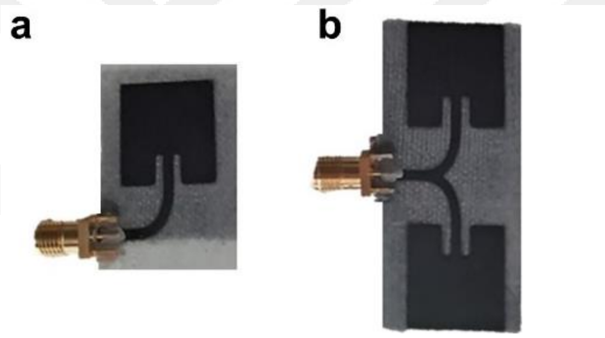

Figure 6.6 : Printed radiating patch of a) the first antenna design and b) of the symmetric antenna design.

However, a noticeable discrepancy was observed between the experimentally measured S_{11} results, as shown in Figure 6.7, and the simulated predictions (see Figure 6.5). While the simulations provided an ideal theoretical framework, the real-world printed antennas exhibited variations in resonant frequencies, return loss depths, and overall bandwidth compared to their simulated counterparts. For instance, for the first design antenna, simulation results show a resonant dip at around 3.0 GHz, suggesting good impedance matching and potential radiation at that frequency. However, the experimental results differ significantly: a shallow dip is observed around 5.0 GHz, and a deeper resonance occurs near 7.0 GHz, as shown in Figure 6.7. Similarly, for the symmetric antenna design, the simulation shows shallow resonances near 2.0 GHz and 6.0 GHz, with a deeper resonance occurring around 9.0 GHz. In contrast, the experimental data display a single pronounced resonance around 8.0 GHz, suggesting a compression or merging of multiple expected resonant modes.

These observed divergences for both designs can be attributed to several practical factors inherent in the fabrication and measurement processes. Key among these are potential variations in the printed trace dimensions and thickness due to the spray printing process, which deviate from the perfectly defined geometries in the simulation model. These variations, including slight under-printing of trace widths or differences in gap spacing, can shift the effective electrical length of the antenna. Furthermore, the actual electrical conductivity and permittivity of the composite material (printed CNTNC on GFRP) may not precisely match the idealized values used in the simulation, leading to inherent shifts in resonance. For the symmetric design, additional factors like overlapping effects of substrate non-uniformity or boundary conditions not fully captured in the simulation, as well as minor misalignments or inconsistencies during fabrication, could have significantly altered the current distribution. Lastly, minor imperfections in the contact resistance at the SMA connector interfaces and environmental factors during testing can also contribute to these observed differences.

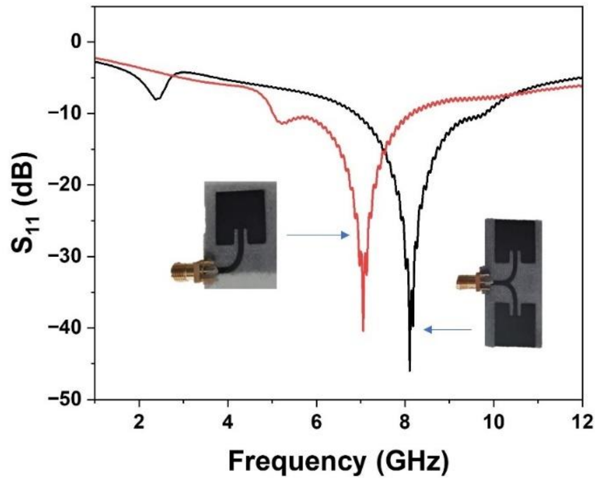

Figure 6.7 : Frequency response of the spray-printed CNTNC-based antenna in the unbent position for the two designs.

6.3.3 Antenna sensor response under bending

This subsection details the experimental investigation into the mechanical robustness and strain-sensing capabilities of the antenna sensors under bending forces. Moving beyond uniaxial strain, the host composite structures integrated with the antenna sensors were subjected to bending at three distinct angles: an unbent (flat) condition serving as the baseline, a slightly bent state (approximately 8 mm radius of curvature), and a more significantly bent state (approximately 7 mm radius of curvature) (see Figure 3.11 for more details about bending test procedure). The bending direction is shown in Figure 6.8.

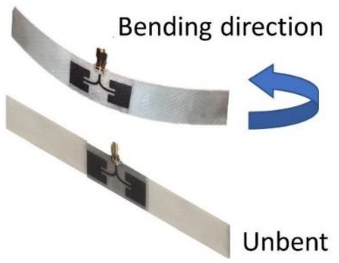

Figure 6.8 : Schematic representation of the bending direction, where the radiating patch is subjected to tensile stress (see Figure 0.1 and read Section 3.11 for more details about bending test procedure).

The frequency response of the spray-printed CNTNC-based antenna (first design) shows a clear shift in resonant frequency after bending at two different curvatures, compared to the unbent state, as demonstrated in Figure 6.9. This shift indicates that mechanical deformation affects the antenna's electromagnetic characteristics. This phenomenon is primarily attributed to the bending-induced variations in current distribution and the effective electrical length of the printed patch and ground plane under strain. Such predictable frequency shifts are highly desirable for wireless strain sensing applications, and this observation aligns with similar results reported for wireless antenna sensors subjected to mechanical deformation [368]. However, further experimental validation is needed to assess the repeatability and sensitivity of this response under varying strain conditions.

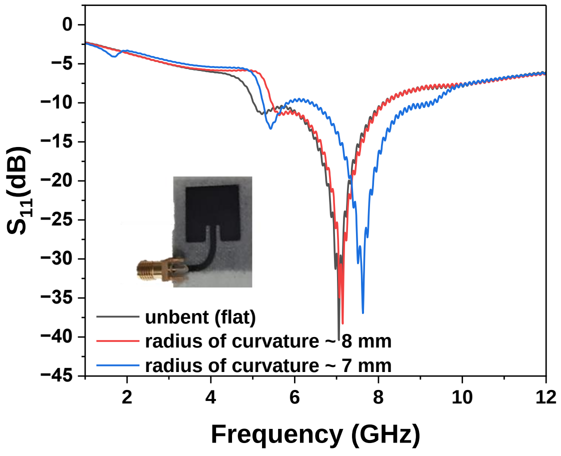

Figure 6.9 : Frequency response of the spray-printed CNTNC-based antenna (first design) in the unbent state and after bending at two radii of curvature.

A similar trend in frequency shift was observed for the spray-printed CNTNC-based antenna with the symmetric patch design when bent at two different angles compared to the unbent state, as demonstrated in Figure 6.10. Importantly, the frequency shifts occurred consistently in the same direction as seen in the first design, which confirms the repeatability and reliability of the antenna's response to mechanical bending. This consistency suggests that the antenna's performance is predictable under strain, an encouraging finding for practical applications where mechanical deformation is unavoidable. The symmetric patch design, by maintaining this stable trend, further demonstrates the potential for optimized geometries to enhance antenna resilience under bending.

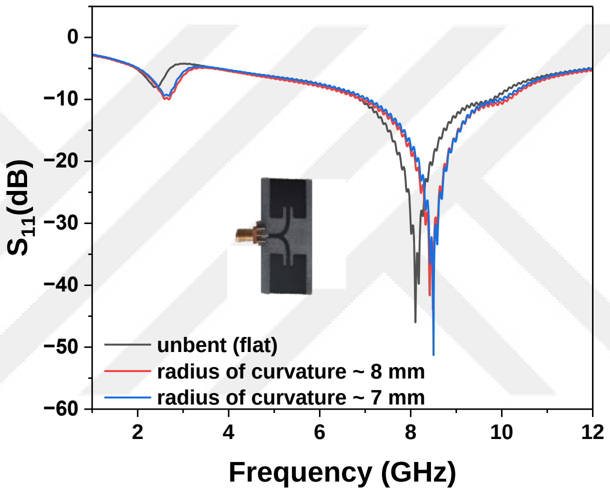

Figure 6.10 : Frequency response of the spray-printed CNTNC-based antenna with the symmetric patch design in the unbent state and after bending at two radii of curvature.

While the observed frequency shift under bending demonstrates the sensor's potential for wireless strain sensing, several aspects require further investigation. In particular, assessment of the radiation pattern in an anechoic chamber is necessary to evaluate the directionality and efficiency of signal emission. Although the sensor exhibited characteristics consistent with communication-capable antenna patch devices, its actual communication range remains unclear due to limitations in the current testing setup. The spray-printed sensors showed promise for transmitting data wirelessly. In future implementations, such antenna patch sensors could be used to communicate information about structural conditions, such as cyclic or residual strain, or overall loading states. Fully characterizing the sensor's radiation behavior and transmission capabilities will be essential to realizing this functionality.

7. CONCLUSIONS AND RECOMMENDATIONS

In this PhD dissertation, carbon nanomaterial-based strain sensors were successfully transferred onto GFRPs, demonstrating their potential as sensory systems for structural health monitoring. The first major finding was the piezoresistivity of CNT/CNC coatings on GFRPs, confirming their applicability for strain sensing.

The second key contribution involved improving the printing quality of screen-printed sensors and correlating it with rheological property changes. This enabled the fabrication of unique strain sensors with different geometries. The electromechanical performance of the sensors was shown to depend on the geometrical pattern, particularly the total conductive path length.

Furthermore, sensor performance was enhanced by hybridizing 1D and 0D particles, as in CB/CNT and CB/CNF-based sensors, which outperformed standalone CNT- and CNF-based sensors. An unexpected but important finding was that CB-based sensors exhibited highly linear and sensitive responses, despite the typical nonlinearity associated with 0D particles under strain. This behavior was attributed to the direct integration of CB as a printed sensor without a polymer matrix.

Finally, the research explored the fabrication of antenna patch sensors via printing, showing early promise for their use in strain sensing applications. This integration of printed antenna patch functionality onto composite structures opens a novel direction toward future wireless sensing systems. Overall, the thesis provides new insights into the formulation–processing–performance relationship for printed carbon-based strain sensors on GFRPs and introduces foundational work combining strain sensing with electromagnetic functionalities.

7.1 Conclusion

The following summary of key findings from Chapter Four highlights the ink formulation process, rheological behavior, and the resulting quality of sensor deposition and performance.

1. Direct coating (direct application of CNTSA/CNC ink onto GFRPs)

The study introduced a straightforward method for applying CNTSA/CNC-based ink onto GFRP substrates. While this approach enabled quick and accessible deposition, it presented limitations in achieving precise control over the printed geometry and the amount of ink delivered. Nevertheless, the CNTSA/CNC-based inks exhibited shear-thinning behavior, and their viscoelastic properties depended on the total solid content, which proved advantageous for compatibility with scalable printing techniques such as screen and spray printing.

2. Screen printing:

Rheological analysis confirmed that all tested carbon nanomaterial-based inks, including CNTSA/CNC-based formulations, exhibited shear-thinning behavior, which is a crucial property for screen printing as it facilitates smooth ink flow through the mesh. To evaluate printability under realistic conditions, a screen printing simulation test was also conducted. The study demonstrated that aqueous-based inks could be successfully printed onto GFRP substrates by carefully adjusting the ink's total concentration. Increasing the concentration shifted the ink's texture from a more fluid, liquid-like consistency to a paste-like state more suitable for deposition. Printability challenges related to surface tension and poor wettability were mitigated by using a water and IPA solvent mixture. Further improvement in wettability and deposition quality was achieved by incorporating TX-100 as a co-surfactant, which significantly enhanced the printability of CB-based inks in particular. The observed improvement in printing quality correlated strongly with changes in the rheological properties of the inks, allowing for a better understanding of changes occurring in the ink.

3. Spray printing method:

The total concentration of the ink was found to significantly influence its viscosity, which in turn affected its sprayability during deposition. Similar to its beneficial role in screen printing, the addition of TX-100 also enhanced printability in spray printing processes. Furthermore, increasing the mask thickness beyond 0.4 millimeters proved advantageous for achieving better print quality.

The following summary of key findings from Chapter Five includes the electrical properties of coated and screen-printed sensors, as well as the electromechanical performance of sensors produced by screen and spray printing.

1. Electrical properties

An increase in the CNC content beyond the one-to-one ratio in the CNTSA/CNC formulations led to a decline in the electrical stability of the printed sensors. This adjustment also impacted the initial resistance values, indicating that excessive CNC content may disrupt the conductive network and compromise the overall sensing performance.

The electrical properties of CNTSA/CNC-based screen-printed sensors were found to depend strongly on the number of printed layers. Increasing the number of layers improved the formation of the conductive network, which in turn enhanced electrical performance. This improvement was reflected in reduced electrical noise and more consistent linearity during tensile loading. Joule heating was not observed at applied voltages below 8 volts. However, as the applied voltage increased, the sensor temperature also rose. This temperature increase limited the sensor's ability to detect strain changes under tensile loading, as the elevated temperature caused a rapid decrease in electrical resistance. As a result, the expected increase in resistance due to tensile strain was effectively counteracted by the thermal drop in resistance, reducing the sensor’s accuracy under such conditions.

2. Electromechanical performance of coated CNTSA/CNC sensors

The performance of the coated CNTSA/CNC-based sensors was significantly affected by the initial CNTSA to CNC loading ratio, highlighting the potential to tailor sensor characteristics through compositional adjustment. To better understand and predict sensor behavior, an existing fitting model was modified and applied to the experimental data. During reliability testing, CNTSA/CNC sensors exhibited a downward drift in their electrical response, indicating a need for further optimization to ensure long-term performance stability.

3. Effect of sensor geometry and carbon type on screen-printed sensors

Sensor geometry was found to have a significant impact on both the reliability and sensitivity of CNTSA/CNC-based strain sensors, although it did not consistently influence linearity. Among the tested patterns, line and o-line geometries demonstrated higher sensitivity compared to grid and omnidirectional configurations. A key factor underlying this performance was the length of the conductive path within each geometry. While earlier studies suggested that higher initial resistance correlates with increased sensitivity, our findings revealed the opposite: lower-resistance patterns (particularly line and o-line) exhibited greater resistance changes and higher sensitivities under strain. However, when the same geometry, such as o-line, was printed with thicker layers that increased the initial resistance, the sensitivity decreased, which is consistent with trends reported in the literature.

Crack formation within the CNTSA/CNC sensors contributed to enhanced sensitivity by disrupting the conductive network and amplifying resistance changes under strain. At the same time, the piezoresistive response of the bridging CNTs between cracks supported a more stable and linear signal during crack propagation, thereby improving the overall sensing performance.

The quality and morphology of the conductive filler materials had a substantial impact on sensor performance. Industrial-grade CNTNC resulted in unreliable sensing behavior, characterized by severe upward drifting during cyclic loading. In contrast, high-quality CNTSA exhibited downward drifting, though it was less pronounced than that observed in CNF-based sensors. Graphene-based sensors demonstrated high sensitivity but suffered from steep downward drift, which limited their reliability. In the case of CB-based sensors, the spherical morphology of CB particles led to higher sensitivity and more consistent performance compared to fibrillated fillers such as CNTSA, CNTNC, and CNF. While CB-based sensors showed slight upward drifting, their overall behavior was more stable. Fibrillated fillers, on the other hand, tended to produce more significant drift during repeated loading cycles, with CNF-based sensors displaying the steepest and least stable response, followed by CNTNC and then CNTSA.

Hybridizing CB with other carbon nanomaterials such as CNTSA, CNTNC, and CNFs led to improved and more reliable sensor performance. This combination balanced the conductive network characteristics of both components, resulting in mid-range sensitivity. The hybrid sensors exhibited higher sensitivity than those made with CNTSA, CNTNC, or CNFs alone, but slightly lower sensitivity compared to sensors based solely on CB. This trade-off highlights the potential of material hybridization for optimizing both sensitivity and stability in printed strain sensors.

4. Electromechanical performance of spray-printed sensors

Spray printing produced narrower sensor lines compared to screen printing, and this reduction in line width contributed to higher gauge factor values, particularly in CB-based sensors. However, the enhanced sensitivity achieved through spray printing came at the cost of other performance metrics, such as durability. Despite differences in printing techniques, both methods exhibited similar performance trends across various sensor types, suggesting that the electromechanical behavior was primarily governed by the filler material and sensor geometry. The choice of deposition technique mainly affected the printing resolution rather than the fundamental sensor performance. Additionally, factors such as sensor thickness and strain history were also found to influence sensor sensitivity and reliability.

5. Asymmetric behavior and directional sensitivity of carbon nanofiller-based sensors

The sensors exhibited asymmetric behavior under both tensile and compression loads during four-point bending tests, regardless of the type of carbon nanofiller.

Grid sensors showed pronounced directional sensitivity, with significantly higher response in the longitudinal direction compared to the transverse direction. Although the type of carbon nanofiller influenced the transverse sensitivity ratio, this ratio remained relatively high, indicating that further design optimizations are necessary to improve transverse performance. In contrast, the omnidirectional sensor demonstrated effective multidirectional sensing capabilities, making it particularly promising for applications requiring strain detection across multiple directions.

6. Multifunctionality of printed sensors

All sensors demonstrated good linearity and a negative temperature TCR over the temperature range from 25°C to 60°C. Among them, CNTSA-based sensors exhibited the highest sensitivity to temperature changes, with a TCR of -0.36 ± 0.04 %/°C, outperforming other sensor types. In contrast, CB-based sensors showed the lowest TCR, indicating less sensitivity to temperature variations.

Under impact testing, CB-based sensors exhibited the highest resistance change, indicating a strong response to impact events. In contrast, CNT and CNF-based sensors showed lower resistance changes but demonstrated greater robustness by sustaining less permanent damage after exposure to impact energy of 0.6 joules.

7. Antenna patch sensors

Antenna patch sensors demonstrated the ability to detect strain during tensile loading, highlighting their potential for SHM by correlating mechanical deformation with shifts in resonant frequency. During bending tests, the resonant frequency consistently shifted as the bending angle increased. These frequency shifts were repeatable and occurred in the same direction for both original and symmetric patch designs, confirming the reliability and stability of the sensors under bending stress.

7.2 Future work

Building on the insights gained from this project, several avenues for future research are recommended to further optimize the printability and performance of carbon nanomaterial-based strain sensors on GFRP substrates.

Future work should focus on further investigating and optimizing sensor geometries to enhance transverse sensitivity ratios (preferably bringing them below 1%). Additionally, new designs should be explored to achieve more symmetric responses under both tensile and compressive loading conditions.

To ensure long-term functionality in SHM applications, future work should incorporate fatigue testing, and environmental exposure protocols, including high-humidity and temperature cycling. In parallel, the combined effects of strain history and loading frequency on sensor degradation must be systematically examined. These studies will inform the development of calibration protocols that integrate temperature compensation and strain history for improved accuracy and reliability. Complementary data-driven approaches, such as machine learning and advanced signal processing, could be leveraged to mitigate signal drift, enhance interpretation, and predict failure modes.

Future research will explore the integration of printed sensors with low-power wireless modules to enable real-time data transmission for structural health monitoring applications. Additionally, the development of self-powered sensing systems, incorporating energy-harvesting mechanisms such as piezoelectric or triboelectric layers, will be investigated. To evaluate long-term durability and reliability, further studies will assess the effects of varying bending radii and cyclic bending. Incorporating detailed electromagnetic simulations will also help elucidate the influence of geometric factors (such as symmetry) on antenna performance under mechanical stress. Finally, extending testing to include wireless communication parameters such as gain, efficiency, and real-time signal stability will be critical to validating the functionality of these antenna-based sensors in practical flexible and wearable electronic systems.

Collectively, these future efforts aim to bridge the gap between nanomaterial formulation, sensor architecture, and integrated system performance, paving the way for scalable, multifunctional, and reliable printed sensing technologies for aerospace and beyond.

REFERENCES

[1] **Wu, H., Liu, Y., Ding, Y., Liu, J.** (2004) Methods to reduce direct maintenance costs for commercial aircraft, *Aircraft Engineering and Aerospace Technology 76* 15–18. https://doi.org/10.1108/00022660410514964.

[2] S**tatista Infographics** (2020) The Mammoth Cost Of Operating America's Combat Aircraft. https://www.statista.com/chart/ 23618/operating-cost-per-aircraft (accessed March 27, 2023).

[3] **Fioriti, M., Vercella, V., Viola, N.** (2018) Cost-Estimating Model for Aircraft Maintenance, *Journal of Aircraft 55* 1564–1575. https://doi.org/10.2514/1.C034664.

[4] **Aviation Industry Adjusts to Increasing Demand for Aircraft Maintenance Technicians, (n.d.).** //interactive.aviationtoday.com/avionics-magazine/march-april-2022/aviation-industry-adjusts-to-increasing-demand-for-aircraft-maintenance-technicians/ (accessed April 4, 2023).

[5] **Giurgiutiu, V.** (2016) Chapter 1 - Introduction, in: V. Giurgiutiu (Ed.), Structural Health Monitoring of Aerospace Composites, Academic Press, Oxford: pp. 1–23. https://doi.org/10.1016/B978-0-12-409605-9.00001-5.

[6] **AERO - Boeing 787 from the Ground Up, (n.d.).** https://www.boeing.com/ commercial/aeromagazine/articles/qtr_4_06/article_04_2.html (accessed November 22, 2021).

[7] **Towsyfyan, H., Biguri, A., Boardman, R., Blumensath, T.** (2020) Successes and challenges in non-destructive testing of aircraft composite structures, C*hinese Journal of Aeronautics 33* 771–791. https://doi.org/10.1016/j.cja.2019.09.017.

[8] **Aliabadi, M.H.F., Khodaei, Z.S.** (2017) Structural Health Monitoring For Advanced Composite Structures, World Scientific.

[9] **Giannakeas, I.N., Sharif Khodaei, Z., Aliabadi, M.H.** (2022) Digital clone testing platform for the assessment of SHM systems under uncertainty, *Mechanical Systems and Signal Processing 163* 108150. https://doi.org/10.1016/j.ymssp.2021.108150.

[10] **Boller, C., & Staszewski, W. J.** (2004). Aircraft structural health and usage monitoring. *Health Monitoring of Aerospace Structures*, 29-73.https://doi.org/10.1002/0470092866.ch2.

[11] **Zh, S., & Ye, L.** (2009). Identification of damage using Lamb waves. https://doi.org/10.1007/978-1-84882-784-4.

[12] **Roskowicz, M., Smal, T., & Szrama, S.** (2018). New challenges and technologies related to aircrafts' battle damages. *Scientific Journal of the Military University of Land Forces*, *50*.

[13] **Features, Eurofighter Typhoon (n.d.).** https://www.eurofighter.com/the-aircraft/features (accessed April 13, 2023).

[14] **Boller, C.** (2014). Implementation Strategies for SHM in Civil and Military Applications. *Structural Health Monitoring of Military Vehicles; Suleman, A., Ed.; STO-EN-AVT-220. STO Educational Notes*.

[15] **Boller, C., & Buderath, M.** (2007). Fatigue in aerostructures—where structural health monitoring can contribute to a complex subject. *Philosophical Transactions of the Royal Society A: Mathematical, Physical and Engineering Sciences*, *365*(1851), 561-587. https://doi.org/10.1098/rsta.2006.1924.

[16] **Hunt, S. R., & Hebden, I. G.** (2001). Validation of the Eurofighter Typhoon structural health and usage monitoringsystem. *Smart materials and structures*, *10*(3), 497. https://doi.org/10.1088/0964-1726/10/3/311.

[17] **Salmanpour, M. S., Sharif Khodaei, Z., & Aliabadi, M. F.** (2017). Impact damage localisation with piezoelectric sensors under operational and environmental conditions. *Sensors*, *17*(5), 1178. https://doi.org/10.3390/s17051178.

[18] **Goossens, S., Geernaert, T., Khodaei, Z. S., Karachalios, E., Saenz-Castillo, D., & Berghmans, F.** (2020, April). Barely visible impact damage detection and location on composite materials by surface-mounted and embedded aerospace-compatible optical fibre Bragg grating sensors. In *Optical Sensing and Detection VI* (Vol. 11354, pp. 64-76). SPIE. https://doi.org/10.1117/12. 2559262.

[19] **Briand, W., Rébillat, M., Guskov, M., & Mechbal, N.** (2021). Damage imaging post processing for delamination size assessment of CFRP aeronautic structures. In *European Workshop on Structural Health Monitoring: Special Collection of 2020 Papers-Volume 1* (pp. 140-148). Springer International Publishing. https://doi.org/10.1007/978-3-030-64594-6_15.

[20] **Qiu, L., Deng, X., Yuan, S., Huang, Y., & Ren, Y.** (2018). Impact monitoring for aircraft smart composite skins based on a lightweight sensor network and characteristic digital sequences. *Sensors*, *18*(7), 2218. https://doi.org/10.3390/s18072218.

[21] **Wang, Y., Qiu, L., Luo, Y., Ding, R., & Jiang, F.** (2020). A piezoelectric sensor network with shared signal transmission wires for structural health monitoring of aircraft smart skin. *Mechanical systems and signal processing*, *141*, 106730. https://doi.org/10.1016/j.ymssp.2020.106730.

[22] **Yeager, M., Todd, M., Gregory, W., & Key, C.** (2017). Assessment of embedded fiber Bragg gratings for structural health monitoring of composites. *Structural Health Monitoring*, *16*(3), 262-275. https://doi.org/10.1177/1475921716665563.

[23] **Takeda, T.**, **Shindo, Y.**, **Fukuzaki, T.**, & **Narita, F.** (2014). Short beam interlaminar shear behavior and electrical resistance-based damage self-sensing of woven carbon/epoxy composite laminates in a cryogenic environment. *Journal of Composite Materials*, *48*, 119–128. https://doi.org/10.1177/0021998312469240.

[24] **Giurgiutiu, V.** (2016). Other Sensors for SHM of Aerospace Composites. In *Structural Health Monitoring of Aerospace Composites* (pp. 297–315). Elsevier. https://doi.org/10.1016/B978-0-12-409605-9.00008-8.

[25] **V Button, V.L.D.S.N.** (2015). Displacement, Velocity, and Acceleration Transducers. In *Principles of Measurement and Transduction of Biomedical Variables* (pp. 155–219). Elsevier. https://doi.org/10.1016/B978-0-12-800774-7.00005-2.

[26] **S Luo, S.** (2016). Direct laser writing for creating porous graphitic structures and their use for flexible and highly sensitive sensor and sensor arrays. 10.

[27] **Arana, G.**, **Gamboa, F.**, & **Avilés, F.** (2023). Piezoresistive and thermoresistive responses of carbon nanotube-based strain gauges with different grid geometric parameters. *Sensors and Actuators A: Physical*, *359*, 114477. https://doi.org/10.1016/j.sna.2023.114477.

[28] **Groo, L.**, **Nasser, J.**, **Inman, D.J.**, & **Sodano, H.A.** (2021). Transfer printed laser induced graphene strain gauges for embedded sensing in fiberglass composites. *Composites Part B: Engineering*, *219*, 108932. https://doi.org/10.1016/j.compositesb.2021.108932.

[29] **Zymelka, D.**, **Yamashita, T.**, **Takamatsu, S.**, **Itoh, T.**, & **Kobayashi, T.** (2017). Thin-film flexible sensor for omnidirectional strain measurements. *Sensors and Actuators A: Physical*, *263*, 391–397. https://doi.org/10.1016/j.sna.2017.05.040.

[30] **Arana, G.**, **González-Díaz, M.O.**, **Castillo-Atoche, A.**, & **Avilés, F.** (2023). Improving adhesion between polyimide surface and carbon nanotube arrays for strain-sensing devices. *Materials Today Communications*, *34*, 105008. https://doi.org/10.1016/j.mtcomm.2022.105008.

[31] **Arana, G.**, **Mora, A.**, **Pérez, I.**, & **Avilés, F.** (2023). Design and analysis of a carbon nanotube-based strain gauge via multiscale modeling. *Meccanica*, *58*, 1717–1732. https://doi.org/10.1007/s11012-023-01689-8.

[32] **Liu, L.**, **Niu, S.**, **Zhang, J.**, **Mu, Z.**, **Li, J.**, **Li, B.**, **Meng, X.**, **Zhang, C.**, **Wang, Y.**, **Hou, T.**, **Han, Z.**, **Yang, S.**, & **Ren, L.** (2022). Bioinspired, Omnidirectional, and Hypersensitive Flexible Strain Sensors. *Advanced Materials*, *34*, 2200823. https://doi.org/10.1002/adma.202200823.

[33] **Kim, K.**, **Kim, H.J.**, **Zhang, H.**, **Park, W.**, **Meyer, D.**, **Kim, M.K.**, **Kim, B.**, **Park, H.**, **Xu, B.**, **P. Kollbaum, P.**, **Boudouris, B.W.**, & **Lee, C.H.** (2021). All-printed stretchable corneal sensor on soft contact lenses for noninvasive and painless ocular electrodiagnosis. *Nat Commun*, *12*, 1544. https://doi.org/10.1038/s41467-021-21916-8.

[34] **Zymelka, D.**, & **Kobayashi, T.** (2021). Fabrication Process and Evaluation of Printed Strain Sensors for Detection of Maximum Strain Direction. In *2021 21st International Conference on Solid-State Sensors, Actuators and Microsystems (Transducers)* (pp. 1339–1342). https://doi.org/10.1109/Transducers50396.2021.9495699.

[35] **Yi, Y.**, **Wang, B.**, & **Bermak, A.** (2019). A Low-Cost Strain Gauge Displacement Sensor Fabricated via Shadow Mask Printing. *Sensors*, *19*, 4713. https://doi.org/10.3390/s19214713.

[36] **Kim, S.-Y.**, **Choi, B.-G.**, **Oh, G.-W.**, **Kim, C.-J.**, **Jung, Y.-S.**, **Jang, J.-S.**, **Joung, K.-Y.**, **Suh, J.-H.**, & **Kang, I.** (2021). Piezoresistive Characteristics of Nanocarbon Composite Strain Sensor by Its Longitudinal Pattern Design. *Applied Sciences*, *11*, 5760. https://doi.org/10.3390/app11135760.

[37] **Chun, S.**, **Cho, S.B.**, **Son, W.**, **Kim, Y.**, **Jung, H.**, **Kim, Y.-J.**, & **Choi, C.** (2019). Serpentine-pattern effects on the biaxial stretching of percolative graphene nanoflake films. *Nanotechnology*, *31*, 085303. https://doi.org/10.1088/1361-6528/ab5419.

[38] **Han, C.-J.**, **Chiang, H.-P.**, & **Cheng, Y.-C.** (2018). Using Micro-Molding and Stamping to Fabricate Conductive Polydimethylsiloxane-Based Flexible High-Sensitivity Strain Gauges. *Sensors*, *18*, 618. https://doi.org/10.3390/s18020618.

[39] **Agarwala, S.**, **Goh, G.L.**, & **Yeong, W.Y.** (2018). Aerosol Jet Printed Strain Sensor: Simulation Studies Analyzing the Effect of Dimension and Design on Performance (September 2018). *IEEE Access*, *6*, 63080–63086. https://doi.org/10.1109/ACCESS.2018.2876647.

[40] **Zhang, Y.**, **Anderson, N.**, **Bland, S.**, **Nutt, S.**, **Jursich, G.**, & **Joshi, S.** (2017). All-printed strain sensors: Building blocks of the aircraft structural health monitoring system. *Sensors and Actuators A: Physical*, *253*, 165–172. https://doi.org/10.1016/j.sna.2016.10.007.

[41] **De Luca, A.**, **Caputo, F.**, **Sharif Khodaei, Z.**, & **Aliabadi, M.H.** (2018). Damage characterization of composite plates under low velocity impact using ultrasonic guided waves. *Composites Part B: Engineering*, *138*, 168–180. https://doi.org/10.1016/j.compositesb.2017.11.042.

[42] **Giurgiutiu, V.** (2016). Chapter 5 - Damage and Failure of Aerospace Composites. In **V. Giurgiutiu** (Ed.), *Structural Health Monitoring of Aerospace Composites* (pp. 125–175). Academic Press. https://doi.org/10.1016/B978-0-12-409605-9.00005-2.

[43] **Tabian, I.**, **Fu, H.**, & **Sharif Khodaei, Z.** (2019). A Convolutional Neural Network for Impact Detection and Characterization of Complex Composite Structures. *Sensors*, *19*, 4933. https://doi.org/10.3390/s19224933.

[44] **Sharif Khodaei, Z.**, & **Aliabadi, M.H.** (2018). Impact Detection and Identification with Piezoceramic Sensors: Passive Sensing. In *Computational and Experimental Methods in Structures* (pp. 215–265). https://doi.org/10.1142/9781786343932_0007.

[45] **Morris, A.S.**, & **Langari, R.** (2021). Chapter 13 - Sensor technologies. In **A.S. Morris**, & **R. Langari** (Eds.), *Measurement and Instrumentation (Third Edition)* (pp. 381–411). Academic Press. https://doi.org/10.1016/B978-0-12-817141-7.00013-X.

[46] **Giurgiutiu, V.** (2018). 7.19 Smart Materials and Health Monitoring of Composites. In **P.W.R. Beaumont**, & **C.H. Zweben** (Eds.), *Comprehensive Composite Materials II* (pp. 364–381). Elsevier. https://doi.org/10.1016/B978-0-12-803581-8.10043-8.

[47] **Carboni, M.**, **Gianneo, A.**, & **Giglio, M.** (2015). A Lamb waves based statistical approach to structural health monitoring of carbon fibre reinforced polymer composites. *Ultrasonics*, *60*, 51–64. https://doi.org/10.1016/j.ultras.2015.02.011.

[48] **Elgamal, M.A.**, **Elgamal, H.**, & **Kouritem, S.A.** (2024). Optimized multi-frequency nonlinear broadband piezoelectric energy harvester designs. *Sci Rep*, *14*, 11401. https://doi.org/10.1038/s41598-024-61355-1.

[49] **Masmoudi, S.**, **El Mahi, A.**, & **Turki, S.** (2016). Fatigue behaviour and structural health monitoring by acoustic emission of E-glass/epoxy laminates with piezoelectric implant. *Applied Acoustics*, *108*, 50–58. https://doi.org/10.1016/j.apacoust.2015.10.024.

[50] **Masmoudi, S.**, **El Mahi, A.**, & **Turki, S.** (2015). Use of piezoelectric as acoustic emission sensor for in situ monitoring of composite structures. *Composites Part B: Engineering*, *80*, 307–320. https://doi.org/10.1016/j.compositesb.2015.06.003.

[51] **Su, Z.**, & **Ye, L.** (2009). *Identification of Damage Using Lamb Waves: From Fundamentals to Applications*. Springer Science & Business Media.

[52] **Thomas, G.R.**, & **Khatibi, A.A.** (2017). Durability of Structural Health Monitoring Systems under Impact Loading. *Procedia Engineering*, *188*, 340–347. https://doi.org/10.1016/j.proeng.2017.04.493.

[53] **Ren, F.**, **Giannakeas, I.N.**, **Sharif Khodaei, Z.**, & **Aliabadi, M.H.F.** (2024). The temperature effects on embedded PZT signals in structural health monitoring for composite structures with different thicknesses. *NDT & E International*, *141*, 102988. https://doi.org/10.1016/j.ndteint.2023.102988.

[54] **Lin, M.**, **Qing, X.**, **Kumar, A.**, & **Beard, S.J.** (2001). SMART Layer and SMART Suitcase for structural health monitoring applications. In *Smart Structures and Materials 2001: Industrial and Commercial Applications of Smart Structures Technologies* (pp. 98–106). SPIE. https://doi.org/10.1117/12.429646.

[55] **Qing, X.P.**, **Beard, S.J.**, **Kumar, A.**, **Chan, H.-L.**, & **Ikegami, R.** (2006). Advances in the development of built-in diagnostic system for filament wound composite structures. *Composites Science and Technology*, *66*, 1694–1702. https://doi.org/10.1016/j.compscitech.2005.11.007.

[56] **Tian, J.**, **Li, Z.**, **Sun, Y.**, & **Yao, Y.** (2019). High-Sensitivity Fiber-Optic Strain Sensor Based on the Vernier Effect and Separated Fabry–Perot Interferometers. *Journal of Lightwave Technology*, *37*, 5609–5618. https://doi.org/10.1109/JLT.2019.2936174.

[57] **Ramakrishnan, M.**, **Rajan, G.**, **Semenova, Y.**, & **Farrell, G.** (2016). Overview of Fiber Optic Sensor Technologies for Strain/Temperature Sensing Applications in Composite Materials. *Sensors*, *16*, 99. https://doi.org/10.3390/s16010099.

[58] **Ramly, R.**, **Kuntjoro, W.**, & **Rahman, M.K.A.** (2012). Using Embedded Fiber Bragg Grating (FBG) Sensors in Smart Aircraft Structure Materials. *Procedia Engineering*, *41*, 600–606. https://doi.org/10.1016/j.proeng.2012.07.218.

[59] **Giraldo, C.M.**, **Zúñiga Sagredo, J.**, **Sánchez Gómez, J.**, & **Corredera, P.** (2017). Demonstration and Methodology of Structural Monitoring of Stringer Runs out Composite Areas by Embedded Optical Fiber Sensors and Connectors Integrated during Production in a Composite Plant. *Sensors*, *17*, 1683. https://doi.org/10.3390/s17071683.

[60] **Goossens, S.**, **De Pauw, B.**, **Geernaert, T.**, **Salmanpour, M.S.**, **Sharif Khodaei, Z.**, **Karachalios, E.**, **Saenz-Castillo, D.**, **Thienpont, H.**, & **Berghmans, F.** (2019). Aerospace-grade surface mounted optical fibre strain sensor for structural health monitoring on composite structures evaluated against in-flight conditions. *Smart Mater. Struct.*, *28*, 065008. https://doi.org/10.1088/1361-665X/ab1458.

[61] **Monastyreckis, G.**, **Stepura, A.**, **Soyka, Y.**, **Maltanava, H.**, **Poznyak, S.K.**, **Omastová, M.**, **Aniskevich, A.**, & **Zeleniakiene, D.** (2021). Strain Sensing Coatings for Large Composite Structures Based on 2D MXene Nanoparticles. *Sensors*, *21*, 2378. https://doi.org/10.3390/s21072378.

[62] **Wang, M.**, **Li, N.**, **Wang, G.-D.**, **Lu, S.W.**, **Zhao, Q.D.**, & **Liu, X.L.** (2021). High-sensitive flexural sensors for health monitoring of composite materials using embedded carbon nanotube (CNT) buckypaper. *Composite Structures*, *261*, 113280. https://doi.org/10.1016/j.compstruct.2020.113280.

[63] **Administrator, N.** (2015). Composite Crew Module (CCM) Pressure Vessel Pathfinder Development. NASA. http://www.nasa.gov/offices/nesc/home/Feature_CCM.html (*Accessed April 10, 2023*).

[64] **Higson, G.R.** (1964). Recent advances in strain gauges. *J. Sci. Instrum.*, *41*, 405. https://doi.org/10.1088/0950-7671/41/7/301.

[65] **Zhang, J.X.J.**, & **Hoshino, K.** (2019). Mechanical transducers: Cantilevers, acoustic wave sensors, and thermal sensors. In *Molecular Sensors and Nanodevices* (pp. 311–412). Elsevier. https://doi.org/10.1016/B978-0-12-814862-4.00006-5.

[66] Dewes.d.o.o. (n.d.). Strain measurement | Dewesoft. https://training.dewesoft.com/online/course/strain-measurement-using-strain-gage-sensors (*Accessed January 6, 2025*).

[67] **Bolton, W.** (2004). Instrumentation system elements. In *Instrumentation and Control Systems* (pp. 17–67). Elsevier. https://doi.org/10.1016/B978-075066432-5/50002-4.

[68] **Bajpai, P.** (2018). Process Control. In *Biermann's Handbook of Pulp and Paper* (pp. 483–492). Elsevier. https://doi.org/10.1016/B978-0-12-814238-7.00024-6.

[69] Standard Test Method for Tensile Properties of Polymer Matrix Composite Materials. (n.d.). https://www.astm.org/d3039_d3039m-17.html (*Accessed December 8, 2022*).

[70] **Giurgiutiu, V.** (2016). Chapter 8 - Other Sensors for SHM of Aerospace Composites. In **V. Giurgiutiu** (Ed.), *Structural Health Monitoring of Aerospace Composites* (pp. 297–315). Academic Press. https://doi.org/10.1016/B978-0-12-409605-9.00008-8.

[71] Design, Fabrication and Integration of Large-scale Stretchable Strain Sensor Networks - ProQuest. (n.d.). https://www.proquest.com/openview/19422e19dc7e15b57406a9b6c1f496f3/1?pq-origsite=gscholar&cbl=18750&diss=y (*Accessed October 28, 2024*).

[72] **Zarrintaj, P.**, **Jouyandeh, M.**, **Ganjali, M.R.**, **Hadavand, B.S.**, **Mozafari, M.**, **Sheiko, S.S.**, **Vatankhah-Varnoosfaderani, M.**, **Gutiérrez, T.J.**, & **Saeb, M.R.** (2019). Thermo-sensitive polymers in medicine: A review. *European Polymer Journal*, *117*, 402–423. https://doi.org/10.1016/j.eurpolymj.2019.05.024.

[73] **Zhang, X.**, **Xiang, D.**, **Zhu, W.**, **Zheng, Y.**, **Harkin-Jones, E.**, **Wang, P.**, **Zhao, C.**, **Li, H.**, **Wang, B.**, & **Li, Y.** (2020). Flexible and high-performance piezoresistive strain sensors based on carbon nanoparticles@polyurethane sponges. *Composites Science and Technology*, *200*, 108437. https://doi.org/10.1016/j.compscitech.2020.108437.

[74] **Yee, M.J.**, **Mubarak, N.M.**, **Abdullah, E.C.**, **Khalid, M.**, **Walvekar, R.**, **Karri, R.R.**, **Nizamuddin, S.**, & **Numan, A.** (2019). Carbon nanomaterials based films for strain sensing application—A review. *Nano-Structures & Nano-Objects*, *18*, 100312. https://doi.org/10.1016/j.nanoso.2019.100312.

[75] **Zheng, Y.**, **Li, Y.**, **Li, Z.**, **Wang, Y.**, **Dai, K.**, **Zheng, G.**, **Liu, C.**, & **Shen, C.** (2017). The effect of filler dimensionality on the electromechanical performance of polydimethylsiloxane based conductive nanocomposites for flexible strain sensors. *Composites Science and Technology*, *139*, 64–73. https://doi.org/10.1016/j.compscitech.2016.12.014.

[76] **Hisham, M.**, **Shebeeb C, M.**, **D, C.**, **Jacob, L.**, & **Butt, H.** (2024). Additive manufacturing of carbon nanocomposites for structural applications. *Journal of Materials Research and Technology*, *28*, 4674–4693. https://doi.org/10.1016/j.jmrt.2024.01.049.

[77] **De Volder, M.F.L.**, **Tawfick, S.H.**, **Baughman, R.H.**, & **Hart, A.J.** (2013). Carbon Nanotubes: Present and Future Commercial Applications. *Science*, *339*, 535–539. https://doi.org/10.1126/science.1222453.

[78] **Gao, B.**, **Chen, Y.F.**, **Fuhrer, M.S.**, **Glattli, D.C.**, & **Bachtold, A.** (2005). Four-Point Resistance of Individual Single-Wall Carbon Nanotubes. *Phys. Rev. Lett.*, *95*, 196802. https://doi.org/10.1103/PhysRevLett.95.196802.

[79] **Zhou, C.**, **Kong, J.**, & **Dai, H.** (2000). Intrinsic Electrical Properties of Individual Single-Walled Carbon Nanotubes with Small Band Gaps. *Phys. Rev. Lett.*, *84*, 5604–5607. https://doi.org/10.1103/PhysRevLett.84.5604.

[80] **Fuhrer, M.S.**, **Nygård, J.**, **Shih, L.**, **Forero, M.**, **Yoon, Y.-G.**, **Mazzoni, M.S.C.**, **Choi, H.J.**, **Ihm, J.**, **Louie, S.G.**, **Zettl, A.**, & **McEuen, P.L.** (2000). Crossed Nanotube Junctions. *Science*, *288*, 494–497.

[81] **J Tersoff, J.** (1999). Contact resistance of carbon nanotubes. *Appl. Phys. Lett.*, *74*, 2122–2124. https://doi.org/10.1063/1.123776.

[82] **Buldum, A.**, & **Lu, J.P.** (2001). Contact resistance between carbon nanotubes. *Phys. Rev. B*, *63*, 161403. https://doi.org/10.1103/PhysRevB.63.161403.

[83] **Lekawa-Raus, A.**, **Patmore, J.**, **Kurzepa, L.**, **Bulmer, J.**, & **Koziol, K.** (2014). Electrical Properties of Carbon Nanotube Based Fibers and Their Future Use in Electrical Wiring. *Advanced Functional Materials*, *24*, 3661–3682. https://doi.org/10.1002/adfm.201303716.

[84] **Costa, P.**, **Silva, J.**, **Sencadas, V.**, **Costa, C.M.**, **van Hattum, F.W.J.**, **Rocha, J.G.**, & **Lanceros-Mendez, S.** (2009). The effect of fibre concentration on the α to β-phase transformation, degree of crystallinity and electrical properties of vapour grown carbon nanofibre/poly(vinylidene fluoride) composites. *Carbon*, *47*, 2590–2599. https://doi.org/10.1016/j.carbon.2009.05.011.

[85] **Zheng, S.**, **Deng, J.**, **Yang, L.**, **Ren, D.**, **Huang, S.**, **Yang, W.**, **Liu, Z.**, & **Yang, M.** (2014). Investigation on the piezoresistive behavior of high-density polyethylene/carbon black films in the elastic and plastic regimes. *Composites Science and Technology*, *97*, 34–40. https://doi.org/10.1016/j.compscitech.2014.04.001.

[86] **Rao, R.K.**, **Gautham, S.**, & **Sasmal, S.** (2024). A Comprehensive Review on Carbon Nanotubes Based Smart Nanocomposites Sensors for Various Novel Sensing Applications. *Polymer Reviews*, *64*, 575–638. https://doi.org/10.1080/15583724.2024.2308889.

[87] **Wichmann, M.H.G.**, **Buschhorn, S.T.**, **Gehrmann, J.**, & **Schulte, K.** (2009). Piezoresistive response of epoxy composites with carbon nanoparticles under tensile load. *Phys. Rev. B*, *80*, 245437. https://doi.org/10.1103/PhysRevB.80.245437.

[88] **Park, M.**, **Kim, H.**, & **Youngblood, J.P.** (2008). Strain-dependent electrical resistance of multi-walled carbon nanotube/polymer composite films. *Nanotechnology*, *19*, 055705. https://doi.org/10.1088/0957-4484/19/05/055705.

[89] **Oliva-Avilés, A.I.**, **Avilés, F.**, & **Sosa, V.** (2011). Electrical and piezoresistive properties of multi-walled carbon nanotube/polymer composite films aligned by an electric field. *Carbon*, *49*, 2989–2997. https://doi.org/10.1016/j.carbon.2011.03.017.

[90] **Duan, L.**, **D'hooge, D.R.**, & **Cardon, L.** (2020). Recent progress on flexible and stretchable piezoresistive strain sensors: From design to application. *Progress in Materials Science*, *114*, 100617. https://doi.org/10.1016/j.pmatsci.2019.100617.

[91] **Avilés, F.**, **Oliva-Avilés, A.I.**, & **Cen-Puc, M.** (2018). Piezoresistivity, Strain, and Damage Self-Sensing of Polymer Composites Filled with Carbon Nanostructures. *Advanced Engineering Materials*, *20*, 1701159. https://doi.org/10.1002/adem.201701159.

[92] **Datta, S.**, **Neerukatti, R.K.**, & **Chattopadhyay, A.** (2018). Buckypaper embedded self-sensing composite for real-time fatigue damage diagnosis and prognosis. *Carbon*, *139*, 353–360. https://doi.org/10.1016/j.carbon.2018.06.059.

[93] **Luo, S.**, **Obitayo, W.**, & **Liu, T.** (2014). SWCNT-thin-film-enabled fiber sensors for lifelong structural health monitoring of polymeric composites - From manufacturing to utilization to failure. *Carbon*, *76*, 321–329. https://doi.org/10.1016/j.carbon.2014.04.083.

[94] **Wang, Y.**, **Wang, Y.**, **Wan, B.**, **Han, B.**, **Cai, G.**, & **Li, Z.** (2018). Properties and mechanisms of self-sensing carbon nanofibers/epoxy composites for structural health monitoring. *Composite Structures*, *200*, 669–678. https://doi.org/10.1016/j.compstruct.2018.05.151.

[95] **Park, J.-M.**, **Jang, J.-H.**, **Wang, Z.-J.**, **Kwon, D.-J.**, & **DeVries, K.L.** (2010). Self-sensing of carbon fiber/carbon nanofiber–epoxy composites with two different nanofiber aspect ratios investigated by electrical resistance and wettability measurements. *Composites Part A: Applied Science and Manufacturing*, *41*, 1702–1711. https://doi.org/10.1016/j.compositesa.2010.08.005.

[96] **Cheng, B.**, **Chang, S.**, **Li, H.**, **Li, Y.**, **Shen, W.**, **Shang, Y.**, & **Cao, A.** (2020). Highly Stretchable and Compressible Carbon Nanofiber–Polymer Hydrogel Strain Sensor for Human Motion Detection. *Macromolecular Materials and Engineering*, *305*, 1900813. https://doi.org/10.1002/mame.201900813.

[97] **Lee, J.-H.**, **Kim, J.**, **Liu, D.**, **Guo, F.**, **Shen, X.**, **Zheng, Q.**, **Jeon, S.**, & **Kim, J.-K.** (2019). Highly Aligned, Anisotropic Carbon Nanofiber Films for Multidirectional Strain Sensors with Exceptional Selectivity. *Advanced Functional Materials*, *29*, 1901623. https://doi.org/10.1002/adfm.201901623.

[98] **Wu, S.**, **Zhang, J.**, **Ladani, R.B.**, **Ravindran, A.R.**, **Mouritz, A.P.**, **Kinloch, A.J.**, & **Wang, C.H.** (2017). Novel Electrically Conductive Porous PDMS/Carbon Nanofiber Composites for Deformable Strain Sensors and Conductors. *ACS Appl. Mater. Interfaces*, *9*, 14207–14215. https://doi.org/10.1021/acsami.7b00847.

[99] **Zhu, J.**, **Wei, S.**, **Ryu, J.**, & **Guo, Z.** (2011). Strain-Sensing Elastomer/Carbon Nanofiber "Metacomposites." *J. Phys. Chem. C*, *115*, 13215–13222. https://doi.org/10.1021/jp202999c.

[100] **Tallman, T.N.**, **Gungor, S.**, **Wang, K.W.**, & **Bakis, C.E.** (2015). Tactile imaging and distributed strain sensing in highly flexible carbon nanofiber/polyurethane nanocomposites. *Carbon*, *95*, 485–493. https://doi.org/10.1016/j.carbon.2015.08.029.

[101] **Paleo, A.**, **van Hattum, F.**, **Nunes-Pereira, J.**, **Rocha, J.G.**, **Oliveira da Silva, J.**, **Sencadas, V.**, & **Lanceros-Méndez, S.** (2010). The piezoresistive effect in polypropylene—carbon nanofibre composites obtained by shear extrusion. *Smart Materials and Structures*, *19*, 065013. https://doi.org/10.1088/0964-1726/19/6/065013.

[102] **Zegeye, E.**, **Ghamsari, A.K.**, **Jin, Y.**, & **Woldesenbet, E.** (2013). The strain sensing property of carbon nanofiber/glass microballoon epoxy nanocomposite. *Smart Mater. Struct.*, *22*, 065010. https://doi.org/10.1088/0964-1726/22/6/065010.

[103] **Novoselov, K.S.**, **Geim, A.K.**, **Morozov, S.V.**, **Jiang, D.**, **Zhang, Y.**, **Dubonos, S.V.**, **Grigorieva, I.V.**, & **Firsov, A.A.** (2004). Electric Field Effect in Atomically Thin Carbon Films. *Science*, *306*, 666–669. https://doi.org/10.1126/science.1102896.

[104] **Cooper, D.R.**, **D'Anjou, B.**, **Ghattamaneni, N.**, **Harack, B.**, **Hilke, M.**, **Horth, A.**, **Majlis, N.**, **Massicotte, M.**, **Vandsburger, L.**, **Whiteway, E.**, & **Yu, V.** (2012). Experimental Review of Graphene. *ISRN Condensed Matter Physics*, *2012*, 1–56. https://doi.org/10.5402/2012/501686.

[105] **Malik, R.**, **Tomer, V.K.**, & **Chaudhary, V.** (2019). Chapter 16 - Hybridized Graphene for Chemical Sensing. In **M. Jawaid**, **R. Bouhfid**, & **A. el Kacem Qaiss** (Eds.), *Functionalized Graphene Nanocomposites and Their Derivatives* (pp. 323–338). Elsevier. https://doi.org/10.1016/B978-0-12-814548-7.00016-7.

[106] **Bragaglia, M.**, **Paleari, L.**, **Lamastra, F.R.**, **Puglia, D.**, **Fabbrocino, F.**, & **Nanni, F.** (2021). Graphene nanoplatelet, multiwall carbon nanotube, and hybrid multiwall carbon nanotube–graphene nanoplatelet epoxy nanocomposites as strain sensing coatings. *Journal of Reinforced Plastics and Composites*, *40*, 632–643. https://doi.org/10.1177/0731684421994324.

[107] **Sankar, V.**, **Nambi, A.**, **Bhat, V.N.**, **Sethy, D.**, **Balasubramaniam, K.**, **Das, S.**, **Guha, M.**, & **Sundara, R.** (2020). Waterproof Flexible Polymer-Functionalized Graphene-Based Piezoresistive Strain Sensor for Structural Health Monitoring and Wearable Devices. *ACS Omega*, *5*, 12682–12691. https://doi.org/10.1021/acsomega.9b04205.

[108] **Sethy, D.**, **Makireddi, S.**, **Varghese, F.V.**, & **Balasubramaniam, K.** (2019). Piezoresistive behaviour of graphene nanoplatelet (GNP)/PMMA spray coated sensors on a polymer matrix composite beam. *Express Polym. Lett.*, *13*, 1018–1025. https://doi.org/10.3144/expresspolymlett.2019.88.

[109] **Hu, C.**, **Li, Z.**, **Wang, Y.**, **Gao, J.**, **Dai, K.**, **Zheng, G.**, **Liu, C.**, **Shen, C.**, **Song, H.**, & **Guo, Z.** (2017). Comparative assessment of the strain-sensing behaviors of polylactic acid nanocomposites: reduced graphene oxide or carbon nanotubes. *J. Mater. Chem. C*, *5*, 2318–2328. https://doi.org/10.1039/C6TC05261D.

[110] **Reghat, M.**, **Mirabedini, A.**, **Tan, A.M.**, **Weizman, Y.**, **Middendorf, P.**, **Bjekovic, R.**, **Hyde, L.**, **Antiohos, D.**, **Hameed, N.**, **Fuss, F.K.**, & **Fox, B.** (2021). Graphene as a piezo-resistive coating to enable strain monitoring in glass fiber composites. *Composites Science and Technology*, *211*, 108842. https://doi.org/10.1016/j.compscitech.2021.108842.

[111] **Martín-martínez, J.M.** (2002). Chapter 13 - Rubber base adhesives. In **D.A. Dillard**, **A.V. Pocius**, & **M. Chaudhury** (Eds.), *Adhesion Science and Engineering* (pp. 573–675). Elsevier Science B.V. https://doi.org/10.1016/B978-044451140-9/50013-5.

[112] **Fan, Y.**, **Fowler, G.D.**, & **Zhao, M.** (2020). The past, present and future of carbon black as a rubber reinforcing filler – A review. *Journal of Cleaner Production*, *247*, 119115. https://doi.org/10.1016/j.jclepro.2019.119115.

[113] **Biscoe, J.**, & **Warren, B.E.** (1942). An X-Ray Study of Carbon Black. *Journal of Applied Physics*, *13*, 364–371. https://doi.org/10.1063/1.1714879.

[114] **Ji, X.**, **Li, H.**, **Hui, D.**, **Hsiao, K.-T.**, **Ou, J.**, & **Lau, A.K.T.** (2010). I–V characteristics and electro-mechanical response of different carbon black/epoxy composites. *Composites Part B: Engineering*, *41*, 25–32. https://doi.org/10.1016/j.compositesb.2009.05.001.

[115] **Zheng, Y.**, **Li, Y.**, **Dai, K.**, **Liu, M.**, **Zhou, K.**, **Zheng, G.**, **Liu, C.**, & **Shen, C.** (2017). Conductive thermoplastic polyurethane composites with tunable piezoresistivity by modulating the filler dimensionality for flexible strain sensors. *Composites Part A: Applied Science and Manufacturing*, *101*, 41–49. https://doi.org/10.1016/j.compositesa.2017.06.003.

[116] **Tallman, T.N.**, **Gungor, S.**, **Wang, K.W.**, & **Bakis, C.E.** (2015). Damage detection via electrical impedance tomography in glass fiber/epoxy laminates with carbon black filler. *Structural Health Monitoring*, *14*, 100–109. https://doi.org/10.1177/1475921714554142.

[117] **Zhao, J.**, **Dai, K.**, **Liu, C.**, **Zheng, G.**, **Wang, B.**, **Liu, C.**, **Chen, J.**, & **Shen, C.** (2013). A comparison between strain sensing behaviors of carbon black/polypropylene and carbon nanotubes/polypropylene electrically conductive composites. *Composites Part A: Applied Science and Manufacturing*, *48*, 129–136. https://doi.org/10.1016/j.compositesa.2013.01.004.

[118] **Huang, K.**, **Ning, H.**, **Hu, N.**, **Wu, X.**, **Wang, S.**, **Weng, S.**, **Yuan, W.**, **Alamusi**, **Wu, L.**, & **Liu, Y.** (2019). Synergistic effect of CB and MWCNT on the strain-induced DC and AC electrical properties of PVDF-HFP composites. *Carbon*, *144*, 509–518. https://doi.org/10.1016/j.carbon.2018.12.059.

[119] **Kurian, A.S.**, **Mohan, V.B.**, & **Bhattacharyya, D.** (2018). Embedded large strain sensors with graphene-carbon black-silicone rubber composites. *Sensors and Actuators A: Physical*, *282*, 206–214. https://doi.org/10.1016/j.sna.2018.09.017.

[120] **Zhang, F.**, **Wu, S.**, **Peng, S.**, **Sha, Z.**, & **Wang, C.H.** (2019). Synergism of binary carbon nanofibres and graphene nanoplates in improving sensitivity and stability of stretchable strain sensors. *Composites Science and Technology*, *172*, 7–16. https://doi.org/10.1016/j.compscitech.2018.12.031.

[121] **Ke, K.**, **Yue, L.**, **Shao, H.**, **Yang, M.-B.**, **Yang, W.**, & **Manas-Zloczower, I.** (2021). Boosting electrical and piezoresistive properties of polymer nanocomposites via hybrid carbon fillers: A review. *Carbon*, *173*, 1020–1040. https://doi.org/10.1016/j.carbon.2020.11.070.

[122] **Ke, K.**, **Pötschke, P.**, **Wiegand, N.**, **Krause, B.**, **Voit, B.**, & **Manas-Zloczower, I.** (2016). Tuning the Network Structure in Poly(vinylidene fluoride)/Carbon Nanotube Nanocomposites Using Carbon Black: Toward Improvements of Conductivity and Piezoresistive Sensitivity. *ACS Appl. Mater. Interfaces*, *8*, 14190–14199. https://doi.org/10.1021/acsami.6b03451.

[123] **Huang, L.**, **Chen, J.**, **Xu, Y.**, **Hu, D.**, **Cui, X.**, **Shi, D.**, & **Zhu, Y.** (2021). Three-dimensional light-weight piezoresistive sensors based on conductive polyurethane sponges coated with hybrid CNT/CB nanoparticles. *Applied Surface Science*, *548*, 149268. https://doi.org/10.1016/j.apsusc.2021.149268.

[124] **Ma, P.-C.**, **Liu, M.-Y.**, **Zhang, H.**, **Wang, S.-Q.**, **Wang, R.**, **Wang, K.**, **Wong, Y.-K.**, **Tang, B.-Z.**, **Hong, S.-H.**, **Paik, K.-W.**, & **Kim, J.-K.** (2009). Enhanced Electrical Conductivity of Nanocomposites Containing Hybrid Fillers of Carbon Nanotubes and Carbon Black. *ACS Appl. Mater. Interfaces*, *1*, 1090–1096. https://doi.org/10.1021/am9000503.

[125] **Arif, M.F.**, **Kumar, S.**, **Gupta, T.K.**, & **Varadarajan, K.M.** (2018). Strong linear-piezoresistive-response of carbon nanostructures reinforced hyperelastic polymer nanocomposites. *Composites Part A: Applied Science and Manufacturing*, *113*, 141–149. https://doi.org/10.1016/j.compositesa.2018.07.021.

[126] **Chang, F.-Y.**, **Wang, R.-H.**, **Yang, H.**, **Lin, Y.-H.**, **Chen, T.-M.**, & **Huang, S.-J.** (2010). Flexible strain sensors fabricated with carbon nano-tube and carbon nano-fiber composite thin films. *Thin Solid Films*, *518*, 7343–7347. https://doi.org/10.1016/j.tsf.2010.04.108.

[127] **Ke, K.**, **Solouki Bonab, V.**, **Yuan, D.**, & **Manas-Zloczower, I.** (2018). Piezoresistive thermoplastic polyurethane nanocomposites with carbon nanostructures. *Carbon*, *139*, 52–58. https://doi.org/10.1016/j.carbon.2018.06.037.

[128] **Zhang, W.**, **Liu, Q.**, & **Chen, P.** (2018). Flexible Strain Sensor Based on Carbon Black/Silver Nanoparticles Composite for Human Motion Detection. *Materials (Basel)*, *11*, 1836. https://doi.org/10.3390/ma11101836.

[129] **Min, S.-H.**, **Lee, G.-Y.**, & **Ahn, S.-H.** (2019). Direct printing of highly sensitive, stretchable, and durable strain sensor based on silver nanoparticles/multi-walled carbon nanotubes composites. *Composites Part B: Engineering*, *161*, 395–401. https://doi.org/10.1016/j.compositesb.2018.12.107.

[130] **Narongthong, J.**, **Das, A.**, **Le, H.H.**, **Wießner, S.**, & **Sirisinha, C.** (2018). An efficient highly flexible strain sensor: Enhanced electrical conductivity, piezoresistivity and flexibility of a strongly piezoresistive composite based on conductive carbon black and an ionic liquid. *Composites Part A: Applied Science and Manufacturing*, *113*, 330–338. https://doi.org/10.1016/j.compositesa.2018.08.004.

[131] **Yan, T.**, **Wang, Z.**, **Wang, Y.-Q.**, & **Pan, Z.-J.** (2018). Carbon/graphene composite nanofiber yarns for highly sensitive strain sensors. *Materials & Design*, *143*, 214–223. https://doi.org/10.1016/j.matdes.2018.02.006.

[132] **Song, J.-H.**, **Kim, H.-J.**, **Kim, M.-S.**, **Min, S.-H.**, **Wang, Y.**, & **Ahn, S.-H.** (2020). Direct printing of performance tunable strain sensor via nanoparticle laser patterning process. *Virtual and Physical Prototyping*, *15*, 265–277. https://doi.org/10.1080/17452759.2020.1733431.

[133] **Hu, N.**, **Itoi, T.**, **Akagi, T.**, **Kojima, T.**, **Xue, J.**, **Yan, C.**, **Atobe, S.**, **Fukunaga, H.**, **Yuan, W.**, **Ning, H.**, **Surina**, & **Liu, Y.**, **Alamusi**. (2013). Ultrasensitive strain sensors made from metal-coated carbon nanofiller/epoxy composites. *Carbon*, *51*, 202–212. https://doi.org/10.1016/j.carbon.2012.08.029.

[134] **Go, M.**, **Qi, X.**, **Matteini, P.**, **Hwang, B.**, & **Lim, S.** (2021). High resolution screen-printing of carbon black/carbon nanotube composite for stretchable and wearable strain sensor with controllable sensitivity. *Sensors and Actuators A: Physical*, *332*, 113098. https://doi.org/10.1016/j.sna.2021.113098.

[135] **Franco, M.**, **Alves, R.**, **Perinka, N.**, **Tubio, C.**, **Costa, P.**, & **Lanceros-Mendéz, S.** (2020). Water-Based Graphene Inks for All-Printed Temperature and Deformation Sensors. *ACS Appl. Electron. Mater.*, *2*, 2857–2867. https://doi.org/10.1021/acsaelm.0c00508.

[136] **Wang, H.** (2018). Dramatically enhanced strain- and moisture-sensitivity of bioinspired fragmentized carbon architectures regulated by cellulose nanocrystals. *Chemical Engineering Journal*, *10*.

[137] **Liang, J.**, **Tong, K.**, & **Pei, Q.** (2016). A Water-Based Silver-Nanowire Screen-Print Ink for the Fabrication of Stretchable Conductors and Wearable Thin-Film Transistors. *Advanced Materials*, *28*, 5986–5996. https://doi.org/10.1002/adma.201600772.

[138] **Yang, X.**, **li, X.**, **Kong, Q.-Q.**, **Liu, Z.**, **Chen, J.-P.**, **Jia, H.**, **Liu, Y.**, **Xie, L.-J.**, & **Chen, C.-M.** (2019). One-pot ball-milling preparation of graphene/carbon black aqueous inks for highly conductive and flexible printed electronics一**步球磨法制**备石墨烯/炭黑水性导电油墨应用于柔性电子器件. *Science China Materials*, *63*. https://doi.org/10.1007/s40843-019-1210-3.

[139] **Qin, Z.**, **Sun, X.**, **Yu, Q.**, **Zhang, H.**, **Wu, X.**, **Yao, M.**, **Liu, W.**, **Yao, F.**, & **Li, J.** (2020). Carbon Nanotubes/Hydrophobically Associated Hydrogels as Ultrastretchable, Highly Sensitive, Stable Strain, and Pressure Sensors. *ACS Appl. Mater. Interfaces, 12,* 4944–4953. https://doi.org/10.1021/acsami.9b21659.

[140] **Alzakia, F.I.**, **Jonhson, W.**, **Ding, J.**, & **Tan, S.C.** (2020). Ultrafast Exfoliation of 2D Materials by Solvent Activation and One-Step Fabrication of All-2D-Material Photodetectors by Electrohydrodynamic Printing. *ACS Appl. Mater. Interfaces*, *12*, 28840–28851. https://doi.org/10.1021/acsami.0c06279.

[141] **R Rastogi, R.**, **Kaushal, R.**, **Tripathi, S.K.**, **Sharma, A.L.**, **Kaur, I.**, & **Bharadwaj, L.M.** (2008). Comparative study of carbon nanotube dispersion using surfactants. *Journal of Colloid and Interface Science*, *328*, 421–428. https://doi.org/10.1016/j.jcis.2008.09.015.

[142] **Aramfard, M.**, **Kaynan, O.**, **Hosseini, E.**, **Zakertabrizi, M.**, **Pérez, L.M.**, & **Asadi, A.** (2022). Aqueous Dispersion of Carbon Nanomaterials with Cellulose Nanocrystals: An Investigation of Molecular Interactions. *Small*, 2202216. https://doi.org/10.1002/smll.202202216.

[143] **Li, M.-C.**, **Wu, Q.**, **Moon, R.J.**, **Hubbe, M.A.**, & **Bortner, M.J.** (2021). Rheological Aspects of Cellulose Nanomaterials: Governing Factors and Emerging Applications. *Advanced Materials*, *33*, 2006052. https://doi.org/10.1002/adma.202006052.

[144] **Wang, S.**, **Zhang, X.**, **Wu, X.**, **Lu, C.**, & **Tailoring, P.C.N.O.** (2016). Natural rubber composites for flexible strain sensors via a cellulose nanocrystal templated assembly. *Soft Matter*, *12*, 845–852. https://doi.org/10.1039/C5SM01958C.

[145] **Liu, X.**, **Su, G.**, **Guo, Q.**, **Lu, C.**, **Zhou, T.**, **Zhou, C.**, & **Zhang, X.** (2018). Hierarchically Structured Self-Healing Sensors with Tunable Positive/Negative Piezoresistivity. *Adv. Funct. Mater.*, *28*, 1706658. https://doi.org/10.1002/adfm.201706658.

[146] **Shariatnia, S.**, **Kumar, A.V.**, **Kaynan, O.**, & **Asadi, A.** (2020). Hybrid Cellulose Nanocrystal-Bonded Carbon Nanotubes/Carbon Fiber Polymer Composites for Structural Applications. *ACS Appl. Nano Mater.*, *3*, 5421–5436. https://doi.org/10.1021/acsanm.0c00785.

[147] **Ibanez Labiano, I.**, **Arslan, D.**, **Ozden Yenigun, E.**, **Asadi, A.**, **Cebeci, H.**, & **Alomainy, A.** (2021). Screen Printing Carbon Nanotubes Textiles Antennas for Smart Wearables. *Sensors*, *21*, 4934. https://doi.org/10.3390/s21144934.

[148] **Hajian, A.**, **Lindström, S.B.**, **Pettersson, T.**, **Hamedi, M.M.**, & **Wågberg, L.** (2017). Understanding the Dispersive Action of Nanocellulose for Carbon Nanomaterials. *Nano Lett.*, *17*, 1439–1447. https://doi.org/10.1021/acs.nanolett.6b04405.

[149] **Mougel, J.-B.**, **Adda, C.**, **Bertoncini, P.**, **Capron, I.**, **Cathala, B.**, & **Chauvet, O.** (2016). Highly Efficient and Predictable Noncovalent Dispersion of Single-Walled and Multi-Walled Carbon Nanotubes by Cellulose Nanocrystals. *J. Phys. Chem. C, 120,* 22694–22701. https://doi.org/10.1021/acs.jpcc.6b07289.

[150] **Yan, Q.**, **Xie, W.**, **Zhou, M.**, & **Fu, H.** (2020). An ultrasensitive and highly compressive piezoresistive sensor based on a biopolyol-reinforced polyurethane sponge coated with silver nanoparticles and carbon nanotubes/cellulose nanocrystals. *J. Mater. Chem. C*, *8*, 16603–16614. https://doi.org/10.1039/D0TC04141F.

[151] **Olivier, C.**, **Moreau, C.**, **Bertoncini, P.**, **Bizot, H.**, **Chauvet, O.**, & **Cathala, B.** (2012). Cellulose Nanocrystal-Assisted Dispersion of Luminescent Single-Walled Carbon Nanotubes for Layer-by-Layer Assembled Hybrid Thin Films. *Langmuir*, *28,* 12463–12471. https://doi.org/10.1021/la302077a.

[152] **Hua, C.**, **Li, X.**, **Shen, L.**, **Lei, H.**, **Guo, X.**, **Liu, Z.**, **Kong, Q.**, **Xie, L.**, & **Chen, C.-M.** (2017). Influence of co-solvent hydroxyl group number on properties of water-based conductive carbon pastes. *Particuology*, *33*, 35–41. https://doi.org/10.1016/j.partic.2016.10.005.

[153] **Hu, G.**, **Yang, L.**, **Yang, Z.**, **Wang, Y.**, **Jin, X.**, **Dai, J.**, **Wu, Q.**, **Liu, S.**, **Zhu, X.**, **Wang, X.**, **Wu, T.-C.**, **Howe, R.C.T.**, **Albrow-Owen, T.**, **Ng, L.W.T.**, **Yang, Q.**, **Occhipinti, L.G.**, **Woodward, R.I.**, **Kelleher, E.J.R.**, **Sun, Z.**, **Huang, X.**, **Zhang, M.**, **Bain, C.D.**, & **Hasan, T.** (2020). A general ink formulation of 2D crystals for wafer-scale inkjet printing. *Science Advances*, *6*, eaba5029. https://doi.org/10.1126/sciadv.aba5029.

[154] **Sico, G.**, **Montanino, M.**, **De Girolamo Del Mauro, A.**, **Imparato, A.**, **Nobile, G.**, & **Minarini, C.** (2016). Effects of the ink concentration on multi-layer gravure-printed PEDOT:PSS. *Organic Electronics*, *28*, 257–262. https://doi.org/10.1016/j.orgel.2015.10.031.

[155] **Kopola, P.**, **Aernouts, T.**, **Guillerez, S.**, **Jin, H.**, **Tuomikoski, M.**, **Maaninen, A.**, & **Hast, J.** (2010). High efficient plastic solar cells fabricated with a high-throughput gravure printing method. *Solar Energy Materials and Solar Cells*, *94*, 1673–1680.

[156] **Leng, T.**, **Pan, K.**, **Zhang, Y.**, **Li, J.**, **Afroj, S.**, **Novoselov, K.S.**, & **Hu, Z.** (2019). Screen-Printed Graphite Nanoplate Conductive Ink for Machine Learning Enabled Wireless Radiofrequency-Identification Sensors. *ACS Appl. Nano Mater.*, *2,* 6197–6208. https://doi.org/10.1021/acsanm.9b01034.

[157] Isopropyl Alcohol | CH3CHOHCH3 | CID 3776 - PubChem. (n.d.). *PubChem*. Accessed August 15, 2024, from https://pubchem.ncbi.nlm.nih.gov/compound/Isopropyl-Alcohol#section=Flash-Point.

[158] **Park, J.-G.**, **Lee, S.-H.**, **Ryu, J.-S.**, **Hong, Y.-K.**, **Kim, T.-G.**, & **Busnaina, A.** (2006). Interfacial and Electrokinetic Characterization of IPA Solutions Related to Semiconductor Wafer Drying and Cleaning. *Journal of The Electrochemical Society - J ELECTROCHEM SOC*, *153*. https://doi.org/10.1149/1.2214532.

[159] **Ullah, I.**, **Baloch, M.K.**, **Niaz, S.**, **Sultan, A.**, & **Ullah, I.** (2019). Solubilizing Potential of Ionic, Zwitterionic and Nonionic Surfactants Towards Water Insoluble Drug Flurbiprofen. *J Solution Chem*, *48*, 1603–1616. https://doi.org/10.1007/s10953-019-00938-3.

[160] **Laghaei, R.**, **Fashandi, H.**, & **Hejazi, S.M.** (2024). Tailoring surface energy of cellulose nanocrystals (CNCs) via low-pressure plasma polymerization to control the interfacial properties in polycaprolactone (PCL)/CNC nanocomposite. *Cellulose*, *31*, 1621–1640. https://doi.org/10.1007/s10570-023-05699-3.

[161] **Tzetzis, D.** (2012). Characterisation of GFRP surfaces amenable for bonding and their effect on the strength of co-cured vacuum resin infused single lap joints. *Journal of Adhesion Science and Technology*, *26*, 2683–2707. https://doi.org/10.1080/01694243.2012.698524.

[162] **Roh, E.**, **Hwang, B.-U.**, **Kim, D.**, **Kim, B.-Y.**, & **Lee, N.-E.** (2015). Stretchable, Transparent, Ultrasensitive, and Patchable Strain Sensor for Human–Machine Interfaces Comprising a Nanohybrid of Carbon Nanotubes and Conductive Elastomers. *ACS Nano*, *9*, 6252–6261. https://doi.org/10.1021/acsnano.5b01613.

[163] **Yang, Y.**, **Wang, H.**, **Hou, Y.**, **Nan, S.**, **Di, Y.**, **Dai, Y.**, **Li, F.**, & **Zhang, J.** (2022). MWCNTs/PDMS composite enabled printed flexible omnidirectional strain sensors for wearable electronics. *Composites Science and Technology*, *226*, 109518. https://doi.org/10.1016/j.compscitech.2022.109518.

[164] **Firouzeh, A.**, **Foba Amon-Junior, A.**, & **Paik, J.** (2015). Soft piezoresistive sensor model and characterization with varying design parameters. *Sensors and Actuators A: Physical*, *233*, 158–168. https://doi.org/10.1016/j.sna.2015.06.007.

[165] **Zhang, Z.**, **Innocent, M.T.**, **Tang, N.**, **Li, R.**, **Hu, Z.**, **Zhai, M.**, **Yang, L.**, **Ma, W.**, **Xiang, H.**, & **Zhu, M.** (2022). Electromechanical Performance of Strain Sensors Based on Viscoelastic Conductive Composite Polymer Fibers. *ACS Appl. Mater. Interfaces*, *14*, 44832–44840. https://doi.org/10.1021/acsami.2c12120.

[166] **Castro, H.F.**, **Correia, V.**, **Pereira, N.**, **Costab, P.**, **Oliveiraa, J.**, & **Lanceros-Méndez, S.** (2018). Printed Wheatstone bridge with embedded polymer based piezoresistive sensors for strain sensing applications. *Additive Manufacturing*, *20*, 119–125. https://doi.org/10.1016/j.addma.2018.01.004.

[167] **Georgopoulou, A.**, & **Clemens, F.** (2020). Piezoresistive Elastomer-Based Composite Strain Sensors and Their Applications. *ACS Appl. Electron. Mater.*, *2*, 1826–1842. https://doi.org/10.1021/acsaelm.0c00278.

[168] **Melnykowycz, M.**, **Koll, B.**, **Scharf, D.**, & **Clemens, F.** (2014). Comparison of Piezoresistive Monofilament Polymer Sensors. *Sensors*, *14*, 1278–1294. https://doi.org/10.3390/s140101278.

[169] **Lozano-Pérez, C.**, **Cauich-Rodríguez, J.V.**, & **Avilés, F.** (2016). Influence of rigid segment and carbon nanotube concentration on the cyclic piezoresistive and hysteretic behavior of multiwall carbon nanotube/segmented polyurethane composites. *Composites Science and Technology*, *128*, 25–32. https://doi.org/10.1016/j.compscitech.2016.03.010.

[170] **Li, X.**, **Hua, T.**, & **Xu, B.** (2017). Electromechanical properties of a yarn strain sensor with graphene-sheath/polyurethane-core. *Carbon*, *118*, 686–698. https://doi.org/10.1016/j.carbon.2017.04.002.

[171] **Fiorillo, A.S.**, **Critello, C.D.**, & **Pullano, S.A.** (2018). Theory, technology and applications of piezoresistive sensors: A review. *Sensors and Actuators A: Physical*, *281*, 156–175. https://doi.org/10.1016/j.sna.2018.07.006.

[172] **Gong, S.**, **Zhu, Z.H.**, & **Meguid, S.A.** (2014). Carbon nanotube agglomeration effect on piezoresistivity of polymer nanocomposites. *Polymer*, *55*, 5488–5499. https://doi.org/10.1016/j.polymer.2014.08.054.

[173] **Li, C.**, **Thostenson, E.T.**, & **Chou, T.-W.** (2007). Dominant role of tunneling resistance in the electrical conductivity of carbon nanotube–based composites. *Applied Physics Letters*, *91*, 223114. https://doi.org/10.1063/1.2819690.

[174] **De Vivo, B.**, **Lamberti, P.**, **Spinelli, G.**, **Tucci, V.**, **Vertuccio, L.**, & **Vittoria, V.** (2014). Simulation and experimental characterization of polymer/carbon nanotubes composites for strain sensor applications. *Journal of Applied Physics*, *116*, 054307. https://doi.org/10.1063/1.4892098.

[175] **Bao, W.S.**, **Meguid, S.A.**, **Zhu, Z.H.**, & **Meguid, M.J.** (2011). Modeling electrical conductivities of nanocomposites with aligned carbon nanotubes. *Nanotechnology*, *22*, 485704. https://doi.org/10.1088/0957-4484/22/48/485704.

[176] **Bao, W.S.**, **Meguid, S.A.**, **Zhu, Z.H.**, & **Weng, G.J.** (2012). Tunneling resistance and its effect on the electrical conductivity of carbon nanotube nanocomposites. *Journal of Applied Physics*, *111*, 093726. https://doi.org/10.1063/1.4716010.

[177] **Foygel, M.**, **Morris, R.D.**, **Anez, D.**, **French, S.**, & **Sobolev, V.L.** (2005). Theoretical and computational studies of carbon nanotube composites and suspensions: Electrical and thermal conductivity. *Phys. Rev. B*, *71*, 104201. https://doi.org/10.1103/PhysRevB.71.104201.

[178] **Sam-Daliri, O.**, **Faller, L.-M.**, **Farahani, M.**, **Roshanghias, A.**, **Oberlercher, H.**, **Mitterer, T.**, **Araee, A.**, & **Zangl, H.** (2018). MWCNT–Epoxy Nanocomposite Sensors for Structural Health Monitoring. *Electronics*, *7*, 143. https://doi.org/10.3390/electronics7080143.

[179] **Cao, X.**, **Wei, X.**, **Li, G.**, **Hu, C.**, **Dai, K.**, **Guo, J.**, **Zheng, G.**, **Liu, C.**, **Shen, C.**, & **Guo, Z.** (2017). Strain sensing behaviors of epoxy nanocomposites with carbon nanotubes under cyclic deformation. *Polymer*, *112*, 1–9. https://doi.org/10.1016/j.polymer.2017.01.068.

[180] **Bao, W.S.**, **Meguid, S.A.**, **Zhu, Z.H.**, **Pan, Y.**, & **Weng, G.J.** (2012). A novel approach to predict the electrical conductivity of multifunctional nanocomposites. *Mechanics of Materials*, *46*, 129–138. https://doi.org/10.1016/j.mechmat.2011.12.006.

[181] **Zhang, X.-W.**, **Pan, Y.**, **Zheng, Q.**, & **Yi, X.-S.** (2000). Time dependence of piezoresistance for the conductor-filled polymer composites. *Journal of Polymer Science Part B: Polymer Physics*, *38*, 2739–2749. https://doi.org/10.1002/1099-0488(20001101)38:21<2739::AID-POLB40>3.0.CO;2-O.

[182] **Simmons, J.G.** (1963). Generalized Formula for the Electric Tunnel Effect between Similar Electrodes Separated by a Thin Insulating Film. *Journal of Applied Physics*, *34*, 1793–1803. https://doi.org/10.1063/1.1702682.

[183] **Panozzo, F.**, **Zappalorto, M.**, & **Quaresimin, M.** (2017). Analytical model for the prediction of the piezoresistive behavior of CNT modified polymers. *Composites Part B: Engineering*, *109*, 53–63. https://doi.org/10.1016/j.compositesb.2016.10.034.

[184] **Dios, J.R.**, **Garcia-Astrain, C.**, **Gonçalves, S.**, **Costa, P.**, & **Lanceros-Méndez, S.** (2019). Piezoresistive performance of polymer-based materials as a function of the matrix and nanofiller content to walking detection application. *Composites Science and Technology*, *181*, 107678. https://doi.org/10.1016/j.compscitech.2019.107678.

[185] **Ferreira, A.**, **Martínez, M.T.**, **Ansón-Casaos, A.**, **Gómez-Pineda, L.E.**, **Vaz, F.**, & **Lanceros-Mendez, S.** (2013). Relationship between electromechanical response and percolation threshold in carbon nanotube/poly(vinylidene fluoride) composites. *Carbon*, *61*, 568–576. https://doi.org/10.1016/j.carbon.2013.05.038.

[186] **Wichmann, M.H.G.**, **Buschhorn, S.T.**, **Gehrmann, J.**, & **Schulte, K.** (2009). Piezoresistive response of epoxy composites with carbon nanoparticles under tensile load. *Phys. Rev. B*, *80*, 245437. https://doi.org/10.1103/PhysRevB.80.245437.

[187] **Onsager, L.** (1949). The Effects of Shape on the Interaction of Colloidal Particles. *Annals of the New York Academy of Sciences*, *51*, 627–659. https://doi.org/10.1111/j.1749-6632.1949.tb27296.x.

[188] **Chen, L.**, **Chen, G.H.**, & **Lu, L.** (2007). Piezoresistive Behavior Study on Finger-Sensing Silicone Rubber/Graphite Nanosheet Nanocomposites. *Advanced Functional Materials*, *17*, 898–904. https://doi.org/10.1002/adfm.200600519.

[189] **Takeda, T.**, **Shindo, Y.**, **Kuronuma, Y.**, & **Narita, F.** (2011). Modeling and characterization of the electrical conductivity of carbon nanotube-based polymer composites. *Polymer*, *52*, 3852–3856. https://doi.org/10.1016/j.polymer.2011.06.046.

[190] **Rein, M.D.**, **Breuer, O.**, & **Wagner, H.D.** (2011). Sensors and sensitivity: Carbon nanotube buckypaper films as strain sensing devices. *Composites Science and Technology*, *71*, 373–381. https://doi.org/10.1016/j.compscitech.2010.12.008.

[191] **Lu, S.**, **Chen, D.**, **Wang, X.**, **Shao, J.**, **Ma, K.**, **Zhang, L.**, **Araby, S.**, & **Meng, Q.** (2017). Real-time cure behaviour monitoring of polymer composites using a highly flexible and sensitive CNT buckypaper sensor. *Composites Science and Technology*, *152*, 181–189. https://doi.org/10.1016/j.compscitech.2017.09.025.

[192] **Liu, L.**, **Wu, J.**, & **Zhou, Y.** (2016). Enhanced delamination initiation stress and monitoring sensitivity of quasi-isotropic laminates under in-plane tension by interleaving with CNT buckypaper. *Composites Part A: Applied Science and Manufacturing*, *89*, 10–17. https://doi.org/10.1016/j.compositesa.2016.03.006.

[193] **Wang, G.D.**, **Li, N.**, **Melly, S.K.**, **Peng, T.**, **Li, Y.C.**, **Zhao, Q.D.**, & **Ji, S.D.** (2019). Monitoring the drilling process of GFRP laminates with carbon nanotube buckypaper sensor. *Composite Structures*, *208*, 114–126. https://doi.org/10.1016/j.compstruct.2018.10.016.

[194] **Tzounis, L.**, **Zappalorto, M.**, **Panozzo, F.**, **Tsirka, K.**, **Maragoni, L.**, & **Paipetis, A.S.** (2019). Highly conductive ultra-sensitive SWCNT-coated glass fiber reinforcements for laminate composites structural health monitoring. *Composites Part B: Engineering*, *169*, 37–44. https://doi.org/10.1016/j.compositesb.2019.03.070.

[195] **Trigwell, S.**, **Dervishi, E.**, & **Biris, A.S.** (2017). Multifunctional carbon nanotube coatings used as strain sensors for composite tanks. *Particulate Science and Technology*, *35*, 674–681. https://doi.org/10.1080/02726351.2016.1194346.

[196] **Wei, L.-J.**, & **Oxley, C.H.** (2016). Carbon based resistive strain gauge sensor fabricated on titanium using micro-dispensing direct write technology. *Sensors and Actuators A: Physical*, *247*, 389–392. https://doi.org/10.1016/j.sna.2016.06.025.

[197] **Owens, C.E.**, **Headrick, R.J.**, **Williams, S.M.**, **Fike, A.J.**, **Pasquali, M.**, **McKinley, G.H.**, & **Hart, A.J.** (2021). Substrate-Versatile Direct-Write Printing of Carbon Nanotube-Based Flexible Conductors, Circuits, and Sensors. *Advanced Functional Materials*, *31*, 2100245. https://doi.org/10.1002/adfm.202100245.

[198] **Rodríguez-González, J.A.**, **Rubio-González, C.**, & **Soto-Cajiga, J.A.** (2019). Piezoresistive Response of Spray-coated Multiwalled Carbon Nanotube/Glass Fiber/Epoxy Composites under Flexural Loading. *Fibers Polym*, *20*, 1673–1683. https://doi.org/10.1007/s12221-019-8711-8.

[199] **Ferreira, A.**, & **Lanceros-Mendez, S.** (2016). Piezoresistive response of spray-printed carbon nanotube/poly(vinylidene fluoride) composites. *Composites Part B: Engineering*, *96*, 242–247. https://doi.org/10.1016/j.compositesb.2016.03.098.

[200] **Sethy, D.**, & **Balasubramaniam, K.** (2022). Smart Graphene Nanoplatelet Strain Sensor for Natural Frequency Sensing of Stainless Steel (SS304) and Human Health Monitoring. *Materials*, *15*, 3924. https://doi.org/10.3390/ma15113924.

[201] **Hwang, M.-Y.**, **Han, D.-H.**, & **Kang, L.-H.** (2019). Piezoresistive Multi-Walled Carbon Nanotube/Epoxy Strain Sensor with Pattern Design. *Materials*, *12*, 3962. https://doi.org/10.3390/ma12233962.

[202] **Lee, G.-Y.**, **Kim, M.-S.**, **Min, S.-H.**, **Kim, H.-S.**, **Kim, H.-J.**, **Keller, R.**, **Ihn, J.-B.**, & **Ahn, S.-H.** (2019). Highly Sensitive Solvent-free Silver Nanoparticle Strain Sensors with Tunable Sensitivity Created Using an Aerodynamically Focused Nanoparticle Printer. *ACS Appl. Mater. Interfaces*, *11*, 26421–26432. https://doi.org/10.1021/acsami.9b00943.

[203] **Zhang, Y.**, **Wang, B.**, **Liu, X.**, **Ni, P.**, & **Yan, W.** (2021). Analysis of temperature threshold in flight test. *IOP Conf. Ser.: Earth Environ. Sci.*, *784*, 012016. https://doi.org/10.1088/1755-1315/784/1/012016.

[204] **Haider, M.F.**, **Kumar, A.**, **Li, I.**, & **Chang, F.-K.** (2022). Sensors, Sensor Network, and SHM. In N. Meyendorf, N. Ida, R. Singh, & J. Vrana (Eds.), *Handbook of Nondestructive Evaluation 4.0* (pp. 569–602). Springer International Publishing. https://doi.org/10.1007/978-3-030-73206-6_58.

[205] **Luo, S.**, & **Liu, T.** (2013). SWCNT/Graphite Nanoplatelet Hybrid Thin Films for Self-Temperature-Compensated, Highly Sensitive, and Extensible Piezoresistive Sensors. *Advanced Materials*, *25*, 5650–5657. https://doi.org/10.1002/adma.201301796.

[206] **Lee, J.S.**, **Oh, J.**, **Jun, J.**, & **Jang, J.** (2015). Wireless Hydrogen Smart Sensor Based on Pt/Graphene-Immobilized Radio-Frequency Identification Tag. *ACS Nano*, *9*, 7783–7790. https://doi.org/10.1021/acsnano.5b02024.

[207] **Kim, S.G.**, **Jun, J.**, **Lee, J.S.**, & **Jang, J.** (2019). A highly sensitive wireless nitrogen dioxide gas sensor based on an organic conductive nanocomposite paste. *J. Mater. Chem. A*, *7*, 8451–8459. https://doi.org/10.1039/C9TA00198K.

[208] **Shen, S.**, **Fan, Z.**, **Deng, J.**, **Guo, X.**, **Zhang, L.**, **Liu, G.**, **Tan, Q.**, & **Xiong, J.** (2018). An LC Passive Wireless Gas Sensor Based on PANI/CNT Composite. *Sensors*, *18*, 3022. https://doi.org/10.3390/s18093022.

[209] **Huang, X.**, **Leng, T.**, **Georgiou, T.**, **Abraham, J.**, **Nair, R.R.**, **Novoselov, K.S.**, & **Hu, Z.** (2018). Graphene Oxide Dielectric Permittivity at GHz and Its Applications for Wireless Humidity Sensing. *Sci Rep*, *8*, 43. https://doi.org/10.1038/s41598-017-16886-1.

[210] **Ge, W.**, **Pei, L.**, **Liu, Y.**, & **Baktur, R.** (2020). Carbon-nanotube-loaded planar gas and humidity sensor. *Microwave and Optical Technology Letters*, *62*, 3857–3863. https://doi.org/10.1002/mop.32544.

[211] **Bhattacharjee, M.**, **Nikbakhtnasrabadi, F.**, & **Dahiya, R.** (2021). Printed Chipless Antenna as Flexible Temperature Sensor. *IEEE Internet of Things Journal*, *8*, 5101–5110. https://doi.org/10.1109/JIOT.2021.3051467.

[212] **Escobedo, P.**, **Bhattacharjee, M.**, **Nikbakhtnasrabadi, F.**, & **Dahiya, R.** (2021). Smart Bandage With Wireless Strain and Temperature Sensors and Batteryless NFC Tag. *IEEE Internet of Things Journal*, *8*, 5093–5100. https://doi.org/10.1109/JIOT.2020.3048282.

[213] **Wang, Y.**, **Zhang, C.**, **Li, J.**, **Ding, G.**, & **Duan, L.** (2017). Fabrication and characterization of ITO thin film resistance temperature detector. *Vacuum*, *140*, 121–125. https://doi.org/10.1016/j.vacuum.2016.07.028.

[214] **Cui, Z.**, **Poblete, F.R.**, & **Zhu, Y.** (2019). Tailoring the Temperature Coefficient of Resistance of Silver Nanowire Nanocomposites and their Application as Stretchable Temperature Sensors. *ACS Appl. Mater. Interfaces*, *11*, 17836–17842. https://doi.org/10.1021/acsami.9b04045.

[215] **Liu, G.**, **Tan, Q.**, **Kou, H.**, **Zhang, L.**, **Wang, J.**, **Lv, W.**, **Dong, H.**, & **Xiong, J.** (2018). A Flexible Temperature Sensor Based on Reduced Graphene Oxide for Robot Skin Used in Internet of Things. *Sensors*, *18*, 1400. https://doi.org/10.3390/s18051400.

[216] **Wen, D.-L.**, **Liu, X.**, **Deng, H.-T.**, **Sun, D.-H.**, **Qian, H.-Y.**, **Brugger, J.**, & **Zhang, X.-S.** (2019). Printed silk-fibroin-based triboelectric nanogenerators for multi-functional wearable sensing. *Nano Energy*, *66*, 104123. https://doi.org/10.1016/j.nanoen.2019.104123.

[217] **Yao, L.**, **Wang, X.**, **Xu, F.**, **Zhao, D.**, **Jiang, M.**, & **Qiu, Y.** (2009). Fabrication and impact performance of three-dimensionally integrated microstrip antennas with microstrip and coaxial feeding. *Smart Mater. Struct.*, *18*, 095034. https://doi.org/10.1088/0964-1726/18/9/095034.

[218] **Yao, L.**, & **Qiu, Y.** (2009). Design and fabrication of microstrip antennas integrated in three dimensional orthogonal woven composites. *Composites Science and Technology*, *69*, 1004–1008. https://doi.org/10.1016/j.compscitech.2009.01.013.

[219] **Matsuzaki, R.**, **Melnykowycz, M.**, & **Todoroki, A.** (2009). Antenna/sensor multifunctional composites for the wireless detection of damage. *Composites Science and Technology*, *69*, 2507–2513. https://doi.org/10.1016/j.compscitech.2009.07.002.

[220] **Matsuzaki, R.**, & **Todoroki, A.** (2006). Wireless detection of internal delamination cracks in CFRP laminates using oscillating frequency changes. *Composites Science and Technology*, *66*, 407–416. https://doi.org/10.1016/j.compscitech.2005.07.016.

[221] **Xu, F.**, **Zhang, K.**, & **Qiu, Y.** (2020). Light-weight, high-gain three-dimensional textile structural composite antenna. *Composites Part B: Engineering*, *185*, 107781. https://doi.org/10.1016/j.compositesb.2020.107781.

[222] **Xu, F.**, & **Qiu, Y.** (2016). Simulation and electromagnetic performance of cylindrical two-element microstrip antenna array integrated in 3D woven glass fiber/epoxy composites. *Materials & Design*, *89*, 1048–1056. https://doi.org/10.1016/j.matdes.2015.10.091.

[223] **Xu, F.**, **Sun, L.**, **Zhang, K.**, **Wang, L.**, & **Qiu, Y.** (2018). Electromagnetic performance and impact damage of the microstrip antennas integrated in cylindrical three dimensional woven composite structures. *Polym. Compos.*, *39*, 3259–3267. https://doi.org/10.1002/pc.24338.

[224] **Zhang, K.**, **Zheng, L.**, **Farha, F.I.**, **Wang, L.**, & **Xu, F.** (2020). Three-Dimensional Textile Structural Conical Conformal Microstrip Antennas for Multifunctional Flexible Electronics. *ACS Appl. Electron. Mater.*, *2*, 1440–1448. https://doi.org/10.1021/acsaelm.0c00200.

[225] **Liu, C.**, **Fang, Q.**, & **Lafdi, K.** (2020). Novel wireless sensing design for composite durability study. *Composites Communications*, *22*, 100511. https://doi.org/10.1016/j.coco.2020.100511.

[226] **Lampani, L.**, & **Gaudenzi, P.** (2018). Innovative composite material component with embedded self-powered wireless sensor device for structural monitoring. *Composite Structures*, *202*, 136–141. https://doi.org/10.1016/j.compstruct.2018.01.011.

[227] **Wang, L.**, **Chung, K.L.**, **Zong, W.**, & **Feng, B.** (2021). A Highly Sensitive Microwave Patch Sensor for Multidirectional Strain Sensing Based on Near Orthogonal Modes. *IEEE Access*, *9*, 24669–24681. https://doi.org/10.1109/ACCESS.2021.3056132.

[228] **Sindhu, B.**, **Kothuru, A.**, **Sahatiya, P.**, **Goel, S.**, & **Nandi, S.** (2021). Laser-Induced Graphene Printed Wearable Flexible Antenna-Based Strain Sensor for Wireless Human Motion Monitoring. *IEEE Trans. Electron Devices*, *68*, 3189–3194. https://doi.org/10.1109/TED.2021.3067304.

[229] **Cho, C.**, **Yi, X.**, **Li, D.**, **Wang, Y.**, & **Tentzeris, M.M.** (2016). Passive Wireless Frequency Doubling Antenna Sensor for Strain and Crack Sensing. *IEEE Sensors J.*, *16*, 5725–5733. https://doi.org/10.1109/JSEN.2016.2567221.

[230] **He, Y.**, **Li, M.M.**, **Wan, G.C.**, & **Tong, M.S.** (2020). A Passive and Wireless Sensor Based on RFID Antenna for Detecting Mechanical Deformation. *IEEE Open J. Antennas Propag.*, *1*, 426–434. https://doi.org/10.1109/OJAP.2020.3015782.

[231] **Kim, D.H.**, **Hwang, W.**, **Park, H.C.**, & **Park, W.S.** (2005). Fatigue Characteristics of a Surface Antenna Structure Designed for Satellite Communication. *Journal of Reinforced Plastics and Composites*, *24*, 35–51. https://doi.org/10.1177/0731684405041718.

[232] **Singh, R.**, **Singh, E.**, & **Nalwa, H.S.** (2017). Inkjet printed nanomaterial based flexible radio frequency identification (RFID) tag sensors for the internet of nano things. *RSC Adv.*, *7*, 48597–48630. https://doi.org/10.1039/C7RA07191D.

[233] **Wang, Y.**, **Yan, C.**, **Cheng, S.**, **Xu, Z.**, **Sun, X.**, **Xu, Y.**, **Chen, J.**, **Jiang, Z.**, **Liang, K.**, & **Feng, Z.** (2019). Flexible RFID Tag Metal Antenna on Paper-Based Substrate by Inkjet Printing Technology. *Adv. Funct. Mater.*, *29*, 1902579. https://doi.org/10.1002/adfm.201902579.

[234] **Leng, T.**, **Huang, X.**, **Chang, K.**, **Chen, J.**, **Abdalla, M.A.**, & **Hu, Z.** (2016). Graphene Nanoflakes Printed Flexible Meandered-Line Dipole Antenna on Paper Substrate for Low-Cost RFID and Sensing Applications. *IEEE Antennas and Wireless Propagation Letters*, *15*, 1565–1568. https://doi.org/10.1109/LAWP.2016.2518746.

[235] **Wang, P.**, **Dong, L.**, **Wang, H.**, **Li, G.**, **Di, Y.**, **Xie, X.**, & **Huang, D.** (2021). Passive Wireless Dual-Tag UHF RFID Sensor System for Surface Crack Monitoring. *Sensors*, *21*, 882. https://doi.org/10.3390/s21030882.

[236] **Kuhn, M.F.**, **Breier, G.P.**, **Dias, A.R.P.**, & **Clarke, T.G.R.** (2018). A Novel RFID-Based Strain Sensor for Wireless Structural Health Monitoring. *J Nondestruct Eval*, *37*, 22. https://doi.org/10.1007/s10921-018-0475-3.

[237] **Islam, M.T.**, **Alam, T.**, **Yahya, I.**, & **Cho, M.** (2018). Flexible Radio-Frequency Identification (RFID) Tag Antenna for Sensor Applications. *Sensors*, *18*, 4212. https://doi.org/10.3390/s18124212.

[238] **Lockyer, A.J.**, **Alt, K.H.**, **Coughlin, D.P.**, **Durham, M.D.**, **Kudva, J.N.**, **Goetz, A.C.**, & **Tuss, J.** (1999). Design and development of a conformal load-bearing smart skin antenna: overview of the AFRL Smart Skin Structures Technology Demonstration (S3TD). In *Smart Structures and Materials 1999: Industrial and Commercial Applications of Smart Structures Technologies* (pp. 410–424). SPIE. https://doi.org/10.1117/12.351578.

[239] **Mbanya Tchafa, F.**, & **Huang, H.** (2018). Microstrip patch antenna for simultaneous strain and temperature sensing. *Smart Material Structures*, *27*, 065019. https://doi.org/10.1088/1361-665X/aabd47.

[240] **Park, J.**, **Kim, J.-K.**, **Kim, D.-S.**, **Shanmugasundaram, A.**, **Park, S.A.**, **Kang, S.**, **Kim, S.-H.**, **Jeong, M.H.**, & **Lee, D.-W.** (2019). Wireless pressure sensor integrated with a 3D printed polymer stent for smart health monitoring. *Sensors and Actuators B: Chemical*, *280*, 201–209. https://doi.org/10.1016/j.snb.2018.10.006.

[241] **Tata, U.**, **Huang, H.**, **Carter, R.L.**, & **Chiao, J.C.** (2009). Exploiting a patch antenna for strain measurements. *Meas. Sci. Technol.*, *20*, 015201. https://doi.org/10.1088/0957-0233/20/1/015201.

[242] **Mohammad, I.**, **Gowda, V.**, **Zhai, H.**, & **Huang, H.** (2011). Detecting crack orientation using antenna sensors. In M. Tomizuka (Ed.), *San Diego, California, USA* (p. 798145). https://doi.org/10.1117/12.880663.

[243] **Yi, X.**, **Cho, C.**, **Cooper, J.**, **Wang, Y.**, **Tentzeris, M.M.**, & **Leon, R.T.** (2013). Passive wireless antenna sensor for strain and crack sensing—electromagnetic modeling, simulation, and testing. *Smart Mater. Struct.*, *22*, 085009. https://doi.org/10.1088/0964-1726/22/8/085009.

[244] **Li, Z.**, **Chang, S.**, **Khuje, S.**, & **Ren, S.** (2021). Recent Advancement of Emerging Nano Copper-Based Printable Flexible Hybrid Electronics. *ACS Nano*, *15*, 6211–6232. https://doi.org/10.1021/acsnano.1c02209.

[245] **You, C.S.**, **Hwang, W.**, & **Eom, S.Y.** (2005). Design and fabrication of composite smart structures for communication, using structural resonance of radiated field. *Smart Mater. Struct.*, *14*, 441–448. https://doi.org/10.1088/0964-1726/14/2/019.

[246] **Gaspari, F.**, & **Quaranta, S.** (2019). Chapter 3 - Nanostructured Materials for RFID Sensors. In O.V. Zenkina (Ed.), *Nanomaterials Design for Sensing Applications* (pp. 93–128). Elsevier. https://doi.org/10.1016/B978-0-12-814505-0.00003-5.

[247] **Na, W.**, **Lee, J.**, **Jun, J.**, **Kim, W.**, **Kim, Y.K.**, & **Jang, J.** (2019). Highly sensitive copper nanowire conductive electrode for nonenzymatic glucose detection. *Journal of Industrial and Engineering Chemistry*, *69*, 358–363. https://doi.org/10.1016/j.jiec.2018.09.050..

[248] **Xu, Z.**, **He, X.**, **Liang, M.**, **Sun, L.**, **Li, D.**, **Xie, K.**, & **Liao, L.** (2019). Catalytic reduction of 4-nitrophenol over graphene supported Cu@Ni bimetallic nanowires. *Materials Chemistry and Physics*, *227*, 64–71. https://doi.org/10.1016/j.matchemphys.2019.01.065.

[249] **Li, Z.**, **Scheers, S.**, **An, L.**, **Chivate, A.**, **Khuje, S.**, **Xu, K.**, **Hu, Y.**, **Huang, Y.**, **Chang, S.**, **Olenick, K.**, **Olenick, J.**, **Choi, J.H.**, **Zhou, C.**, & **Ren, S.** (2020). All-Printed Conformal High-Temperature Electronics on Flexible Ceramics. *ACS Appl. Electron. Mater.*, *2*, 556–562. https://doi.org/10.1021/acsaelm.9b00798.

[250] **Yang, L.**, **Zhang, R.**, **Staiculescu, D.**, **Wong, C.P.**, & **Tentzeris, M.M.** (2009). A Novel Conformal RFID-Enabled Module Utilizing Inkjet-Printed Antennas and Carbon Nanotubes for Gas-Detection Applications. *IEEE Antennas and Wireless Propagation Letters*, *8*, 653–656. https://doi.org/10.1109/LAWP.2009.2024104.

[251] **Rizwan, M.**, **Kutty, A.A.**, **Kgwadi, M.**, **Drysdale, T.D.**, **Sydänheimo, L.**, **Ukkonen, L.**, & **Virkki, J.** (2017). Possibilities of Fabricating Copper-Based RFID Tags With Photonic-Sintered Inkjet Printing and Thermal Transfer Printing. *IEEE Antennas and Wireless Propagation Letters*, *16*, 1828–1831. https://doi.org/10.1109/LAWP.2017.2682319.

[252] **Shin, K.-Y.**, **Lee, J.S.**, **Hong, J.-Y.**, & **Jang, J.** (2014). One-step fabrication of a highly conductive and durable copper paste and its flexible dipole tag-antenna application. *Chemical Communications*, *50*, 3093–3096. https://doi.org/10.1039/C3CC49782H.

[253] **Ding, S.**, **Jiu, J.**, **Gao, Y.**, **Tian, T.**, **Araki, T.**, **Sugahara, T.**, **Nagao, S.**, **Nogi, M.**, **Koga, H.**, **Suganuma, K.**, & **Uchida, H.** (2016). One-Step Fabrication of Stretchable Copper Nanowire Conductors by a Fast Photonic Sintering Technique and Its Application in Wearable Devices. *ACS Appl. Mater. Interfaces*, *8*, 6190–6199. https://doi.org/10.1021/acsami.5b10802.

[254] **Tang, Q.-Y.**, **Pan, Y.-M.**, **Chan, Y.C.**, & **Leung, K.W.** (2012). Frequency-tunable soft composite antennas for wireless sensing. *Sensors and Actuators A: Physical*, *179*, 137–145. https://doi.org/10.1016/j.sna.2012.03.024.

[255] **Amram Bengio, E.**, **Senic, D.**, **Taylor, L.W.**, **Headrick, R.J.**, **King, M.**, **Chen, P.**, **Little, C.A.**, **Ladbury, J.**, **Long, C.J.**, **Holloway, C.L.**, **Babakhani, A.**, **Booth, J.C.**, **Orloff, N.D.**, & **Pasquali, M.** (2019). Carbon nanotube thin film patch antennas for wireless communications. *Appl. Phys. Lett.*, *114*, 203102. https://doi.org/10.1063/1.5093327.

[256] **Kim, S.**, **Georgiadis, A.**, & **Tentzeris, M.** (2018). Design of Inkjet-Printed RFID-Based Sensor on Paper: Single- and Dual-Tag Sensor Topologies. *Sensors*, *18*, 1958. https://doi.org/10.3390/s18061958.

[257] **Liu, L.**, **Ding, L.**, **Zhong, D.**, **Han, J.**, **Wang, S.**, **Meng, Q.**, **Qiu, C.**, **Zhang, X.**, **Peng, L.-M.**, & **Zhang, Z.** (2019). Carbon Nanotube Complementary Gigahertz Integrated Circuits and Their Applications on Wireless Sensor Interface Systems. *ACS Nano*, acsnano.8b09488. https://doi.org/10.1021/acsnano.8b09488.

[258] **Alibakhshikenari, M.**, **Virdee, B.S.**, **Salekzamankhani, S.**, **Aïssa, S.**, **See, C.H.**, **Soin, N.**, **Fishlock, S.J.**, **Althuwayb, A.A.**, **Abd-Alhameed, R.**, **Huynen, I.**, **McLaughlin, J.A.**, **Falcone, F.**, & **Limiti, E.** (2021). High-isolation antenna array using SIW and realized with a graphene layer for sub-terahertz wireless applications. *Sci Rep*, *11*, 10218. https://doi.org/10.1038/s41598-021-87712-y.

[259] **Scidà, A.**, **Haque, S.**, **Treossi, E.**, **Robinson, A.**, **Smerzi, S.**, **Ravesi, S.**, **Borini, S.**, & **Palermo, V.** (2018). Application of graphene-based flexible antennas in consumer electronic devices. *Materials Today*, *21*, 223–230. https://doi.org/10.1016/j.mattod.2018.01.007.

[260] **Huang, X.**, **Leng, T.**, **Zhu, M.**, **Zhang, X.**, **Chen, J.**, **Chang, K.**, **Aqeeli, M.**, **Geim, A.K.**, **Novoselov, K.S.**, & **Hu, Z.** (2016). Highly Flexible and Conductive Printed Graphene for Wireless Wearable Communications Applications. *Sci Rep*, *5*, 18298.

[261] **Lee, J.S.**, **Kim, M.**, **Lee, C.**, **Cho, S.**, **Oh, J.**, & **Jang, J.** (2015). Platinum-decorated reduced graphene oxide/polyaniline:poly(4-styrenesulfonate) hybrid paste for flexible dipole tag-antenna applications. *Nanoscale*, *7*, 3668–3674. https://doi.org/10.1039/C4NR06189F.

[262] **Zhang, J.**, **Song, R.**, **Zhao, X.**, **Fang, R.**, **Zhang, B.**, **Qian, W.**, **Zhang, J.**, **Liu, C.**, & **He, D.** (2020). Flexible Graphene-Assembled Film-Based Antenna for Wireless Wearable Sensor with Miniaturized Size and High Sensitivity. *ACS Omega*, *5*, 12937–12943. https://doi.org/10.1021/acsomega.0c00263.

[263] **Tang, D.**, **Wang, Q.**, **Wang, Z.**, **Liu, Q.**, **Zhang, B.**, **He, D.**, **Wu, Z.**, & **Mu, S.** (2018). Highly sensitive wearable sensor based on a flexible multi-layer graphene film antenna. *Science Bulletin*, *63*, 574–579. https://doi.org/10.1016/j.scib.2018.03.014.

[264] **Kou, H.**, **Zhang, L.**, **Tan, Q.**, **Liu, G.**, **Lv, W.**, **Lu, F.**, **Dong, H.**, & **Xiong, J.** (2018). Wireless flexible pressure sensor based on micro-patterned Graphene/PDMS composite. *Sensors and Actuators A: Physical*, *277*, 150–156. https://doi.org/10.1016/j.sna.2018.05.015.

[265] **Wu, B.**, **Zhang, X.**, **Huang, B.**, **Zhao, Y.**, **Cheng, C.**, & **Chen, H.** (2017). High-Performance Wireless Ammonia Gas Sensors Based on Reduced Graphene Oxide and Nano-Silver Ink Hybrid Material Loaded on a Patch Antenna. *Sensors*, *17*, 2070. https://doi.org/10.3390/s17092070.

[266] **Akindoyo, J.O.**, **Ismail, N.H.**, & **Mariatti, M.** (2021). [Title Missing]. *J Mater Sci: Mater Electron*, *32*, 12648–12660. https://doi.org/10.1007/s10854-021-05900-y.

[267] **S Thibert, S.**, **Jourdan, J.**, **Bechevet, B.**, **Chaussy, D.**, **Reverdy-Bruas, N.**, & **Beneventi, D.** (2014). Influence of silver paste rheology and screen parameters on the front side metallization of silicon solar cell. *Materials Science in Semiconductor Processing*, *27*, 790–799. https://doi.org/10.1016/j.mssp.2014.08.023.

[268] **Hong, H.** (2021). Rheological properties and screen printability of UV curable conductive ink for flexible and washable E-textiles. *Journal of Materials Science*, *11*.

[269] **Wenzel, R.N.** (1936). RESISTANCE OF SOLID SURFACES TO WETTING BY WATER. *Ind. Eng. Chem.*, *28*, 988–994. https://doi.org/10.1021/ie50320a024.

[270] **Alrai, A.**, **Beyhan, E.**, **Asadi, A.**, **Ozden-Yenigun, E.**, & **Cebeci, H.** (2023). Tailoring piezoresistive response of carbon nanotubes sensors by hybridization of cellulose nanocrystals for composite structures. *Sensors and Actuators A: Physical*, *362*, 114633. https://doi.org/10.1016/j.sna.2023.114633.

[271] **Al-Bahrani, M.**, & **Cree, A.** (2019). A simple criterion to evaluate the degree of damage in composite materials after sudden impact loads by exploiting the MWCNTs piezoresistive property. *Carbon*, *150*, 505–517. https://doi.org/10.1016/j.carbon.2019.05.053.

[272] **Srivatsa, S.**, **Belthangadi, P.**, **Ekambaram, S.**, **Pai, M.**, **Sen, P.**, **Uhl, T.**, **Kumar, S.**, **Grabowski, K.**, & **Nayak, M.M.** (2020). Dynamic response study of Ti 3 C 2 -MXene films to shockwave and impact forces. *RSC Advances*, *10*, 29147–29155. https://doi.org/10.1039/D0RA04879H.

[273] **Al-Bahrani, M.**, & **Cree, A.** (2019). A simple criterion to evaluate the degree of damage in composite materials after sudden impact loads by exploiting the MWCNTs piezoresistive property. *Carbon*, *150*, 505–517. https://doi.org/10.1016/j.carbon.2019.05.053.

[274] **Gao, L.**, **Chou, T.-W.**, **Thostenson, E.T.**, **Zhang, Z.**, & **Coulaud, M.** (2011). In situ sensing of impact damage in epoxy/glass fiber composites using percolating carbon nanotube networks. *Carbon*, *49*, 3382–3385. https://doi.org/10.1016/j.carbon.2011.04.003.

[275] **Onogi, S.**, & **Asada, T.** (1980). Rheology and Rheo-Optics of Polymer Liquid Crystals. In G. Astarita, G. Marrucci, & L. Nicolais (Eds.), *Rheology: Volume 1: Principles* (pp. 127–147). Springer US. https://doi.org/10.1007/978-1-4684-3740-9_9.

[276] **Casado, U.**, **Mucci, V.L.**, & **Aranguren, M.I.** (2021). Cellulose nanocrystals suspensions: Liquid crystal anisotropy, rheology and films iridescence. *Carbohydrate Polymers*, *261*, 117848. https://doi.org/10.1016/j.carbpol.2021.117848.

[277] **C Qiao, C.**, **Chen, G.**, **Zhang, J.**, & **Yao, J.** (2016). Structure and rheological properties of cellulose nanocrystals suspension. *Food Hydrocolloids*, *55*, 19–25. https://doi.org/10.1016/j.foodhyd.2015.11.005.

[278] **Li, M.-C.**, **Wu, Q.**, **Song, K.**, **Lee, S.**, & **Wu, Y.** (2015). Cellulose Nanoparticles: Structure–Morphology–Rheology Relationships. *ACS Sustainable Chemistry & Engineering*, 150407061249007. https://doi.org/10.1021/acssuschemeng.5b00144.

[279] **Bercea, M.**, & **Navard, P.** (2000). Shear Dynamics of Aqueous Suspensions of Cellulose Whiskers. *Macromolecules*, *33*, 6011–6016. https://doi.org/10.1021/ma000417p.

[280] **Zhang, Q.**, **Rastogi, S.**, **Chen, D.**, **Lippits, D.**, & **Lemstra, P.J.** (2006). Low percolation threshold in single-walled carbon nanotube/high density polyethylene composites prepared by melt processing technique. *Carbon*, *44*, 778–785. https://doi.org/10.1016/j.carbon.2005.09.039.

[281] **Du, F.**, **Scogna, R.C.**, **Zhou, W.**, **Brand, S.**, **Fischer, J.E.**, & **Winey, K.I.** (2004). Nanotube Networks in Polymer Nanocomposites: Rheology and Electrical Conductivity. *Macromolecules*, *37*, 9048–9055. https://doi.org/10.1021/ma049164g.

[282] **Fan, Z.**, & **Advani, S.G.** (2007). Rheology of multiwall carbon nanotube suspensions. *Journal of Rheology*, *51*, 585–604. https://doi.org/10.1122/1.2736424.

[283] **Chiou, K.**, **Byun, S.**, **Kim, J.**, & **Huang, J.** (2018). Additive-free carbon nanotube dispersions, pastes, gels, and doughs in cresols. *Proc. Natl. Acad. Sci. U.S.A.*, *115*, 5703–5708. https://doi.org/10.1073/pnas.1800298115.

[284] **Xiao, K.**, **Zhang, L.**, & **Zarudi, I.** (2007). Mechanical and rheological properties of carbon nanotube-reinforced polyethylene composites. *Composites Science and Technology*, *67*, 177–182. https://doi.org/10.1016/j.compscitech.2006.07.027.

[285] **Rigueur, J.L.**, **Hasan, S.A.**, **Mahajan, S.V.**, & **Dickerson, J.H.** (2010). Buckypaper fabrication by liberation of electrophoretically deposited carbon nanotubes. *Carbon*, *48*, 4090–4099. https://doi.org/10.1016/j.carbon.2010.07.016.

[286] **Zhu, T.**, **Zhang, Y.**, **Luo, L.**, & **Zhao, X.** (2019). Facile Fabrication of NiO-Decorated Double-Layer Single-Walled Carbon Nanotube Buckypaper for Glucose Detection. *ACS Appl. Mater. Interfaces*, *11*, 10856–10861. https://doi.org/10.1021/acsami.9b00803.

[287] **Zhang, J.**, & **Jiang, D.** (2012). Influence of geometries of multi-walled carbon nanotubes on the pore structures of Buckypaper. *Composites Part A: Applied Science and Manufacturing*, *43*, 469–474. https://doi.org/10.1016/j.compositesa.2011.11.016.

[288] **Whitby, R.L.D.**, **Fukuda, T.**, **Maekawa, T.**, **James, S.L.**, & **Mikhalovsky, S.V.** (2008). Geometric control and tuneable pore size distribution of buckypaper and buckydiscs. *Carbon*, *46*, 949–956. https://doi.org/10.1016/j.carbon.2008.02.028.

[289] **Marani, D.**, **Gadea, C.**, **Hjelm, J.**, **Hjalmarsson, P.**, **Wandel, M.**, & **Kiebach, R.** (2015). Influence of hydroxyl content of binders on rheological properties of cerium–gadolinium oxide (CGO) screen printing inks. *Journal of the European Ceramic Society*, *35*, 1495–1504. https://doi.org/10.1016/j.jeurceramsoc.2014.11.025.

[290] **Spieser, H.**, **Jardin, A.**, **Deganello, D.**, **Gethin, D.**, **Bras, J.**, & **Denneulin, A.** (2021). Rheology of cellulose nanofibrils and silver nanowires for the development of screen-printed antibacterial surfaces. *J Mater Sci*, *56*, 12524–12538. https://doi.org/10.1007/s10853-021-06082-y.

[291] **Somalu, M.R.**, **Muchtar, A.**, **Daud, W.R.W.**, & **Brandon, N.P.** (2017). Renewable and Sustainable Energy Reviews. *Renewable and Sustainable Energy Reviews*, *75*, 426–439. https://doi.org/10.1016/j.rser.2016.11.008.

[292] **Adhikari, J.**, **Perwez, Md.S.**, **Das, A.**, & **Saha, P.** (2021). Development of hydroxyapatite reinforced alginate–chitosan based printable biomaterial-ink. *Nano-Structures & Nano-Objects*, *25*, 100630. https://doi.org/10.1016/j.nanoso.2020.100630.

[293] **Fazilati, M.**, **Ingelsten, S.**, **Wojno, S.**, **Nypelö, T.**, & **Kádár, R.** (2021). Thixotropy of cellulose nanocrystal suspensions. *Journal of Rheology*, *65*, 1035–1052. https://doi.org/10.1122/8.0000281.

[294] **Shrivastava, S.**, & **Das, A.** (2019). Interaction between ethoxylated emulsifiers and propylene glycol based solvents: Gelation and rheology study. *Colloids and Surfaces A: Physicochemical and Engineering Aspects*, *582*, 123905. https://doi.org/10.1016/j.colsurfa.2019.123905.

[295] **Durairaj, R.**, **Ramesh, S.**, **Mallik, S.**, **Seman, A.**, & **Ekere, N.** (2009). Rheological characterisation and printing performance of Sn/Ag/Cu solder pastes. *Materials & Design*, *30*, 3812–3818. https://doi.org/10.1016/j.matdes.2009.01.028.

[296] **Pillai, A.S.**, **Chandran, A.**, **Peethambharan, S.K.**, & **Mallik, S.** (2021). MWCNT Ink with PEDOT:PSS as a multifunctional additive for energy efficient flexible heating applications. *Applied Materials Today*, *23*, 100987. https://doi.org/10.1016/j.apmt.2021.100987.

[297] **Turan, K.**, **Kaur, P.**, **Manhas, D.**, **Sharma, J.**, & **Verma, G.** (2020). Novel insights into the dispersed and acid-mediated surface modification of the carbon nanofibers. *Materials Chemistry and Physics*, *239*, 121978. https://doi.org/10.1016/j.matchemphys.2019.121978.

[298] **Kolb, C.G.**, **Lehmann, M.**, **Lindemann, J.-L.**, **Bachmann, A.**, & **Zaeh, M.F.** (2021). Improving the Dispersion Behavior of Organic Components in Water-Based Electrode Dispersions for Inkjet Printing Processes. *Applied Sciences*, *11*, 2242. https://doi.org/10.3390/app110502242.

[299] **Patist, A.**, **Bhagwat, S.S.**, **Penfield, K.W.**, **Aikens, P.**, & **Shah, D.O.** (2000). On the measurement of critical micelle concentrations of pure and technical-grade nonionic surfactants. *Journal of Surfactants and Detergents*, *3*, 53–58. https://doi.org/10.1007/s11743-000-0113-4.

[300] **Phillips, C.**, **Al-Ahmadi, A.**, **Potts, S.-J.**, **Claypole, T.**, & **Deganello, D.** (2017). The effect of graphite and carbon black ratios on conductive ink performance. *J Mater Sci*, *52*, 9520–9530. https://doi.org/10.1007/s10853-017-1114-6.

[301] **Potts, S.-J.**, **Korochkina, T.**, **Holder, A.**, **Jewell, E.**, **Phillips, C.**, & **Claypole, T.** (2022). The influence of carbon morphologies and concentrations on the rheology and electrical performance of screen-printed carbon pastes. *J Mater Sci*, *57*, 2650–2666. https://doi.org/10.1007/s10853-021-06724-1.

[302] **Yang, M.**, **Parupelli, S.K.**, **Xu, Z.**, & **Desai, S.** (2024). Understanding the Effect of Dispersant Rheology and Binder Decomposition on 3D Printing of a Solid Oxide Fuel Cell. *Micromachines*, *15*, 636. https://doi.org/10.3390/mi15050636.

[303] **A Klinkova, A.**, & **Thérien-Aubin, H.** (2024). Chapter 4 - Carbon nanostructures. In A. Klinkova & H. Thérien-Aubin (Eds.), *Nanochemistry* (pp. 111–141). Elsevier. https://doi.org/10.1016/B978-0-443-21447-9.00003-5.

[304] **Kochkodan, O.**, & **Maksin, V.** (2020). Mixed adsorption of hexadecylpyridinium bromide and Triton X surfactants at graphitized carbon black. *J Serb Chem Soc*, *85*, 781–794. https://doi.org/10.2298/JSC190416112K.

[305] **Li, X.**, **Go, M.**, **Lim, S.**, **An, T.K.**, **Jeong, Y.J.**, & **Kim, S.H.** (2019). Electrohydrodynamic (EHD) jet printing of carbon-black composites for solution-processed organic field-effect transistors. *Organic Electronics*, *73*, 279–285. https://doi.org/10.1016/j.orgel.2019.06.023.

[306] **McManus, D.**, **Vranic, S.**, **Withers, F.**, **Sanchez-Romaguera, V.**, **Macucci, M.**, **Yang, H.**, **Sorrentino, R.**, **Parvez, K.**, **Son, S.-K.**, **Iannaccone, G.**, **Fiori, G.**, & **Casiraghi, C.** (2017). Water-based and biocompatible 2D crystal inks for all-inkjet-printed heterostructures. *Nature Nanotech*, *12*, 343–350. https://doi.org/10.1038/nnano.2016.281.

[307] **Akindoyo, J.O.**, **Ismail, N.H.**, & **Mariatti, M.** (2021). Development of environmentally friendly inkjet printable carbon nanotube-based conductive ink for flexible sensors: effects of concentration and functionalization. *J Mater Sci: Mater Electron*, *32*, 12648–12660. https://doi.org/10.1007/s10854-021-05900-y.

[308] **Islam, M.F.**, **Rojas, E.**, **Bergey, D.M.**, **Johnson, A.T.**, & **Yodh, A.G.** (2003). High Weight Fraction Surfactant Solubilization of Single-Wall Carbon Nanotubes in Water. *Nano Lett.*, *3*, 269–273. https://doi.org/10.1021/nl025924u.

[309] **Kuzubasoglu, B.A.**, **Sayar, E.**, & **Bahadir, S.K.** (2021). Inkjet-Printed CNT/PEDOT:PSS Temperature Sensor on a Textile Substrate for Wearable Intelligent Systems. *IEEE Sensors Journal*, *21*, 13090–13097. https://doi.org/10.1109/JSEN.2021.3070073.

[310] **Xin, F.**, & **Xu, G.Z.** (2011). The Effect of Triton® X-100 on CNT/PP Composite's Electrical Conductivity. *AMR*, *284–286*, 1836–1841. https://doi.org/10.4028/www.scientific.net/AMR.284-286.1836.

[311] **Orrill, M.**, **Abele, D.**, **Wagner, M.J.**, & **LeBlanc, S.** (2021). Sterically Stabilized Multilayer Graphene Nanoshells for Inkjet Printed Resistors. *Electronic Materials*, *2*, 394–412. https://doi.org/10.3390/electronicmat2030027.

[312] **Guillet, J.-F.**, **Valdez-Nava, Z.**, **Golzio, M.**, & **Flahaut, E.** (2019). Electrical properties of double-wall carbon nanotubes nanocomposite hydrogels. *Carbon*, *146*, 542–548. https://doi.org/10.1016/j.carbon.2019.01.090.

[313] **Loh, K.J.**, **Lynch, J.P.**, **Shim, B.S.**, & **Kotov, N.A.** (2008). Tailoring Piezoresistive Sensitivity of Multilayer Carbon Nanotube Composite Strain Sensors. *Journal of Intelligent Material Systems and Structures*, *19*, 747–764. https://doi.org/10.1177/1045389X07079872.

[314] **K.J. Loh, J.P. Lynch, B.S. Shim, N.A. Kotov,** Tailoring Piezoresistive Sensitivity of Multilayer Carbon Nanotube Composite Strain Sensors, Journal of Intelligent Material Systems and Structures 19 (2008) 747–764. https://doi.org/10.1177/1045389X07079872.

[315] **Frank, S.**, **Poncharal, P.**, **Wang, Z.L.**, & **de Heer, W.A.** (1998). Carbon Nanotube Quantum Resistors. *Science*, *280*, 1744–1746. https://doi.org/10.1126/science.280.5370.1744.

[316] **Zheng, W.**, **Xie, J.**, **Zhang, J.**, **Tang, C.**, & **Zhao, Z.** (2018). Influence of Polymethylsilsesquioxane Content to the Thermal Stability of Meta-Aramid Fiber Insulation Paper. *Materials*, *11*, 2317. https://doi.org/10.3390/ma11112317.

[317] **Pavlopoulou, S.**, **Roy, S.S.**, **Gautam, M.**, **Bradshaw, L.**, & **Potluri, P.** (2017). Numerical and Experimental Investigation of the Hydrostatic Performance of Fibre Reinforced Tubes. *Appl Compos Mater*, *24*, 417–448. https://doi.org/10.1007/s10443-016-9563-7.

[318] **Mdarhri, A.**, **Carmona, F.**, **Brosseau, C.**, & **Delhaes, P.** (2008). Direct current electrical and microwave properties of polymer-multiwalled carbon nanotubes composites. *Journal of Applied Physics*, *103*, 054303. https://doi.org/10.1063/1.2841461.

[319] **Tanaka, T.**, **Sano, E.**, **Imai, M.**, & **Akiyama, K.** (2010). Electrical conductivity of carbon-nanotube/cellulose composite paper. *Journal of Applied Physics*, *107*, 054307. https://doi.org/10.1063/1.3319675.

[320] **Qi, X.**, **Ha, H.**, **Hwang, B.**, & **Lim, S.** (2020). Printability of the Screen-Printed Strain Sensor with Carbon Black/Silver Paste for Sensitive Wearable Electronics. *Applied Sciences*, *10*, 6983. https://doi.org/10.3390/app10196983.

[321] **Bouhamed, A.**, **Al-Hamry, A.**, **Müller, C.**, **Choura, S.**, & **Kanoun, O.** (2017). Assessing the electrical behaviour of MWCNTs/epoxy nanocomposite for strain sensing. *Composites Part B: Engineering*, *128*, 91–99. https://doi.org/10.1016/j.compositesb.2017.07.005.

[322] **Chen, X.**, **Wang, F.**, **Shu, L.**, **Tao, X.**, **Wei, L.**, **Xu, X.**, **Zeng, Q.**, & **Huang, G.** (2022). A Single-material-printed, Low-cost design for a Carbon-based fabric strain sensor. *Materials & Design*, *221*, 110926. https://doi.org/10.1016/j.matdes.2022.110926.

[323] **Agarwala, S.**, **Goh, G.L.**, **Yap, Y.L.**, **Goh, G.D.**, **Yu, H.**, **Yeong, W.Y.**, & **Tran, T.** (2017). Development of bendable strain sensor with embedded microchannels using 3D printing. *Sensors and Actuators A: Physical*, *263*, 593–599. https://doi.org/10.1016/j.sna.2017.07.025.

[324] **Barnett, C.J.**, **McGettrick, J.D.**, **Gangoli, V.S.**, **Kazimierska, E.**, **Orbaek White, A.**, & **Barron, A.R.** (2021). Effect of Applied Pressure on the Electrical Resistance of Carbon Nanotube Fibers. *Materials (Basel)*, *14*, 2106. https://doi.org/10.3390/ma14092106.

[325] **Khalid, H.R.**, **Jang, D.**, **Abbas, N.**, **Haider, M.S.**, **Bukhari, S.N.A.**, **Mirza, C.R.**, **Elboughdiri, N.**, & **Ahmad, F.** (2022). Electrical Stability and Piezoresistive Sensing Performance of High Strain-Range Ultra-Stretchable CNT-Embedded Sensors. *Polymers*, *14*, 1366. https://doi.org/10.3390/polym14071366.

[326] **Andreghetto, D.H.**, & **Fuzari, G. de C.** (2020). Piezoresistive epoxy resin films with carbon black particles for small-strain sensors. *Polym. Bull.*, *77*, 3725–3734. https://doi.org/10.1007/s00289-019-02908-7.

[327] **Wang, X.**, **Sparkman, J.**, & **Gou, J.** (2017). Strain sensing of printed carbon nanotube sensors on polyurethane substrate with spray deposition modeling. *Composites Communications*, *3*, 1–6. https://doi.org/10.1016/j.coco.2016.10.003.

[328] **Chu, K.**, **Lee, S.-C.**, **Lee, S.**, **Kim, D.**, **Moon, C.**, & **Park, S.-H.** (2014). Smart conducting polymer composites having zero temperature coefficient of resistance. *Nanoscale*, *7*, 471–478. https://doi.org/10.1039/C4NR04489D.

[329] **Zhang, X.**, **Li, J.**, **Gao, Q.**, **Wang, Z.**, **Ye, N.**, **Li, J.**, & **Lu, Y.** (n.d.). Nerve-Fiber-Inspired Construction of 3D Graphene "Tracks" Supported by Wood Fibers for Multifunctional Biocomposite with Metal-Level Thermal Conductivity. *Advanced Functional Materials*, 2213274. https://doi.org/10.1002/adfm.202213274.

[330] **Rinaldi, A.**, **Proietti, A.**, **Tamburrano, A.**, **Ciminello, M.**, & **Sarto, M.S.** (2015). Graphene-Based Strain Sensor Array on Carbon Fiber Composite Laminate. *IEEE Sensors Journal*, *15*, 7295–7303. https://doi.org/10.1109/JSEN.2015.2472595.

[331] **Yin, F.**, **Ye, D.**, **Zhu, C.**, **Qiu, L.**, & **Huang, Y.** (2017). Stretchable, Highly Durable Ternary Nanocomposite Strain Sensor for Structural Health Monitoring of Flexible Aircraft. *Sensors*, *17*, 2677. https://doi.org/10.3390/s17112677.

[332] **Vertuccio, L.**, **Vittoria, V.**, **Guadagno, L.**, & **De Santis, F.** (2015). Strain and damage monitoring in carbon-nanotube-based composite under cyclic strain. *Composites Part A: Applied Science and Manufacturing*, *71*, 9–16. https://doi.org/10.1016/j.compositesa.2015.01.001.

[333] **Pham, G.T.**, **Park, Y.-B.**, **Liang, Z.**, **Zhang, C.**, & **Wang, B.** (2008). Processing and modeling of conductive thermoplastic/carbon nanotube films for strain sensing. *Composites Part B: Engineering*, *39*, 209–216. https://doi.org/10.1016/j.compositesb.2007.02.024.

[334] **Santos, A.**, **Amorim, L.**, **Nunes, J.P.**, **Rocha, L.A.**, **Silva, A.F.**, & **Viana, J.C.** (2019). Aligned carbon nanotube based sensors for strain sensing applications. *Sensors and Actuators A: Physical*, *289*, 157–164. https://doi.org/10.1016/j.sna.2019.02.026.

[335] **Wang, Y.**, **Wang, S.**, **Li, M.**, **Gu, Y.**, & **Zhang, Z.** (2018). Piezoresistive response of carbon nanotube composite film under laterally compressive strain. *Sensors and Actuators A: Physical*, *273*, 140–146. https://doi.org/10.1016/j.sna.2018.02.032.

[336] **Alian, A.R.**, & **Meguid, S.A.** (2019). Multiscale modeling of the coupled electromechanical behavior of multifunctional nanocomposites. *Composite Structures*, *208*, 826–835. https://doi.org/10.1016/j.compstruct.2018.10.066.

[337] **Montazerian, H.**, **Dalili, A.**, **Milani, A.S.**, & **Hoorfar, M.** (2019). Piezoresistive sensing in chopped carbon fiber embedded PDMS yarns. *Composites Part B: Engineering*, *164*, 648–658. https://doi.org/10.1016/j.compositesb.2019.01.090.

[338] **Zhang, F.**, **Hu, H.**, **Hu, S.**, & **Yue, J.** (2021). Significant strain-rate dependence of sensing behavior in TiO2@carbon fibre/PDMS composites for flexible strain sensors. *J Adv Ceram*, *10*, 1350–1359. https://doi.org/10.1007/s40145-021-0509-7.

[339] **Yang, H.**, **Gong, L.H.**, **Zheng, Z.**, & **Yao, X.F.** (2020). Highly stretchable and sensitive conductive rubber composites with tunable piezoresistivity for motion detection and flexible electrodes. *Carbon*, *158*, 893–903. https://doi.org/10.1016/j.carbon.2019.11.079.

[340] **Moriche, R.**, **Jiménez-Suárez, A.**, **Sánchez, M.**, **Prolongo, S.G.**, & **Ureña, A.** (2018). Sensitivity, influence of the strain rate and reversibility of GNPs based multiscale composite materials for high sensitive strain sensors. *Composites Science and Technology*, *155*, 100–107. https://doi.org/10.1016/j.compscitech.2017.12.002.

[341] **Cao, X.**, **Wei, X.**, **Li, G.**, **Hu, C.**, **Dai, K.**, **Guo, J.**, **Zheng, G.**, **Liu, C.**, **Shen, C.**, & **Guo, Z.** (2017). Strain sensing behaviors of epoxy nanocomposites with carbon nanotubes under cyclic deformation. *Polymer*, *112*, 1–9. https://doi.org/10.1016/j.polymer.2017.01.068.

[342] **Komorek, A.**, **Komorek, Z.**, **Krzyzak, A.**, **Przybylek, P.**, & **Szczepaniak, R.** (2017). Impact of Frequency of Load Changes in Fatigue Tests on the Temperature of the Modified Polymer. *Int J Thermophys*, *38*, 128. https://doi.org/10.1007/s10765-017-2254-2.

[343] **Mirzaei, A.H.**, & **Shokrieh, M.M.** (2023). Evolution of the temperature rise and damage in laminated composites with stress concentration under fatigue loading. *Composites Part B: Engineering*, *254*, 110607. https://doi.org/10.1016/j.compositesb.2023.110607.

[344] **Tanabi, H.**, & **Erdal, M.** (2019). Effect of CNTs dispersion on electrical, mechanical and strain sensing properties of CNT/epoxy nanocomposites. *Results in Physics*, *12*, 486–503. https://doi.org/10.1016/j.rinp.2018.11.081.

[345] **Hu, N.**, **Karube, Y.**, **Yan, C.**, **Masuda, Z.**, & **Fukunaga, H.** (2008). Tunneling effect in a polymer/carbon nanotube nanocomposite strain sensor. *Acta Materialia*, *56*, 2929–2936. https://doi.org/10.1016/j.actamat.2008.02.030.

[346] **Alamusi.**, **Hu, N.**, **Fukunaga, H.**, **Atobe, S.**, **Liu, Y.**, & **Li, J.** (2011). Piezoresistive Strain Sensors Made from Carbon Nanotubes Based Polymer Nanocomposites. *Sensors*, *11*, 10691–10723. https://doi.org/10.3390/s111110691.

[347] **Wang, Y.**, **Wang, Y.**, **Wan, B.**, **Han, B.**, **Cai, G.**, & **Li, Z.** (2018). Properties and mechanisms of self-sensing carbon nanofibers/epoxy composites for structural health monitoring. *Composite Structures*, *200*, 669–678. https://doi.org/10.1016/j.compstruct.2018.05.151.

[348] **Qu, Y.**, **Dai, K.**, **Zhao, J.**, **Zheng, G.**, **Liu, C.**, **Chen, J.**, & **Shen, C.** (2014). The strain-sensing behaviors of carbon black/polypropylene and carbon nanotubes/polypropylene conductive composites prepared by the vacuum-assisted hot compression. *Colloid Polym Sci*, *292*, 945–951. https://doi.org/10.1007/s00396-013-3143-2.

[349] **Salaeh, S.**, **Das, A.**, **Stöckelhuber, K.W.**, & **Wießner, S.** (2020). Fabrication of a strain sensor from a thermoplastic vulcanizate with an embedded interconnected conducting filler network. *Composites Part A: Applied Science and Manufacturing*, *130*, 105763. https://doi.org/10.1016/j.compositesa.2020.105763.

[350] **Yazdani, H.**, **Hatami, K.**, **Khosravi, E.**, **Harper, K.**, & **Grady, B.P.** (2014). Strain-sensitive conductivity of carbon black-filled PVC composites subjected to cyclic loading. *Carbon*, *79*, 393–405. https://doi.org/10.1016/j.carbon.2014.07.082.

[351] **Avilés, F.**, **Oliva-Avilés, A.I.**, & **Cen-Puc, M.** (2018). Piezoresistivity, Strain, and Damage Self-Sensing of Polymer Composites Filled with Carbon Nanostructures. *Advanced Engineering Materials*, *20*, 1701159. https://doi.org/10.1002/adem.201701159.

[352] **Paleari, L.**, **Bragaglia, M.**, **Fabbrocino, F.**, & **Nanni, F.** (2021). Structural Monitoring of Glass Fiber/Epoxy Laminates by Means of Carbon Nanotubes and Carbon Black Self-Monitoring Plies. *Nanomaterials*, *11*, 1543. https://doi.org/10.3390/nano11061543.

[353] **Qiao, Y.**, **Wang, Y.**, **Tian, H.**, **Li, M.**, **Jian, J.**, **Wei, Y.**, **Tian, Y.**, **Wang, D.-Y.**, **Pang, Y.**, **Geng, X.**, **Wang, X.**, **Zhao, Y.**, **Wang, H.**, **Deng, N.**, **Jian, M.**, **Zhang, Y.**, **Liang, R.**, **Yang, Y.**, & **Ren, T.-L.** (2018). Multilayer Graphene Epidermal Electronic Skin. *ACS Nano, 12,* 8839–8846. https://doi.org/10.1021/acsnano.8b02162.

[354] **Fu, X.-W.**, **Liao, Z.-M.**, **Zhou, J.-X.**, **Zhou, Y.-B.**, **Wu, H.-C.**, **Zhang, R.**, **Jing, G.**, **Xu, J.**, **Wu, X.**, **Guo, W.**, & **Yu, D.** (2011). Strain dependent resistance in chemical vapor deposition grown graphene. *Applied Physics Letters*, *99*, 213107. https://doi.org/10.1063/1.3663969.

[355] **Zhang, Z.**, **Xiang, D.**, **Wu, Y.**, **Zhang, J.**, **Li, Y.**, **Wang, M.**, **Li, Z.**, **Zhao, C.**, **Li, H.**, **Wang, P.**, & **Li, Y.** (2022). Effect of Carbon Black on the Strain Sensing Property of 3D Printed Conductive Polymer Composites. *Appl Compos Mater*, *29*, 1235–1248. https://doi.org/10.1007/s10443-022-10017-4.

[356] **Zheng, Y.**, **Li, Y.**, **Dai, K.**, **Wang, Y.**, **Zheng, G.**, **Liu, C.**, & **Shen, C.** (2018). A highly stretchable and stable strain sensor based on hybrid carbon nanofillers/polydimethylsiloxane conductive composites for large human motions monitoring. *Composites Science and Technology*, *156*, 276–286. https://doi.org/10.1016/j.compscitech.2018.01.019.

[357] **Anike, J.C.**, **Le, H.H.**, **Brodeur, G.E.**, **Kadavan, M.M.**, & **Abot, J.L.** (2017). Piezoresistive Response of Integrated CNT Yarns under Compression and Tension: The Effect of Lateral Constraint. *C*, *3*, 14. https://doi.org/10.3390/c3020014.

[358] **X Xia, X.**, **Zhao, S.**, **Zhang, J.**, **Fang, C.**, & **Weng, G.J.** (2022). A unified investigation into the tensile and compressive sensing performance in highly sensitive MWCNT/epoxy nanocomposite strain sensor through loading-dependent tunneling distance. *Composites Science and Technology*, *230*, 109723. https://doi.org/10.1016/j.compscitech.2022.109723.

[359] **Zhang, Y.**, **Anderson, N.**, **Bland, S.**, **Nutt, S.**, **Jursich, G.**, & **Joshi, S.** (2017). All-printed strain sensors: Building blocks of the aircraft structural health monitoring system. *Sensors and Actuators A: Physical*, *253*, 165–172. https://doi.org/10.1016/j.sna.2016.10.007.

[360] **Wang, X.**, **Li, J.**, **Song, H.**, **Huang, H.**, & **Gou, J.** (2018). Highly Stretchable and Wearable Strain Sensor Based on Printable Carbon Nanotube Layers/Polydimethylsiloxane Composites with Adjustable Sensitivity. *ACS Appl. Mater. Interfaces*, *10*, 7371–7380. https://doi.org/10.1021/acsami.7b17766.

[361] **Song, X.**, **Liu, S.**, **Gan, Z.**, **Lv, Q.**, **Cao, H.**, & **Yan, H.** (2009). Controllable fabrication of carbon nanotube-polymer hybrid thin film for strain sensing. *Microelectronic Engineering*, *86*, 2330–2333. https://doi.org/10.1016/j.mee.2009.04.012.

[362] **Zhao, H.**, & **Bai, J.** (2015). Highly Sensitive Piezo-Resistive Graphite Nanoplatelet–Carbon Nanotube Hybrids/Polydimethylsilicone Composites with Improved Conductive Network Construction. *ACS Appl. Mater. Interfaces, 7*, 9652–9659. https://doi.org/10.1021/acsami.5b01413.

[363] **Her, S.-C.**, & **Hsu, W.-C.** (2020). Sensing Performance and Mechanical Properties of Buckypaper Impregnated with Epoxy Resin. *Nanomaterials (Basel), 10*, 2258. https://doi.org/10.3390/nano10112258.

[364] **Jehn, J.**, **Oser, P.**, **Courrau, M.A.M.**, **Kaiser, M.**, **Wu, D.**, **Grosse, C.U.**, **Moosheimer, U.**, **Ruediger, A.**, & **Schindler, C.** (2021). Fully Inkjet-Printed Carbon Nanotube-PDMS-Based Strain Sensor: Temperature Response, Compressive and Tensile Bending Properties, and Fatigue Investigations. *IEEE Access, 9*, 72207–72216.

[365] **Huber, R.**, **Eizaguirre, S.**, **Mescher, H.**, **Willig, C.**, **Zhang, Q.**, & **Lemmer, U.** (2023). Fully Printed Temperature Sensor Array Comprising 625 60×60 μm2 pixels. *Advanced Sensor Research*, *2*, 2200031. https://doi.org/10.1002/adsr.202200031.

[366] **Buga, C.S.**, & **Viana, J.C.** (2024). Development and characterization of flexible carbon temperature sensors: a study on different inks and sensor designs. *Sensors and Actuators A: Physical*, *378*, 115823. https://doi.org/10.1016/j.sna.2024.115823.

[367] **Mahmoud, H.A.**, **Nesser, H.**, **Mostafa, T.M.**, **Ahmed, S.**, & **Lubineau, G.** (2025). A Fully Printable Strain Sensor Enabling Highly-Sensitive Wireless Near-Field Interrogation. *Advanced Science*, *12*, 2411346. https://doi.org/10.1002/advs.202411346.

[368] **Yao, J.**, **Tjuatja, S.**, & **Huang, H.** (2015). Real-Time Vibratory Strain Sensing Using Passive Wireless Antenna Sensor. *IEEE Sensors Journal*, *15*, 4338–4345. https://doi.org/10.1109/JSEN.2015.2416672.

CURRICULUM VITAE

Name Surname : Adel ALRAI

EDUCATION :

- **B.Sc.** : 2015, University of Sunderland, Mechanical Engineering
- **M.Sc.** : 2019, Istanbul Technical University, Mechanical Engineering, Materials and Manufacture

PROFESSIONAL EXPERIENCE AND REWARDS:

- 2019 – 2025: Researcher at ITU Aerospace Research Center
- 2022: 2224-A Grant Program for Participation in Scientific Meeting Abroad-TUBITAK

PUBLICATIONS, PRESENTATIONS AND PATENTS ON THE THESIS:

- **Alrai, A**., Yildiz, A., Zırhlı, O., Köken, D., Cebeci, F. Ç., Yıldız, K., Cebeci, H. "*A comparative study on the pattern effect of screen-printed CNT/CNC strain sensors*". Submitted to Sensors and Actuators A: Physical.
- **Alrai, A**., Beyhan, E., Asadi, A., Ozden-Yenigun, E., Cebeci, H. "*Tailoring Piezoresistive Response of Carbon Nanotubes Sensors by Hybridization of Cellulose Nanocrystals for Composite Structures*". Sensors and Actuators A: Physical, Volume 362, 1 November 2023, Article 114633. https://doi.org/10.1016/j.sna.2023.114633
- **Alrai, A.**, Arslan-Çatak, D., Tepe, F., Yüksel, R., Köken, D., Yildiz, K., Yildiz, A., Cebeci, H. " *Wire and Wireless Carbon Sensors for Real-Time Material Health Monitoring*". Presented at LOPEC 2025 – Large-area, Organic & Printed Electronics Convention, 25–27 February 2025, Munich, Germany
- **Alrai, A.**, Yorulmaz, Y., Zirhli, O., Cebeci, F.Ç., Köken, D., Cebeci, H. "*Tailorable Multifunctional Sensors for Structural Health Monitoring of Composite Structures*". AIAA SCITECH 2024 Forum, 8 January - 12 January 2024, 2463. https://doi.org/10.2514/6.2024-2463

- **Alrai, A.**, Köken, D., Cebeci, H. "*Adhesive-free Carbon-based Strain Sensor: Influence of Geometrical Patterns*". 21st International Conference on Fracture, Damage and Structural Health Monitoring, 12–14 September 2023, Imperial College London, UK
- **Alrai, A.**, Ozden-Yenigun, E., Cebeci, F.Ç., Asadi, A., Köken, D., Cebeci, H. "*One-Step Method for Printing Strain Sensors on GFRP: Assessment of Sensor Pattern Effect*". Presented at the Twenty-Third International Conference on Composite Materials (ICCM23), 30 July – 4 August 2023, Belfast, UK
- **Alrai, A.**, Beyhan, E., Asadi, A., Özden-Yenigun, E., Cebeci, H. "*Toward Sustainable Active Cellulose Nanocrystals-Based Ink for Structural Health Monitoring*". In Composites Meet Sustainability – Proceedings of the 20th European Conference on Composite Materials (ECCM20), 26-30 June, 2022, Lausanne, Switzerland

OTHER PUBLICATIONS, PRESENTATIONS AND PATENTS:

- **Alrai, A**., Yildiza, A., Zırhlı, O., Köken, D., Cebeci, F. Ç., Yıldız, K., Cebeci, H. "*A comparative study on the pattern effect of screen-printed CNT/CNC strain sensors*". Submitted to Sensors and Actuators A: Physical.
- Kaan, Y., **Alrai, A.**, Erturk, M., Koken, D. Bozali, B., Zakaria, A.Z., Cebeci, F. Ç., Ozden-Yenigun, E., Cebeci, H. "*Morphology-Property Relationship in Radially Oriented Anchored Carbon Nanotubes on Polybenzimidazole Nanofibers*". Journal of Materials Science, June 2023. https://doi.org/10.1007/s10853-023-08620-2
- **Rai, A.A.**, Stojanovska, E., Akgul, Y., Khan M., Kilic, A., Safak, Y. "*Preparation of co PVDF/modacrylic/SiO2 nanofibrous membrane: Composite separator for safe and high performance lithium-ion batteries*". J Appl Polym Sci. 2021;49835. https://doi.org/10.1002/app.49835
- **Rai, A.A.**, Yanilmaz, M. "*High-performance nanostructured bio-based carbon electrodes for energy storage applications*". Cellulose 28, 5169–5218 (2021). https://doi.org/10.1007/s10570-021-03881-z
- **Rai, A.A.**, Stojanovska, E., Fidan, G., Yetgin, E., Polat, Y., Kilic, A., Demir, A., Safak, Y., "*Structure and performance of electroblown PVDF-based nanofibrous electret filters*". Polym Eng Sci. 2020;1–8. https://doi.org/10. 1002/pen.25372
- **Rai, A.A.**, Stojanovska, E., Kilic, A., Safak, Y., Demir, A. "*PVDF/Modacrylic-Based Nanofibrous Membrane as Separator for Battery Applications*". International Fiber and Polymer Research Symposium, May 2-3, 2019 Istanbul, Turkey
- **Rai, A.A.**, Stojanovska, E., Yetgin, E., Fidan, G., Kilic, A., Safak, Y., Demir, A. "*Developing and Characterization of PVDF-Based Electret Filter Media*". International Fiber and Polymer Research Symposium, May 2-3, 2019 Istanbul, Turkey